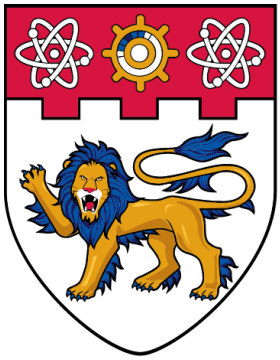

NANYANG TECHNOLOGICAL UNIVERSITY
SINGAPORE

Ionic regulation of mycobacterial infection by potassium and potassium channel

CAREY LIM FANG HUI

SCHOOL OF BIOLOGICAL SCIENCES

2022

Ionic regulation of mycobacterial infection by potassium and potassium channel

CAREY LIM FANG HUI

SCHOOL OF BIOLOGICAL SCIENCES

A thesis submitted to the Nanyang
Technological University in partial fulfilment of
the requirement for the degree of
Doctor of Philosophy

2022

Statement of Originality

I hereby certify that the work embodied in this thesis is the result of original research done by me except where otherwise stated in this thesis. The thesis work has not been submitted for a degree or professional qualification to any other university or institution. I declare that this thesis is written by myself and is free of plagiarism and of sufficient grammatical clarity to be examined. I confirm that the investigations were conducted in accord with the ethics policies and integrity standards of Nanyang Technological University and that the research data are presented honestly and without prejudice.

24 May 2022

.....
Date

.....
CAREY LIM FANG HUI

Supervisor Declaration Statement

I have reviewed the content and presentation style of this thesis and declare it of sufficient grammatical clarity to be examined. To the best of my knowledge, the thesis is free of plagiarism and the research and writing are those of the candidate's except as acknowledged in the Author Attribution Statement. I confirm that the investigations were conducted in accord with the ethics policies and integrity standards of Nanyang Technological University and that the research data are presented honestly and without prejudice.

24 May 2022

.....
Date

.....
DR. AMIT SINGHAL

Authorship Attribution Statement

This thesis contains material from one paper published in the following peer-reviewed journal in which I am listed as an author. Chapter 3 contains material published in:

Ricardo C. H. del Rosario*, Jeremie Poschmann*, Carey Lim#, Catherine Y. Cheng#, Pavanish Kumar, Catherine Riou, Seow Theng Ong, Sherif Gerges, Hajira Shreen Hajan, Dilip Kumar, Mardiana Marzuki, Xiaohua Lu, Andrea Lee, Giovani Claresta Wijaya, Nirmala Arul Rayan, Zhong Zhuang, Elsa Du Bruyn, Cynthia Bin Eng Chee, Bernett Lee, Josephine Lum, Francesca Zolezzi, Michael Poidinger, Olaf Rotzschke, Chiea Chuen Khor, Robert J. Wilkinson, Yee T. Wang, George K Chandy, Gennaro De Libero, Amit Singhal & Shyam Prabhakar. *Histone acetylome-wide associations in immune cells from individuals with active Mycobacterium tuberculosis infection*. Nature Microbiology, 7(2), 312-326. (2022) DOI: 10.1038/s41564-021-01049-w

*, # these authors contributed equally

The contributions of the co-authors are as follows:

- Drs. Amit Singhal and Shyam Prabhakar provided guidance for the manuscript content and edited the manuscript drafts.
- Ricardo C. H. del Rosario and Jeremie Poschmann generated the libraries for H3K27Ac ChIP Sequencing and performed bioinformatics analysis.
- I performed the following experiments for the manuscript: Western immunoblotting, immunofluorescence imaging, apoptosis assays, CFU enumeration assays, growth curve assay and analysis of bulk RNA-seq data, which are included in Figure 5 and Extended Data Figure 4 of the manuscript.

24 May 2022

.....
Date

.....
CAREY LIM FANG HUI

Table of Contents

ACKNOWLEDGEMENTS

I would firstly like to thank NTU School of Biological Sciences for offering me a PhD candidature and A*STAR Graduate Academy for the support and funding over the past four years and more. Accordingly, I would also like to thank A*STAR Singapore Immunology Network (SIgN) for accepting me as a student under the NTU-NUS-SIgN PhD programme, and providing a conducive scientific environment for my work and growth. Subsequently, I would like to thank A*STAR Infectious Diseases Labs (ID Labs) for taking over my studentship and nursing an exciting scientific habitat revolving around infectious disease. I am grateful to my supervisor, Dr Amit Singhal, for taking me under his wing, mentoring and providing what was necessary for this project. I would also like to extend my gratitude to my co-supervisor, Assoc Prof Kevin Pethe, and Thesis Advisory Committee (TAC) members – Prof Christiane Ruedl, Assoc Prof Su I-Hsin, Prof George Chandy, and Qualifying Examination Panel member – Assoc Prof Pablo Bifani, for taking time out of their busy schedules to provide invaluable advice toward this project.

Next, I would like to express my thanks to my lab members: Research officers Mardiana Marzuki, Andrea Lee and Kimberly Lim for their patient mentorship in many techniques and BSL3 training, friendship and administrative support over the years. Research Fellows Dr Dilip Kumar for imparting valuable skills especially in molecular biology and always being keen to discuss science, Dr Fang Wenning, who is akin to an older sister to me, Dr Chen Yao, who has been very humble and helpful and Dr Thomas Loy who has been a constant supply of friendship, scientific banter and valuable encouragement. Past lab members whom I should acknowledge include Dr Catherine Cheng, Dr Julia Bohme and Louise Fraser. I am thankful for the great memories created in this lab. While not a fellow lab member, I also would like to extend my appreciation to my fellow PhD mate, Christopher Lee, who is a great friend and has unwaveringly provided me enormous support, both practically and emotionally. Additionally, I am grateful to the various SIgN platforms and service providers for making the work infinitely easier than it would be otherwise, as well as internal and external collaborators for their necessary contributions.

Outside of work, I would like to thank my parents for always supporting my decisions, making accommodations to my schedules, and providing for me such that I never needed to worry about anything. I also must thank my amazing partner, Zenn, for always having my back, making me laugh, quelling my anxieties and being hugely understanding over the last few years.

A strong social support network is paramount while traversing the PhD journey, thus each person named has been indispensable to my experience.

Lastly, but importantly, I would like to thank my God for His grace and for making all things beautiful in its time.

LIST OF FIGURES

LIST OF TABLES

ABBREVIATIONS

3-MA	3-methyladenine
AEC-I/II	Alveolar epithelial type I/II cells
AIM2	absent in melanoma 2
AM	Alveolar Macrophages
APC	Antigen-presenting cells
ATB	Active tuberculosis
ATP	Adenosine triphosphate
BafA	Bafilomycin A
BAL	Broncheoalveolar lavage
BCG	Bacillus Calmette Guérin
BM	Bone marrow
BMDM	Bone marrow-derived macrophages (mouse)
BUNV	Bunyavirus
CCL	CC chemokine ligand
cDC1/2	Conventional dendritic cells 1 or 2
CFU	Colony-forming units
ChIP-seq	Chromatin-immunoprecipitation sequencing
cMoP	Common monocyte progenitor
CMP	Common myeloid progenitor
CRISPR	Clustered Regularly Interspaced Short Palindromic Repeats
CV	Caudal vein
CXCL	CXC chemokine ligand
DA	Differentially acetylated
DAMPS	Damage-associated molecular patterns
DCR-1	Down syndrome chromosome regioni-1
DCs	Dendritic cells
DC-SIGN	DC-specific intercellular adhesion molecule-3 grabbing nonintegrin
DEGs	Differentially expressed genes
DMGs	Differentially methylated genes
EAE	Experimental autoimmune encephalomyelitis
EIS	Enhanced intracellular survival
ELISA	enzyme-linked immunosorbent assay
EV	Extracellular vesicles
FAO	Fatty acid oxidation
FDR	False discovery rate

GFP	Green fluorescent protein
GM-CSF	Granulocyte-macrophage colony-stimulating factor
GMP	Granulocyte-monocyte progenitor
H&E	Hematoxylin and eosin
HAWAS	Histone acetylome-wide association study
HDAC1	Histone deacetylase 1
HDT	Host-directed therapeutics
HIF1α	Hypoxia-inducible factor alpha
i.t.	Intra-tracheal
i.v.	Intravenous
iBALT	Inducible bronchus-associated lymphoid tissue
IFNγ	Interferon gamma
IL	Interleukin
IMs	Interstitial macrophages
INH	Isonizaid
iNOS	Inducible nitric oxide synthase
IPG-4	ION potassium green 4
K^+	Potassium
K2P	Two-pore potassium channel
Kca	Calcium-dependent potassium channel
KCNJ	Potassium Inwardly Rectifying Channel Subfamily J
Kir	Inwardly rectifying potassium channel
Kv	Voltage gated potassium channel
LDN	Low-density neutrophils
LPS	Lipopolysaccharide
LT/ST-HSC	Long term/short term hematopoietic stem cell
LTBI	Latent tuberculosis infection
M.m	Mycobacterium marinum
ManLAM	Mannose-capped lipoarabinomannan
MCs	Monocyte-derived macrophages (mouse)
M-CSF	Macrophage colony-stimulating factor
MDM	Monocyte-derived macrophages (human)
MDR-TB	Multi-drug resistant tuberculosis
MDSC	Myeloid-derived suppressor cells
MHC	Major histocompatibility complex
Mm	Mycobcaterium marinum

MOI	Multiplicity of infection
MPP	Multipotent progenitor
mROS	Mitochondrial reactive oxygen species
Mtb	Mycobacterium tuberculosis
mTOR	Mammalian target of rapamycin
NAC	N-acetyl-cysteine
NAD^+	Nicotinamide adenine dinucleotide
NETs	Neutrophil extracellular traps
NF-κB	Nuclear factor kappa B
NK cells	Natural killer cells
NLRP3	NLR family pyrin domain containing 3
NMDG	N-methyl-D-glucamine
NO	Nitric oxide
NSAID	Non-steroidal anti-inflammatory drugs
OCR	Oxygen consumption rate
PAMPs	Pathogen-associated molecular pattern
PCA	Principle component analysis
PCR	Polymerase chain reaction
PI	Propidium iodide
PMA	Phorbol 12-myristate 13-acetate
PMN-MDSC	Polymorphonuclear myeloid-derived suppressor cells
PRR	Pathogen recognition receptor
RNA-seq	RNA sequencing
RNI	Reactive nitrogen intermediates
ROS/ROI	Reactive oxygen species/intermediates
RPKM	Reads Per Kilobase of transcript per Million
RT-qPCR	Quantitative real time polymerase chain reaction
siRNA	Small interfering RNA
SNP	Single nucleotide polymorphism
SSAT	spermidine/spermine acetyltransferase
T2D	Type 2 diabetes
TB	Tuberculosis
TGF-β	Transforming growth factor beta
TLR	Toll-like receptor
TM	Transmembrane
TMRM	Tetramethylrhodamine

TNFα	Tumour necrosis factor alpha
TNT	Tuberculosis necrotizing toxin
TPM	Transcripts per million
TpMo	Transitional pre-monocytes
TSS	Transcription start site
WT	Wild-type
XDR-TB	Extensively drug resistant tuberculosis
YFP	Yellow fluorescent protein

SUMMARY

Gene expression studies on whole blood from active tuberculosis (ATB) patients suggest that alterations in pathways such as interferon signalling, inflammation, apoptosis and pattern recognition receptor signalling may contribute to TB pathogenesis. Our group performed an epigenetic (Histone Acetylome-Wide Association Study, HAWAS) and transcriptomic analysis of blood $CD14^+$ monocytes and granulocytes from ATB patients, which demonstrated robust upregulation of acetylation near the *KCNJ15* gene that coincides with increased *KCNJ15* expression. *KCNJ15* encodes Kir4.2, an inwardly rectifying potassium ion (K^+) channel. We investigated the function of *KCNJ15* during mycobacterial infection *in vitro* in the monocyte-macrophage system, as well as *in vivo* using a knockout mouse model. *In vitro* experiments revealed that *KCNJ15* was indeed upregulated in monocytes and macrophages upon mycobacterial infection in a TLR2-dependent manner. Using a gain and loss-of-function approach, we show that *KCNJ15* plays a role in promoting inflammasome activation and apoptosis in human monocytes. Furthermore, its ability to localize to the lysosome may have implications for pathogen killing and other cellular processes. The *in vivo* study in mice found that loss of *Kcnj15* improved restriction of lung BCG burden at 14 days post-infection (d.p.i), which was associated with reduced $Ly6C^{hi}$ monocytes and increased macrophage and dendritic cell populations in the lung of infected mice. Moreover, BCG-infected $Kcnj15^{KO}$ AMs exhibited an altered gene expression profile which suggested dysregulation of cholesterol metabolism.

Potassium channels are important in regulating K^+ import and homeostasis, which is crucial to cellular function at steady state and during stress. The movement of K^+ ions across cell membrane can be dictated by high K^+ in the extracellular environment ($[K^+]_e$). We found that the microenvironment of necrotic mycobacterial granuloma possessed a high K^+ milieu. *In vitro* examination of the role of high $[K^+]_e$ in monocytes showed that K^+ influx resulted in mitochondrial dysfunction and ROS generation, which culminated in mTOR-mediated autophagy induction which aided in restricting *Mycobacterium tuberculosis* (*Mtb*) growth. Increasing systemic K^+ in zebrafish and mice models of mycobacterial infection appeared to bolster the acute inflammatory response, resulting in enhanced mycobacterial control.

In summary, we explored the role of a Kir channel, Kir4.2 (*KCNJ15*) and high $[K^+]_e$ on the acute host immune response against mycobacterial infection. This may provide insight into future potassium-homeostasis oriented host-directed therapeutics, such as the use of K^+ channel blockers and dietary supplements.

Chapter 1: Introduction

1.1 Tuberculosis

Tuberculosis (TB) is one of the leading infectious disease killers globally, surpassing HIV/AIDS in 2017, and only recently usurped by none other than SARS-CoV-2 in 2020. The latest World Health Organization (WHO) Global Tuberculosis Report estimated that 9.9 million people developed TB in 2020, while death rates increased to 1.5 million, partly owing to the COVID-19 pandemic and disruption of health services [2, 3]. Although the number of people who succumb to TB had been gradually decreasing prior to the COVID-19 pandemic, mathematical modelling estimated individuals carrying latent TB infection (LTBI) to comprise 23% of the population in 2014 [4]. The same people harbouring LTBI are at risk of presenting with the disease later in life [5], making TB disease a long-term healthcare problem.

The current standard treatment regimen for active TB entails a 6-month course of 4 first-line antibiotics (isoniazid, rifampicin, ethambutol and pyrazinamide) [1]. This imposes a huge burden on patients in terms of treatment complexity, duration and negative side effects experienced. While patients closely following the 6-month long regimen are typically effectively cleared of bacillary load, the long-drawn process invites the risk of toxicity and non-compliance that can lead to the development of drug-resistant TB. In fact, in 2017, 18% of relapse patients were found with multidrug-resistant TB (MDR-TB), which is harder to treat [5].

TB is perpetrated by *Mycobacterium tuberculosis* (*Mtb*), and most often presents as a chronic pulmonary disease. Infection occurs when *Mtb* enters the pulmonary system through the airways, and is often first phagocytosed by alveolar macrophages (AMs). Infected AMs carrying intracellular *Mtb* traverse into the lung interstitium initiating an anti-bacterial inflammatory response and signal for the further recruitment of innate responders [6]. Typically, the innate response may fail to establish sterilization, and forms the innate granuloma, consisting a mass of innate infiltrates harbouring live *Mtb* in its core. Over the course of the infection, antigen-presenting cells (APCs) engage the *Mtb*-specific adaptive response, leading to an influx of effector T cells and B cells into the lung. Eventually, infiltrating lymphocytes establish a physical mantle around the innate granuloma, encasing innate cells (primarily macrophages) and *Mtb* within it, which is suggested to limit bacterial spread and inflammation to other parts of the lung parenchyma (Fig 1) [7, 8, 9, 10]. Some granulomas continue to harbour live *Mtb* which establishes dormancy within infection-permissive macrophages [11]. Eventually, various host-related factors such as immune suppression and deregulated pro-and anti-inflammatory signals can lead to the breakdown of granuloma structure, allowing re-activated *Mtb* to exit ruptured lesions and be transmitted through the airways (Fig 1) [8, 11].

Chronic *Mtb* infection thus famously results in lasting lung parenchyma damage, bronchiectasis and associated health problems such as coughing and breathlessness [12]. Indeed, individuals having a history of TB were at risk of developing chronic obstructive pulmonary disease (COPD) and also had a higher long-term mortality than the general population [13, 14]. Hence, it is certainly a priority for many researchers to seek out TB therapeutics, both for treatment and prevention of this chronic disease that can have long-lasting health effects.

1.2 Antibiotics and vaccines against TB

As mentioned, the current standard treatment for TB involves a 6-month long antibiotic regimen, which encompasses 4 months of isoniazid and rifampicin, followed by 2 months continuation with additional pyrazinamide and ethambutol administration [1]. This treatment method boasts a success rate of over 86% (2019 data), but can fall short when dealing with patients with MDR-TB, extensively drug-resistant TB (XDR-TB) or HIV co-morbidity[2]. Development of adverse side effects and the strict daily treatment routine often results in non-compliance, allowing drug-resistance to develop [1]. Recommendations from WHO suggest that MDR-TB cases are treated with a customized cocktail of four to six medicines which include second-line antibiotics like levofloxacin/moxiflocaxin, bedaquiline and linozelid and additional antibiotics where suitable [15]. Clearly, as drug-resistant TB infections continue to increase [2], we are in dire need of novel antibiotics and combinatorial treatment regimens for more effective treatment of TB.

Emerging from the almost 40-year dearth of new antimicrobials against *Mtb* was the now FDA-approved bedaquiline (2012) for the treatment of MDR-TB [16]. Bedaquiline is drug of the first of its kind, an inhibitor of mycobacterial F-ATP synthase which impairs ATP production that is necessary for *Mtb* replication as well as its survival in dormancy, giving it formidable bactericidal activity [17, 18]. However, its bactericidal ability is slightly delayed, most likely due to the time needed to deplete existing ATP stores [19].

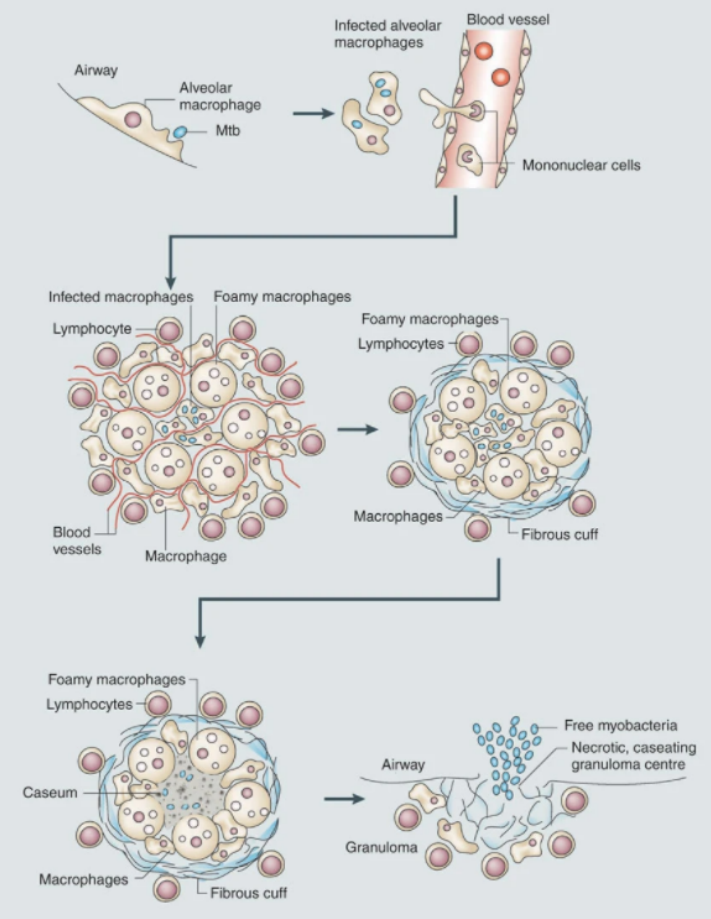

Figure 1. *Mtb* infection and development of the TB granuloma [8].

The nitromidazole, Delamanid, is another strong newcomer, a potent cell wall synthesis inhibitor that showed great efficacy in killing replicating, dormant and intracellular *Mtb*, and reduced sputum conversion time in drug susceptible TB patients [20, 21]. This drug provided favourable outcomes in drug-resistant patients when included in drug regimens [20, 21].

The most recently approved TB drug was Pretomanid, for use in conjunction with bedaquiline and linezolid (BPaL) to treat XDR-TB as a shorter and more effective treatment regimen (2019) [22]. Pretomanid is also a nitromidazole prodrug, acting as a mycolic acid cell wall synthesis inhibitor, similar to delamanid and isoniazid. In fact, a 2022 advisory from WHO suggested that the BPaLM regimen– comprising bedaquiline, pretomanid, linezolid and moxifloxacin, when employed against drug resistant infections, showed improved efficacy and safety [23].

While new developments in the antibiotic discovery arena are exciting, the prospect of antimicrobial resistance eventually rearing its head is still troubling. Furthermore, TB remains the top bacterial infectious disease, and the sheer number of TB patients implies that antibiotic usage is extremely high. In fact, resistance to bedaquiline in the clinical setting emerged quickly since

its approval and wide-spread use, with cases demonstrating cross-resistance to clofazimine [24, 25, 26]. We thus need to consider other tenable strategies to combat TB disease, such as its prevention via vaccination strategies.

The live-attenuated Bacille Calmette–Guérin (BCG) vaccine has been employed for just over a century [27]. The standard BCG vaccine administered intra-dermally to neonates is excellent at preventing infant mortality from extra-pulmonary TB. However, it is clear that the same provides poorer protection from pulmonary *Mtb* infection, the more prevalent disease form, which becomes even less efficient with age [28]. Numerous reasons explain the poor efficacy of intra-dermal BCG vaccination, including the limited delivery of antigen to draining lymph nodes for T cell activation and the poor induction of airway luminal T cells [29, 30]. Indeed, intra-dermal vaccination provided a decent systemic response but poor mucosal protection [31].

Numerous groups have taken to studying the BCG vaccine response using varying routes of administration. A recent study demonstrated that intra-venous BCG vaccination of macaques conferred profound protection against *Mtb* growth and lung pathology compared to intra-dermal and aerosol vaccination, and was associated with enhanced $CD4^+$ and $CD8^+$ T cell responses [32]. Many are also interested in studying the effects of mucosal BCG delivery. BCG administration through the intra-nasal route in mice showed effective pre-activation of alveolar macrophages, and was able to reduce lung burden of *Mtb* and *S. aureus* upon challenge [33]. The non-specific effect against *S. aureus* could be due to the known effect of BCG on trained immunity [34]. Another study also indicated that intra-nasal BCG induced a population of lung-resident mycobacteria-specific $CD4^+$ T cells and was associated with better protection against *Mtb* [35].

Novel mycobacterial vaccine candidates are also being explored. These include the use of novel mycobacterial antigens, killed whole-cell mycobacteria, and attenuated viable mycobacteria [36]. For example, aerosol immunization with an attenuated *Mtb* strain, *Mtb*Δ*sigH*, (comprising a regulon that promotes *Mtb* survival when exposed to host oxidative killing), induced the robust formation of inducible bronchus-associated lymphoid tissue (iBALT) structures, accumulation of memory $CD4^+$ and $CD8^+$ T cells in the airways, and enhanced control of *Mtb* burden, when compared to BCG vaccination [37]. Notably, MVA85A has already been tested in clinical trials, and was able to elicit robust Ag85A-specific Th1 responses in both HIV uninfected and infected patients that lasted up to six years [38]. Another promising candidate having underwent phase I/II clinical trials is M72/AS01, which also induces strong and long-lasting $CD4^+$ T cell responses [39].

Despite the need for improved and optimized TB vaccines, vaccine development and testing are invariably extremely long-term and expensive processes. With the high global incidence rate of TB, we still require flexibility in our treatment options. Since antibiotic development is a likewise

high-risk and complex process, it is in this light that we turn to consider alternative treatment options, such as host-directed therapeutics (HDTs) [40, 41].

1.3 Mtb-host interaction – Opportunities for host-directed therapeutics

Mtb interacts extensively with the host once it enters the airways. The fact that *Mtb* is often able to prevent phagolysosomal destruction and even escape from the phagolysosome, successfully surviving as an intracellular pathogen, indicates that there are many layers of the host cell anti-bacterial response that are hijacked by *Mtb* [42, 43]. A number of host-directed strategies have been tested with the purpose of enhancing killing of intracellular *Mtb*. HDTs that have demonstrated improved *Mtb* killing through means such as increased phagolysosome maturation, reactive oxygen species (ROS) production and autophagy induction include Sirtuin1 activators, baicalin, Metformin, Vitamin D, statins, Gefitinib and Imatinib (a tyrosine kinase inhibitor) (Fig 2) [44, 45, 46, 47, 48, 49, 50 51].

Aside from *Mtb* restriction at the cellular level, we know that *Mtb* infection elicits inflammation in the lung, which exacerbates lung pathology especially in chronic disease, where for example, a hyperactive Th17 response that leads to deregulated neutrophil infiltration and tissue destruction is considered unproductive inflammation [52, 53]. Indeed, production of matrix metalloproteinases during infection also causes matrix destruction and cavity formation [54, 55]. Furthermore, lung tissue injury is directly correlated with TB mortality [56]. Thus, dampening chronic inflammation and tissue damage during TB is a central focus of HDT development. Anti-inflammatory HDTs are typically intended for use alongside conventional antibiotic treatment, and thus aim to reduce treatment duration and ameliorate long-lasting effects of lung damage. Of course, boosting bactericidal function is likely also correlated with earlier resolution of infection, which will naturally minimize damage caused by inflammation. Additionally, HDT candidates like Bevacizumab, an igG anti-VEGFA antibody, target *Mtb*-induced abnormal angiogenesis around granulomas, which can lead to reduced drug delivery, tissue hypoxia and stunted recruitment of immune cells [57].

To this end, numerous HDT candidates targeting inflammation and lung injury are published in the literature, some of which are being evaluated in clinical trials. These include, but are not limited to, matrix metalloproteinase (MMP) inhibitors, non-steroidal anti-inflammatory drugs (NSAID), corticosteroids, phosphodiesterase inhibitors, statins and Metformin and are detailed in Figure 2 [44, 46, 51, 58, 59, 60, 61, 62].

HDTs presents a practical and convenient way to design combinatorial therapy for the best outcome in TB disease treatment as many of the investigated drugs are already FDA-approved

for treatment of other clinical conditions. Furthering the development of therapeutics that modulate the host requires a comprehensive understanding of the host response during *Mtb* infection, which is no small feat considering the myriad of immune and non-immune cell types that come into contact with *Mtb* and also engage in a coordinated response to the infection. In the next chapter, we highlight some of the key players in the response to *Mtb* infection, and their unique roles in *Mtb* restriction and pathology.

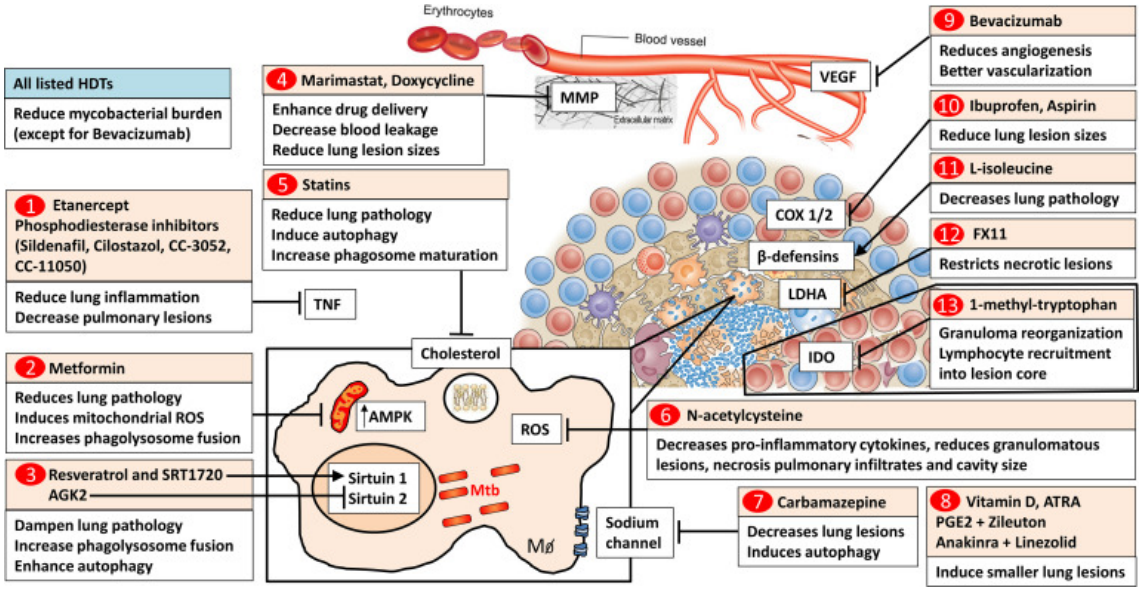

Figure 2. Illustration of host-directed therapeutics under study and their mechanisms-of-action in countering *Mtb* infection and pathology, by Guler *et al.* (2021) [57].

1.4 Immune cells and host response to Mtb

1.4.1 Neutrophils

Neutrophils are one of the first responders to pulmonary insult, efficiently migrating to the lungs during mycobacterial infection and playing a crucial role in the early response to *Mtb* infection. In fact, early depletion of neutrophils led to higher CFU burden in lungs, whereas late depletion after 2 weeks did not have a similar effect [63]. Conversely, another study showed that depletion of neutrophils a day prior to *Mtb* infection resulted in no change in CFU or survival of mice but inhibited granuloma formation [64]. In a zebrafish model of *M. marinum* infection, neutrophils are recruited to the early granuloma in response to dying macrophages and carry out bacterial killing via oxidative mechanisms [65]. Importantly, neutrophil count or neutrophilia in human patients was positively associated with severity of TB and mortality [66, 67].

Neutrophils were shown to actively carry *Mtb* in the airways of active TB patients [68]. At a cellular level, neutrophils are armed with an arsenal of antimicrobial functions. Neutrophils produce neutrophil extracellular traps (NETs), which are able to trap and immobilize *Mtb*, preventing its dissemination and is suggested to promote the effective concentration of delivered antimicrobial agents [69, 70]. NETs are also phagocytosed by macrophages which induces their activation and inflammatory cytokine production [71]. Neutrophils also commonly utilize oxidative burst to neutralize bacterial pathogens [72]. Additionally, neutrophil-produced enzymes Cathepsin G and elastase are vital for controlling lung mycobacterial load, exerting potent antimicrobial functions [73]. *Mtb*-infected neutrophils also release extracellular vesicles (EVs) containing TLR2/6 agonists, that can trigger macrophage activation and release of pro-inflammatory cytokines such as TNFα and IL-6, as well as induce autophagy which contributes to bacterial killing [74].

Interestingly, patients with active TB were found to harbour an increased proportion of low-density neutrophils (LDNs) which correlated with disease severity. These low-density neutrophils were less able to carry out expected antimicrobial functions such as phagocytosis and NETosis and furthermore inhibited mycobacteria-specific T cell expansion [75, 76]. Importantly, LDNs have now been reported in various inflammatory conditions where they are associated with immunopathology [77, 78]. In this light, many have suggested that LDNs are immature neutrophils released during emergency hematopoiesis in response to infection and inflammation [79].

Besides executing direct bacterial killing, neutrophils also dabble in regulation of the innate-adaptive immune interface. Neutrophils, through TNFα production and direct binding with DC-SIGN receptors on immature dendritic cells (DCs), induce their maturation and boost activation of the Th1 response [80]. Similarly, neutrophil depletion delayed DC trafficking to lymph nodes and activation of CD4 response in a separate study [81]. This role of neutrophils in DC activation was suggested to be dependent on *Mtb*-induced apoptosis [82, 83].

Certainly, neutrophils are vital in the early response to mycobacterial infection, and can exert bactericidal activities and boost the activation of the adaptive arm. However, it is widely understood that neutrophilic inflammation is highly associated with pathologic lung injury during chronic TB disease [84 85]. Comparisons between genetically resistant and susceptible mice strains to *Mtb* infection showed that neutrophil recruitment was enhanced in susceptible mice [86]. Indeed, the cross-talk between immune players significantly influence neutrophil activity and its contribution to bacterial control or hyper-inflammation. For example, loss of nitric oxide (NO) production by macrophages in $Nos2^{-/-}$ mice led to increased neutrophil influx, providing a metabolically growth permissive niche for *Mtb* growth [87]. Because of this, targeting neutrophil accumulation in TB disease in the hopes to ameliorate lung damage is a glowing area of HDT

research [88, 89]. The antibiotic doxycycline is one such candidate which was demonstrated to reduce inflammatory gene expression in blood cells and ameliorate tissue-destructive MMP expression in sputum of TB patients, including MMP-8 and MMP-9 which can be secreted by neutrophils [90, 91].

However, it is important to consider at which stage of the disease course neutrophil recruitment should be restrained, considering its early contribution to *Mtb* killing and containment.

1.4.2 Alveolar Macrophages

Alveolar macrophages (AMs) reside within the airways and behave as sentinel cells which maintain airway homeostasis. Under steady-state conditions, they are largely responsible for the maintenance of the surfactant layer lining the airways [92]. Naturally, AMs are some of the initial immune cells to encounter any airborne pathogen that reaches the pulmonary system. With its phagocytic capabilities, AMs are able to uptake bacterial pathogens easily and can employ bactericidal mechanisms, such as the production and delivery of ROS and RNI and utilizing phagolysosomal destruction [93, 94]. *Mtb*-infected AMs are also fully able to respond with the production of pro-inflammatory cytokines [94, 95].

While they have the potential to control infection, it is recognized that AMs play a crucial role in permitting the establishment of *Mtb* infection and growth. Huang *et al.* showed that resident AMs, which are largely derived from fetal liver monocytes, are less able to control infection than monocyte-derived interstitial macrophages (IMs) [96]. Indeed, AMs, which preferentially engage fatty acid oxidation (FAO), were shown to be permissive to *Mtb* growth [96]. While airway infection with non-virulent BCG is largely contained in the airway AM locale, *Mtb*-infected AMs do not eliminate the pathogen but instead translocate into the lung interstitium, allowing the pathogen to be uptaken by other immune cells such as IMs, monocytes and neutrophils, and these translocated AMs exhibited a distinct transcriptomic profile from airway AMs [6, 97]. This phenomenon was dependent on both *Mtb* ESX-1 and host IL-1β production [6].

It may not be surprising that AMs may be less able to control *Mtb* infection since their normal function in the airway at steady state is more homeostasis focused. Even so, AMs could be primed or "trained" to enhance their ability to control *Mtb* infection. In an intra-nasal BCG vaccine model, BCG infection in the airways boosted AM expression of activation markers such as CD68 and iNOS, while transcriptomic analysis revealed enrichment of glycolytic genes in primed AMs. Consequently, vaccinated mice were better able to control a secondary challenge with *Mtb* at 7 months post-vaccination [33]. One study suggested that AMs patrol the airways and migrate toward bacterial pathogens in order to ingest them, concealing them from neutrophil detection and in

doing so, limit unnecessary inflammation [98]. Certainly, AMs may orchestrate a balance between *Mtb* killing and inflammation onset.

Additionally, AMs do not exist as a homogenous population [99, 100], which can contribute to heterogeneity in their response to intracellular mycobacterial infection. AMs are largely comprised of resident macrophages seeded during development, which are invariably exposed to airway pathogens and particulates and may die over the lifespan of the organism. While resident AMs populations are known to be self-renewing [101], it was also demonstrated that the AMs can be replenished by the mobilized bone-marrow monocyte pool, which is often the case during pulmonary infection, where monocytes are swiftly recruited to the lung in a CCR2-dependent manner and can differentiate into SiglecF^{lo} mo-AMs [102, 103].

All in all, AMs represent a population of immune cells that cannot be excluded from any analysis of *in vivo Mtb* infection, owing to their unique function, proximity to infection and heterogeneity.

1.4.3 Monocytes and monocyte-derived macrophages

Monocytes are innate cells which originate from bone marrow development, patrol in the periphery and are rapidly recruited to sites of infection through chemokine gradients, most notably through CCL2 stimulation [104, 105]. Based on phenotype and function, monocytes in mice are categorized into three subsets: Ly6C^{hi}CD43^{-} (classical), Ly6C^{+}CD43^{+} (intermediate), and Ly6C^{lo}CD43^{+} (non-classical) [106]. The corresponding monocyte subsets in human are: CD14^{+}CD16^{-} (classical), CD14^{+}CD16^{+} (intermediate) and CD14^{dim}CD16^{+} (non-classical) monocytes [107]. Monocytes are capable phagocytes, and are armed with the typical anti-bacterial arsenal, being able to eliminate intracellular bacteria through means such as phagolysosomal digestion, production of ROS and autophagy [45, 108, 109]. Many early studies on monocytes involved the induction of apoptosis by *Mtb* infection, which was found to be caspase-1-dependent and mediated by a 19kDa *Mtb* lipoprotein [110], a process that was suggested to be host-protective [111]. Many studies on monocytes in *Mtb* infection, however, are limited to *in vitro* infections of monocytic cell lines or primary cultures.

Monocytes have also been implicated in the concept of "trained immunity", a phenomenon where first exposure to stimulation or infection epigenetically and metabolically imprints the cell, allowing heightened protection against secondary infection[112]. This was famously demonstrated through monocyte stimulation with *C. albicans*-derived β-glucan, which resulted in a metabolic shift to glycolysis that was dependent on the dectin-1-Akt-mTOR-HIF1a axis, and provided protection against *C. albicans* and *S. aureus* infection [112]. β-glucan was then subsequently shown

to also elicit trained immunity in monocytes against *Mtb* infection in an IL-1-dependent manner [113].

While monocytes can certainly kill bacteria, it is unclear how much of its role in protection against *in vivo Mtb* infection is through direct killing, versus its capacity to differentiate into macrophages and DCs. Importantly, ablating inflammatory monocytes using CCR2-DTR mice during *Mtb* infection prevented trafficking of live bacteria to the mediastinal lymph node, limited $CD4^+$ T cell expansion and worsened lung *Mtb* burden, but was not directly responsible for CD4 priming [114]. Indeed, monocytes may have a pivotal function in *Mtb* dissemination to draining lymph nodes and peripheral organs, and T cell activation. Notably, in *M. marinum*-infected zebrafish, $CCR2^+$ monocytes have also been shown to partake in bacterial dissemination [115].

$CCR2^+$ monocytes migrate into the lungs and are also continuously recruited to replenish and maintain the immune granuloma [116, 117]. Indeed, adoptively transferred monocytes actively differentiated into iNOS-producing pulmonary macrophages and DCs in the *Mtb*-infected mice [118]. Monocyte-derived macrophages (MDMs) and other monocyte-derived cells (referred to as MCs) may play a significant role in resolving infections. Conventionally, monocytes contribute heavily to the interstitial macrophage population, but as mentioned, have also been found constitute mo-AMs during influenza infection [102]. Nonetheless, resident and monocyte-derived macrophage populations, hailing from separate ontologies, are well understood to deviate in their response to infection.

Dual-RNA sequencing of both AMs and IMs and *Mtb*-contained within each cell type revealed that IMs relied heavily on glycolytic metabolism, NO production and iron sequestration to control *Mtb* growth. Concurrently, *Mtb* which resided in IMs responded by upregulating iron acquisition-related genes, stress response and dormancy genes [119]. This suggests that IMs were indeed programmed to better hold *Mtb* infection at bay. Moreover, the divergent responses between *Mtb*-infected AMs and IMs were further found to be epigenetically regulated (differential chromatin openness compared to uninfected counterpart) [99].

Single-cell sequencing of *Mtb*-infected macrophages provided additional resolution to the rather heterogeneous pulmonary IM populations, distinguishing them into three sub-populations. The first (IM1) represented a tissue-resident population already present in uninfected mice that expressed *Zeb2* as a tissue residency marker, *Il1β*, *Nlrp3* and *IL-17A*-related gene signatures. IM2s leaned toward expression of complement factors and harbored an anti-inflammatory M2-like profile. IM3, conversely, inclined toward an M1 phenotype, up-regulating glycolysis, oxidative response and inflammatory genes, possessing a transcriptional profile intermediate to monocyte and macrophages [99]. This suggests that the role of each IM subset in controlling *Mtb* infection might be distinct.

Mtb infection is known to drive differentiation of monocytes into "foamy" macrophages, which are lipid-laden macrophages with heightened fatty acid uptake and utilization of FAO [120, 121]. Foamy macrophages are typically found surrounding necrotic regions in *Mtb* granulomas [122]. AMs typically already rely on FAO and are less able to control infection, thus being closer to an M2 macrophage phenotype [96, 123]. Thus, as primary targets of infection, they easily accumulate lipid inclusions, which is suggested to provide a metabolically beneficial niche for *Mtb* survival and dormancy [120]. Monocyte-derived IMs are initially differentiated into M1-like macrophages, which rely on glycolysis, NF-kB pathway activation and chemotaxis [119]. Studies have, however, shown that while *Mtb* virulence factor ESAT-6 drives initial M1 polarization, it later reprograms M1 macrophages into M2 phenotype [124]. Indeed, M2-like macrophages appeared to predominate in granulomatous tissue of *Mtb* patients [125]. Therefore, it is likely that both AMs and IMs, as well as recruited monocyte-derived macrophages can develop into mycobacterial-permissive foamy macrophages. *Mtb*, thus, first drives the inflammatory response to initiate granuloma formation, and then dampens macrophage bactericidal capabilities and creates for itself a niche for growth and survival. Hence, limiting foamy macrophage development is also a keen area for HDT research [120].

1.4.4 Myeloid-derived suppressor cells (MDSCs)

Myeloid-derived suppressor cells (MDSCs) typically represent two populations of immunosuppressive cells. Polymorphonuclear (PMN)-MDSCs are neutrophilic/granulocytic while M-MDSCs are monocytic and both develop in response to chronic inflammatory cytokine signalling [126]. In mice, both populations are currently difficult to distinguish from classical neutrophil and inflammatory monocyte populations, although new markers to distinguish MDSCs in humans are being discovered [127]. Indeed, MDSCs seem to play a role in numerous other pathologies but have been quite extensively studied in the context of cancer. MDSCs play an immunosuppressive role through various means such as (i) secretion of anti-inflammatory cytokines IL-10 and TGF-β, (ii) production of ROS and NO which signals anti-inflammatory M2 differentiation, (iii) reduction of available cardinal amino acids required for T-cell activation through Arg1 and iNOS expression and others [128].

The role of MDSCs in *Mtb* infection has come to the fore quite recently. Much of this was due to the technical limitations of isolating each MDSC population using specific markers, especially in mice [127]. We know that acute inflammation is beneficial for *Mtb* clearance but chronic inflammation worsens pathology. Therefore, the role of MDSCs in both acute and chronic stages of *Mtb* infection may be significant, but is still controversial [129].

A number of studies have examined MDSC populations in TB patients. Work on blood PMN-MDSCs from ATB patients and healthy controls determined that ATB patients had a higher frequency of PMN-MDSC, whereas M-MDSCs were not detected [130]. Furthermore, PMN-MDSC percentages were correlated with lower radiological disease severity in patients [130]. Indeed, another study found ATB patients harboured more $CD15^+$ MDSCs and these purified MDSCs effectively suppressed T cell proliferation [131]. Further, it was shown that increased blood MDSCs in ATB patients were effectively reduced after completion of TB antibiotic treatment [132]. Additionally, MDSCs were increased in non-necrotic granulomas from ATB patients and expressed higher Nos2, Arg1 and HIF1α, associating with a immunosuppressive phenotype [133].

In mice, PMN-MDSCs (designated by $Ly6G^+Gr1^{dim}CD11b^+$) accumulated in lungs, spleen and bone marrow 24 days post *Mtb* infection, prior to fatal disease. Adoptive transfer of these isolated induced-MDSCs from bone marrow into recipient mice followed by *Mtb* infection resulted in lower lung IFNγ levels, slightly increased wasting but no significant difference in bacterial burden [134]. MDSCs themselves do phagocytose *Mtb* and release both pro and anti-inflammatory cytokines (IL-6, IL1α, IL-10) [129]. At the metabolic level, tumour-associated MDSCs upregulate genes related to fatty acid accumulation and FAO, which was necessary for their immunosuppressive function [135]. As such, there may be implications of such metabolic reprogramming of MDSCs in the context of *Mtb* infection as increased lipid stores may provide a nutrient-rich intracellular environment for *Mtb* growth [136].

IL-4R is also seen to be expressed on MDSCs in tumours and blockade of this receptor by aptamers induced apoptosis of MDSCs [137]. Accordingly, a study utilizing DABIL-4, a diphtheria toxin-based fusion protein, to deplete $IL4R^+$ MDSCs in *Mtb*-infected mice resulted in increased proliferation of $CD4^+$ and $CD8^+$ T cells and reduced lung CFU [138]. Hence, although MDSCs and their specific function in either acute or chronic TB infection are not yet extensively delineated, they present a promising potential target for TB HDT development.

1.4.5 Dendritic cells (DCs) and the T cell response

While the present study focus primarily on the acute innate response to *Mtb* infection, the role that the adaptive arm plays in reigning in infection and inflammation is paramount. In primary infection, DCs play a key role in bridging the gap between the early response and initiating the adaptive response. As APCs, DCs recognize and uptake *Mtb* through various pathogen-associated molecular pattern (PAMP) interactions with pathogen-recognition receptors (PRRs). For example, *Mtb* lipoproteins such as LprA, LpqH and LprG, can engage TLR2 receptors [139]. DC-SIGN is also a pivotal receptor in DC-mycobacterial interaction, as it binds mycobacterial

ManLAM (a cell wall glycolipid) and allows for bacterial internalization and DC migration [140, 141].

With *Mtb* infection, the trafficking of migratory DCs to the draining lymph nodes and subsequent initiation of T cell expansion is delayed, taking up to 9-11 days post-infection, resulting in the arrival of activated T cells at the site of infection only after 14-21 days [142, 143]. The reason behind this delay is not fully understood, but it is suggested that antigen presentation by DCs deriving from the infected lung is impaired, and that live bacterial dissemination to the draining lymph nodes and *in situ* antigen production was necessary for $CD4^+$ T cell activation [144]. Furthermore, most of the bacilli are harboured by AMs during early infection, which are generally non-migratory, further delaying transport of *Mtb* to the draining lymph nodes [145]. To this end, another group showed that *Mtb* infection enhanced antigen export in a Kinesin2-dependent manner, reducing the efficiency of MHC class II antigen-presentation on infected DCs which limits $CD4^+$ T cell activation [146]. It is thus thought that neutrophils act as an antigen-shuttling middleman between AMs and DCs, being vital for DC antigen presentation [82, 145].

Even after the formation of the granuloma, DCs were shown to carry *Mtb* and emigrate away from the lesion, likely towards the lymph nodes. During this migration process, some DCs get arrested by mycobacteria-specific T cells and can eventually seed new granulomas, contributing to dissemination of lung pathology [147]. *Mtb*-infected DCs produce IFNαβ, which leads to CXCL10 production that potently recruits NK and T cells to the site of infection [148]. Loss of IL-12p40 was also demonstrated to inhibit DC migration and activation of naïve $CD4^+$ T cells [149]. Besides activation of $CD4^+$ T cells, DCs are also able to conduct Annexin-1-dependent efferocytosis and cross-present *Mtb* antigens to $CD8^+$ T cells. Animals deficient in Annexin-1 thus have impaired $CD8^+$ responses and poorer survival rates [150].

The $CD4^+$ T cell response is critical for host control of *Mtb* infection. Its primary contribution lies in the early production of IFNγ, which enhances $CD8^+$ T cell response, cytotoxicity and production of both IFNγ and TNFα [151, 152]. Mice that lack IFNγ indeed show uncontrolled *Mtb* growth and rapidly succumb to the disease [153]. IFNγ is crucial for macrophage activation during *Mtb*-infection, enhancing ROS production, inflammatory cytokine production and promoting metabolic shift towards glycolysis, which is known to be *Mtb*-restrictive, through the activation of the HIF1α master regulator [154, 155]. $CD4^+$ T cells are also capable of cytolytic activity [156].

The exact roles of $CD8^+$ T cells during *Mtb* infection are less clear. Activated $CD8^+$ T cells also produce inflammatory IFNγ and TNFα, which contribute to enhanced innate control of *Mtb* [152]. However, $CD8^+$ T cells are known to execute cytotoxic functions. Both $CD4^+$ and $CD8^+$ T cells, when stimulated with *Mtb in vivo*, could lyse *Mtb*-infected monocytes, however inhibition of perforin or CD95-CD95L interactions did not limit *Mtb* growth [157]. *In vivo* studies by adoptive

transfer of $CD8^+$ T cells however, demonstrated that they mediated significant protection against *Mtb* that was perforin-dependent [156].

Antigen presentation and activation of the T cell responses are thus important for *Mtb*-restriction, although immune evasion strategies by *Mtb* delay and impair the speed of the adaptive response, perpetuating the infection which contributes to the chronic nature of TB disease.

1.4.6 Alveolar epithelial type II cells

The pulmonary airway comprises three main cell types of interest: AMs, alveolar type I (AEC-I) and alveolar epithelial type II cells (AEC-II). AEC-I are the primary mediators of gas exchange in the alveolus, whereas AEC-II cells produce and secrete surfactant, regulating alveolus surface tension and demonstrate immune-modulatory capabilities [158]. As such, AEC-II cells are also regarded as the protectors of the airway.

Many *in vitro* studies utilize the human AEC-II cancer cell line, A549 to model AEC-II behaviour during infection. While AEC-II are not phagocytic cells by nature, they uptake *Mtb* during infection and allow intracellular replication [159]. Transcriptomic analysis of *Mtb* growing within A549 cells compared to in 7H9 media showed upregulation of various mycobacterial virulence factors as well as metabolic genes, indicating a suitable intracellular niche for *Mtb* replication [160]. Although AEC-II are non-immune cells, they still harbour mechanisms to limit infection. For example, AEC-II cells can actively secrete antimicrobial peptides in response to *Mtb* infection, such as β-defensins, hepicidin and cathelicidins [161, 162, 163].

During infection, AEC-II play a significant immune-modulatory function. These cells express Toll-like receptor 2 and 4 (TLR2, TLR4) as well as Nod-like receptors (NLRs) and are thus responsive to incoming airway pathogens [164, 165, 166]. Importantly, AEC-II are active producers of pro-inflammatory cytokines and chemokines in response to bacterial infections. To this end, it has been demonstrated that *Mtb*-infected A549 cells secrete IFNγ [167], and additionally, BCG infection also induces CXCL8, CXCL10 and IL-8 secretion, which are potent chemoattractants for neutrophils, monocytes and macrophages [168, 169, 170]. Furthermore, lung sections of active TB patients showed that AEC-II cells expressed IL-18 [171]. Clearly, AEC-II cells, which reside at the very site of initial infection, plays a considerable role in recruiting immune cells into the airways during early infection.

AEC-II can be also differentiated from AEC-I by their expression of MHC-II. While this invariably allows them to present antigen to $CD4^+$ T cells, whether or not they express the necessary co-stimulatory factors to successfully activate T cells remains controversial [172, 173].

However, it was demonstrated that T7 mouse AEC-II cell line pulsed with *Mtb* antigens was able to activate $CD4^+$ T cells from *Mtb*-infected mice but not from uninfected mice [172].

As cells which reside in the airway and come into direct contact with *Mtb* infection, AEC-II are not to be overlooked in their potential to modulate the immune response during infection.

1.4.7 Summary of Mtb-host interaction

The origins of TB disease is thought to date back thousands of years. Certainly, the *Mtb* bacilli has plagued and indeed co-evolved with humans [174, 175]. This is evident in its ability to subvert the host response, adapt to intracellular survival, impair efficient adaptive immune activation and incite granuloma formation to provide itself a nutrient-rich niche for dormancy and long-term survival. These strategies allowed TB to persist in the population and become a top infectious disease killer. Our understanding of the elaborate host response to *Mtb* infection thus provides the groundwork for the development of protective vaccines, antimicrobials and host-directed therapies, and are briefly summarized in Fig 3.

However, as much of the research into *Mtb* infection biology and pathogenesis is carried out using mouse models, there may be numerous inconsistencies when compared to *Mtb* infection in humans. For example, *Mtb* infection in humans are thought to be seeded by only a few bacilli, whereas most mouse models of infection have administered *Mtb* of CFUs in the range of 50-200 [176, 177], which can lead to confounding results. Similarly, only specific strains of mice are able to recapitulate caseous, necrotic granuloma pathology [178], demonstrating that genetic variations complicate our understanding of the host response to *Mtb* infection as modelled in mice. Hence, it is greatly valuable to conduct TB research in the human context, to attain a more accurate understanding of *Mtb* infection.

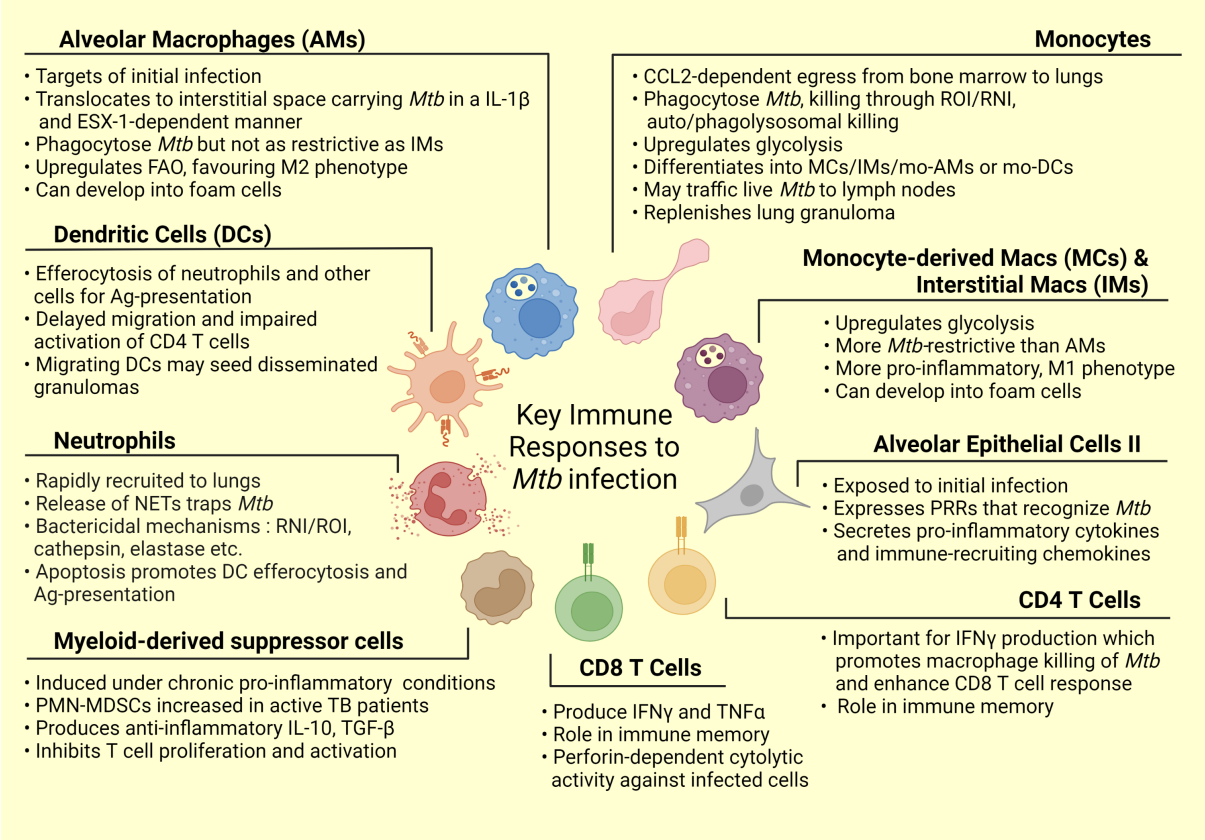

Figure 3. Summary of the key immune-related responses to pulmonary *Mtb* infection

1.5 Intracellular Mtb immune evasive mechanisms

Mtb is taken up by various phagocytic cells such as neutrophils, monocytes, macrophages and DCs. Within the host intracellular environment, *Mtb* engage numerous strategies to evade intracellular killing and subvert the host response. Ordinarily, phagosomes carrying bacteria mature and eventually fuse with lysosomes for pathogen eradication by hydrolytic enzymes. *Mtb,* however, is notorious for its ability to subvert killing by the phagolysosomal maturation process, being able to escape the phagosome, prevent phagolysosomal fusion and inhibit or resist killing by acidification (Fig 4).

Mtb is able to damage the phagolysosomal membrane and escape into the cytosol, a process that is dependent on ESAT-6 and the ESX-1 secretion system [179]. Concurrently, live *Mtb* also prevents phagolysosomal fusion by the retention of coronin-1, which typically coats phagosomes and are released prior to fusion, mediated by binding of mycobacterial protein CIP50 [180, 181]. Additionally, *Mtb* can also apparently de-regulate actin polymerization by the interaction of its surface protein heparin-binding hemagglutinin (HBHA) with G-actin, impairing phago-lysosomal fusion [182, 183]. The modulation of host Rab (Ras superfamily of GTPases) proteins, which decorate and regulate phagosome-endolysosomal maturation, by *Mtb,* has also been observed. Rab7-RILP interaction

is important for phagolyosomal fusion, however live BCG-containing Rab7-phagosomes fail to achieve RILP recruitment, suggesting that BCG may secrete factors that perpetuate Rab7 inactivity and prevent fusion [184, 185]. Additionally, Rab14 is recruited only to *Mtb*-containing phagosomes, and silencing of Rab14 released the block on phagolysosomal fusion [186].

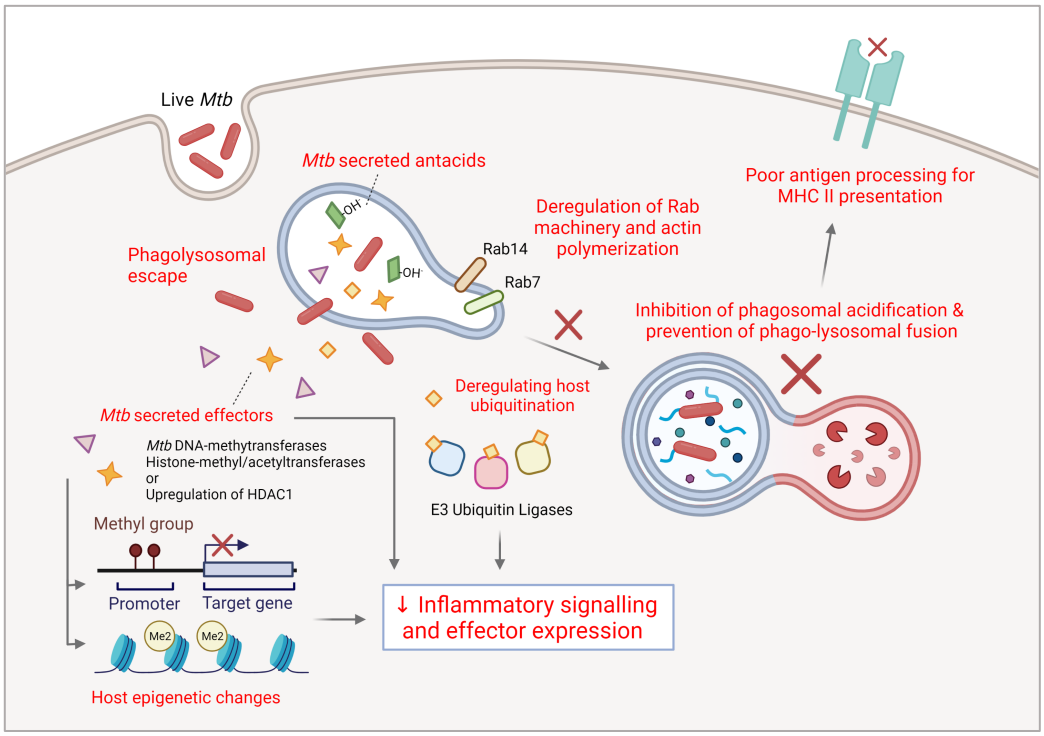

Figure 4. Illustration of host-evasive and host-modulating processes employed by *Mtb* during infection

Acidification of the phagolysosome is likely crucial for the optimal function of proteolytic enzymes, but this process is undermined by *Mtb* from many angles. *Mtb* was discovered to produce 1-TbAd, a lipid which accumulates in acidic organelles and acts as a strong conjugate base, neutralizing pH and causing lysosomal swelling [187]. The expression of *Mtb* potassium/proton antiporter *KefB* was also found to antagonize phagosomal acidification [188]. In a more roundabout way, a study also found that *Mtb* induced GM-CSF production in macrophages that resulted in STAT-signalling mediated CISH expression, which targeted the V-ATPase for degradation via ubiquitination, leading to impaired acidification [189]. Importantly, it is also thought that the phagosomal acidification step is in fact, a pre-requisite for phago-lysosomal fusion [190, 191]. In any case, it is abundantly clear that *Mtb* infection effectively disrupts phagosome maturation and lysosome-mediated killing. Furthermore, defects in phago-lysosomal fusion decreases the effectiveness of antigen processing and presentation, which can diminish the induction of protective immunity [192].

When *Mtb* escapes from the phagosome, bacterial nucleic acids are released into the cytosol where they can be detected by intracellular PRRs. *Mtb* genomic DNA activates AIM2 inflammasome, however it was shown that while non-virulent mycobacteria stimulated AIM2 inflammasome, virulent mycobacteria caused a significantly dampened AIM2 response by deregulating IFNβ signalling [193]. *Mtb* protein *pknF* was also found to inhibit NLRP3 inflammasome activation and IL-1β secretion in macrophages [194].

Another more recently explored strategy of *Mtb* immune subversion is its deregulating and hijacking of the host ubiquitin system. *Rv3354* was demonstrated to inhibit Cullin-based E3 ubiquitin ligase activity by binding to host metalloproteinase JAMM [195]. Further, *Mtb*-secreted effector PtPA was found to bind E3 ubiquitin ligase, TRIM27, and subsequently inhibit JNK/p38 MAPK signalling and apoptosis induction [196]. Another *Mtb* effector, Rv0222, was found to inhibit TRAF6 signalling-mediated NF-κB and AP-1 activation and thus inflammatory cytokine gene expression, through its ubiquitination by ANAP3 E3 ubiquitin ligase [197]. Indeed, *Mtb*-secreted factors actively co-opt the host ubiquitin ligases to promote its survival and diminish the inflammatory response.

Mtb intracellular infection and its secretion of potent effectors evidently precipitates extensive modulation of host proteins and cell-regulation processes. While the host senses *Mtb* infection and responds accordingly, *Mtb* is simultaneously adapted to overcome host restriction. It is difficult to delineate whether certain host responses are attributed to active manipulation by *Mtb*, or are host-evolved responses.

We next describe studies which interestingly examine how *Mtb* infection changes the host epigenetic landscape that in turn regulates transcriptomic gene expression.

1.6 Mtb and the host epigenome

Mtb is capable of altering the host epigenome to benefit its survival. One of the key ways it executes epigenetic changes is via the expression of various bacterial DNA methyltransferases that directly interact with the host genome.

Rv1988 is a *Mtb*-encoded histone methyltransferase that is secreted and localized to the host DNA where it can regulate gene expression. *Rv1988*-mediated H3R42me2, a histone mark at the DNA entry/exit region of the nucleosome, results in the dampening of immune activation and host inflammatory gene signatures, which include ROS and NO-production genes, *NOS2*, *NOX1,* and *TRAF3* [198]. In fact, XDR-TB strains express higher amounts of *Rv1988* [199]. *Mtb* also expresses a

secreted DNA methyltransferase, *Rv2966c*, which carries out methylation of host non-CpG dinucleotides, although the genes regulated are unclear [200].

Epigenetic editing does not stem from *Mtb*-derived methylases alone. In fact, studies have examined specific host-encoded mediators of the host epigenome modulation induced upon *Mtb* infection. For example, the induction by *Mtb* of *NQO1* and *TRXR1*, antioxidant genes important for dampening the bactericidal oxidative response, are mediated by SET8, a histone methylase that targets H4 lysine 20 (H4K20me1) [201]. Matrix metalloproteinases MMP-1 and MMP-3, which play a big role in tissue cavitation and damage, which are secreted by macrophages infected with *Mtb*, are also epigenetically regulated by histone modifications [202]. Further, *Mtb Rv3763*-mediated TLR2 signalling led to hypo-acetylation of the *CIITA* promoter and thus reduced expression of class II MHC molecules, which impairs antigen presentation [203]. This demonstrates that *Mtb* may hijack the host epigenetic processes to promote its survival and exacerbate pathology.

Studies have examined the epigenetic differences in patients with active TB compared to healthy controls. One study found global H3K14 hypo-acetylation and H3K27 hyper-methylation in PBMCs of active TB patients as well as a concomitant upregulation of histone deacetylase 1 (*HDAC1*) [204]. Indeed, the expression of *HDAC1* was also increased in *Mtb*-infected macrophages which correlated with global H3 hypo-acetylation [205]. Conversely, *Mtb* secreted enhanced intracellular survival (EIS) protein was shown to acetylate H3, elevating *IL-10* expression and inhibiting downstream autophagy induction in THP-1 macrophages[206].

Analysis of differentially DNA methylated genes (DMGs) from PBMCs in one study revealed autophagy as the top enriched pathway, and also found that hypo-methylation of anti-inflammatory mediator *FOXO3* in patients was associated with higher one-year mortality rates [207]. Interestingly, it also appeared that the majority of TB-related DMGs from this study were hypomethylated [207]. Another group found that monocyte-differentiated macrophages from active TB patients expectedly had significant differential DNA methylation profiles in immune pathway genes. Notably, patients had hyper-methylation of *IL17A* and *NF-κB* family genes [208]. Separately, DNA methylation status of *TLR2* in whole blood of TB patients was also assessed, which demonstrated that *TLR2* hyper-methylation correlated with increased gene expression in monocytes but decreased expression in NK cells, which was associated with disease severity and one-year mortality [209].

However, not all epigenetic changes in response to *Mtb* infection are pro-pathogen survival. Naturally, the host machinery also responds in order to restrict infection. For example, the NLRP3 promoter is de-methylated in response to *Mtb* infection, increasing its expression and thus enhancing the inflammatory response [210].

Evidently, a large portion of the literature on *Mtb*-mediated host epigenetic changes focused on DNA methylation and less on histone modifications. In the next section, we describe a study conducted by our group which demonstrated the effectiveness and reliability of studying histone modifications (namely, H3K27Ac) in innate immune cells from active TB patients, as a tool to understand crosstalk of *Mtb*-host interaction, and the subsequent investigation of a specific *Mtb*-infection associated gene-of-interest [211].

1.7 Mtb infection and modulation of KCNJ15/Kir4.2 – Outcome of TB-HAWAS study

Our group recently conducted a comprehensive histone acetylation-wide association study (HAWAS) of peripheral blood monocytes and granulocytes from ATB patients and age-matched healthy controls from Singapore and South Africa [211]. Chromatin immunoprecipitation sequencing (ChIP-seq) for H3K27Ac (a marker for active enhancers/promoters) was conducted on $CD14^+$ monocytes and granulocytes, which was correlated with a RNA sequencing (RNA-seq) dataset. Analysis of differentially acetylated peaks in monocytes revealed an overall enhancement of voltage-gated potassium channel family members (*P*-value=9.8e-5). Most notably, the inwardly rectifying potassium channel subfamily J member 15 (*KCNJ15*) gene locus was ascribed 8 upregulated peaks, indicative of significant chromatin changes to this gene during *Mtb* infection. Transcriptomic data also corroborated this finding, showing that *KCNJ15* transcripts were upregulated in peripheral blood of active TB patients. Infection of primary monocytes with *Mtb* also showed increased *KCNJ15* expression, suggesting the induction of this channel to be a result of mycobacterial infection and not a marker of predisposition to TB disease [211]. This study, thus, forms the basis of our investigation into potassium (K^+) channel and K^+ homeostasis in the immune response to mycobacterial infections.

1.8 Clinical importance of K^+

Potassium (K^+) is the most abundant cation in living organisms, and plays vital functions in various physiological processes. Most of K^+ resides intracellularly, with only 2% of total body K^+ existing in the extracellular fluid [212]. In humans, serum K^+ levels are maintained generally between 3mM-8mM, falling below or going above this range would be considered hypokalemia or hyperkalemia respectively. Certainly, K^+ is tightly and efficiently regulated by the body primarily through the renal system, where most additional K^+ is secreted from the body in the urine or quickly up taken by cells, especially the muscles [213]. Elevated plasma K^+ also stimulates

aldosterone synthesis that promotes urinary K^+ secretion by the renal system [213]. The effects of hypo- or hyperkalemia are most salient in the arenas of heart and bone health.

K^+ exerts its effects on cardiovascular health through its direct regulation of blood pressure. Increasing dietary K^+ can indeed alleviate cardiovascular risk factors such as hypertension [214]. Hence, reducing dietary sodium (Na^+) intake and increasing K^+ intake is recommended to lower blood pressure [215]. Increased K^+ can decrease Na^+ reabsorption in the kidneys, but this natriuretic effect cannot explain the entirety of K^+-mediated blood pressure reduction. While the specific mechanism behind this is not completely understood, it is thought that K^+ has effects on vascular tone and sympathetic nervous system, which can thus affect blood pressure [216]. A longitudinal study demonstrated that every additional 10mM of K^+ intake daily reduced 12-year mortality to stroke by 40% [217].

Increased K^+ intake is beneficial to bone strength. In fact, a trial of high dose organic K^+ salt supplementation reduced calcium loss [216]. However, there are mixed results regarding the mechanism that underlies this association [216]. One theory posits that the body regulates consumption of acidogenic diets by compensating with the release of alkali K^+ and Ca^{2+} from the bone, thus increasing K^+ intake can inhibit this process.

Additionally, K^+ is necessary for depolarization of pancreatic β-cells which allows insulin secretion. Thus hypokalemia causes glucose intolerance by inhibiting proper insulin action [215]. As such, sustained or severe dysregulation of K^+ in the body resulting in hypo- or hyperkalemia can have fatal consequences. Cardiac dysrhythmia is one of the most common and fatal outcomes of hyperkalemia that results from K^+ modulation of action potential physiology [218]. In the same vein, hyperkalemia can also result in peripheral neuropathy [219]. Conversely, hypokalemia occurs most often due to excessive loss of K^+ in the urine (kaliuresis) due to kidney disorders or diuretic usage, and leads to various health problems such as cardiac arrhythmias and heart failure, digestive tract paralysis, cramps and weakness and rhabdomyolysis [220].

Clearly, homeostasis and tight regulation of K^+ in the body is paramount, disruption of which, can cause extensive multi-organ damage. However, majority of K^+ stores are intracellular, suggesting that regulation of K^+ would also have profound effects at the cellular level.

1.9 Overview of potassium homeostasis in cells

This study posits that potassium and its homeostasis plays a significant role in the immune response to *Mtb* infection. At the cellular context, evidence reveals the far-reaching influence of potassium homeostasis beyond that of action potential regulation, extending to various cellular functions such as inflammation, cell motility and autophagy. Certainly, K^+ could affect these

cellular processes in a way that alters the immune response during infection, such as the migration of innate and adaptive immune cells to sites of infection, autophagic destruction of intracellular pathogens and initiation of the inflammasome response which will be detailed in section 1.14 [221, 222, 223].

In each of these processes, K^+ homeostasis is largely modulated by K^+ channels, which exist in various families and are differentially regulated. Understanding the roles of the large selection of K^+ channels encoded in our genome provides insight into how the simple process of potassium transport can affect health and disease.

1.10 Potassium channel families

K^+ channels are the largest superfamily of ion-selective channels, spanning over 80 subunit-encoding genes. Mammalian K^+ channels are thus abundant in variety and are expressed across various cell types heterogeneously. All K^+ channels possess a pore-loop which contains the consensus sequence T-X-G-Y(F)-G, and forms the selectivity filter for passage of K^+ ions [224]. The many K^+ channels can be classified by the number of transmembrane (TM) domains per subunit, with inwardly rectifying (Kir) channels, two-pore K^+ channels (K2P), and both voltage-gated (Kv) and calcium-activated K^+ (KCa) channels comprising 2 TM, 4 TM and 6 TM regions respectively (Fig 5) [225]. At a cellular level, most K^+ channels act transiently, responding to physiological cues, while a few exist in a constitutively active state [224]. While each subclass of K^+ channels are pivotal to specific functions and cell types, the most well-studied channels fall under Kv and KCa channel families.

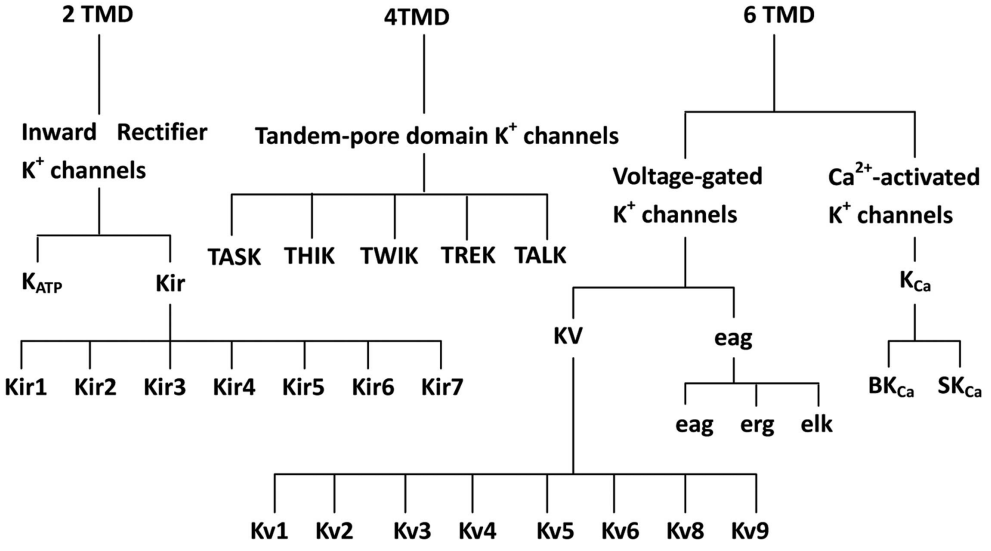

Figure 5. Potassium channel superfamily [225]

Naturally, Kv channels are highly sensitive to changes in membrane potential, making them important players in action potential physiology and thus in nervous system and cardiac function [226, 227, 228]. Kv channels have also been highly implicated in the activation of immune cells, mainly T cells, and regulation of vascular tone [229, 230, 231]. Some KCa channels can be voltage-sensitive, but they are all certainly sensitive to intracellular Ca^{2+} changes, making them susceptible to regulation by Ca^{2+}-mediated signaling [224]. KCa channels have thus been heavily implicated in processes such as neurotransmitter release, immune cell activation and regulation of smooth muscle tone [232, 233, 234, 235]. Kv and KCa channels and their widespread function in immune regulation are further described in section 1.11.

K2P channels, unlike Kv channels, are not regulated by membrane potential changes. Most K2P channels are pH-sensitive and are insensitive to classical K^+ channel blockers and were overlooked as most viewed their function as simply being leak channels [236]. K2P channels are involved in wide-ranging processes, such as renal reabsorption and inflammasome activation [236, 237, 238].

All members of the K^+ channel family dabble in K^+ ion transport, but appear to be differentially regulated, whether by changes in membrane potential, pH, cellular signaling or Ca^{2+} fluxes etc. Indeed, the large heterogeneity of K^+ transport channels demonstrates that there can be significant redundancy between channels, a fact that is important to bear in mind when dissecting the contribution of a single K^+ channel in a specific context. In fact, it is challenging to summarize a generic role for any one family of channels since they can have varying roles for different cell types and niches.

For the purposes of this study, we will examine more closely, the biology and literature behind the Kir channel family.

1.11 Kir channels

Inwardly-rectifying (Kir) potassium channels are encoded by the *KCNJ* gene family. All Kir channels share a similar topology, comprising two membrane-spanning transmembrane (TM) domains connected by a pore-forming loop (H5), and cytoplasmic N and C-termini (Fig 6A) [239]. A functional Kir channel comprises four subunits associating to form homotetramers or heterotetramers, some of which become associated with regulatory elements such as sulfonylurea regulatory components or G-proteins [239]. Also, Kir channels are readily inhibited by polyamine blockade and Mg^{2+} ions from the cytoplasmic side which can inhibit outward current [239].

The 15 members of the *KCNJ* family are classified into 4 subgroups; (1) K^+ transport channels, (2) Classical K^+ channels, (3) ATP-sensitive and (4) G-protein gated K^+ channels (Fig 6B) [239]. Indeed, the variation in function and regulation of each *KCNJ* family member is reflected in their significance in a wide range of diseases. However, only a few members of the *KCNJ* family have been well studied. Much of our understanding of Kir channel roles is derived from disease association with *KCNJ* gene mutations and polymorphisms.

KCNJ1, *KCNJ10*, *KCNJ13*, *KCNJ15* and *KCNJ16* encode channels that are classified as K^+ transport channels. Kir1.1 (*KCNJ1*) is almost exclusively expressed in the kidneys and male reproductive tissues, and mutations have been reported to cause Bartter's syndrome which manifests as defects in renal ion handling [240]. Kir4.1 (*KCNJ10*) is mainly expressed in the brain and kidneys as well. Most of the literature revolving around *KCNJ10* describe the effect of genetic mutations that have been implicated with EAST or SeSAME syndrome, which is short for and encompasses, the onset of epilepsy, ataxia, mental retardation, sensorineural deafness and electrolyte balance impairments [241, 242, 243]. Mice deficient in *KCNJ10* show similar symptoms, confirming the direct role of Kir4.1 loss-of-function in precipitating these phenotypes [241]. Mutations in *KCNJ16*, which has specific pH-sensitive properties, leads to renal salt wasting and metabolic acidosis [244]. Slightly different from the rest is *KCNJ13*, which is not well studied but is correlated with inherited retinal degeneration [245].

KCNJ2, *KCNJ4*, *KCNJ12* and *KCNJ14* encode channels that are classified as classical K^+ channels. While Kir2.2 (*KCNJ12*), Kir2.3 (*KCNJ4*) and Kir2.4 (*KCNJ14*) can be almost considered unstudied, Kir2.1 (*KCNJ2*), a constitutively active channel which exhibits strong inward rectification [239], has been widely studied. It is associated with cardiac function, whereby mutation and defective translocations lead to disorders such as familial atrial fibrillation and Andersen's syndrome [246, 247, 248]. Neutrophils have been found to express functional Kir2.1 channels which may be crucial to their function in a growth factor-dependent manner [249]. Blocking of Kir2.1 with ML133, a small molecule selective inhibitor, also inhibited migration, proliferation and microglial response to inflammatory stimuli, likely via modulating Ca^{2+} movement and signalling [250].

KCNJ3, KCNJ5, *KCNJ6* and *KCNJ9* encode G-protein-gated Kir channels. GIRK4/Kir3.4 (*KCNJ5*) is expressed in numerous organs such as the adrenal glands, lung, pancreas, heart and brain [239, 251]. Accordingly, *KCNJ5* mutations were well associated with the onset of sporadic and familial hyperaldosteronism. Mutations in the GIRK4 selectivity filter were determined to cause Na^+ entry and aberrant Ca^{2+} signalling, leading to aldosterone production [252]. Kir3.2 (*KCNJ6*) and GIRK3 (*KCNJ9*), on the other hand, is expressed almost solely in the brain, and are associated

with pain perception, reward-processing and addiction [253, 254, 255, 256]. A clear function of *KCNJ3* is not yet well established.

Famously, the ATP-dependent Kir6.2 (*KCNJ11*) has been broadly linked with diabetes aetiology. A portion of permanent neonatal diabetes cases have been attributed to activating mutations in *KCNJ11* [257]. Furthermore, patients responded to treatment by oral sulfonylurea drugs which target the sulfonylurea group regulating ATP-dependent Kir6.2 activity, replacing insulin treatment altogether [258]. Also, in adult type 2 diabetes (T2D) patients, the E23K polymorphism in *KCNJ11* was linked to increased susceptibility to T2D in Caucasian populations, weight gain and obesity [259]. *KCNJ8*, another ATP-dependent Kir channel, is widely expressed but is mostly unstudied except for some having implications in cardiac function [260].

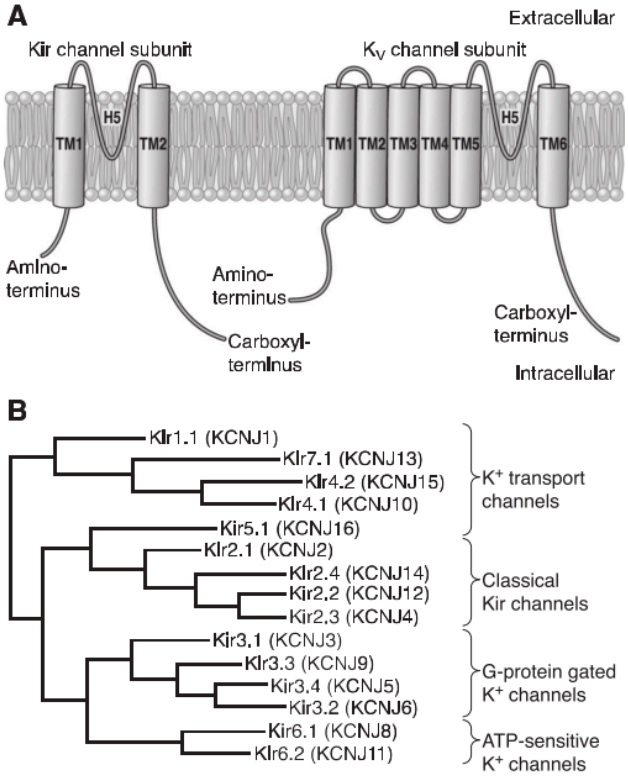

Figure 6. Kir channel structure and family members. A) Typical structure of a Kir channel subunit. **B)** Kir family channels and their classifications. Adapted from Hibino *et al*. [239]

1.12 KCNJ15/Kir4.2

Kir4.2 (encoded by *KCNJ15*) is less studied compared to some of its peers. Kir4.2 is expressed in many tissues of the body, but RNA expression is largely concentrated at the kidneys and endocrine organs [251]. Interestingly, single-cell transcriptomics of human blood immune subsets showed that neutrophils highly express *KCNJ15*, while monocytes also do so but at a much lower

level [261]. Kir4.2 can form either homotetramers or heterotetramers with Kir5.1, and is pH-sensitive [239].

Kir4.2 appears to dabble in the regulation of cellular secretion, such as that of gastric acid and insulin. In the stomach, mRNA expression of Kir4.2 is higher than any other potassium channel [262]. It was discovered that Kir4.2 remained dispersed in the cytoplasm in resting conditions but translocated to the apical membrane of parietal cells when stimulated with histamine [262]. Kir4.2 localization to the apical membrane is suggested to supply K^+ to facilitate H,K-ATPase transport of protons [263]. A separate study also revealed similar apical translocation in support of proton secretion in human airway gland serous cells of the lungs [264].

Kir4.2 has also been implicated in the context of glucose regulation and diabetes, with the increased expression of Kir4.2 mRNA in islets of Langerhans in patients with T2D. Furthermore, glucose stimulates Kir4.2 expression in INS1 cells *in vitro* while knockdown of Kir4.2 in diabetic and nondiabetic mice enhanced insulin secretion. This indicates that Kir4.2 suppresses insulin secretion in the islets, contributing to diabetes pathology [265]. The same group then conducted fine mapping of SNPs in Japanese patients with T2D and identified the SNP rs3746876 of *KCNJ15* as a new T2D susceptibility marker [266]. A later replication study limited this association to obese T2D patients in the Japanese population [267] .

Potassium channels are known to be pivotal to neuronal activity, hence it is no surprise that studies have also revealed potential involvement of Kir4.2 in neurodevelopmental and neurological disorders. A recent whole-genome sequencing study of Alzheimer's identified a common *KCNJ15* variant which could affect the age of onset of disease. Further network analysis of the datasets suggested that risk variants in *KCNJ15* locus could exert their effect through immune-related pathways [268]. Interestingly, in humans, *KCNJ15* is mapped to the Down syndrome chromosome region-1 (DCR1) on chromosome 21 which is suggested to harbour genes that contribute to the presentation of Down syndrome phenotypes [269]. *KCNJ6* is also mapped to the DCR1, where a specific mutation was also linked to Keppen-Lubinsky syndrome (with clinical symptoms resembling that of Down Syndome) [270]. However, so far no other genetic variations in *KCNJ15* have been discovered which manifest similar clinical features.

At a cellular level, Kir4.2 was recently suggested to be a sensor of weak electrical fields, allowing the cell to respond by galvanotaxis. Knockdown of Kir4.2 revealed a loss in directedness during galvanotaxis of corneal epithelial cells. It was discovered that the channel's link to cellular motility lay in its coupling with polyamine-catabolizing enzyme spermidine/spermine acetyltransferase (SSAT) which in turn, activate the channel by reducing polyamine blockade [271]. SSAT interacts with α9β1 integrin that can bind VCAM-1 expressed on endothelial cells [272, 273]. This gives us further understanding on how Kir4.2 affects transmigration and extravasation of

cells from the bloodstream. Further study into how metabolic control of polyamine levels affect Kir channel function could provide interesting mechanistic insights.

Evidently, Kir4.2 plays diverse roles in many cell types and cellular functions, however its role in innate immunity is yet to be explored. In this light, the functional consequences of Kir4.2 upregulation in the monocytes of *Mtb*-infected patients remains to be understood.

1.13 Potassium at the interface of pathogenesis and nutritional immunity

Nutritional immunity is a process which involves the hosts ability to control intracellular pathogens by restricting their access to essential nutrients. Intracellular metal ions such as iron (Fe^{2+} / Fe^{3+}), Copper (Cu^{2+}) and zinc (Zn^{2+}) are known to be important for host control of pathogens and are regularly manipulated by bacterial invaders in an attempt to evade immune destruction. Iron limitation is a strategy employed by the innate immune system to inhibit infection through means such as reducing iron reabsorption and removal of iron from the phagosome [274] [275, 276, 277] [278] [279] [280]. Changes in the ionic environment can also influence immune cell activation states which affect their ability to control infections. High NaCl was shown to prime a pro-inflammatory activation state of macrophages. AMs of mice fed a high-salt diet showed increased pro-inflammatory gene expression and aggravated inflammation in a model of acute lung injury [281]. A separate group also found that salt-induced pro-inflammatory macrophages worsened CNS autoimmunity in an experimental autoimmune encephalomyelitis (EAE) mouse model for multiple sclerosis [282].

Compared to the function of metal ions in nutritional immunity, the role of K^+ in the realm of host-pathogen interaction has been much less characterized. As single-celled organisms, bacteria thrive best when optimal intracellular K^+ levels are maintained to facilitate efficient cellular processes and metabolism. Many bacterial species have evolved potassium transport systems to cope with dynamic environmental challenges to manipulate K^+ availability and establish successful infection. Trk channels are a common K^+ transporter in bacteria that have a modest affinity for K^+ and primarily plays a role in K^+ uptake [283]. *S. typhimurium* lacking the Trk transporter was impaired in its ability to infect epithelial cells and led to reduced virulence in infected animals [284]. In a separate study, the gene *Rv3237c,* encoding for a TrkA family potassium transporter, was induced in *Mtb*-infected macrophages, suggesting that *Mtb* increases its K^+ uptake during infection [285]. Likewise, *F. tularensis* lacking the homolog TrkH was inhibited in bacterial growth, virulence and dissemination in the mouse [286]. While the Trk channel displays moderate affinity for K^+, a second K^+ transport system is de-repressed if it is not sufficient to supply the need for K^+. The Kdp transport system boasts a high affinity Kdp channel induced by species like *E. coli* to scavenge traces of K^+ in the environment [287]. The Kdp channel has also

been implicated in dormancy of *Mtb*, where it is upregulated during persistence in the host and is suggested to help scavenge K^+ in that state [288]. Also, deleting the *KdpDE* operon increased virulence of *Mtb* [289], highlighting the fact that K^+ homeostasis can affect bacterial infectivity and pathogenicity.

1.14 Potassium and potassium channels in regulating the immune response

While virulence and survival of bacterial pathogens can also be modulated by K^+ availability, our study focuses more on the host K^+ channels and homeostasis of K^+. Once again, research into K^+-mediated immune regulation is not very comprehensive compared to that of Ca^{2+}, Fe^{2+} and Zn^{2+}. Here, we briefly describe the existing literature implicating K^+ in the immune response in various contexts.

1.14.1 Inflammasome activation

The requirement of K^+ efflux for NLRP3 inflammasome activation is now common knowledge [290, 291]. However, its precise mechanism remains unknown. The NLRP3 inflammasome is triggered by a large variety of ligands such as PAMPs (bacterial components, viral RNA etc.),DAMPS (extracellular ATP, amyloid-ß etc.) which trigger non-canonical NLRP3, and crystalline substances like cholesterol crystals and silica particulate matter which induce canonical NLRP3 signalling [291]. Most NLRP3 stimuli, regardless of canonical or non-canonical pathway activation, converge on their requirement of K^+ efflux which is necessary and sufficient for inflammasome activation (Fig 7) [292].

Some have suggested that K^+ efflux is upstream of mitochondrial ROS (mROS) production in the activation of NLRP3. One study showed that K^+ efflux facilitates Ca^{2+} influx via the P2X7 receptor, and this Ca^{2+} signalling triggers mROS production which culminates in inflammasome activation [293]. This is supported by other work which showed that treatment with small molecules inducing mitochondrial dysfunction can trigger NLRP3 independent of K^+ efflux [294]. Recent studies also demonstrated that K^+ efflux was required for NEK7 interaction with NLRP3 which precedes inflammasome formation, shedding more light on the still poorly understood link between intracellular K^+ and inflammasome signalling [295, 296].

A few K^+ channels have now been linked to NLRP3 inflammasome activation and IL-1ß release. The K2P K^+ channel TWIK2 was shown to play a significant role in K^+ efflux in mouse macrophages during NLRP3 activation [237]. Another K2P channel, THIK-1, is endogenously expressed in microglia and its blockade reduces IL-1β production during activation [297]. Similarly, inhibition of MaxiK channel also prevented LPS-induced NFκB signalling and cytokine secretion [298]. Specific Kv1.5 blocker DPO-1 was also able to limit monosodium urate crystal-induced caspase-1 and IL1β release in LPS-primed macrophages [299].

On the other hand, studies have also shown that knockout of Kir6.2 and TREK1 enhanced NLRP3 activation and worsened inflammatory organ injury [300, 301]. Furthermore, Kir2.1 activation was associated with downregulation of NLRP3, caspase-1, IL-1β and IL-18 genes in H9C2 cardiomyocytes, seeming to play a role in ameliorating cardiac inflammation [302]. This suggests that during activation, some K^+ channels result in net efflux activating NLRP3, whereas others may reign in the degree of the response through K^+ influx. In addition, it is clear that the different channels could play a redundant role in K^+ transport leading up to inflammasome response, as their function and expression levels may differ across different cell types and tissue niches.

Recently, a known inhibitor of TWIK2 - ML365, was tested for its efficacy in limiting inflammasome activation, with potent results. In fact, pre-treatment with ML365 was also able to limit the severity of LPS-induced endotoxic shock [303]. Clearly, understanding K^+ channel and their role during inflammasome activation can lead to interesting avenues for anti-inflammatory therapy through utilizing K^+ channel blockers and activators.

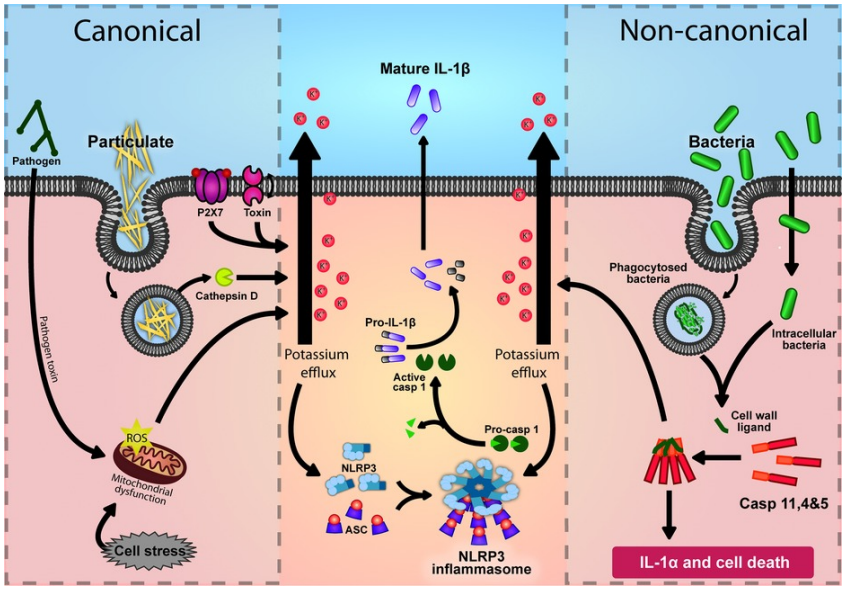

Figure 7. Canonical and non-canonical inflammasome activation and their convergence on K^+ efflux for NLRP3 activation by Rivers-Auty and Brough (2015) [292].

1.14.2 Immune activation

In the arena of K^+-mediated immune cell regulation, most of the focus has been placed on T cell activation. Recent publications have highlighted the importance of K^+ in regulating T cell responses in the context of tumour-infiltrating lymphocytes. Necrotic tumour tissue release their intracellular contents, creating a microenvironment saturated with K^+ (up to 40mM). Eil *et al.* found that increased extracellular K^+ ($[K^+]_e$) led to inhibition of T cell receptor (TCR)-driven

AkT-mTOR signalling and reduction of T cell effector programmes [304]. They later showed that high $[K^+]_e$ inhibited T cell nutrient uptake, leading to metabolic reliance on mitochondrial OXPHOS and reduction in available acetyl-CoA. This resulted in reduced histone acetylation and led to suppression of effector programmes while inducing stemness-associated programmes, enabling the T cells to control tumour growth effectively [305]. A separate study using human peripheral blood T cells suggested that high $[K^+]_e$-mediated T cell suppression was modulated by KCa3.1 [306].

It is interesting to observe that a simple change in $[K^+]_e$ could result in such profound cellular changes and exert an impact on tumour control. Many bacterial infections can result in cellular death by apoptosis, necrosis or pyroptosis. The latter two can occur as an endpoint of pathogen-mediated inflammasome activation or ROS generation and results in membrane rupture and release of intracellular contents [307].

In terms of K^+ channels, voltage-gated K^+ channel 1.3 (Kv1.3) has been widely studied for its role in the pro-inflammatory response and T cell activation. Kv1.3 facilitates the release of Ca^{2+} stores into the cytoplasm to initiate signalling and activation of T cell response by providing a counter ion K^+ efflux. Treatment with Kv1.3 blockers inhibit T cell Ca^{2+} signalling, cytokine production and reduce autoantigen-specific T cell proliferation, proving potentially useful as therapeutics for autoimmune diseases [308]. Furthermore, Clofazimine, which is known to block Kv1.3 channels and disrupt Ca^{2+} oscillation and signalling, administered following BCG vaccination, enhanced protection from *Mtb* by expanding BCG-specific effector memory T cells [309, 310]. Specific blockade of Kv1.3 with another inhibitor ImK, reduced $CD8^+$ T cell infiltration and cytotoxicity in a rat model of experimental EAE [311]. Indeed, deletion of Kv1.3 inhibited $CD4^+$ T cell migration into the CNS and shifted T cells into an immunomodulatory phenotype with increased IL-10 production in EAE [312]. In fact, high expression of Kv1.3 in $CD4^+$ and $CD8^+$ T-cells is correlated with pro-inflammatory IL-17a and TNFα in the ulcerative colitis model [313]. Kv1.3 is also highly expressed in microglia in patients with Alzheimer's disease, a disease now often associated with inflammation [314].

Besides T cells, K^+ channels have been noted to also modulate macrophage activation and inflammatory status. In a model of stroke which causes a significant inflammatory response, microglia were shown to upregulate Kir6.2, and treatment with glibenclamide (K_{ATP} blocker) was associated with neuroprotection [315]. Blockers of Kv1.3 such as margatoxin and charybdotoxin also limited macrophage migration and iNOS expression levels [316].

1.14.3 Immune cell migration

K^+ channels are greatly implicated in immune cell migration, where Kv1.3 and KCa3.1 take the spotlight. Gene silencing experiments in RAW264.7 macrophages revealed that Kv1.3 enhances migration via the activation of ERK [317]. Peritoneal administration of margatoxin also alleviated acute liver injury in mice by limiting inflammatory macrophage migration [318]. Indeed, Kv1.3 is highly expressed in inflammatory immune infiltrates consisting of T cells and macrophages in the multiple sclerosis brain [319].

Calcium-dependent K^+ channel (KCa3.1) is also pivotal in T cell activation and migration. Adenosine mediates inhibition of CD8 T cells migration into solid tumours which was reversed with administration of KCa3.1 activator 1-EBIO [320]. Aside from T cells, KCa3.1 is also necessary for mast cell activation and migration [321, 322]. Genetic silencing of KCa3.1 in neutrophils altered cell volume regulation and impaired chemotactic and chemokinetic abilities, causing reduction of neutrophils recruitment to the lungs during acute injury [323]. It is proposed that K^+ channels such as KCa3.1 are polarized on the rear end of a migrating cell, where Ca^{2+} intake and K^+ efflux leads to rear end retraction [324].

1.14.4 Cellular apoptosis

Mitochondrial Kv1.3 channel has been found to facilitate apoptosis of lymphocytes. During apoptosis induction, Bax was demonstrated to interact with MitoKv1.3, blocking the channel. The resulting hyperpolarization of the mitochondrial membrane led to ROS production and cytochrome c release [325]. Indeed, many other Kv channels have also been implicated in cellular apoptosis or survival in other cell types, such as Kv1.1, Kv1.5, Kv11.1 and Kv2.1 [326]. In fact, the authors later demonstrate that inhibiting Kv 1.1 and Kv1.3 also induces apoptosis in lymphocytes as well as macrophages [327]. Another study also showed that 1-EBIO, an opener of KCa channels, induced neutrophil production of mitochondrial ROS and apoptosis [328].

More generally, it was shown that low K^+ conditions induce apoptosis [329, 330]. Likewise, a drop in intracellular K^+ has also been demonstrated be required for apoptosome induction and caspase-1 activation [331, 332]. This phenomenon is interestingly similar to that of K^+ efflux preceding NLRP3 inflammasome activation, and may similarly be regulated by K^+ channels. Thus, K^+ homeostasis can strongly influence apoptosis induction in immune cells, which may be restrictive against intracellular pathogens, and prevent excessive inflammation [333, 334, 335].

1.14.5 Phago-lysosomal compartments and autophagy

While cell surface membranes are well-known to be embedded with various K^+ channels, the membranes forming phagosomes and subsequent endolysosmal structures may also carry these channels trafficked independently or originating from the surface membrane. A range of studies have since shown that intra-phagosomal K^+ regulation could be pivotal to the microbicidal functions of immune cells [336]. In neutrophils, killing activity was shown to be mediated through activation of proteases by K^+ flux. Superoxide (O^-_2) generation causes an influx of K^+ into the phagocytic vacuole for charge compensation, and the increase in ionic strength concurrently activates granule proteases [337]. In a similar vein, novel lysosomal channel TMEM175 was found to regulate lysosomal potential and pH and was necessary for effective phagolysosomal fusion [338].

One study tested the effect of common inhibitors of Ca^{2+} and K^+ transport in the killing of intracellular *Mtb* and found that efflux pump inhibitors enhanced killing by infected macrophages [339]. To explain this, the authors proposed a model; phagocytosis of *Mtb* through membrane invagination led to a phagolysosome where ion pumps extrude K^+ and Ca^{2+} from the vacuole to the cytoplasm. When phenothiazine, an ATP-sensitive K^+ channel inhibitor, is administered, the efflux of K^+ and Ca^{2+} from the phagolysosome is prevented. This causes the build-up of H^+, allowing the hydrolases to be activated leading to the digestion of the bacterium [340]. The importance of compartmentalized K^+has also been found in the context of viral infections. Bunyavirus (BUNV) can activate host K^+ channels, manipulating host cell K^+ currents to maintain its replicative cycle [341]. BUNV traffics through endosomes containing high [K^+], and inhibition of K^+ channels arrested virus trafficking.

The role of K^+ in regulating autophagy is not particularly well understood, but studies using specific K^+ channel activators and blockers have shed light on this process [342]. Kv11.3 (hERG3) activator - NS1643 was able to enhance autophagy induction via an AMPK-dependent pathway, while concurrently inhibiting cell proliferation [343]. Mitochondrial K_{ATP} channels have also been implicated in angiotensin-mediated autophagy induction in VSMC cells, although inhibition with 5-HD was suggested to limit autophagy by reducing ROS production [344]. Clarithromycin treatment also enhanced initial autophagic flux by blocking hERG1 interaction with PI3k and preventing Akt phosphorylation.

It is thus reasonable to suggest that the role of K^+ transport in phagolysosomal acidification is likely to provide a counter-ion for H^+ movement, while induction of autophagy by channel modulators has more of an indirect effect, stimulating autophagy via metabolic and oxidative cellular signals.

Evidently, K^+ channel modulation and movement of K^+ ions can have a significant impact on immune responses to bacterial infections at many different levels. As we consider how K^+ movement can affect the host response to *Mtb* infection, we focus our attention on the mycobacterial granuloma, a potential site for deregulated K^+ homeostasis.

1.15 The TB granuloma, necrosis and a role for K^+-mediate immune modulation

While the TB granuloma has been considered to be host-protective by limiting *Mtb* spread and hyper-inflammation, it is also the primary centre of lung tissue pathology and transmission [7]. The development and maintenance of granuloma integrity has been shown to be IFNγ and TNFα-dependent [345, 346, 347] . Studies have shown that each granuloma within a single host is distinct, exhibiting varying levels of sterilizing outcomes and necrotic pathology [348, 349]. In fact, a very recent study demonstrated time-dependent robust differences in immune cell composition and bacterial restriction in an individual granuloma in *Mtb*-infected macaques, that might result in a differential outcome [350]. Host dysfunction such as the stress response mediated by INF-I [351] and *Mtb*-induced ferroptosis [352], or the production of *Mtb* virulence factors including anti-inflammatory lipoxins which suppress macrophage membrane repair [353, 354], and NAD^+ depleting tuberculosis necrotizing toxin (TNT) [355] are examples of perturbations that have been shown to contribute to macrophage necrosis which may skew granulomas toward necrotic pathology.

Necrosis is characterized by the irreversible disruption of the plasma membrane and release of intracellular contents, which can lead to extensive inflammation if uncontrolled [356]. The nature of the microenvironment of granuloma centres undergoing necrosis is surprisingly understudied. In fact, few studies have directly assessed intra-granuloma conditions. It is widely accepted that hypoxic conditions exist within necrotic lesions [357, 358]. Other literature conject that the granuloma exists under high oxidative and nitrosative stress conditions, demonstrated in a guinea-pig model of *Mtb* infection, where granulomas stained strongly for glutathione and Nrf2 [359, 360].

During necrosis, the release of intracellular material such as intracellular ions can alters the immediate microenvironment of necrotic granulomas. K^+ is the cation of greatest abundance, ranging from 130-150mM intracellularly, whereas extracellular and serum K^+ levels typically lie between 3-8mM. Indeed, it is conceivable that necrosis of cells within granulomas results in a significant increase in extracellular K^+ ($[K^+]_e$) in the microenvironment, which may have noteworthy effects on neighbouring cells.

1.16 Aims and significance

We have previously demonstrated that *KCNJ15* is induced both at an epigenetic and transcriptomic level in monocytes of active TB patients, and that expression of *KCNJ15* is associated with mycobacterial control. We therefore hypothesize that *KCNJ15* is induced upon infection and enhances mycobacterial-restrictive cellular programmes, aiding in intracellular infection control. In order to investigate the mechanisms behind *KCNJ15* function in this context, the first aim of this study was to:

1) Delineate the role of *KCNJ15*/Kir4.2 in mycobacterial infection using *in vitro* and *in vivo* models.

To this end, we employed an *in vitro* gain and loss-of-function model using the THP-1 monocytic cell line, where *KCNJ15* was lentivirally overexpressed or knocked out using CRISPR-Cas9 system. Additionally, we generated a *Kcnj15* knockout mouse for *in vivo* studies.

Secondly, we hypothesize that necrosis occurring within mycobacterial granulomas allows intracellular K^+ content to be released into the microenvironment, resulting in higher extracellular K^+. Exposure to such increased K^+ concentrations could benefit intracellular mycobacterial control by surrounding innate cells such as monocytes and macrophages since CD8 T cells under similar conditions demonstrated improved tumour growth restriction [361]. Therefore the second aim of this study was to:

2) Investigate levels of $[K^+]_e$ in the necrotic mycobacterial granuloma and delineate the effect of high $[K^+]_e$ on innate immune control of intracellular mycobacterial infection.

Necrotic mycobacterial granulomas were investigated for their extracellular K^+ content using a zebrafish model of *Mycobacterium marinum* infection, as well as a mouse model of hepatic granuloma formation. The mechanistic effect of high $[K^+]_e$ on monocyte and macrophages were explored *in vitro*.

K^+ channels are popular druggable targets, with many broad-spectrum and specific inhibitors and activators already in the market. Besides Ba^{2+} which blocks Kir channels in general, a specific blocker of Kir4.2 has not yet been discovered. Understanding whether *KCNJ15*/Kir4.2 expression is host protective or detrimental during mycobacterial infection in terms of mycobacterial restriction and inflammatory phenotype will allow us to consider the development of Kir4.2-specific activators or blockers to enhance mycobacterial clearance or limit pathogenic inflammation. As always, gaining comprehensive knowledge on the biology of a target in a specific context is key to designing effective therapeutics.

Grasping the tissue microenvironment and how it provides specific conditions and signals for cells in that locale is now paramount to understanding cellular responses. The mycobacterial granuloma presents a complex niche that is dynamic in terms of its immune composition and progression over the disease course. We focus mainly on assessing the presence of high $[K^+]_e$ in the granuloma that can be derived from cellular necrosis and how the same can influence immune cell restriction of mycobacteria. This undertaking represents one of the few efforts to examine the intra-granuloma ionic microenvironment and our findings may provide insights into granuloma progression, the effects of K^+ homeostasis on immune anti-microbial function in general, and whether modulating K^+ availability may benefit the host during bacterial infections.

Chapter 2: Materials and Methods

2.1 Ethics statement

Human blood collection and experiments were approved by Institutional Review Boards (IRB) of NHG-DSRB and A*STAR-IRB, Singapore. Apheresis cone blood was obtained from unidentifiable platelet donors (IRB reference: #2026-026, HSA Application #202106-16). Mouse experiments (IACUC: #211645) were reviewed and approved by BRC (Biological Resource Centre), A*STAR Institutional Animal Care and USE Committee (IACUC) under rules and regulation of the National Advisory Committee for Laboratory Animal Research (NACLAR). Mouse experiments with *Mtb*-infected mice were conducted at International Centre for Genetic Engineering and Biotechnology (ICGEB), New Delhi, were reviewed and approved under ICGEB/IAEC/18092021/CI-15.

2.2 Cell culture

THP-1 monocytes (ATCC, TIB-202) were cultured in RPMI containing 10% FBS, 1X Sodium pyruvate, 1X MEM NEAA, 1X GlutaMax and 1X Kanamycin (Gibco). LentiX^{TM}-293T cells (Takara, # 632180) were cultured in DMEM containing 10% FBS, 1X Sodium pyruvate, 1X MEM NEAA, 1X GlutaMax and 1X Penicillin/Streptomycin. For selection of cells stably incorporating expression plasmids containing puromycin resistance cassette, 2μg/mL puromycin (Gibco, #A1113803) was added to media for 2-3 days alongside an uninfected/untransfected control. To generate THP-1 macrophages, THP-1 monocytes were cultured in 100ng/uL phorbol 12-myristate 13-acetate (PMA) (Sigma, #P1585) for 24h, swapped to fresh media for a further 24h before infection. For treatment of potassium, KCl (BDH, #101985) was prepared in antibiotic-free RPMI and filter-sterilized before adding to culture.

2.3 Mtb/BCG culture

Wild-type (WT) or mCherry-tagged Bacillus Calmette–Guérin (*M. Bovis* BCG) were grown in 7H9 media (Difco, #DF0713-17-9) supplemented with 10% ADS, 0.2% glycerol and 0.05% Tween 80 and 50μg/mL Hygromycin B (for fluorescent BCG) in standing culture at 37°C. Bacteria stocks were frozen down in 10-15% glycerol between 0.4-0.6 OD_{600} and aliquots plated on 7H11 agar (Difco, #DF0838-17-9) supplemented with 10% Middlebrook OADC Enrichment medium (BD Biosciences, #212351) to determine bacterial CFU. Aliquots were freshly thawed for infection experiments.

2.4 Isolation and culture of human CD14$^+$ monocytes

Anapheresis donor blood was processed by Ficoll-Paque (Cytiva, #17144003) density gradient centrifugation at 2000rpm, with zero acceleration and decceleration, and PBMC layer was extracted. Human CD14$^+$ monocytes were isolated using EasySep^{TM} Human CD14 Positive Selection Kit II (Stemcell, #17858). To differentiate CD14$^+$ monocytes into monocyte-derived macrophages (MDMs), monocytes were cultured at 1*10^6 cells/3mL differentiation medium consisting of RPMI supplemented with 50ng/mL recombinant human M-CSF (R&D Systems, #216-MC-005) and incubated for 5 days. MDM were harvested with 2mM EDTA in PBS for downstream experiments.

2.5 In vitro Mtb/BCG infection assay

Cells (THP-1/primary monocytes/MDMs) were cultured in antibiotic-free RPMI for infection purposes. Freshly thawed BCG/*Mtb* was diluted in 10mL antibiotic-free RPMI and pelleted at 3800rpm for 10 min, re-suspended in media and de-clumped using a water bath sonicator for 5 min. BCG/*Mtb* was then topped up with RPMI and added to cells at MOI 5:1 (5 bacilli to one eukaryotic cell) and seeded at a cell density of 3*10^6/mL. Infected cells were incubated for 3 h, then harvested in media and centrifuged at 800 rpm to remove extracellular bacteria. Infected cells were counted and seeded at 1x10^6/mL for further incubation (24-72 h), and appropriate treatments added at this time. At specific timepoints, cells were washed in PBS prior to lysis in TRIzol (Life technologies, #15596018) (for RNA), or in RIPA buffer (Sigma, #R0278) (for proteins) on ice.

For CFU enumeration, infected cells were seeded at 5*10^4 cells in 200uL per well in triplicates in a U-bottom 96-well plate, with or without inhibitors/treatments. Adherent cells (PMA-differentiated THP1, MDMs) were infected directly in 96-well plates (5*10^4 cells per replicate) at MOI 5:1 and cell density of 1*10^6/mL. At the respective infection timepoints, plates were centrifuged, pellets were washed once in PBS and lysed in 200uL 0.06% SDS for 10 min. Serial dilution was carried out and cell lysates plated on 7H11 agar. Colonies were counted after plates were incubated at 37°C for 14-18 days.

The working concentrations of N-acetyl-cysteine (NAC) (Sigma, #A7250), 3-methyladenine (3-MA) (Abcam, #ab120841) and Wortmannin (Selleckchem, #S2758) are 5mM, 50μM, 10mM and 10μm respectively.

2.6 Generation of plasmids, lentiviral vectors and transfection

For CRISPR-Cas9 knockout, an oligomer-based paired guide RNA (pgRNA)-CRISPR/CAS9 lentivirus approach was taken, utilizing Library cloning vectors (pAdaptor and pDonor for gRNA cloning) and lentiviral expression plasmids (PHASE-DEST-CAS9-T2A-GFP). pAdaptor was generated by cloning the gRNA scaffold together with U6 promoter flanked by BbsI site in pUC57 using ClaI and BstbI sites. BbsI digestion of PCR amplified product using universal primers flanking the adaptor releases an adaptor fragment which accepts BbsI compatible single gRNAs at each end. pDonor plasmid was generated from Gateway™ pENTR™ 11 Dual Selection Vector (Thermo Fisher, #A10467). A T1 and T2 region containing BbsI site was deleted using NheI and AflII. A cassette (LoxP-U6 promoter-Bbs I-CHL-CCDB–Bbs I - gRNA scaffold) was cloned between AttL1 and AttL2 using XhoI and KpnI. Lentiviral expression vectors to generate knock outs (Cas9-GFP) was generated by cloning in CMV-CAS9-T2A-GFP (System Biosciences, #CD500B-1) using NheI and SwaI restriction sites (PHASE-MCS-CMV-CAS9-T2A-GFP). This was followed by blunt end cloning of DEST cassette upstream to CMV (PHASE-MCS-CMV-CAS9-T2A-GFP). Plasmids are illustrated in Figure 8.

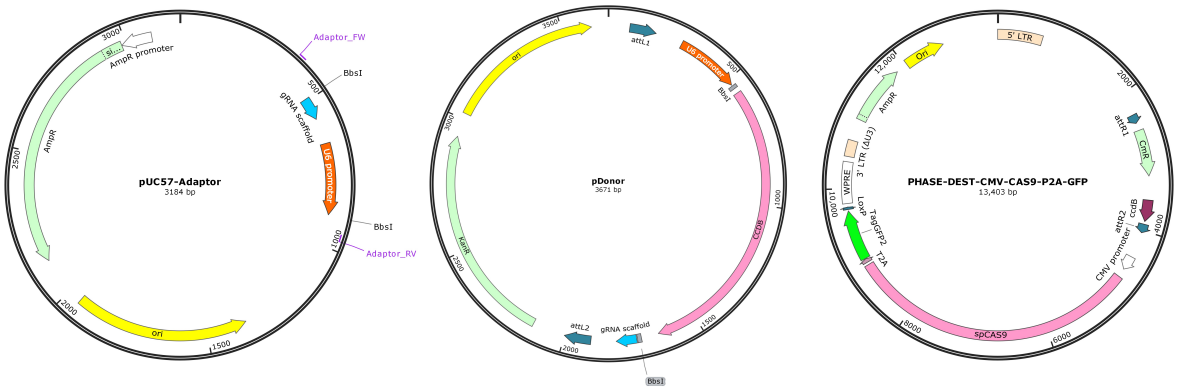

Figure 8. Plasmid vectors used in CRISPR-Cas9 knockout generation.

A set of forward and reverse 25 bases long oligomers (Forward gRNA seq: *TTCACATCGGCATGTCCAGC*, Reverse gRNA seq: *GTGGTATCTCTCTCCAAAAA*) for gRNA targeting human *KCNJ15* Exon 4 (only 1 coding exon) genes were ordered from Integrated DNA Technologies (Fig 9). For cloning, gRNAs were mixed at equimolar concentrations, phosphorylated and annealed. The adaptor was PCR amplified using a set of universal primer and pAdaptor plasmid as a template, digested with BbsI, purified and ligated with annealed oligos (1:20 dilution) as described above.

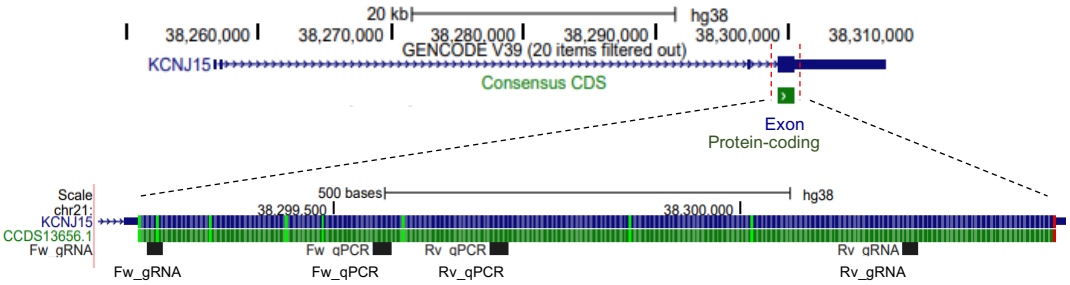

Figure 9. Human *KCNJ15* gene track. Snapshot of human *KCNJ15* gene track (blue) and Consensus CDS protein-coding region (green). Zoomed-in region represents Exon 4, and black bars represent designed gRNAs and RT-qPCR primers used. Obtained and adapted from UCSC Genome Browser [362], at http://genome.ucsc.edu.

The ligation reaction was purified using MinElute PCR column purification (Qiagen, #28004) and gel extraction. (Qiagen, #28604). Ligated gRNAs-adaptors were ligated to BbsI digested pDonor and transformed into TOP10 cells and plated with kanamycin selection. Plasmids were purified from resulting bacterial clones *KCNJ15* specific paired guide RNAs were confirmed based on Sanger sequencing. gRNAs were then shuttled efficiently to the DEST containing lentiviral CAS9 expression plasmids using Gateway LR Clonase II system (Invitrogen, #12538120).

Viral particles were produced by co-transfection of *KCNJ15* gRNA-containing lentiviral plasmids, together with packaging plasmids. LentiX cells were cultured to a confluency of 80% prior to transfection. Phage plasmids and lentivirus packaging plasmids were transfected into LentiX cells using Xfect™ Transfection Reagent (Takara, #631317) according to the manufacturer's protocol. LentiX was allowed to produce lentivirus for 72 h prior to supernatant collection, filtration through a 0.45µM filter and virus concentration using LentiX Concentrator (Takara, #631231). Concentrated virus (MOI 10:1) was delivered to THP-1 with 8µg/mL polybrene (Sigma, #107689) with centrifugation at 2200g for 1h at 22°C and incubated for 5 days.

Successfully transfected THP-1 cells are GFP-labelled, hence single-cell sorting into individual 96-wells was conducted on the BD FACSAria™ III sorter. Sorted clones were expanded in culture for 3-4 weeks prior to DNA extraction and PCR screening for gene editing using primers flanking the CRISPR guide region (Table 2). To validate gene editing, PCR products were sequenced to check for exon deletions. Methods for CRISPR/Cas9 knockout are adapted from *Kumar et al., "NFκB-p65 - ATP13A2 axis mediated metabolic adaptation supports acute myeloid leukaemia pathologies"* (Submitted).

For generation of GFP-tagged Kir4.2 overexpressing THP-1, pUC-KCNJ15Frag-Linker-GFP was obtained and cloned into pENTR vector and then shuttled into lentiviral expression vector via Gateway reaction as above. Following lentiviral infection, THP-1 cells were incubated for 48h, prior to selection with puromycin for successfully transfected cells.

2.7 siRNA gene silencing

For knockdown of HIF1α, THP-1 monocytes were seeded at a density of $0.6*10^6$/mL in 2 ml RPMI antibiotic-free complete RPMI in a 6 well plate. 40nM of negative control or HIF1α siRNA (IDT, # hs.Ri.HIF1A.13.1) and 9µL Lipofecamine RNAimax (Thermo Fisher, #13778100) were prepared in serum-free RPMI for transfection per well. siRNA-Lipofectamine mixture was incubated at RT for 20 min before adding into each well. Cells were generally incubated for 24h prior to harvesting for experiments.

For knockdown of ATG5, gene silencing was done using Thermo Fisher neon transfection system. $5*10^6$ THP-1 cells were re-suspended in 100µl of resuspension buffer and 50nM siRNA added (Dharmacon, #M-004374-04-0005). Nucleofection was carried out using these transfection condition: Voltage: 1150, Width: 30, Pulse: 2. After transfection, the cell suspension was added to pre-warmed media in culture plate. H37Rv *Mtb* infection was performed 16 hrs post siRNA transfection. Execution of some *Mtb in vitro* experiments were carried out in collaboration with Surbhi Verma in the lab of Dr Dhiraj Kumar, ICGEB, New Delhi.

2.8 Inflammasome activation and enzyme-linked immunosorbent assay (ELISA)

THP-1 monocytes were seeded at a density of $1*10^6$/mL and treated with 1µg/mL LPS (O111:B4, Sigma, #L2630), or 1µg/mL Pam2CSK4 (Invivogen, #tlrl-pm2s-1) for 24h. Wells were harvested and centrifuged to collect supernatant for ELISA. ELISA was carried out on cell supernatants, serum (dilution 1:4) or lung homogenate samples (dilution 1:10). Samples were assayed for cytokine levels using human IL-1β (Thermo Fisher**,** #88-7261-86) or mouse CCL2 (R&D Systems, #DY479) ELISA kits according to their respective manufacturer's protocols. Results were acquired on a Tecan Infinite Pro 200 Plate Reader using the Tecan i-control™ software.

2.9 SDS-PAGE and Western Immunoblotting

Eukaryotic cells lysed in RIPA buffer were incubated on ice for 30 min, followed by centrifugation and collection of supernatant for storage at -80°C. Protein was quantified using

Pierce BCA Protein Assay Kit (Thermo Fisher, #23225). 20-50µg protein was prepared in 4X Laemmli sample buffer (BioRad, #1610747) and loaded onto Mini-PROTEAN® TGX Stain-Free™ Precast Gels (BioRad) and run at 120V. Stain-free gels were visualized using the ChemiDoc Imaging System (BioRad) and transferred onto PVDF membranes. Membranes were blocked in 5% BSA (Cell Signalling) with 0.5% Tween-20 in TBS (TBS-T) for 1h at RT. Primary antibodies were then diluted in 5% BSA in TBS-T and incubated with membranes overnight at 4°C with agitation. Blots were washed thrice in TBS-T and incubated with secondary antibody for 1h at RT. Blots were washed again and visualized with Luminata Forte Western HRP substrate (EMD Millipore, #LUF0500). For phospho-proteins, membranes were blotted with anti-phospho-antibodies diluted in 5% BSA in TBS-T, then total-protein antibodies followed by β-actin, with stripping in between each step. Immunoblot antibodies used are listed below in Table 1.

Target (anti-)	Company	Catalog No.	Dilution
KCNJ15 (Kir4.2)	Sigma	HPA016702	1:800
KCNJ15 (Kir4.2)	Alomone Labs	APC-058	1:800
β-actin	Cell Signaling	4967	1:1000
Actin	Abcam	ab3280	1: 2000
pS6	Cell Signaling	4858	1:3000
S6	Cell Signaling	2217	1:1500
pmTOR	Cell Signaling	2791	1:1000
mTOR	Cell Signaling	2972	1:1000
pAkt	Cell Signaling	4060	1:1500
Akt	Cell Signaling	4961P	1:1000
LC3II	Cell Signaling	3868	1:1000
APAF-1	Cell Signaling	5088	1:1000
Anti-rabbit HRP	Cell Signaling	7074	1:5000
Anti-mouse HRP	Cell Signaling	7076	1:5000

Table 1. Antibodies used in western immunoblotting.

2.10 Quantitative Real-time PCR (RT-qPCR)

For RNA extraction, 80µL chloroform was added to 400µL TRIzol cell lysate. The mixture was centrifuged for 5 min at 4°C and aqueous layer extracted. One volume of 70% ethanol was added, and the contents transferred to an RNeasy column from the RNeasy Mini Kit (Qiagen, #74106). RNA clean-up was conducted according to the manufacturer's instructions. Extracted RNA was quantified on a Nanodrop 2000 (Thermo Fisher). For RT-qPCR of single-exon genes (i.e. *KCNJ15*), RNAse-free DNAse Set (Qiagen, #79254) was used to remove gDNA contamination. 0.5-1µg of RNA was used for cDNA synthesis with iScript™ Reverse Transcription Supermix for RT-qPCR (BioRad, 1708841) according to manufacturer's instructions. Control samples without addition of reverse transcriptase were included in the run to ensure gDNA contamination did not confound the results. qRT-PCR was performed using iTaq™ Universal SYBR® Green

Supermix (Biorad, #1725124) and run using Biorad CFX96^{TM}. Primers are listed in Table 2 and human *KCNJ15* targeting regions demarcated in Figure 9.

Gene	F/R	Sequence (5'-3')	Purpose
Human *KCNJ15*/Kir4.2	F	CCCGGTGAGCCCATTTCAAATC	RT-qPCR
Human *KCNJ15*/Kir4.2	R	GACCAACTGAGCAACCAACAGG	RT-qPCR
Mouse *KCNJ15*/Kir4.2	F	ACCCCGAGTCATGTCAAAGAG	RT-qPCR
Mouse *KCNJ15*/Kir4.2	R	GCTTGTATCGCCACTTCATGT	RT-qPCR
KCNJ15/Kir4.2	F	CAAAGCCTCTGCTCCTCACTC	Knockout validation
KCNJ15/Kir4.2	R	GAGAAGTACAGGCAGGAGGATC	Knockout validation

Table 2. List of primers for RT-qPCR of *KCNJ15*. Primers for PCR validation of KCNJ15 knockout and guideRNA sequences used for CRISPR-Cas9 knockout of *KCNJ15*.

2.11 Immunofluorescence and microscopy

Cells were fixed with 4% paraformaldehyde (PFA) for 20 minutes and then washed twice with 1X PBS. The cells were then permeabilized with 0.2 % TritonX-100 for 15 min and subsequently blocked in 3% BSA for 1 hr. Further, cells were incubated with primary antibody for 1-2 hrs and washed twice with PBST. Later, cells were incubated with fluorescent tagged secondary antibody for 1 hr. Where needed, Cells were stained with Hoescht 33342 (Invitrogen, #H21492) for 10 min and washed. Cells were then mounted on glass slides using prolong gold antifade mountant (Invitrogen, #P36930). On some occasions, cells were seeded into ibidi μ-slides (Ibidi, #80607) for imaging. Confocal imaging was done on an Olympus Fluoview FV1000 or Nikon Ti-E microscope equipped with 60X/1.4 NA plan-apochromat DIC objective lens. The analysis was performed on Imaris 9.6.1 imaging software or FIJI software. Antibodies and dilutions used in staining are listed in Table 3.

For lysosome visualization, cells were stained live with 50nM LysoTrackerTM Deep Red (Invitrogen, L12492). Cells were washed with PBS and stained with Hoescht 33342. Cells were then washed and imaged.

Target (anti-)	Company	Catalog No.	Dilution
KCNJ15	Sigma	HPA016702	1:500
HIF1α-Alexa Fluor488	Abcam	ab208419	1:200
LC3B	Novus Biologicals	NB100-2200	1:100
Anti-Rabbit Alexa Fluor 647	Cell Signaling	4414	1:500
Anti-rabbit Alexa Fluor 488	Invitrogen	A11034	1:400

Table 3. Antibodies for immunofluorescence staining.

2.12 Wild-type (WT) and Kcnj15^{KO} mice

Kcnj15^{KO} mice were generated in-house by *in-vitro* fertilization of C57BL/6 females with *Kcnj15^{KO}* sperm from MRC Harwell/EMMA Strain Repository (Strain designation: B6;129P2-Kcnj15tm1Dgen/H, EMMA ID: EM:02298). Offspring were genotyped for mutant strains by PCR. Primers used are

1) 5' GGAAGATAGCATGGGGACACTCCTC 3'
2) 5' GGTGGGATTAGATAAATGCCTGCTCT 3'
3) 5' TTGCTGCCACCTTTGTGATGACCTG 3'

Both WT and *Kcnj15^{KO}* mice used in experiments were derived from the same parental lineage. For experiments, age and gender-matched mice were used between 8-12 weeks of age.

2.13 Mice BCG infection experiments and organ processing

Mice were infected with $1.5*10^6$ CFU of BCG in 50µL PBS via the intra-tracheal route [363]. Briefly, mice were anaesthetized with isofluorane, suspended upright using a nylon string and 50µL of solution administered in the oral cavity with its tongue movement restricted using a pair of forceps to prevent swallowing. The nasal passage was covered and mice were made to undergo 4-5 tidal breaths before returning to cages. At the appropriate timepoint, mice were euthanized by CO_2 inhalation and left and right lungs, spleen, blood and hind legs were harvested where needed.

At specific time points post-infection, right lungs were processed for staining by cutting up into fine pieces and incubating with 1.4 mg/ml Collagenase A (Roche, #110887930001) and 30 µg/ml DNAse I (Sigma, #DN25) in complete RPMI for 1h at 37°C, followed by passing through a 70µM cell strainer. Red blood cells were lysed with ACK lysing buffer (Gibco, #A1049201). Total lung cells were re-suspended in 1mL media in preparation for staining. Blood was drawn from inferior vena cava in EDTA-coated syringes and incubated in ACK lysis buffer on ice for 10 min, followed by centrifugation at 300g for 10 min. Blood cells underwent a second red blood cell lysis step prior to seeding for staining. Hind legs were stripped of skin and muscle to obtain clean femurs. Femurs were cut on both ends and flushed with PBS with a 26G needle. Bone marrow was passed through a 70µM cell strainer, and red blood cells lysed prior to seeding for staining.

Left lung and spleen were harvested in 1mL PBS in gentleMACS™ M-Tubes (Miltenyi, #130-093-236) and dissociated using a gentleMACS Dissociator (Protocol: RNA_02.01.). For CFU enumeration, spleen and lung lysates were serially diluted in PBS and plated in triplicates on 7H11 agar containing 100µg/mL ampicillin (Sigma, #A9518). Leftover lung lysate was centrifuged and supernatant (lung homogenate) stored at -80°C for ELISA or Luminex Assay.

Where serum was needed, blood was collected into uncoated Eppendorf tubes, centrifuged for 5 min at 8000 rpm, and serum collected and stored at -80°C.

2.14 Staining, flow cytometry and immune profiling

To assay for apoptosis in Chapter 3, $1*10^5$ THP-1 monocytes (treated / untreated) were seeded in 96-U bottom wells. Cells were washed once in PBS, and then once in 1X Annexin V binding buffer. Cells were then re-suspended in 50µL binding buffer and 2.5µL of Annexin V was added into each well. Staining proceeded for 10 mins, and then cells were washed with binding buffer and topped up to 100µl. 2.5µL propidium iodide was added to each well, and cells were acquired immediately on a BD LSRFortessa™. All materials were part of the eBioscience™ Annexin V Apoptosis Detection Kit APC (Invitrogen, #88-8007). For staining of THP-1 monocytes with Ion Potassium Green-4 (AM Salt) (ION Biosciences, #3021C), dye was dissolved in Powerload Concentrate (Thermo Fisher, #P10020), and further diluted in serum-free RPMI containing Probenecid (Thermo Fisher, #36400), to a final dye concentration of 5µM. $1*10^5$ cells were stained in 50µL dye in 96-well plates for 1h at 37°C. For standard curve generation, cells were treated with 50µM Amphotericin B (Sigma, #A9528) after staining and incubated for 10 min, followed by spiking in serum-free RPMI containing a range of KCl concentrations. 10 min later, fluorescence was acquired by flow cytometry on BD LSRFortessa™ using the FITC channel without washing.

For immune profiling in mice in Chapter 4, all of cells harvested from blood, and $1/10^{th}$ of single-cell suspension obtained from processing lungs and bone marrow was seeded into 96-U bottom wells. Cells were washed in PBS once, then stained with LIVE/DEAD™ dye (Aqua Fixable Dead Cell Stain Kit; Invitrogen, # L34957) at RT for 20 min. Live-dead stained cells were washed in FACS buffer (1X PBS, 5mM EDTA, 2% FBS) then blocked with anti-CD16/32 at 4°C for 15 min and washed. Next, cells were stained with antibody cocktail containing Biotin-labelled antibodies at 4°C for 25 min, followed by washing and staining with antibody cocktail containing antibodies against extracellular markers at 4°C for 25 min. After a final wash, cells were fixed with 2% PFA (Electron Micoscopy Sciences, #15710) for 15 min at RT, washed and re-suspended in FACS buffer prior to acquisition on BD LSR II. Antibodies used for staining are listed in Tables 4-7 for each staining panel. Gating strategies are shown in main figures. Compensation beads were prepared using BD™ CompBeads Set Anti-Mouse Ig, κ and Anti-Rat/Hamster Ig, κ (BD Biosciences, #552843 and # 552845). Heat-killed cells were used as a positive control for viability staining with LIVE/DEAD™ stain.

Ab	Labelling	Isotype/Host	Clone	Cat No.	Company	Dilution
Live Dead Aqua	AmCyan				Life Technologies	1/1000
CD45	APC-Cy7	Rat IgG2b, κ	30-F11	103116	BioLegend	1/400
Ly6G	PE-CF594	Rat	1A8	562700	BD Pharm.	1/400
Ly6C	PE-Cy7	Rat IgG2c, κ	HK1.4	128018	BioLegend	1/640
CD11b	BV605	Rat IgG2b, κ	M1/70	101237	BioLegend	1/160
CD43	BUV737	Rat IgG2a, κ	S7	564398	BD Pharm.	1/400
MHCII (I-A/I-E)	BV650	Rat IgG2b, κ	M5/114.15.2	107641	BioLegend	1/320
CD11c	PE	Armenian Hamster IgG	N418	117308	BioLegend	1/400
CD64	BV421	Mouse IgG1, κ	X54-5/7.1	139309	BioLegend	1/50
F4/80	AF488	Rat IgG2a, κ	BM8	123120	BioLegend	1/200
CD24	PerCP-Cy5.5	Rat IgG2b, κ	M1/69	45-0242-82	eBioscience	1/320
CD103	APC	Armenian Hamster IgG	2E7	121414	BioLegend	1/80
CD45R (B220)	Biotin	Rat IgG2a, κ	RA3-6B2	13-0452-85	eBioscience	1/400
NK1.1	Biotin	Mouse IgG2a, κ	PK136	13-5941-85	eBioscience	1/400
CD90.2 (Thy1.2)	Biotin	Rat IgG2a, κ	53-1.2	140314	BioLegend	1/400
Streptavidin	BUV395			564176	BD Horizon	1/100

Table 4. Mouse lung myeloid staining panel and antibodies

Ab	Labelling	Isotype/Host	Clone	Cat No.	Company	Dilution
Live Dead Aqua	AmCyan				Life Technologies	1/1000
CD45	FITC	Rat IgG2b, κ	30-F11	103107	BioLegend	1/400
Ly6G	PE-CF594	Rat	1A8	562700	BD Pharm.	1/400
Ly6C	PE-Cy7	Rat IgG2c, κ	HK1.4	128018	BioLegend	1/640
MHCII (I-A/I-E)	BV650	Rat IgG2b, κ	M5/114.15.2	107641	BioLegend	1/320
CD11b	BV605	Rat IgG2b, κ	M1/70	101237	BioLegend	1/160
CD43	BUV737	Rat IgG2a, κ	S7	564398	BD Pharm.	1/400
CD11c	APC-Cy7	Armenian Hamster IgG	N418	117324	BioLegend	1/40
CD45R (B220)	Biotin	Rat IgG2a, κ	RA3-6B2	13-0452-85	eBioscience	1/400
NK1.1	Biotin	Mouse IgG2a, κ	PK136	13-5941-85	eBioscience	1/400
CD90.2 (Thy1.2)	Biotin	Rat IgG2a, κ	53-1.2	140314	BioLegend	1/400
Streptavidin	BUV395			564176	BD Horizon	1/100

Table 5. Mouse blood myeloid staining panel and antibodies

Ab	Labelling	Isotype/Host	Clone	Cat No.	Company	Dilution
Live Dead Aqua	AmCyan				Life Technologies	1/1000
CD34	FITC	Rat IgG2a, κ	RAM34	553733	BD Pharmingen	1/100
Flt3	PE	Rat IgG2a, κ	A2F10	135306	BioLegend	1/100
CD127	PE-CF594	Rat IgG2b, κ	SB/199	562419	BD Horizon	1/100
CD150	PE-Cy7	Rat IgG2a, λ	TC15-12F12.2	115914	BioLegend	1/400
CD48	PerCP-eFluor™ 710	Armenian Hamster IgG	HM48-1	46-0481-82	eBioscience	1/400
c-Kit (CD117)	Super Bright 436	Rat IgG2b, κ	2B8	62-1171-82	eBioscience	1/400
Sca-1	BV605	Rat IgG2a, κ	D7	108134	BioLegend	1/400
CD11b	BV650	Rat IgG2b, κ	M1/70	563402	BD Horizon	1/400
MHCII	BV711	Rat IgG2b, κ	M5/114.15.2	563414	BD Horizon	1/400
CD41	APC	Rat IgG1, κ	eBioMWReg30	17-0411-82	eBioscience	1/400
CD45	APC-Cy7	Rat IgG2b, κ	30-F11	557659	BD Pharmingen	1/400
CD16/CD32	BUV737	Rat IgG2b, κ	2.4G2	565272	BD Horizon	1/400
CD45R (B220)	Biotin	Rat IgG2a, κ	RA3-6B2	13-0452-85	eBioscience	1/400
NK1.1	Biotin	Mouse IgG2a, κ	PK136	13-5941-85	eBioscience	1/400
CD90.2 (Thy1.2)	Biotin	Rat IgG2a, κ	53-1.2	140314	BioLegend	1/400
Ly6G/Ly6C (Gr-1)	Biotin	Rat IgG2b, κ	RB6-8C5	108404	BioLegend	1/400
Streptavidin	BUV395			564176	BD Horizon	1/100

Table 6. Mouse bone marrow progenitor staining panel and antibodies

Ab	Labelling	Isotype/Host	Clone	Cat No.	Company	Dilution
Live Dead Aqua	AmCyan				Life Technologies	
CD45	APC-Cy7	Rat IgG2b, κ	30-F11	557659	BD Pharmingen	1/400
Ly6C	PE-Cy7	Rat IgG2c, κ	HK1.4	128018	BioLegend	1/640
CD11b	BV605	Rat IgG2b, κ	M1/70	101237	BioLegend	1/160
c-Kit (CD117)	Super Bright 436	Rat IgG2b, κ	2B8	62-1171-82	eBioscience	1/400
Flt3 (CD135)	PE	Rat IgG2a, κ	A2F10	135306	BioLegend	1/100
CD43	BUV737	Rat IgG2a, κ	S7	564398	BD Pharm.	1/400
CXCR4	AF647	Rat IgG2b, κ	L276F12	146504	BioLegend	1/200
Ly6G	PE-CF594	Rat	1A8	562700	BD Pharm.	1/400
CD45R (B220)	Biotin	Rat IgG2a, κ	RA3-6B2	13-0452-85	eBioscience	1/400
NK1.1	Biotin	Mouse IgG2a, κ	PK136	13-5941-85	eBioscience	1/400
CD90.2 (Thy1.2)	Biotin	Rat IgG2a, κ	53-1.2	140314	BioLegend	1/400
Streptavidin	BUV395			564176	BD Horizon	1/100

Table 7. Mouse bone marrow monocytes staining panel and antibodies

For experiments in Chapter 5, monocytes were seeded in 96-U bottom wells for staining. Where applicable, cells were first stained with LIVE/DEAD™ dye (1:1000). Cells were stained with MitoSOX Red (5μM) (Invitrogen, # M36008), CM-H2DCFDA (1μM) (Invitrogen, # C6827), MitoTracker Green FM (50nM) (Invitrogen, #M7514), anti-human HIF1α-PE (1:10) (Biolegend, # 359704), TMRM (1μM) (Sigma, # T5428) or $DIBAC_4(3)$ (1μM) (Invitrogen, # B438) and acquired without fixation with the exception of HIF1α staining. For intracellular staining of phospho-proteins, cells were first stained with LIVE/DEAD™ stain, followed by fixation, permeabilization and staining with the PerFix EXPOSE Phospho-Epitopes Exposure kit (Beckman Coulter, # B26976) following the manufacturer's protocol. Intracellular staining antibodies include: anti-$pS6^{S235/236}$-V450 (BD Biosciences, #561457), anti-$pAkt^{P3473}$-V450 (BD Biosciences, #560858) and anti-$pmTOR^{S2448}$-AF647 (BD Biosciences, #564242). Samples were acquired on a BD LSRFortessa™. All flow cytometry data was analysed using FlowJo Version 10.

2.15 Broncheoalveolar lavage (BAL)

Mice were euthanized by CO_2 inhalation and restrained on a Styrofoam platform. Mice were bled by cutting the inferior vena cava to minimize bleeding in the cervical area. The thoracic cavity is exposed without damaging the lung pleura and ribcage cut away to allow clear visual observation of the lungs. The skin and muscle from the area surrounding the trachea area is removed as much as possible until the trachea is well exposed. A 22G needle is used to create an opening in the top part of trachea without damaging the trachea anywhere else. The needle is removed, and a 20G flexible plastic catheter/gavage needle carefully inserted into the hole made by the needle. Using forceps, a suture thread is passed under the trachea and secured around the catheter with a secure double knot. 500μL of pre-warmed (37°C) sterile BAL buffer (containing 1X PBS, 0.5% FBS, 2mM EDTA,) is drawn into a 1mL syringe and flush into the lungs slowly. Lungs are massaged with blunt forceps, then BAL fluid aspirated slowly into the syringe and collected in a 15mL tube. Lavage procedure is repeated another 4-6 times, pooling the resulting BAL fluid. BAL fluid is centrifuged and lysed of red blood cells if necessary. Resulting cells are counted and seeded in complete RPMI in 6-well plates for 1h to allow AMs to adhere. Media containing non-adherent cells are removed by washing with RPMI, then adhered AMs are lysed in TRIzol for RNA-sequencing. Adherent cells resulting from BAL were validated by flow cytometry for expression of CD45, CD64, CD11c and SiglecF to be AMs with >98% purity (Fig 10).

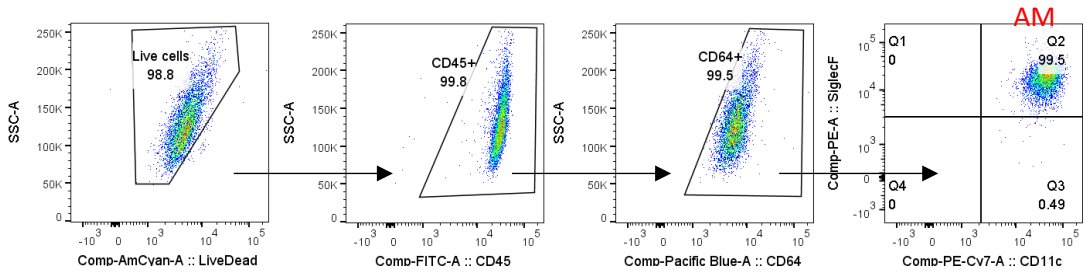

Figure 10. Validation of BAL-harvested AMs by flow cytometry. Cells that are $CD45^+$, $CD64^+$, $CD11c^+$ and $SiglecF^+$ are considered AMs.

2.16 T cell re-stimulation assay

At 14 d.p.i, spleens were harvested and processed by dissociating through a 70µm cell strainer, followed by red blood cell lysis to obtain a single cell suspension. $1*10^6$ spleen cells were seeded in 96-wells with or without 40µg/mL of Tuberculin Purified Protein Derivative (Statens Serum Institut, #DK-2300, Batch RT 50) for 20 h. Cells were then treated with GolgiPlug™ (BD Biosciences, # 555029) at 1:200 dilution and Monensin (Biolegend, #420701) at 1:1000 dilution for 4h. 50ng/mL PMA and 1µg/mL ionomycin (Sigma, #10634) were added to positive control samples for 4h. Antibodies used for extracellular (EC) and intracellular (IC) staining are listed in Table 8.

Ab	Labelling	Isotype/Host	Clone	Cat.-Nr.	Company	Dilution
Live Dead	AmCyan					
CD45 (EC)	BUV 395	LOU/C, LOU/M IgG2b, κ	30-F11	564279	BD	1/400
CD3 (EC)	FITC	Armenian Hamster IgG	145-2C11	100305	BioLegend	1/100
CD4 (EC)	PerCP-Cy5.5	Rat IgG2b, κ	GK1.5	100434	BioLegend	1/800
CD8a (EC)	APC-Cy7	Rat IgG_{2a}, κ	53-6.7	100714	BioLegend	1/400
CD19 (EC)	BV605	Rat IgG2a, λ	6D5	115540	BioLegend	1/160
IFNγ (IC)	APC	Rat IgG1, κ	XMG1.2	505810	BioLegend	1/160
TNFα (IC)	PE-Cy7	Rat / IgG1, κ	MP6-XT22	25-7321-82	Invitrogen	1/200

Table 8. Mouse spleen T cell re-stimulation assay extracellular and intracellular staining panel.

2.17 Seahorse XF extracellular flux assay (Mito Stress Test)

Seahorse Utility plate (Agilent, #103020-100) was hydrated overnight in a 37°C, non-CO_2 incubator. Cell culture plate was coated with poly-L-lysine (Sigma, #P4832) for 10 min at room temperature and washed once with PBS prior to seeding of cells. Isolated monocytes were left uninfected or infected with BCG and treated with 5mM or 60mM KCl for 24h, then harvested and counted. Monocytes were then seeded at $3.5*10^5$ per well in order to achieve confluence.

Plated cells were starved in Mito Stress media (containing 1 mM pyruvate, 2 mM glutamine, and 10 mM glucose) in a non-CO_2 incubator for 1h before initiation of the Mito Stress test. Drugs required for the Mito Stress test were prepared in the utility plate according to manufacturer's instructions. After calibration of utility plate, the culture plate was then loaded into the XF96 analyzer. The drugs injected were Rotenone (1.5µM), Oligomycin (0.5µM) and Antimycin A (0.5µM) provided in the Seahorse XF Cell Mito Stress test kit (Agilent, # 103015-100).

2.18 Bulk RNA-sequencing and analysis

Total RNA was extracted from (i) uninfected human monocytes overexpressing KCNJ15 (*KCNJ15*^{OE}) and control monocytes (Control^{OE}), (ii) uninfected and *Mtb*-infetced human primary monocytes treated or not with extracellular K^+, (iii) AMs from uninfected and BCG-infected WT or kcnj15^{KO} mice; following the double RNA extraction protocol. RNA isolation by acid guanidinium thiocyanate-phenol-chloroform extraction (TRIzol) followed by a Qiagen RNeasy Micro clean-up procedure. RNA was analyzed on Agilent Bioanalyser for quality assessment with RNA Integrity Number (RIN) range from 7.5 to 10. cDNA libraries were prepared using 2 ng of total RNA using the SMARTSeq v2 protocol [364] with the following modifications: 1. Addition of 20 µM TSO; 2. Use of 200 pg cDNA with 1/5 reaction of Illumina Nextera XT kit. The length distribution of the cDNA libraries was monitored using a DNA High Sensitivity Reagent Kit on the Perkin Elmer Labchip. All samples were subjected to an indexed paired-end sequencing run of 2x151 cycles on an Illumina HiSeq 4000 system (28 samples/lane).

Paired-end raw reads were mapped to either GRCh38 human genome build or GRCm38 mouse genome build STAR aligner [365]. Mapped reads were counted for genes using featureCounts [366] based on Gencodev31 (human) or GencodevM22 (mouse) gene annotation [367]. edgeR Bioconductor package [368] was used to calculate log2 transformed counts per million mapped read (log2CPM) and log2 transformed reads per kilobase per million mapped reads (log2RPKM).

Genes with log2CPM inter-quartile range (IQR) less than 0.5 across samples were removed from subsequent differential expression gene (DEG) analysis. DESeq2 [369] was used for differential expression gene (DEG) analysis. Genes with a Benjamini-Hochberg [370] adjusted P-values < 0.05 were considered as differentially expressed genes.

2.19 H3K27Ac ChIP-sequencing and analysis

Uninfected and *Mtb*-infected human primary monocytes treated or not with extracellular K^+ were fixed with 2% PFA for 15 min, quenched with 125mM glycine followed by snap freezing. Approximately 1-2*10^6 fixed human monocytes per sample were thawed on ice. Cell were lysed for 30 min with 500µl FA cell lysis buffer (10mM Tris-HCl (pH 8), 0.25% Triton X-100, 10mM EDTA, 100mM NaCl, Roche 1X Complete Protease Inhibitor) and nuclei were collected and re-suspended in 100µl SDS lysis buffer (1% SDS, 1% Triton X-100, 2mM EDTA, 50mM HEPES-KOH (pH 7.5), 0.1% sodium deoxycholate, Roche 1X Complete Protease Inhibitor). Nuclei were lysed for 20 min and followed by sonication (PIP-450 watts, 30% Duty factor, 24 mins, 500 cycles/bursts) to fragment chromatin (Covaris E220). 5% of total nuclei volume was collected and kept at 4^0C for Input/control (no antibody). Protein-DNA complex were immune-precipitated using 2.5 µg of H3K27ac antibody (Abcam, #ab4729) coupled to 30µl Protein G Dynabeads (Thermo Fisher, # 10003D) overnight at 4°C. Beads were washed (0.1% SDS buffer, LiCl buffer, and 1xTE buffer) and protein-DNA complexes were eluted using 200µl of elution buffer (1% SDS, 10mM EDTA, 50mM Tris-HCl (pH 8)), followed by RNAse treatment (37^0C, 2h), protease treatment and de-crosslinking overnight at 68°C. DNA was transferred to MaXtract tubes (Qiagen) for phenol-chloroform extraction and ethanol purification. Library preparation was performed by NGSP (16 PCR cycles and size selection). In total 17 libraries including input were pooled for sequencing at 1 lane Novaseq S4 (2x151 bp).

Sequencing reads were mapped against the reference genome (hg38 assembly, GRCh38) using Bowtie2 [371] and were filtered for uniquely mapped reads and for blacklisted regions, which are largely comprised of major satellite repeats that may indicate high signals for samples [372]. Peaks were called separately on each of the biological replicate using MACS2 [373]. The extraction of a set of unique genomic intervals (consensus peak set) and differential enrichment analysis to identify sites that are significantly differentially bound between sample groups were carried out with the package Diffbind [374] with the latter using edgeR. Peaks satisfying FDR<0.05 and absolute Log2fold change > 1 were considered for further analysis. Annotation of peaks associated with differentially acetylated sites was carried out next with genomation package [375] with the gencode.v31.annotation.gtf and the genes fall within -100kb to +100kb range of each genomic region were retained. There were some instances where multiple regions were mapped to the same gene and for those the region with the most significant FDR was considered as the best match for the gene. Mapped genes were then filtered out to extract protein coding genes.

2.20 Multiplex Microbead-based Immunoassay (Luminex)

Mouse lung homogenates were collected for Luminex analysis using the Cytokine & Chemokine 36-Plex Mouse ProcartaPlex™ Panel 1A (ThermoFisher, # EPX360-26092-901). Samples were incubated with fluorescent-coded magnetic beads pre-coated with respective antibodies in a black 96-well clear-bottom plate overnight at 4˚C. After incubation, plates were washed 5 times with wash buffer (PBS with 1% BSA (Capricorn Scientific) and 0.05% Tween-20 (Promega)). Sample-antibody-bead complexes were incubated with Biotinylated detection antibodies for 1h and washed 5 times. Subsequently, Streptavidin-PE was added and incubated for another 30 mins. Plates were washed 5 times, before sample-antibody-bead complexes were re-suspended in sheath fluid for acquisition on the FLEXMAP® 3D (Luminex) using xPONENT® 4.0 (Luminex) software. Data analysis was done using Bio-Plex Manager^{TM} 6.1.1 (Bio-Rad). Standard curves were generated with a 5-PL (5-parameter logistic) algorithm, reporting values for both mean florescence intensity (MFI) and concentration data.

2.21 Electrophysiology (Whole-cell patch clamp)

Whole-cell patch clamp experiments were performed by LKCMedicine-ICESing Ion Channel Platform, Lee Kong Chian School of Medicine, Nanyang Technological University. Patch clamp buffer solutions were prepared accordingly: Extracellular solutions (115 mM NaCl, 1 mM $MgCl_2$, 2 mM $CaCl_2$, 10 mM Glucose, 10 mM HEPES) containing 5, 50 or 160mM $[K^+]_e$ by varying KCl, pH=7 adjusted with HCl. Intracellular solutions (115 mM K-Aspartic, 20 mM KCl, 1 mM $MgCl_2$, 5 mM EGTA, 10 mM HEPES, 2 mM Na_2ATP) , pH adjusted to pH= 7, 6, 5, 4 with HCl. Cells were centrifuged at 100 rpm for 3 min. Cell pellet was re-suspended in 1 mL extracellular solution for patch clamp recordings.

Whole-cell patch clamp experiments were performed on a QPatch HTX automated electrophysiology platform (Sophion Biosciences) using disposable 48-channel chip plates (Cat No: SB2040). Cell positioning and sealing parameters were set as follows: positioning pressure -70 mbar, minimum seal resistance 0.1 GΩ, holding potential -90 mV, holding pressure -20 mbar. Suction pulses were added with increased amplitude until whole-cell configuration was achieved. Following establishment of the whole-cell configuration, cells were held at −75 mV. Prior to test article addition, cells were treated with a period of saline to determine the baseline response. Each cell acted as its own control. Currents from each liquid period were recorded multiple times. All tests were performed at RT. The Kir4.2 currents were recorded at holding potential of -75 mV, then ramped from −120 mV to 120 mV over 200 ms, and then stepped back to holding potential, every 5s interval.

The following criteria were used to determine data acceptability: 1) Membrane resistance (Rm) ≥ 200 MΩ. 2) Pre-compound baseline current ≥ 0.3 nA. 3) No apparent rundown or run-up at the end of vehicle period. 4) No apparent leak or stable leakage current, ≤ 25% peak current at holding potential. Inward current amplitudes (pA) recorded at -100 mV were measured using Sophion Qpatch Assay Software 5.6. Last 3 sweeps of peak current amplitudes were averaged and used for data analysis.

2.22 Electrophysiology (Lysosomal patch clamp)

Lysosomal patch clamp experiments were performed by the Electrophysiology Core@NUS Medicine (Centre for Life science, NUS). The method has been described previously [338]. Briefly, Control^{OE} and *KCNJ15*^{OE} THP-1 cells were treated with 1 μM vacuolin-1 overnight prior to patch-clamp recording. The lysosomes are patched with internal solution containing 145mM K-methanesulfonate, 5mM KCl, 10mM HEPES (pH 7.2). The pipette solution contained 145mM K-methanesulfonate, 5mM KCl, 10mM MES (pH 5.5). The potassium current was further inhibited upon perfusion with external NMDA solution containing 145mM NMDG, 5mM KCl, 10mM HEPES (pH 7.2). The net potassium current was obtained by subtracting the peak currents before and after perfusion of NMDA solutions at -100 mV. The current density was obtained by normalizing the net potassium current over the capacitance of lysosome.

2.23 Mtb-infection of mice maintained on custom K^+ diets

Teklad murine diets are customized by Envigo. Normal K^+ diet contained 0.5% K^+ and High K^+ diet contained 5% K^+ (#TD.130041 and #TD.07278 respectively). Normal K^+ diet contained the same amount of K^+ as standard chow, whereas high K^+ diets contained an addition of a 1:1:1 ratio of potassium chloride, potassium citrate, and potassium carbonate.

Mtb infection mice experiments were carried out in the Tuberculosis Aerosol Challenge Facility (TACF, ICGEB, New Delhi, India). After 3 days of diet initiation, mice were subjected to aerosol challenge with 200 CFU in a Wisconsin-Madison chamber according to the standardized protocol (200 million H37Rv-Zurich bacilli in 15 ml sterile saline was poured into the nebulizer for 20 min exposure time). To check for infection establishment, two mice were selected randomly and euthanized 24h post-aerosol infection. Lungs were aseptically harvested and homogenized in 2 mL 1X PBS, and 100μl of neat lung homogenate was plated on 7H11 agar plates to enumerate CFU in lung.

Infection proceeded for 15 days, after which, mice were euthanized and organs harvested. Left lung was homogenized and serially diluted and plated as above for CFU enumeration. Right lung

was processed as stated in Section 2.13 and stained as stated in Section 2.14 for myeloid immune profiling. Middle lobe of right lung was kept in 10% neutral buffered formalin for histopathology analysis.

2.24 Histopathology and IPG-4 staining of tissues

IFNγ-deficient mice were infected with $1.5*10^6$ BCG CFU via intra-venous delivery for 6 weeks, then euthanized and liver was harvested. Liver lobe was immediately flash frozen in OCT reagent and stored until cryo-sectioning. Cryo-sectioned samples were stained with hematoxylin and eosin, or Ion Potassium Green-4 (IPG-4) (Ion Biosciences, # 3023C) K^+ indicator in PBS for 1h at 37C, rinsed off with PBS, coverslipped and imaged on EVOS FL Auto 2 on GFP channel at 40-400X magnification.

For K^+ diet experiments, right middle lung lobe was collected as stated above in Section 2.23. Parffinized sections were sectioned onto glass slides and deparaffinized in 3 xylene washes (5 min each) and then rehydrated in descending grades of alcohol (absolute alcohol, 90% and 70%) followed by 1 wash in water, 5 min each. Slides were then stained with haematoxylin for 5-10 min and washed with water. Slides were next stained with Eosin for 5-10 min and washed with absolute alcohol followed by xylene. Slides were mounted with coverslip and sealed with DPX mounting medium. Execution of *Mtb*-infected mice experiments were carried out in collaboration with Priya Sharma in the lab of Dr Dhiraj Kumar, ICGEB.

2.25 Zebrafish husbandry and M. marinum infection

Zebrafish embryos were produced by natural spawning in the Centenary Institute aquarium under Sydney Local Health District Animal Welfare Committee approval 17-036. Embryos were raised at 28°C in E3 supplemented with methylene blue for the first day, then dechorionated and transferred into E3 supplemented with 20 μg/ml 1-phenyl-2-thiourea to inhibit pigment formation.

48h post fertilisation zebrafish embryos were infected with approximately 200 CFU *M. marinum* M strain carrying the pTEC27/msp12:tdTomato plasmid (Addgene #30182, gift from Prof. Lalita Ramakrishnan, University of Cambridge, UK) by microinjection into the caudal vein (CV) or neural tube (trunk) [376].

2.26 Zebrafish staining with IPG-4 and imaging

ION Potassium Green 4 (IPG-4) TMA salt was dissolved in water to a final concentration of 5 mg/ml and 10 nl was injected into the caudal vein or dorsal aorta of zebrafish larvae. IPG-4 injected animals were imaged on a Leica M205FA using a GFP filter set to collect IPG-4 fluorescent signal and a Cy3 filter set to collect *M. marinum*-TdTomato fluorescent signal. Images were analysed for IPG-4 fluorescence intensity at granulomas, unaffected somatic tissue (background), and the dorsal aorta (vascular baseline fluorescence) in ImageJ using the "Measure" function and recording the "Maximum" value in arbitrary fluorescence units. Fluorescence above background was calculated by subtracting unaffected somite fluorescence intensity from granuloma fluorescence intensity. Granulomas were scored for necrosis on the basis of containing extracellular bacteria.

2.27 Quantification of supernatant K^+ concentration

Monocytes or MDMs were re-suspended in 50-75µl RPMI at different cell concentrations. Cells were subject to two freeze-thaw cycles at -80C and checked under the microscope to verify complete cell lysis. Tubes were centrifuged at maximum speed to pellet cell debris and supernatant was collected. [K^+] in lysed cell supernatants was measured using a HORIBA LAQUAtwin K-11 pen meter according to the manufacturer's instructions. Briefly, the meter is calibrated and then 50µl of supernatant is placed onto a sample sheet laying on the electrode, allowing [K^+] to be measured. Data was calculated and represented as [K^+] in supernatant elicited by the lysis of varying cell numbers in a fixed 50µL RPMI.

Chapter 3: Characterizing the regulation and function of *KCNJ15* in THP-1 monocytes in infection and inflammation

3.1 Mycobacterial infection induces TLR2-dependent KCNJ15 expression in monocytes and macrophages

Epigenetic analysis by H3K27ac ChIP-sequencing determined that the gene locus *KCNJ15* was significantly enriched among differential acetylated peaks in human blood monocytes of ATB patients, which was indeed corroborated with its increased differential expression at the transcriptomic level by RNA-seq analysis (Fig 11A) [211]. In order to ascertain that mycobacterial infection indeed induces expression, monocytes and macrophages were infected with BCG or *Mtb*, and assessed at the transcriptomic and protein level for *KCNJ15*.

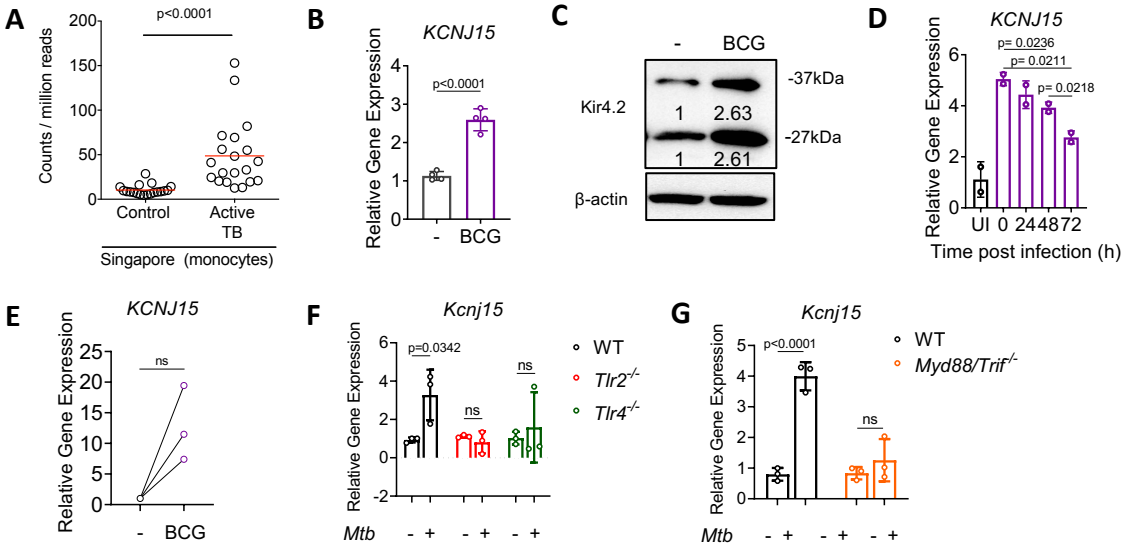

Figure 11. *KCNJ15* expression is induced in monocytes and macrophages in response to *Mtb*/BCG-infection.
A) *KCNJ15* expression levels from RNA-sequencing of monocytes of healthy controls vs active TB patients from a Singapore cohort. Each dot represents n=1 donor. Red line represents median. Methods have been described in del Rosario et al. [211] **B)** Relative expression of human *KCNJ15* by RT-qPCR of 24h BCG-infected THP-1 compared to uninfected cells. **C)** Western immunoblot of Kir4.2 protein from uninfected and 24h BCG-infected THP-1. Numbers represent densitometric analysis for each band size relative to uninfected cells. Representative blot from n=2 experiments is shown. **D)** Relative expression of human *KCNJ15* from THP-1 monocytes infected with *Mtb* and harvested after the indicated timepoints, compared to uninfected cells (n=2 experiments). **E)** Relative expression of human *KCNJ15* by RT-qPCR of 24h BCG-infected human MDMs to uninfected cells (n=3 donors). **F)** Relative expression of mouse *KCNJ15* by qRT-PCR of 24h *Mtb*-infected wild-type (WT), *Tlr2*$^{-/-}$ or *Tlr4*$^{-/-}$ J2 macrophages. **G)** Relative expression of mouse *KCNJ15* by qRT-PCR of 24h *Mtb*-infected WT and *Myd88/Trif*$^{-/-}$ bone marrow-derived macrophages (BMDM). Data in **A** and **B** was analyzed by Unpaired *t*-test. Data in **D** was analyzed by One-way ANOVA. Data in **E** was analyzed by Mann-Whitney test. Data in **F** and **G** were analyzed by Two-way ANOVA. Bar graphs represent Mean ± SD. All experiments were conducted thrice unless otherwise stated. Knockout cell line and BMDM experiments (**F** and **G**) were conducted in collaboration with Lorissa Smulan, Dr Hardy Kornfeld Lab, UMass Chan Medical School.

We found that mycobacterial infection with BCG at MOI 5:1 clearly induces the (i) mRNA expression of *KCNJ15* in THP-1 monocytes by RT-qPCR, and (ii) protein expression of Kir4.2 by western immunoblotting (Fig 11B, C). Infection of human primary $CD14^+$ monocytes with *Mtb* also led to the increased expression of *KCNJ15* mRNA as early as 3h post-infection, which was reduced gradually up to 72h (Fig 11D). A similar phenomenon was also observed when human $CD14^+$ monocyte-derived macrophages (MDMs) were infected with BCG. Notably, in these primary human MDM cultures, non-virulent BCG infection was able to induce a notably high level of *KCNJ15* mRNA with a fold change of up to 20 times although there was significant donor-to-donor variation (Fig 11E).

In particular, western immunoblotting for Kir4.2 protein in BCG-infected THP-1 cells revealed increased protein expression of endogenous Kir4.2 found at both ~37kDa and~ 27kDa (Fig 11C). Prediction of Kir4.2 protein size is estimated at 42.5kDa. However, Ensembl CCDS records has identified various splice variant transcripts, one of which comprises 245 amino acids and its size is estimated to be 27.3kDa [377]. It is possible that THP-1 monocytes express this splice variant of *KCNJ15* endogenously as a 42.5kDa band is not typically detected. Moreover, Kir4.2 has not been widely studied at the protein level, therefore antibodies cross-reactivity could also be a confounder. Since *KCNJ15* is upregulated upon mycobacterial infection, we examined if its gene expression is dependent on signaling induced via host PRRs, such as through TLR2 and TLR4. Lipoproteins and lipoglycans from *Mtb* cell wall are known to engage TLR2 whereas exact agonists of TLR4 remain unclear, although TLR4 signaling indeed plays a role in innate signaling in response to *Mtb* infection [378, 379, 380]. Using mouse macrophage J2 cell line with gene knockout of *Tlr2* or *Tlr4*, it was demonstrated that both *Tlr2* and *Tlr4* knockout abrogated the *Mtb*-induced increase in mRNA expression of *Kcnj15*, although the inhibition by Tlr2 knockout was more significant (Fig 11F). Indeed, *Mtb* infection of bone marrow-derived macrophages (BMDM) derived from *Myd88/Trif*$^{-/-}$ mice also abrogated induction (Fig 11G), indicating that the Myd88 signaling pathway, which exists downstream of TLR2 and TLR4 signaling, is required for the induction of *KCNJ15* expression.

In summary, *KCNJ15* expression is increased upon mycobacterial infection of monocytes and macrophages and is likely dependent on the TLR2-Myd88 signaling pathway. In order to study the functional role of *KCNJ15* in human monocytes and macrophages, we proceeded to generate *KCNJ15* gain and loss-of-function THP-1 cell lines.

3.2 Generation of KCNJ15^{OE} overexpression THP-1 cell line

We generated THP-1 monocytes overexpressing *KCNJ15* using a lentiviral overexpression system. Briefly, *KCNJ15* cDNA was cloned into an overexpression entry vector plasmid and then recombined into the lentiviral overexpression plasmid. Lentivirus were generating by transfection in HEK293 cells, and subsequent lentivirus obtained were used to transduce THP-1 cells. Cells carrying the *KCNJ15* overexpression (viz. *KCNJ15*^{OE}) were selected using antibiotics (Fig 12A).

KCNJ15^{OE} THP-1 cells were validated for expression of *KCNJ15* by both RT-qPCR and western immunoblotting (Fig 12B, C). When Kir4.2 was visualized by immunofluorescence staining, increased plasma membrane expression of the channel was observed (Fig 12D). Notably, we also observe fluorescent puncta within the overexpressing cells. This may suggest that Kir4.2 is heavily accumulated on the membrane of organelles such as the Golgi apparatus or lysosome or that high overexpression levels may induce protein aggregation within the cell. Indeed, the overexpression plasmid did induce a >10,000-fold induction of *KCNJ15* mRNA (Fig 12B). Despite this, *KCNJ15*^{OE} THP-1 cells do not appear to have a perturbed *in vitro* growth profile when compared to THP-1 transduced with only empty overexpression vector (Control^{OE}) (Fig 12E).

We next attempted to assess if the overexpressed Kir4.2 in THP-1 were functionally active and capable of transporting K^+ ions. In order to detect intracellular levels of K^+ ions, we used an intracellular K^+-binding fluorescent dye, Ion Potassium Green-4 (IPG-4, AM salt). Using a standard curve generated by treatment of cells with pore-forming Amphotericin B alongside spiking in of K^+ (Fig 12F left graph), we found that IPG-4 stained *KCNJ15*^{OE} THP-1 appeared to have some degree of increased intracellular K^+ (Fig 12F right graph). Electrophysiological studies of these *KCNJ15*^{OE} THP-1 by whole-cell automated patch clamp validated that increased Kir4.2 expression resulted in an elevated inward current at 50mM extracellular K^+ (Fig 12G). At physiological levels of 4.5mM extracellular K^+, however, we saw no differences in inward current of *KCNJ15*^{OE} cells. Instead, the maintenance of a higher intracellular K^+ may be attributed to reduced outward current in *KCNJ15*^{OE} cells. Expectedly, we also noticed variations in both expression of channel (Fig 12D) as well as inward current (Fig 12G) in individual *KCNJ15*^{OE} THP-1 cells. This is likely due to varying copy numbers of lentiviral overexpression vectors transduced into individual cells, resulting in heterogeneous induction of *KCNJ15*. Nonetheless, the overexpressed cell line remains a useful tool for evaluation of the functional role of *KCNJ15*.

In summary, we determined that *KCNJ15*^{OE} THP-1 carry an excess of functional inwardly rectifying Kir4.2 K^+ channels on the plasma membrane, allowing us to use these cells for further dissection of channel function during mycobacterial infection.

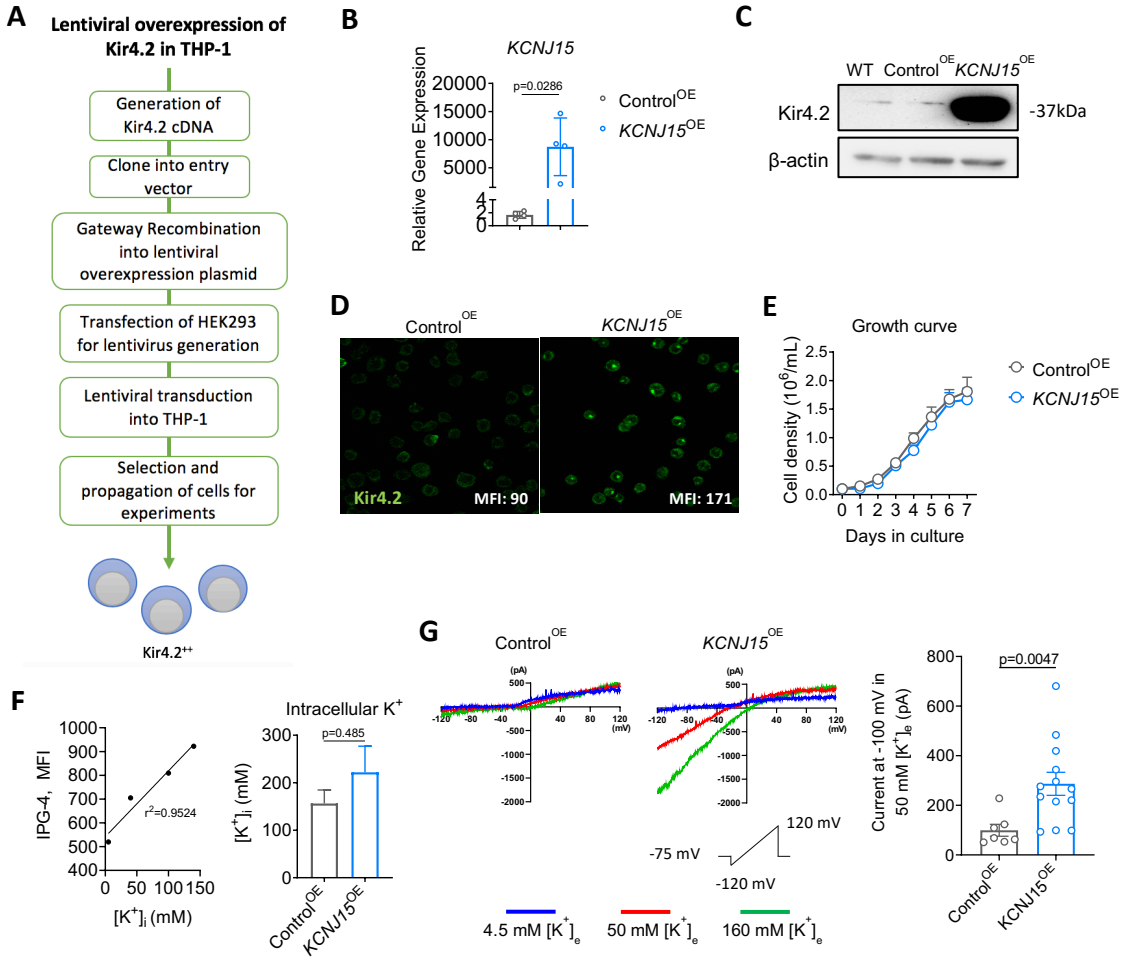

Figure 12. Generation and validation of *KCNJ15*^{OE} THP-1 cell line.
A) Workflow for generating THP-1 overexpressing *KCNJ15* via lentiviral overexpression system. **B)** Relative expression of human *KCNJ15* by qRT-PCR of Control^{OE} and *KCNJ15*^{OE} THP-1 monocytes. **C)** Western immunoblot of Kir4.2 protein from WT, Control^{OE} and *KCNJ15*^{OE} THP-1 monocytes. **D)** Immunofluorescence of Kir4.2 staining of Control^{OE} and *KCNJ15*^{OE} cells. Mean fluorescence intensity per cell was calculated using ImageJ (N=35 cells each). **E)** Growth curve of Control^{OE} and *KCNJ15*^{OE} cells monitored over a 7-day period without subculturing. **F)** Intracellular K^+ concentrations in Control^{OE} and *KCNJ15*^{OE} cells at steady-state measured using intracellular IPG-4 (AM salt) K^+ indicator, quantified against standard curve (left) generated by spiking of various KCl concentrations alongside Amphotericin B treatment (n=2). **G)** Patch clamp recordings of THP-1 Control^{OE} and *KCNJ15*^{OE} cells using a ramp protocol from -120 mV to 120 mV in 200 ms showing currents elicited at 4.5, 50 and 160 mM $[K^+]_e$. Average current amplitude recorded at -100 mV in 50 mM $[K^+]_e$ is shown in bar graph (right) comprising n=7 and 13 cells for Control^{OE} and *KCNJ15*^{OE} respectively (n=2 experiments). Data in **B, F** and **G** are analysed by Mann-Whitney T-test. Mean ± SD are represented. Whole-cell patch clamp experiments were conducted in collaboration with Dr Ong Seow Theng, LKCMedicine-ICESing Ion Channel Platform.

3.3 Generation of KCNJ15^{KO} THP-1 cell line using CRISPR-Cas9 system

We subsequently used the CRISPR/Cas9 system to knock out *KCNJ15* and generated a loss-of-function THP-1 cell line. We employed a paired guide RNA (pgRNA) library strategy, which was used to effectively generate various gene knockouts in THP-1 and U937 cell lines (Fig 13A).

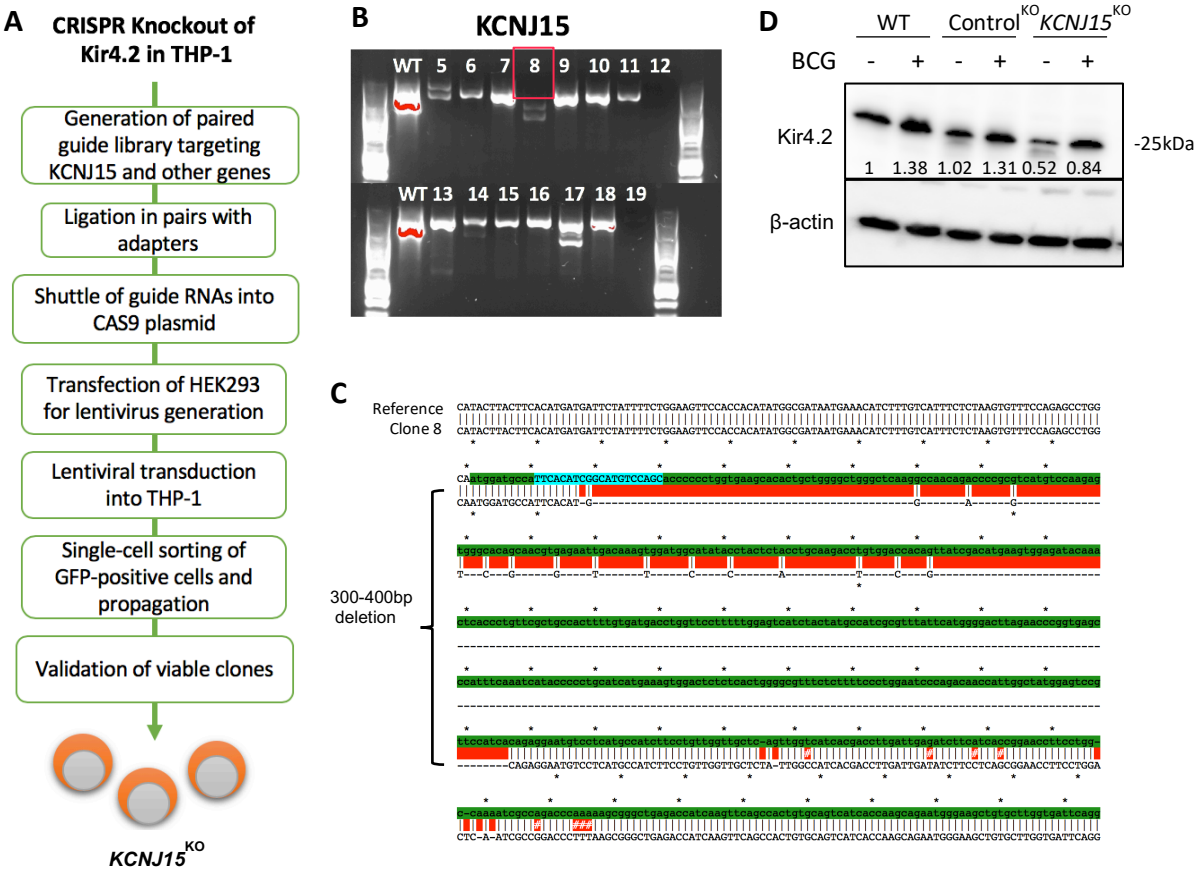

Figure 13. Generation and validation of *KCNJ15*^{KO} THP-1 cell line.
A) Workflow for generating CRISPR/Cas9 knockout *of KCNJ15* in THP-1 monocytes via lentiviral system. **B)** PCR screening of regions flanking targeted CRISPR sites in comparison to WT. Potential knockout Clone #8 is boxed in red. **C)** Sequence alignment of knockout Clone #8 to reference sequence of the same region. Red areas signify regions of mismatch. **D)** Western immunoblot of Kir4.2 protein from WT, Control^{KO} and *KCNJ15*^{KO} (Clone #8) THP-1 cells uninfected or infected with BCG for 24h. Numbers represent densitometric analysis of Kir4.2 protein relative to WT uninfected sample.

However, after several rounds of gene editing and screening > 100 clones, which were derived from sorted single cells, we were only able to generate a heterozygous knockout clone (Clone #8, henceforth termed as *KCNJ15*^{KO}), as observed by the two bands obtained from PCR screening indicating that the two alleles were differentially edited (Fig 13B). Sanger sequencing of the extracted PCR bands, however, showed that a significant 300-400bp deletion had occurred (Fig

13C). Despite this, western immunoblotting for *KCNJ15* protein revealed that although the *KCNJ15*^{KO} cells expressed less *KCNJ15* at steady state, its expression was still upregulated after BCG infection of 24h (Fig 13D). Intracellular K^+ could not be quantified as *KCNJ15*^{KO} CRISPR-edited cells constitutively expressed GFP, used for sorting, while IPG-4 has similar fluorescence properties. Nonetheless, this heterozygous knockout clone was used in conjunction with *KCNJ15*^{OE} for subsequent assays in an attempt to understand the function of *KCNJ15* channel in monocytes.

3.4 KCNJ15 is sensitive to intracellular pH and can localize to the lysosome

In our study we observed co-localization of Kir4.2 to BCG-containing lysosomes (Fig 14A) [211]. Lysosomal localization of Kir4.2 may be attributed to its three lysosomal-targeting dileucine motifs (^{44}DGIYLL^{49}, ^{244}ESPFLI^{249} and ^{364}ELRTLL^{369}). However, as patch clamp of wild-type THP-1 revealed little inward current compared to that of *KCNJ15*^{OE} THP-1 (Fig 12G), it would be difficult to determine if lysosomal-localized endogenous Kir4.2 are functional and participate in lysosomal physiology. Therefore, we examined the localization and functionality of Kir4.2 on lysosomes using *KCNJ15* overexpressing cells. THP-1 carrying overexpression of Kir4.2 tagged to GFP were generated for ease of visualization. Staining of Kir4.2-GFP THP-1 cells with LysoTracker Deep Red showed some co-localization of Kir4.2 channels to the lysosome at steady state (Fig 14B, in yellow).

In order to assess if lysosomal Kir4.2 are functional, lysosomal patch clamp recording [338] was conducted on *KCNJ15*^{OE} cells. Indeed, *KCNJ15*^{OE} lysosomes were found to exhibit higher outward current at -100mV compared to Control^{OE} cells, which was inhibited by N-methyl-D-glucamine (NMDG), a blocker of voltage-gated K^+ channels (Fig 14C, D). While whole-cell patch clamp showed increased inward current in *KCNJ15*^{OE} cells (Fig 14E), it is expected that the current direction would be reversed in the context of lysosomal channel since channel orientation would be reversed when internalized during phagocytosis (Fig 42).

Optimal function of lysosomal enzymes is thought to occur at lower pH, and Kir4.2 has been implicated in co-regulating acid secretion in gastric cells, together with H^+/K^+ ATPase [262]. Some Kir channels are pH sensitive, a feature depending on a highly conserved lysine residue at the N-terminus [190]. Furthermore, additional pH sensitivity of Kir4.2 has been attributed to an extra pH-sensing mechanism located at the C-terminus [239, 381]. Since both N and C-termini of plasma membrane Kir channels are on the cytoplasmic side, we examined the effect of varying intracellular pH levels on inward current in *KCNJ15*^{OE} cells. Unexpectedly, we observed an increase in inward current at -100mV as intracellular pH decreased from 7 to 6 in *KCNJ15*^{OE} cells (Fig 14F). This is opposite from the expected outcome, which is the typical inhibition of channel

function at lower pH [381, 382]. To note, cells were highly unstable when intracellular pH 4 was applied, leaving only n=1 cell in this group. We then also examined the effect of varying extracellular pH, which revealed that *KCNJ15*^{OE} inward currents increased when extracellular pH decreased from 7 to 4 (Fig 14G). Interestingly, the extracellular facing portion of Kir4.2 would be facing the lysosomal lumen in an endolysosomal context (Fig 42). H-ATPases actively transport H^+ into the endolysosome, hence we surmise that Kir4.2 may promote K^+ transport out of the lysosome to the cytosol as H^+ enters the lysosome, acidifying it. In this way, K^+ efflux acts as a counterion for positively charged H^+ to enter.

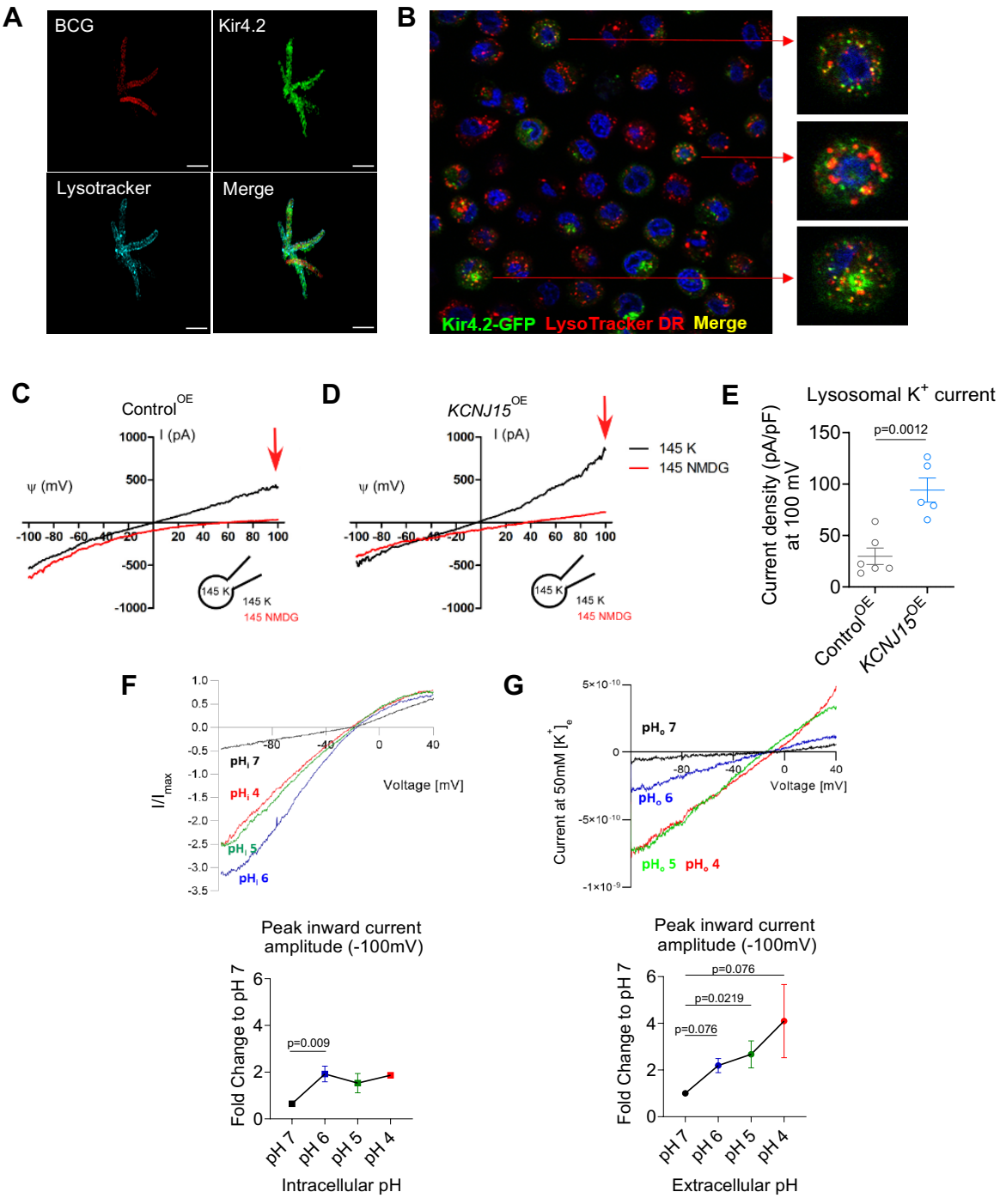

Figure 14. Kir4.2 forms functional channels on lysosomes and is sensitive to intracellular pH.
A) 3D projection of a THP-1 monocyte infected with mCherry-BCG (red), stained with LysoTracker Red (cyan) and Kir4.2 (green). The images were acquired 24 hr post infection by 3D-SIM. Scale bar 2 μm. Methods are described in del Rosario *et al.* [211]. **B)** Confocal microscopy image of THP-1 overexpressing Kir4.2 tagged with GFP and stained with LysoTracker Deep Red. Colocalized regions of Kir4.2 and lysosomes are shown in yellow. Images acquired at 400X. **C, D)** Lysosomal K^+ currents from endolysosomal patch clamp of Control^{OE} and *KCNJ15*^{OE} THP-1 cells. **E)** Lysosomal current density quantified at 100mV (Red arrows in **C**, **D**). **F)** (Top) Exemplar *KCNJ15*^{OE} THP-1 inward current traces and (bottom) peak inward current amplitude at -100mV at varying intracellular pH normalized to that of pH 7 at 50mM $[K^+]_e$, (n>5 cells, pH 4 has only n=1 cell data due to cell instability). **G)** (Top) Exemplar *KCNJ15*^{OE} THP-1 inward current traces and (bottom) peak inward current amplitude at -100mV at varying extracellular pH normalized to that of pH 7 at 50mM $[K^+]_e$ (n=6 cells each). Data in **E** was analysed by Unpaired T-test. Data in **F** and **G** was analysed by Friedman test and Kruskal-Wallis test respectively. Mean ± SD are represented. Whole-cell patch clamp experiments were conducted in collaboration with Dr Ong Seow Theng, LKCMedicine-ICESing Ion Channel Platform. Endolysosomal patch clamp experiments were conducted in collaboration with Dr Huang Hua, National University of Singapore.

In summary, we found that Kir4.2 is sensitive to intracellular and extracellular pH, and co-localizes to the lysosomes where it can function in K^+ transport, presumably to facilitate endolysosomal acidification.

3.5 Gain and loss-of-function of KCNJ15 in THP-1 and its effect on controlling mycobacterial growth

We next examined the role of *KCNJ15* on intracellular mycobacterial growth. Infection of *KCNJ15*^{OE} cells with *Mtb* yielded no improvements in bacterial growth after 48h (Fig 15A). However, infection with BCG instead showed some indication of bacterial growth restriction which persisted till 72h (Fig 15B). On the contrary, *KCNJ15*^{KO} cells did not show increase in BCG growth (Fig 15C), which may be explained due to its heterozygosity and enduring ability to upregulate *KCNJ15* upon mycobacterial infection (Fig 13D). Naturally, *Mtb* is significantly more virulent than its attenuated counterpart, BCG, which may explain why THP-1 *KCNJ15*^{OE} cells are able to better control infection of BCG than that of *Mtb*. The differences between *KCNJ15*^{OE} and *KCNJ15*^{KO} in their ability to control BCG infection were not attributable to altered phagocytic capabilities as uptake of BCG at 3h for both cell lines were equal (Fig 15D). However, we did previously observe that primary monocytes with lentiviral-mediated overexpression of *KCNJ15* was able to better restrict *Mtb* growth (Fig 15E) [211], although this effect was much less pronounced in an overexpressing THP-1 cell line. This data indicates that *KCNJ15*/Kir4.2 expression might be associated with an enhanced control of mycobacterial growth that may depend on the monocyte cell type/state.

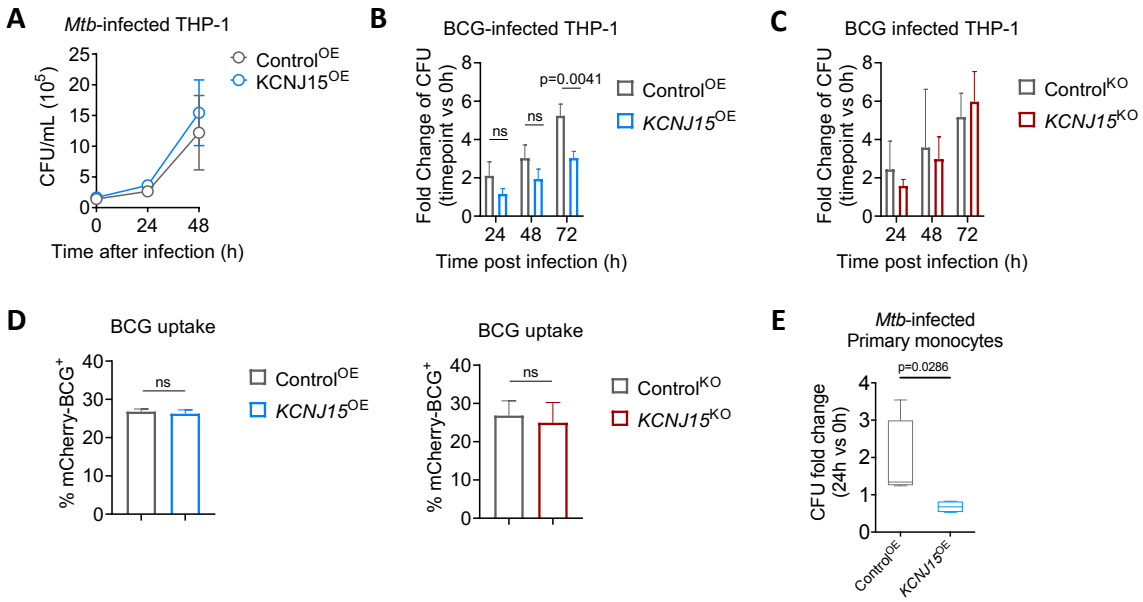

Figure 15. Overexpression of *KCNJ15* improves control of intracellular mycobacterial growth in monocytes.

A) *Mtb* growth in *Mtb*-infected THP-1 at 0, 24 and 48h post-infection (n=2). CFU fold change of BCG growth in **B)** *KCNJ15*^{OE} and **C)** *KCNJ15*^{KO} THP-1 at 24, 48 and 72h post infection in comparison to controls. **D)** Percentage uptake of mCherry-tagged BCG into *KCNJ15*^{OE} and *KCNJ15*^{KO} THP-1 monocytes at 3h post infection detected by flow cytometry. Data is gated on live cells. **E)** CFU fold change of *Mtb* growth in human primary monocytes overexpressing *KCNJ15* (*KCNJ15*^{OE}) or transfected with empty vector (Control^{OE}) at 24h post infection (n= 4 donors) [211]. Data in **A**, **B** and **C** were analyzed by Two-way ANOVA. Data in **D** and **E** were analyzed by Mann-Whitney test [211]. Bar graphs represent Mean ± SD. All experiments were conducted thrice unless otherwise stated.

3.6 Overexpression of KCNJ15 enhances inflammasome response to TLR agonists and mycobacterial infection

Like several intracellular bacterial pathogens, mycobacterial infection invariably results in the engagement of various PRRs on immune cells and non-immune cells alike. Mycobacteria carry numerous PAMPs which engage monocytes/macrophages through various PRRs such as TLR2, TLR9 and C-type lectin receptors [378, 383]. Engagement of TLR receptors often leads to downstream signal transduction that initiates the expression of NF-κB family of transcription factors (TFs), and this is often recognized as Signal 1 in the 2-step process leading up to NLRP3-mediated inflammasome activation [384]. As mentioned previously, reduced intracellular K^+ caused by rapid K^+ efflux is a common trigger in many scenarios leading to NLRP3 activation. TWIK2 and Kir6.2 have prior been implicated in modulating inflammasome activation and thus, we hypothesized that Kir4.2 channel might play a similar role [237, 300]. Indeed, *KCNJ15*^{OE} THP-1 monocytes, which have increased intracellular K^+ pool (Fig 12F), when stimulated with either LPS (TLR4 agonist)

or Pam2CSK4 (TLR1/2 agonist) or infected with BCG, trended towards higher IL-1β secretion a marker of NLRP3 activation [385], compared to Control^{OE} cells (Fig 16A, B).

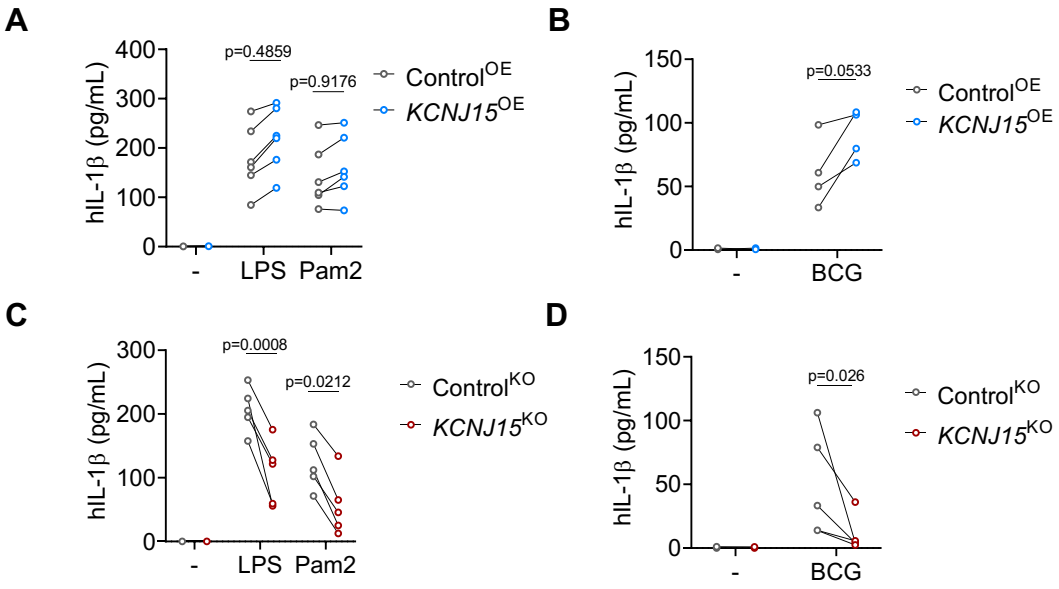

Figure 16. hIL-1β production is enhanced in BCG/TLR-stimulated *KCNJ15*^{OE} cells but dampened in *KCNJ15*^{KO} THP-1.
Analysis of hIL-1β in cell culture supernatant from LPS (1µg/mL) or Pam2CSK4 (1µg/mL) treated **A)** *KCNJ15*^{OE} and **C)** *KCNJ15*^{KO} THP-1 monocytes as well as from BCG-infected **B)** *KCNJ15*^{OE} and **D)** *KCNJ15*^{KO} THP-1 monocytes collected after 24h of infection or treatment. Respective control cells have been included. Each paired dots represents one independent experiment, average value from that experiment has been plotted. Data in **A-D** was analyzed by Two-way ANOVA.

On the other hand, *KCNJ15*^{KO} THP-1 cells (heterozygous knockout, see Section 3.3) showed marked reduction in IL-1β production when stimulated with LPS or Pam2CSK4 (Fig 16C) or infected with BCG (Fig 16D). THP-1 monocytes of human origin do not require a second signal from DAMPs to initiate inflammasome activation, hence TLR agonist treatment alone was sufficient to elicit IL-1β induction [386]. To explain why *KCNJ15*^{KO} cells showed a drastic reduction of inflammasome response although *KCNJ15* expression was shown to still accumulate post-infection (Fig 13D), we could surmise that *KCNJ15* expression takes time to accumulate while inflammasome activation is a much quicker event given that cells already endogenously express NF-κB factors which, at steady-state, are maintained in the cytoplasm in an inactive state via IκB kinases [387]. During TLR-mediated signaling IκB kinases can be phosphorylated by the IKK complex and be degraded quickly, thus allowing nuclear translocation of NF-κB TFs [388]. Of note, due to time constraints, further study into the inflammasome activation aspect of *KCNJ15*/Kir4.2 has not been investigated here (see Chapter 6).

3.7 Transcriptomic analysis of human primary monocytes overexpressing KCNJ15 suggests a role in apoptosis induction

To explore potential pathways by which *KCNJ15* may exert its anti-mycobacterial property, we overexpressed *KCNJ15* in human primary $CD14^+$ monocytes ($KCNJ15^{OE}$-mono) and analyzed their gene expression by RNA-seq. Under naïve conditions, comparing $KCNJ15^{OE}$-mono to $Control^{OE}$-mono cells revealed only 25 significant DEGs (FDR <0.05, Table 9). Certainly, the transcriptomic data might have been more informative if *Mtb/*BCG-infected samples had been included. Nonetheless, we examined these 25 genes and noticed that genes associated to pro-apoptotic pathways were upregulated (*FANCI*, *CCDC180*), whereas genes associated with anti-apoptotic outcomes were downregulated (*CCND1*, *PRSS23*, *FSTL1*) in $KCNJ15^{OE}$-mono (Fig 17A). This suggested that *KCNJ15* might have a role in the induction of apoptosis.

Apoptosis has been demonstrated to be one method by which cells can circumvent infection by intracellular pathogens, by limiting their replication niche while also recruiting surrounding phagocytes to clear apoptotic cell remnants [389, 390, 391]. We thus assayed for apoptosis using Annexin V and propidium iodide (PI) staining in uninfected and BCG-infected $KCNJ15^{OE}$ and $KCNJ15^{KO}$ THP-1 cells. At 24h post infection BCG-infected $KCNJ15^{OE}$ THP-1 cells had higher proportion of early apoptotic (Annexin V^+PI^-) cells (Fig 17C, D). Conversely, BCG-infected $KCNJ15^{KO}$ THP-1 cells had significantly higher late apoptotic cells (Annexin V^+PI^+, Fig 17C, E). No clear differences were observed in percentage of necrotic cells in either of BCG-infected $KCNJ15^{OE}$ or $KCNJ15^{KO}$ THP-1 cells (Fig 17C-E).

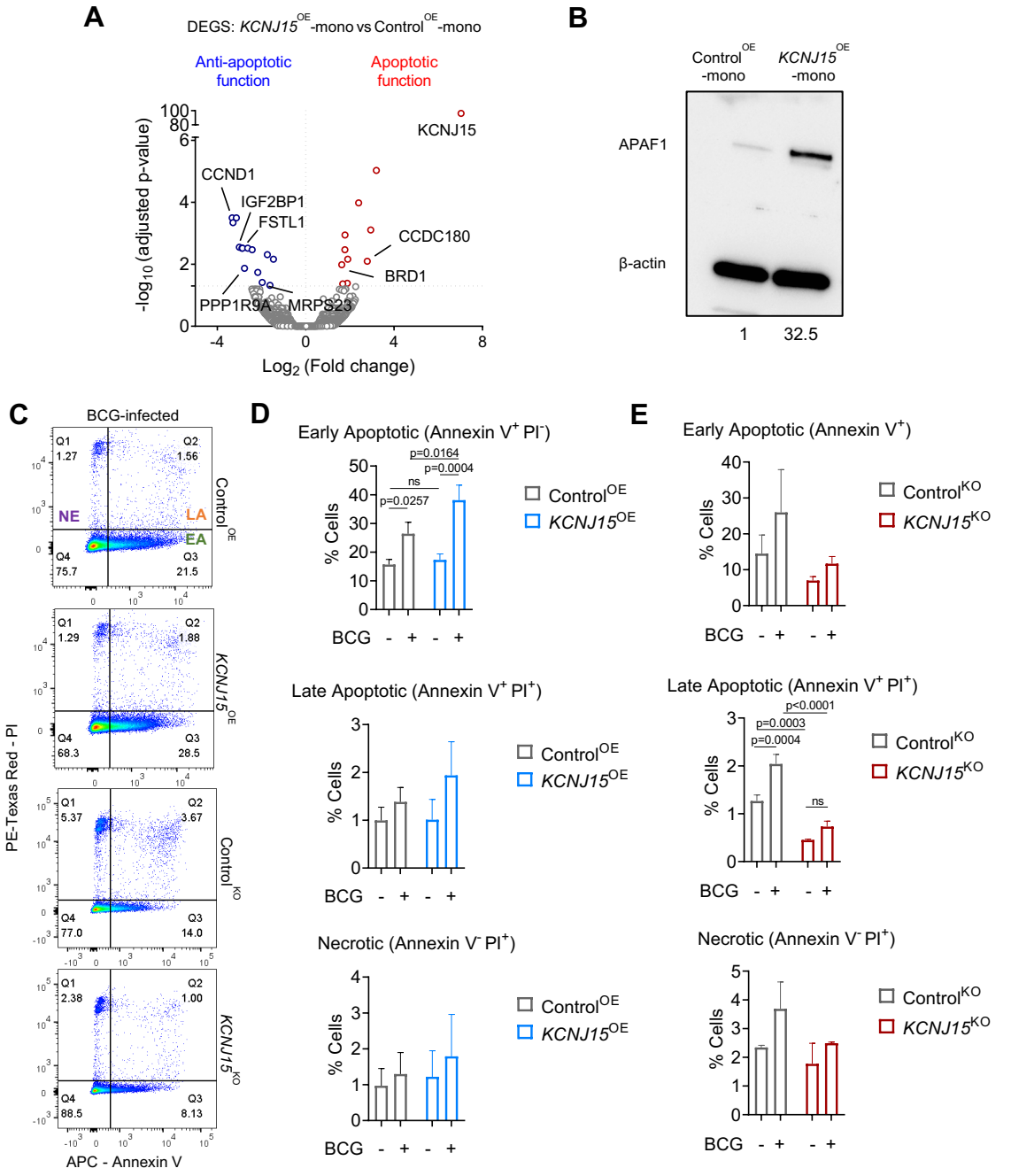

Figure 17. *KCNJ15* overexpressing monocytes demonstrate enhanced apoptosis induction.
A) Volcano plot of all RNA-seq DEGs in pair-wise comparison of *KCNJ15*^{OE} vs Control^{OE} primary CD14^{+} human monocytes (-mono) (n=5 donors each). **B)** Western immunoblot of APAF1 protein in Control^{OE} and *KCNJ15*^{OE} primary monocytes (n=2). Numbers represent densitometric analysis relative to Control^{OE}. **C)** Representative flow cytometry plots of Annexin V-PI apoptosis assay in *KCNJ15*^{OE} and *KCNJ15*^{KO} THP-1 (BCG-infected groups shown). **D, E**) Assessment of early apoptotic, late apoptotic and necrotic populations in *KCNJ15*^{OE} and *KCNJ15*^{KO} THP-1 uninfected or infected with BCG for 24h by Annexin V and propidium iodide (PI) staining. Early apoptosis (EA) – Annexin V^{+}, PI^{-}; Late apoptosis (LA) – Annexin V^{+}, PI^{+}; Necrosis (NE) – Annexin V^{-}, PI^{+}. Data in **D** and **E** were analyzed by two-way ANOVA. Bar graphs represent Mean ± SD. Data are from n=3 experiments unless otherwise stated.

In line with these findings, we also found that *KCNJ15*^{OE}-mono contained increased APAF1 protein (Fig 17B), which is a necessary scaffold protein important in the formation of the

apoptosome, which then culminates in caspase-9-mediated intrinsic apoptosis [392]. Of note, APAF1 overexpression has been shown to correlate with enhanced apoptosis induction [393, 394].

In summary, *KCNJ15* expression was associated with apoptosis induction during BCG infection. Apoptosis is understood to confer some level of host-protective and bacterial-restrictive advantage, however we do not observe in parallel, increased BCG growth in *KCNJ15*^{KO} THP-1 cells (Fig 15C), although CFU restriction in *KCNJ15*^{OE} THP-1 cells was seen (Fig 15B). The differential phenotype of *KCNJ15*^{OE} THP-1 cells (a cell line) and *KCNJ15*^{OE}-mono (primary monocytes) could also be important for the incongruent outcomes in our *in vitro* experiments [395].

Gene Name	Log_2FC	FDR	Relation to Apoptosis	References
KCNJ15	7.03	5.51E-97		
FANCI	3.20	9.31E-06	Pro-apoptotic	Zhang *et al.* [396]
PRDM15	2.40	1.04E-04	Pro-apoptotic (Genes of this family are pro-apototic)	Wu *et al.* [397]
MGC27382	-3.33	3.16E-04		
CCND1	-3.14	3.16E-04	Anti-apoptotic	Wang *et al.* [398]
TMEM128	-3.29	4.54E-04		
PRSS23	2.95	7.83E-04	Anti-apoptotic	Han *et al.* [399]
FAM126B	1.78	1.13E-03		
FSTL1	-3.01	2.81E-03	Anti-apoptotic	Liang *et al.* [400] Ogura *et al.* [401]
REXO5	-2.88	3.01E-03		
ADCY6	-2.86	3.01E-03		
IGF2BP1	-2.63	3.01E-03	Anti-apoptotic	Rebucci *et al.* [402]
CENPJ	-2.42	3.38E-03	Anti-apoptotic	Ding *et al.* [403]
SGF29	1.78	3.38E-03		
GOLGB1	-1.74	4.88E-03		
SOCS7	-1.46	6.82E-03	Anti-apoptotic	Noguchi *et al.* [404]
EPN1	1.90	6.83E-03	Pro-apoptotic	Brophy *et al.* [405]
CCDC180	2.79	7.99E-03	Pro-apoptotic	Aoyama *et al.* [406]
BRD1	1.64	1.03E-02		
PPP1R9A	-2.77	1.35E-02	Anti-apoptotic	Bullock S. A [407]
UMPS	-2.17	1.82E-02		
MRPS23	-1.97	3.86E-02	Anti-apoptotic	Gao *et al.* [408]
SRD5A1	1.88	4.11E-02		
USP37	1.68	4.31E-02	Anti-apoptotic	Qin *et al.* [409]
OSBPL3	-1.62	4.78E-02	Anti-apoptotic	Xue, Scotti and Stofel. [410]

Table 9. List of 25 DEGs between *KCNJ15*^{OE}-mono and Control^{OE}-mono, and their association with apoptotic outcomes.

3.8 Limitations of Chapter 3

While the THP-1 monocytic cell line is a useful tool to study the function of *KCNJ15* due to the ease of using gain and loss-of-function techniques, the endogenous expression of *KCNJ15* in THP-1 is relatively low. Hence, WT THP-1 cells may not be the best cellular model system. On the Human Protein Atlas, THP-1 monocytes are reported to express *KCNJ15* at normalized transcripts per million (nTPM) of 0.5 [411]. Although *KCNJ15* is indeed upregulated upon TLR-mediated engagement by *Mtb*/BCG, its absolute expression remains low. Upwards of 50-80μg of WT THP-1 protein lysate input has to be provided to be able to visualize *KCNJ15* via immunoblotting. Furthermore, as a transformed cancer cell line, THP-1 cells do not represent true monocytes and may demonstrate abnormal immune functions. The unexpected difficulty in obtaining a full knockout clone of *KCNJ15* in THP-1 also poses a problem to our interpretation of the data.

In order to gain a more thorough understanding of the role of *KCNJ15* during mycobacterial infection, we generated a full-body *Kcnj15* knockout mouse model to study *Kcnj15* at a systems level (next chapter).

Chapter 4: Investigating the role of *KCNJ15* in mycobacterial infection *in vivo* using a *Kcnj15*^{KO} mouse model

4.1 Generation and validation of Kcnj15^{KO} mice

Kcnj15^{KO} mice were generated by *in-vitro* fertilization of eggs from super-ovulated wild-type (WT) C57BL/6 female mice with *Kcnj15*^{KO} sperm, followed by loading of embryos into surrogate C57BL/6 female (Performed by IVF platform at BRC, A*STAR). This resulted in the birth of F0 heterozygous offspring, which were further bred to obtain F1 mice (Fig 18A). Aside from PCR genotyping (Fig 18A), the knockout of *Kcnj15* was also confirmed by assessing protein levels in various key organs from WT and *Kcnj15*^{KO} mice. As expected, both the kidneys and stomach expressed high levels of Kir4.2 (expected size ~42.5kdA, red arrow) which was absent in *Kcnj15*^{KO} mice (Fig 18B). Notably, the lungs also showed Kir4.2 expression at the expected band size which was absent in *Kcnj15*^{KO} mice. On the other hand, expression of Kir4.2 specific band in the spleen was virtually undetectable in WT mice (Fig 18B). Overall, this data confirms the loss of Kir4.2 in *Kcnj15*^{KO} mice. Currently, these *Kcnj15*^{KO} mice appear to have only been used in a renal study, revealing deficits in ammonia metabolism and management of acidosis in proximal tubules of mice lacking *Kcnj15* [412].

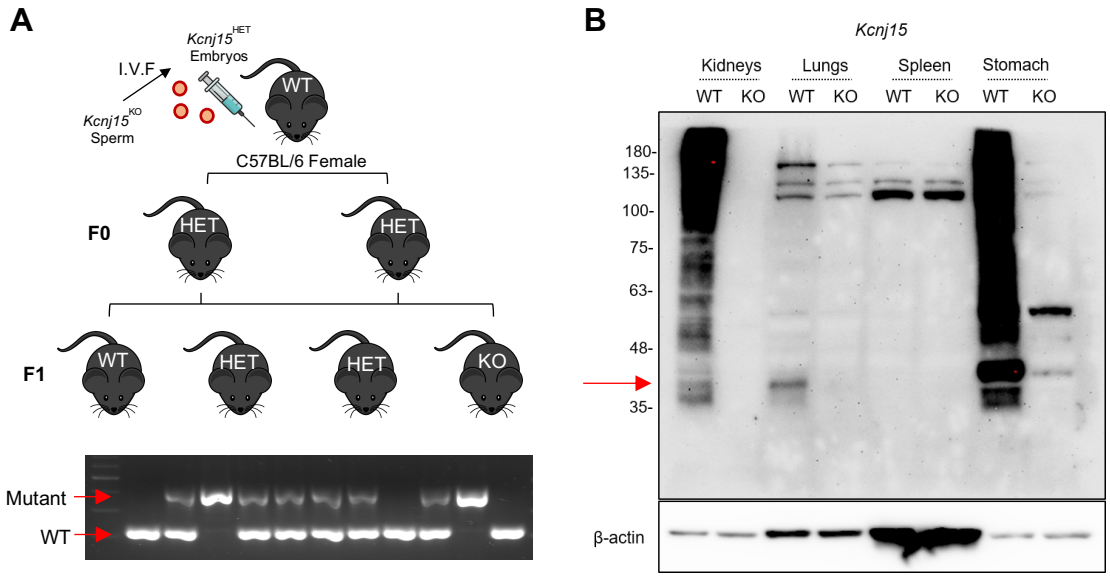

Figure 18. Generation and validation of *Kcnj15*^{KO} full body knockout mice.
A) Schematic of generation of *Kcnj15*^{KO} mice by *in-vitro* fertilization, breeding and PCR genotyping to detect wild-type and mutant bands. **B)** Western immunoblot of protein lysates from kidneys, lungs, spleen and stomach of naïve WT and *Kcnj15*^{KO} mice, blotted for *Kcnj15*/Kir4.2 (Anti-Kir4.2, Alomone) Red arrow indicates Kir4.2 band at ~42.5kDa. 50µg of protein from each organ was loaded and β-actin was used as a loading control.

4.2 Kcnj15^{KO} mice carry reduced BCG burden in lungs which correlates with increased spleen dissemination

We first examined the effect of ablating *Kcnj15* in mice on mycobacterial growth. Due to COVID-19 pandemic driven occupancy of our ABSL3 facility, we were unable to perform mice experiments with *Mtb* under ABSL3 conditions. With no other timely option available, we performed experiments in ABSL2 where we infected mice intratracheally with 1.5*10^6 BCG to model *Mtb* infection. *Kcnj15*^{KO} mice harbored less BCG burden in the lung when evaluated at 14 days post infection (d.p.i). (Fig 19A). While we did not find significant difference in splenic bacillary load (Fig 19B), we observed that lung and spleen bacterial load were inversely correlated (R= -0.343, p=0.0261) (Fig 19C), suggesting that reduced lung bacterial load may correlate with increased dissemination of bacteria to peripheral organs such as the spleen. Furthermore, since we used a whole-body knockout mouse model, whether the reduced lung bacillary load was due to the ablation of *Kcnj15* in immune or non-immune cells is unknown. Future studies will involve the generation of bone-marrow chimeras to examine *Kcnj15* function in immune cells.

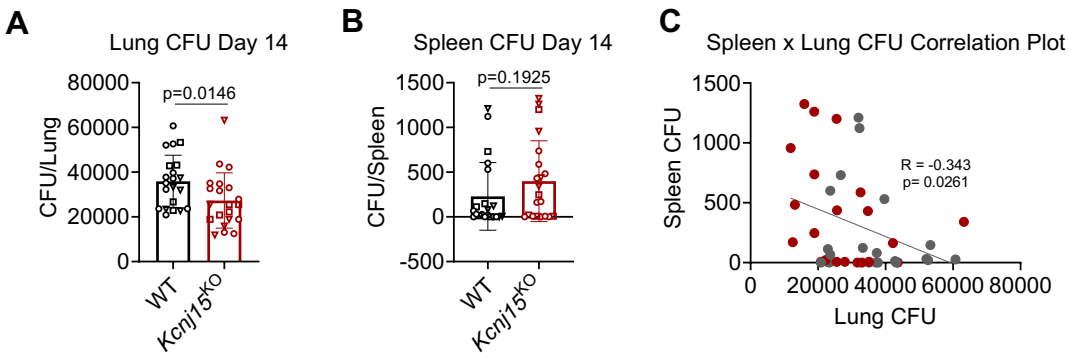

Figure 19. *Kcnj15*^{KO} mice carry reduced lung BCG burden which correlates with increased spleen dissemination.
Bacterial loads in **A)** lung and **B)** spleen of BCG-infected WT and *Kcnj15*^{KO} mice at 14 d.p.i. Compiled data from n=3 independent experiments is shown, with ▽, □, ○ indicating mice from n=3 experiments, bar graphs represent Mean ± SD. **C)** Correlation plot between lung and spleen CFUs are plotted where each dot represents n=1 mice. Red, *Kcnj15*^{KO} mice; Grey, WT mice. Data in **A** and **B** are analyzed by Mann-Whitney test and data in **C** is analyzed by simple linear regression with Pearson's correlation.

4.3 Myeloid immune cell profiling of lungs from BCG-infected Kcnj15^{KO} mice

Since we observed reduced BCG burden in the lungs of *Kcnj15*^{KO} mice at 14 d.p.i. (Fig 19A), a timepoint at which there is no significant initiation of adaptive immunity in mouse models of TB [144, 413], we profiled pulmonary myeloid immune cells by multi-parameter flow cytometry to understand the role of *Kcnj15* in *in vivo* host-mycobacterial interaction. WT and *Kcnj15*^{KO} mice were infected intratracheally with 1.5*10^6 CFU of BCG for 7 or 14 days (Fig 20A). Age-matched

uninfected mice were used as controls. Examination of lung myeloid populations revealed specific differences in BCG-infected *Kcnj15*^{KO} mice.

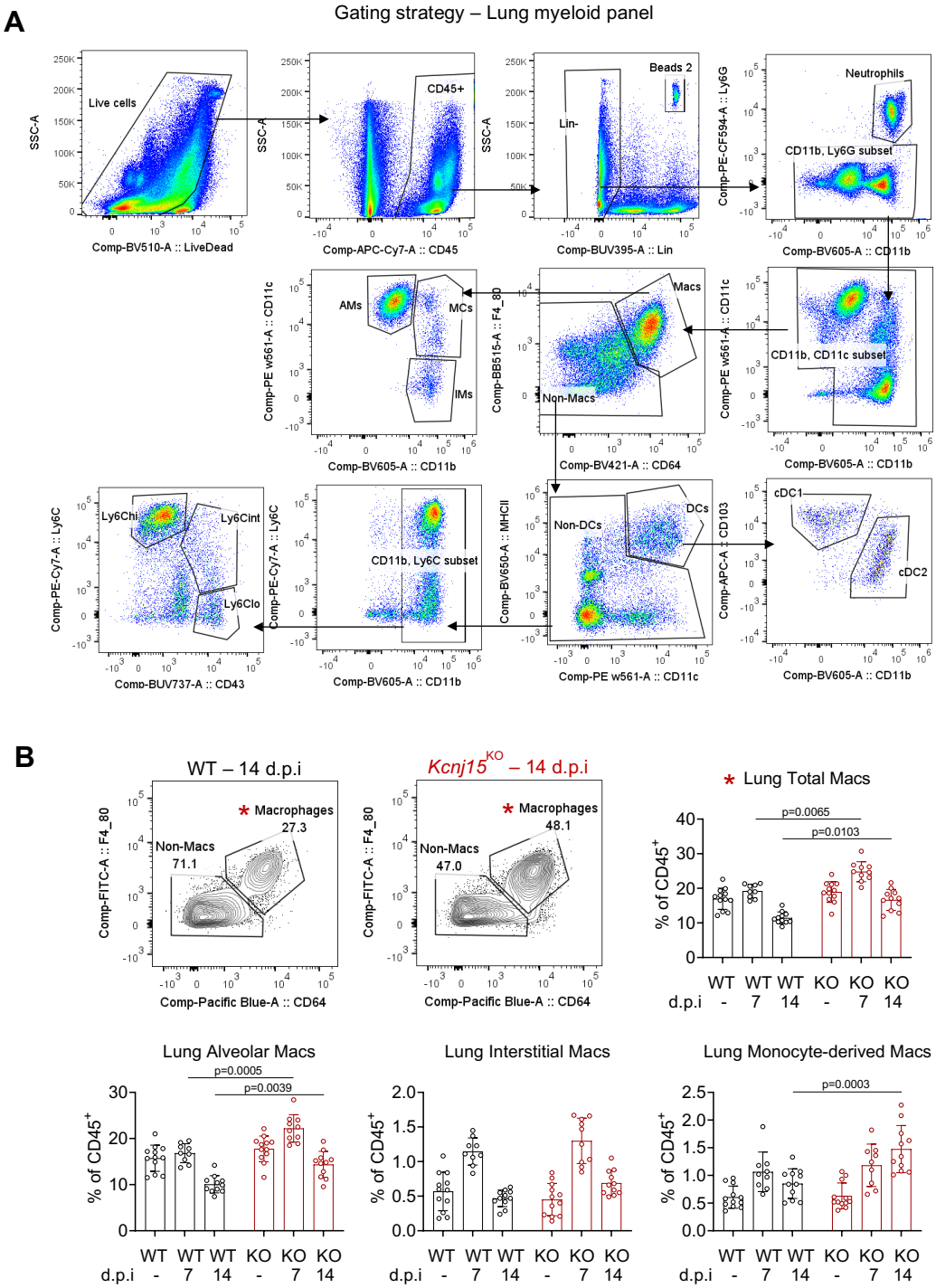

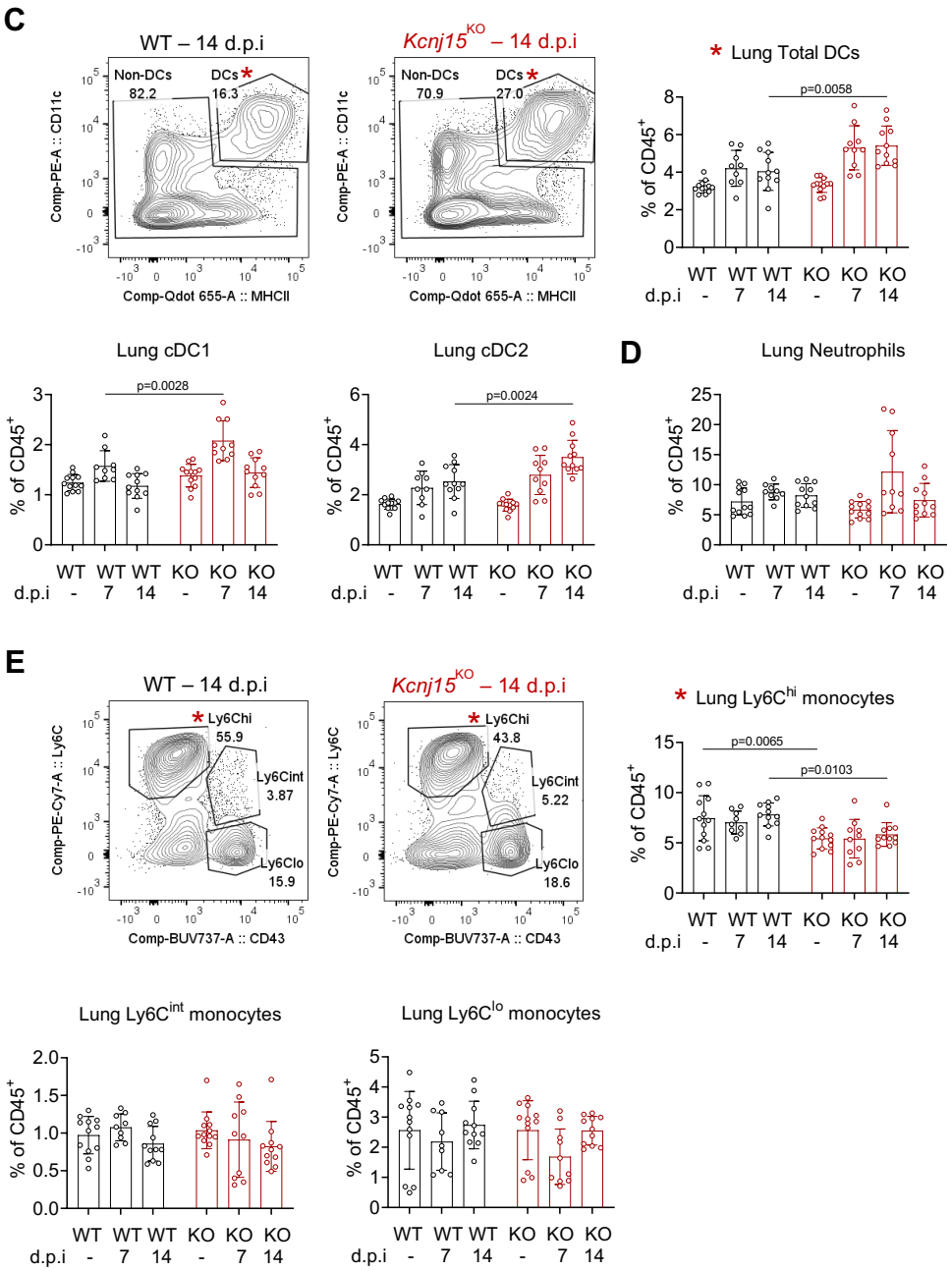

Figure 20. Profiling of myeloid immune populations in WT and *Kcnj15*^{KO} mice during BCG infection. **A)** Gating strategy for analysis of myeloid immune populations in murine lung. Lin^{-} gating removes lymphoid cells by excluding cells expressing CD45R, CD90.2 and NK1.1. **B)** Representative plots showing proportion of total macrophages in WT and *Kcnj15*^{KO} lungs at 14 d.p.i (top left) and quantification of macrophage populations in uninfected and BCG-infected WT and *Kcnj15*^{KO} mice at 7 and 14 d.p.i represented as a percentage of CD45^{+} cells. **C)** Representative plots showing proportion of total DCs (CD11c^{hi} MHCII^{hi}) in WT and *Kcnj15*^{KO} lungs at 14 d.p.i (top left) and quantification of DC populations (cDC1 and cDC2, bottom) and **D)** neutrophils (CD11b^{+} Ly6G^{+}) as a percentage of CD45^{+} cells (right). **E)** Representative plots showing proportion of Ly6C^{hi} monocytes (Ly6C^{hi} CD11b^{hi} CD43^{-}) in WT and *Kcnj15*^{KO} lungs at 14 d.p.i (top left) and quantification of monocyte populations. DCs – Dendritic cells; cDC1 – Conventional DCs type 1 (CD103^{+} CD11b^{-}); cDC2 – Conventional DCs type 2 (CD103^{-} CD11b^{+}). Each dot represents n=1 mice and each bar represent ≥ n=2 experiments, Mean ± SD. Data from **B-E** are analyzed by Two-way ANOVA for differences between WT and *Kcnj15*^{KO} groups (within group analysis not shown).

As expected, total macrophages ($CD64^{+}F4/80^{+}$) increased in proportion within the lung by 7 d.p.i in both BCG-infected WT and *Kcnj15*^{KO} mice, which then subsided by 14 d.p.i (Fig 21B). Indeed, all subsets of macrophages including AMs, IMs, and monocyte-derived macrophages (MCs) showed a similar trend. Each of these populations can be replenished by recruited BM-derived monocytes to the lung during inflammation and infection [102]. *Kcnj15*^{KO} mice demonstrated an increased proportion of lung AMs and MCs over the 14-day infection (Fig 20B). Generally, IMs and MCs both represent interstitial macrophage-like cells seeded by recruited bone marrow monocytes during lung infection with *Mtb* [414, 415]. DCs ($CD64^{-}F4/80^{-}CD11c^{+}MHC\text{-}II^{+}$), likewise, can be differentiated from incoming bone-marrow monocytes or expanded from pre-DCs originating in the bone marrow [416], and was thus observed to accumulate over the 14-day infection period in both WT and *Kcnj15*^{KO} mice (Fig 20C). However, *Kcnj15*^{KO} mice demonstrated higher proportion of both lung cDC1 ($CD103^{+}$ DCs) and cDC2 ($CD11b^{+}$ DCs), compared to their WT counterparts. Neutrophil populations, surprisingly, were not greatly expanded at 7 d.p.i in WT mice, although some mice had increased neutrophils in *Kcnj15*^{KO} mice (Fig 20D). Since neutrophils are one of the earliest responders to pathogenic assault, peak in neutrophil recruitment in the lung of *Kcnj15*^{KO} mice likely occurred at an earlier timepoint (< 7 d.p.i), which was not captured in this dataset. Interestingly, we observed a marked reduction in the presence of lung $Ly6C^{hi}$ monocytes (classical monocytes) both in uninfected and infected *Kcnj15*^{KO} mice compared to WT mice, which was maintained till 14 d.p.i (Fig 20E).

Based on the above lung myeloid phenotyping in uninfected and infected *Kcnj15*^{KO} mice and the fact that *Kcnj15*^{KO} mice were able to better control BCG burden in the lungs but showed increased dissemination to the spleen, the following hypotheses were formulated to further decipher the potential role of *Kcnj15* in immune response to *Mtb* (Fig 21).

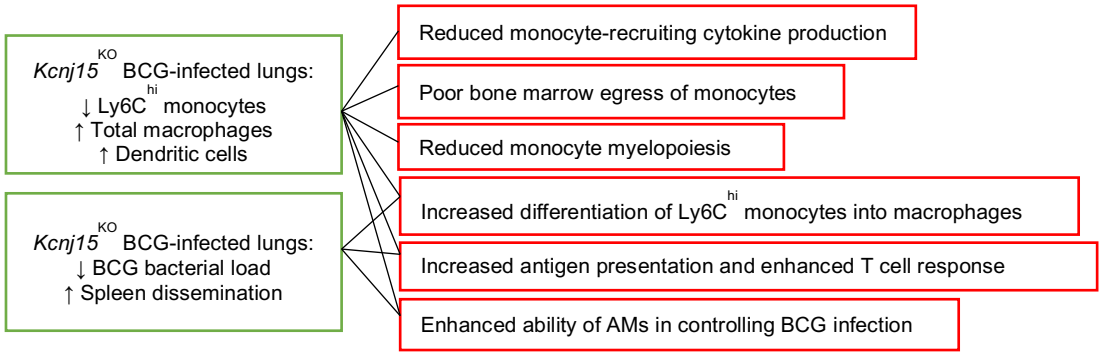

Figure 21. Hypotheses regarding the role of *Kcnj15* in reducing lung BCG burden and regulation of myeloid population changes.

Cytokine and chemokine secretion is vital for monocyte recruitment to sites of infection [104]. We thus first hypothesized that *Kcnj15*^{KO} mice might be deficient in production of pro-inflammatory mediators necessary for efficient Ly6C^{hi} monocyte recruitment to the lung. Monocytes are generated in the bone marrow (BM) niche, from which they egress into the bloodstream and migrate to the site of infection [104]. Thus, we next considered if the reduction in Ly6C^{hi} monocytes in *Kcnj15*^{KO} mice might be due to reduced myelopoiesis of monocytes, limited egress from the BM or reduced emergency hematopoiesis (Fig 21).

Since we also observed an increased proportion of total macrophages including AMs and MCs, as well as DCs (Fig 20B, C), we surmised that there may be an enhanced differentiation of Ly6C^{hi} monocytes to macrophages or DCs in the lung, which could have contributed to improved bacterial clearance. Indeed, macrophages and notably DCs are crucial APCs for initiating the adaptive response, hence we consider that increase in these populations may have resulted in enhanced BCG-specific T cell response by 14 d.p.i, thus aiding in bacterial killing. Lastly, since AMs are situated at the site of airway infection and are capable of phagocytosing *Mtb* [6], we hypothesize that *Kcnj15*^{KO} AMs may harbor heightened bactericidal capabilities. To this end, we conducted transcriptomic analysis to examine this notion.

4.4 Cytokine/chemokine expression analysis in BCG-infected WT and Kcnj15^{KO} mice

Inflammatory cytokines and leukocyte-recruiting chemokines are secreted by both immune and non-immune cells during infection. We examined lung homogenates from uninfected and BCG-infected WT and *Kcnj15*^{KO} mice at 14 d.p.i using a multiplexed cytokine analysis platform.

In general, the level of cytokines/chemokines under homeostatic conditions (uninfected) were similar in the lung homogenates of WT and *Kcnj15*^{KO} mice (Fig 22A). However, among BCG-infected WT and *Kcnj15*^{KO} groups we noticed significant differences in some of the analytes in the lungs. These included IL-17A (CTLA8), IL-15 and GM-CSF ($p=0.0548$), all of which were found to be at a lower level in *Kcnj15*^{KO} mice upon BCG infection as compared to BCG-infected WT mice (Fig 22B). All these 3 cytokines appear to promote a pro-inflammatory phenotype in *Mtb*-infected mice are important for host protection.

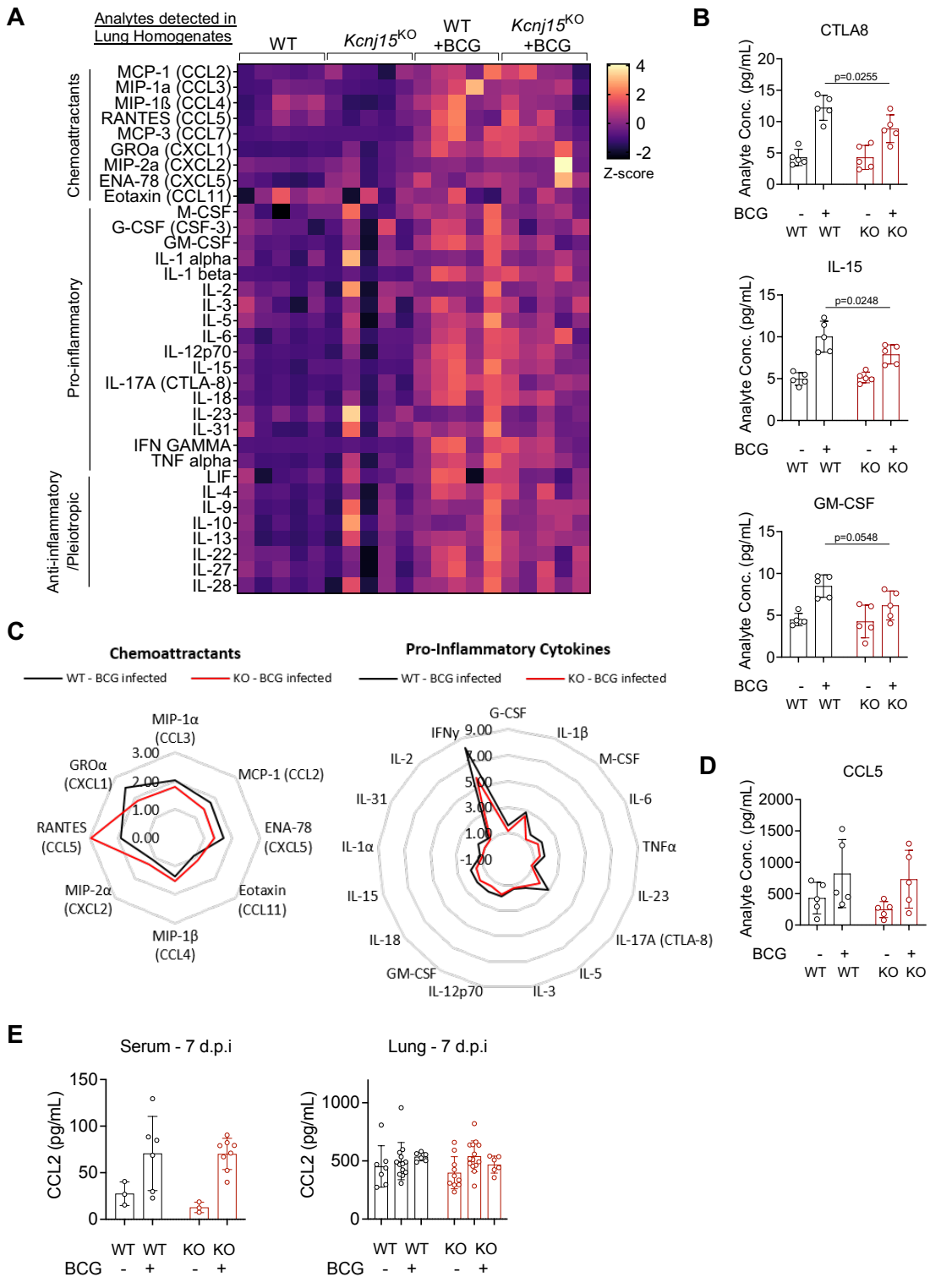

Figure 22. BCG-infected *Kcnj15*^{KO} mice lungs harbor reduced pro-inflammatory cytokine and chemokine expression.

A) 36-plex multi-analyte profiling on lung homogenates of uninfected or BCG-infected (14 d.p.i) WT and *Kcnj15*^{KO} mice (n=5 mice per group). Z-scores for each analyte across all samples were tabulated and plotted as a heatmap. **B)** IL17A (CTLA8), IL-15 and GM-CSF analyte concentrations in lung homogenates from mice in **A**. **C)** Multi-analyte profiling data plotted in radar plot, where values represent fold-change of average concentration of analyte from BCG-infected samples vs uninfected samples for each group (WT or *Kcnj15*^{KO}) in **A**. **D)** CCL5 levels in the lung from mice in **A**. **E**) CCL2 levels in serum and lung

homogenate from uninfected and BCG-infected (7 d.p.i) WT and *Kcnj15*^{KO} mice, detected by sandwich ELISA. Data in **B, D** and **E** was analyzed by Two-way ANOVA. Bar graphs represent Mean ± SD.
IL-15 regulates many immune cell types and is considered pro-inflammatory [417].

Notably, IL-15 is important for CD8^{+} T cell activation. In *Mtb*-infected mice, loss of IL-15 inhibited CD8^{+} expansion in draining lymph nodes and impaired cytotoxic function and IFNγ production, resulting in poorer survival [418]. Next, IL17A is a potent activator of neutrophilic inflammation, and is secreted by immune cells during *Mtb* infection. IL17A production and autocrine signaling by *Mtb*-infected neutrophils also confers it enhanced bactericidal abilities [419], and its deletion worsens bacterial burden in the lung [420]. GM-CSF signaling in macrophages is crucial for *Mtb* restriction [421]. *In vitro* neutralization of GM-CSF was shown to promote an M2 signature in macrophages that was associated with reduced NO production and higher bacterial burden, while *in vivo* neutralization led to increased granuloma formation but no change in bacterial growth [422].

Visualizing the cytokine/chemokine lung data as a radar plot demonstrated that the fold-change induction of cytokines/chemokines upon BCG infection (BCG-infected vs uninfected) in WT mice were higher compared to *Kcnj15*^{KO} mice (Fig 22C). The only outlier in this fold change analysis was CCL5 (Fig 22C), which showed a greater fold change in infected *Kcnj15*^{KO} mice (2.96 times) than in WT mice (1.96 times), though in absolute analyte concentrations there was no statistical difference (Fig 23D). CCL5 along with CCL2, CCL3 and CCL7 are all ligands for CCR2 [104], and thus can contribute to Ly6C^{hi} monocyte recruitment. CCL2 is well known to stimulate Ly6C^{hi} monocyte (which are also CCR2^{hi}) egress from the BM reserve and migration towards lymph nodes or sites of infection [104]. Having observed decreased Ly6C^{hi} monocytes in the lungs (Fig 20D) of *Kcnj15*^{KO} mice, we hypothesized that these mice may harbor reduced CCL2. However, CCL2 levels in lung homogenate and serum at 7 d.p.i were similar between WT and *Kcnj15*^{KO} mice (Fig 22E), suggesting that CCL2 was not responsible for reduced lung Ly6C^{hi} monocytes recruitment in *Kcnj15*^{KO} mice.

Overall, the cytokine/chemokine analysis suggests a somewhat reduced inflammatory milieu in the lung of BCG-infected *Kcnj15*^{KO} mice, a phenotype which was also observed in *KCNJ15*^{KO} THP-1 cells when infected with BCG or stimulated with LPS or Pam2CSK4 (Fig 16C, D). Furthermore, lower levels of various chemoattractant and pro-inflammatory cytokine at 14 d.p.i in *Kcnj15*^{KO} mice correlates with ongoing resolution of infection at that time point, as shown by a reduced BCG burden in the lungs of *Kcnj15*^{KO} mice (Fig 19A). It can be surmised that the higher proportion of macrophages present in *Kcnj15*^{KO} lungs at 7 through 14 d.p.i (Fig. 20B) contributed to more bacterial clearance and thus reduced CFU and inflammation by 14 d.p.i (Fig 19A). Reduced inflammatory mediators at 14 d.p.i may also, in turn, stimulate less Ly6C^{hi} monocyte infiltration.

It may be possible that the *Kcnj15*^{KO} Ly6C^{hi} monocyte pool are primed towards differentiation into macrophages in tissue niches. Further investigation is required to understand the dynamics between the reduction of Ly6C^{hi} monocyte population and expansion of the macrophage or DC compartments in *Kcnj15*^{KO} mice. Alternatively, the decrease in lung Ly6C^{hi} monocytes could be due to deficits in trafficking of monocytes from BM to blood or from the blood into the lungs.

4.5 Blood myeloid populations in Kcnj15^{KO} mice are unchanged at 7 d.p.i

In order to further probe the observed reduction in Ly6C^{hi} monocytes in the lungs of *Kcnj15*^{KO} mice at 14 d.p.i, we investigated the myeloid cells in the blood (Fig 23A). We chose an earlier timepoint of 7 d.p.i to capture the monocyte recruitment process earlier in the infection. By examining the blood myeloid cells profile, we can establish if the loss of Ly6C^{hi} monocytes is also seen in the blood, which could suggest a deficit in upstream BM egress. Indeed, when monocytes are prevented from egressing due to deletion of *Ccr2*, monocytes become drastically reduced in the blood and are instead accumulated in the BM [423]. If blood Ly6C^{hi} monocytes are unchanged, dysregulation of monocyte numbers could be happening at the site of infection (lung).

BCG infection alone did not result in significant expansion of myeloid populations in the blood at 7 d.p.i (Fig 23B), notably, of pro-inflammatory Ly6C^{hi} monocytes and neutrophils. In BCG-infected *Kcnj15*^{KO} mice, however, we saw some highly variable expansion of neutrophils which was not statistically significant, although the same trend was also observed in the lungs at 7 d.p.i (Fig 20D). It is possible that the expansion of pro-inflammatory populations might be better observed at an earlier timepoint to infection (i.e. 1-3 d.p.i) as we did observe expansion of macrophage and DC populations as early as 7 d.p.i (Fig 20B, C), suggesting that pro-inflammatory monocytes could have already largely infiltrated and become differentiated in the lungs.

Interestingly, we found that Ly6C^{hi} monocytes in the blood were already lower in uninfected *Kcnj15*^{KO} mice compared to uninfected WT mice (Fig 23B). This was similarly reflected in the lungs of uninfected *Kcnj15*^{KO} mice (Fig 20E). In BCG-infected mice, however, there was no clear difference in blood Ly6C^{hi} monocytes from *Kcnj15*^{KO} mice compared to WT, although reduction was observed in the lungs (Fig 20E). Aside from these, we found no significant changes to other monocyte populations nor DCs and neutrophils in the blood stemming from the loss of *Kcnj15* expression.

We thus consider that *Kcnj15*^{KO} mice may have an intrinsic deficit in Ly6C^{hi} monocyte development or egress from BM, whereas in BCG-infected conditions, reduction in lung Ly6C^{hi} monocytes may be attributed more to events occurring in the lung niche itself. To investigate the

former, we next profiled the BM monocyte/myeloid and hematopoietic progenitors in WT and *Kcnj15*^{KO} mice.

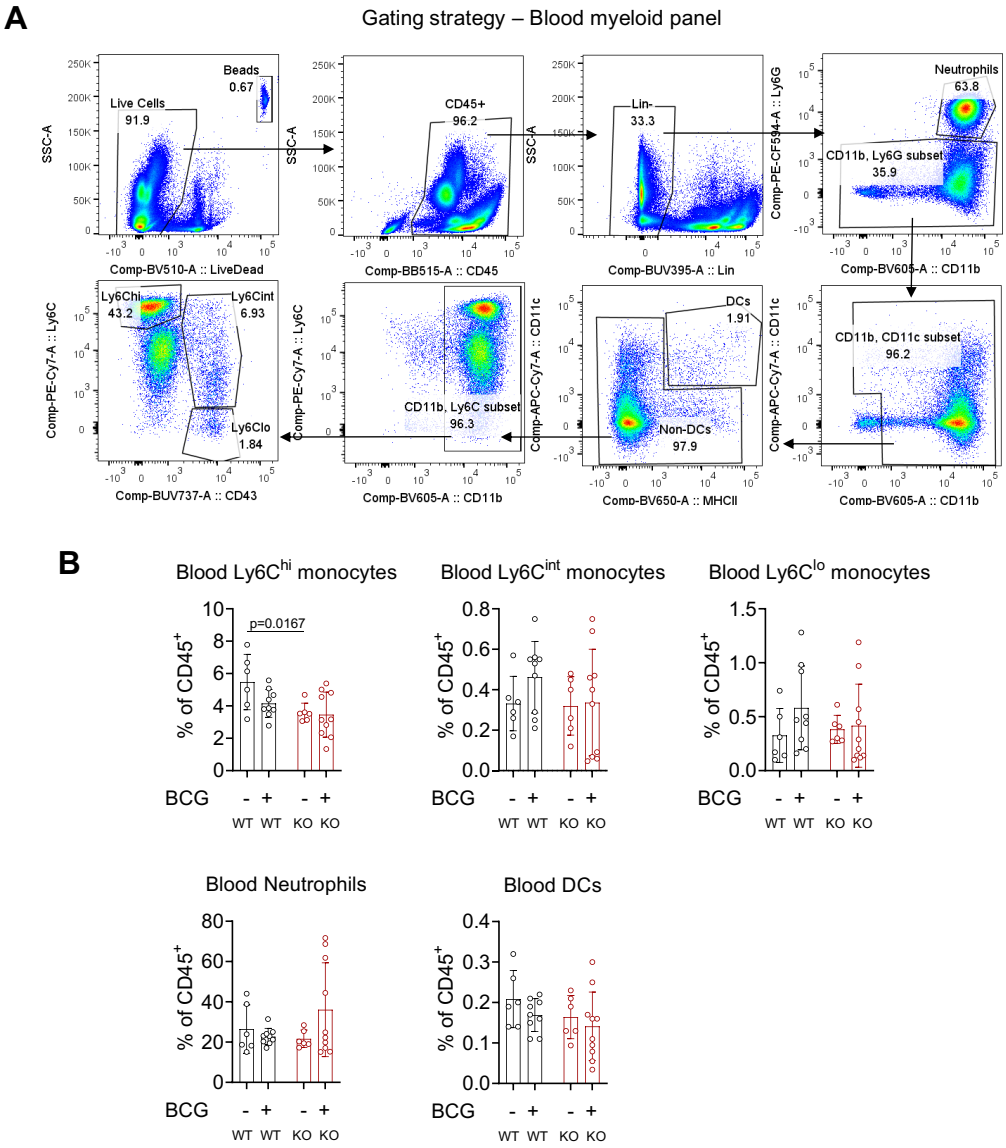

Figure 23. Profiling of blood myeloid immune populations in BCG-infected WT and *Kcnj15*^{KO} mice.

A) Gating strategy for analysis of myeloid populations in murine blood. Lin^{-} gating removes lymphoid cells by excluding cells expressing CD45R, CD90.2 and NK1. **B)** Myeloid immune populations in blood from uninfected and BCG-infected WT and *Kcnj15*^{KO} mice at 7 d.p.i represented as a percentage of CD45^{+} cells. Each dot represents n=1 mice and each bar represents ≥ n=2 experiments, Mean ± SD. Data are analyzed by Two-way ANOVA.

4.6 Bone marrow myeloid and monocyte populations in Kcnj15^{KO} mice at 7 d.p.i

A brief overview of immune cell hematopoiesis and monocyte development in BM is depicted in Figure 24. In the BM, immune cell development begins from the hematopoietic stem cells (HSC), which differentiates into multipotent progenitors (MPP), progressing to common-myeloid

progenitors (CMP) and common lymphoid progenitors (CLP). CMP then differentiates into granulocyte-monocyte progenitors (GMP), which may develop into either granulocytes or common monocyte progenitors (CMoPs). Notably, CMoPs progress into transitional pre-monocytes (TpMo), which acts as a readily mobilizable precursor for active Ly6C^{hi} monocytes during infection or inflammation [424]. Circulating Ly6C^{hi} monocytes are thought to return to the BM niche and develop into Ly6C^{lo} monocytes in the absence of inflammation [104].

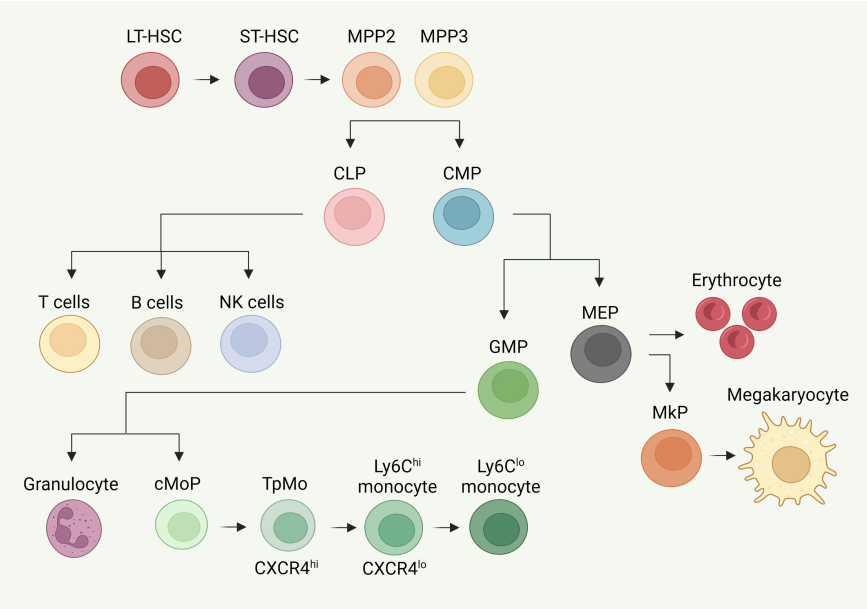

Figure 24. Brief schematic of bone marrow hematopoiesis and monocyte myelopoiesis. Adapted from Chong et al (2016) [424] and Noetzli, French and Machlus (2019) [425].

To gain insight into the reduction of Ly6C^{hi} monocytes in *Kcnj15*^{KO} mice at 14 d.p.i, we assessed BM monocyte populations at 7 d.p.i (Fig 25A). During BCG infection, we observed no clear changes in total BM Ly6C^{hi} monocytes (Fig 25B). However, BCG infection appeared to cause a loss of CXCR4^{lo}Ly6C^{hi} monocytes in WT mice, which was not significant in *Kcnj15*^{KO} mice (Fig 25B). CXCR4 is understood to mark TpMo populations, the loss of which signifies a transition into active mobilization and egress [424, 426]. Thus, reduction in CXCR4^{lo}Ly6C^{hi} monocytes in BM of WT BCG-infected mice is likely due to the egress of these cells into circulation, and this process seems to be slightly hindered in *Kcnj15*^{KO} mice (Fig 25B).

Ly6C^{lo} monocytes were found to be significantly increased with BCG infection in *Kcnj15*^{KO} mice (Fig 25B). Traditionally, Ly6C^{lo} monocytes are understood to play a more homeostatic and tissue-repair function and are not as responsive to inflammatory signals [104], hence we also do not see them accumulating in the lung during infection (Fig 20E). However, the human equivalent, CD16^{+} monocytes, were found to be elevated in blood of ATB patients, which correlated with disease severity [427]. Thus, it may be possible that loss of *Kcnj15* promoted Ly6C^{hi} monocyte regress to

BM and differentiation into Ly6C^{lo} monocytes [104], through some unknown mechanism, or due to quicker resolution of infection and inflammation in *Kcnj15*^{KO} mice. Alternatively, *Kcnj15*^{KO} Ly6C^{lo} monocytes could simply be less mobilized in these mice.

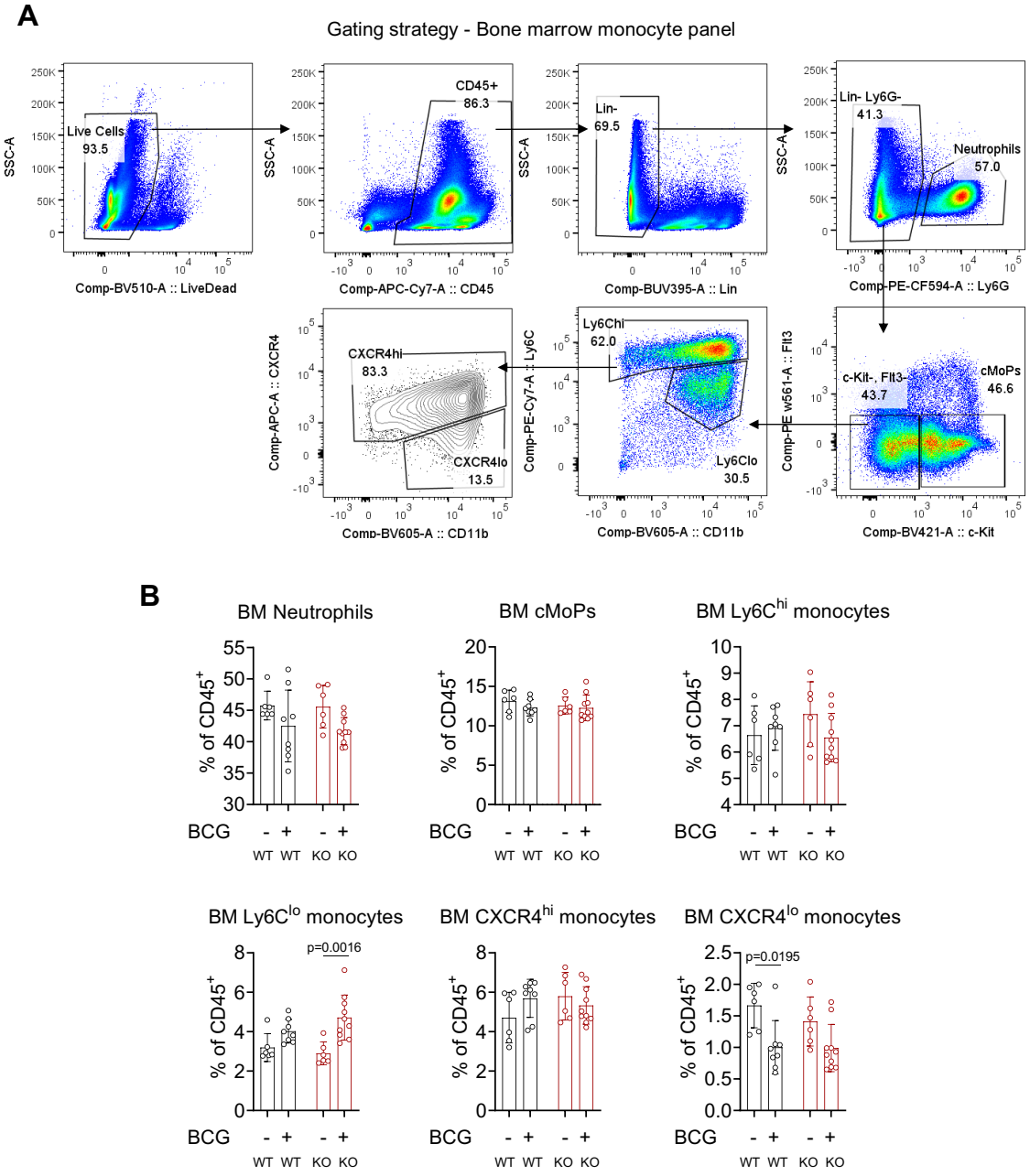

Figure 25. Profiling of bone marrow monocyte and precursor populations in uninfected and BCG-infected WT and *Kcnj15*^{KO} mice.

A) Gating strategy for analysis of monocyte populations in murine bone marrow. Lin$^-$ gating removes lymphoid cells by excluding cells expressing CD45R, CD90.2 and NK1. **B)** Bone marrow monocyte progenitor and subset populations in WT and *Kcnj15*^{KO} mice at 7 d.p.i. cMoPs – Common monocyte progenitor. Each dot represents n=1 mice. Compiled data of n=2 experiments, Mean ± SD. Data are analyzed by Two-way ANOVA.

Notably, in comparing uninfected WT and *Kcnj15*^{KO} mice, we did not notice an obvious accumulation of total Ly6C^{hi} monocytes in the BM (Fig 25B), indicating that monocytes in uninfected *Kcnj15*^{KO} mice were not significantly deficient in bone marrow egress. In summary, we observed that *Kcnj15*^{KO} mice had increased BM Ly6C^{lo} monocytes and slightly reduced mobilization of active CXCR4^{lo}Ly6C^{hi} monocytes during BCG infection. While these may provide a hint towards the reduction of Ly6C^{hi} monocytes in the lungs of BCG-infected *Kcnj15*^{KO} mice, it does not appear to provide a full picture on the matter. We next went a step further to profile BM hematopoietic populations to check for differences in WT and *Kcnj15*^{KO} mice further upstream in myelopoiesis.

4.7 Bone marrow hematopoietic populations in Kcnj15^{KO} mice at 7 d.p.i

Although we saw no stark differences between WT and *Kcnj15*^{KO} mice BM monocyte and precursor populations, we concurrently assessed BM hematopoietic progenitor profiles to make observations on the possible role of *Kcnj15* on steady state and emergency hematopoiesis during infection (Fig 26A). Uninfected WT and *Kcnj15*^{KO} mice did not show any differences in the frequency of progenitor populations (Fig 26B). At 7 d.p.i, BCG-infection induced the expansion of various BM progenitor populations although high variance rendered most of them statistically insignificant. These included LT-HSC, MPP2 (sig. in *Kcnj15*^{KO}), GMP, CMP and CLP populations (sig.) (Fig 26B). There were hardly observable differences in progenitor population expansion between infected WT and *Kcnj15*^{KO} mice, aside from that of MPP2, where *Kcnj15*^{KO} mice showed infection-induced MPP2 expansion that was significant (Fig 26B). Similar expansion was not observed in BCG-infected WT mice. Overall, since there was no change in GMP and CMP (which give rise to monocytes), the reduction of Ly6C^{hi} monocytes in *Kcnj15*^{KO} mice could not be attributed to the deficits in hematopoiesis.

4.8 Reduction of Ly6C^{hi} monocytes in BCG-infected Kcnj15^{KO} mice lung correlates with expansion of lung macrophages

In considering the concurrent reduction of pro-inflammatory Ly6C^{hi} classical monocytes (Fig 20E) in the BCG-infected lungs of *Kcnj15*^{KO} mice along with the accumulation of CD64^{+}F4/80^{+} macrophages and CD11c^{+}MHCII^{hi} DC populations (Fig 20B, C), we hypothesized that infiltrating monocytes, originating from the BM, into the lung of BCG-infected *Kcnj15*^{KO} mice are differentiated into macrophages and dendritic cells in greater amount, bolstering these populations in response to infection.

From our myeloid profiling of BCG-infected WT and *Kcnj15*^{KO} lungs, we extracted correlation data between Ly6C^{hi} monocytes and macrophage and DC populations in these mice. There was a clear inverse association between Ly6C^{hi} monocytes and total macrophages (r=-0.6813, p=0.0005) (Fig 27A). Examining the macrophage subpopulations also showed a distinct negative correlation between Ly6C^{hi} monocytes and AMs (r=-0.6313, p=0.0016) as well as IMs (CD11b^{hi}CD11c^{-}) (r=-0.5663, p=0.006) (Fig 27A). Indeed, both these populations can be replenished by peripheral inflammatory monocytes [96, 102].

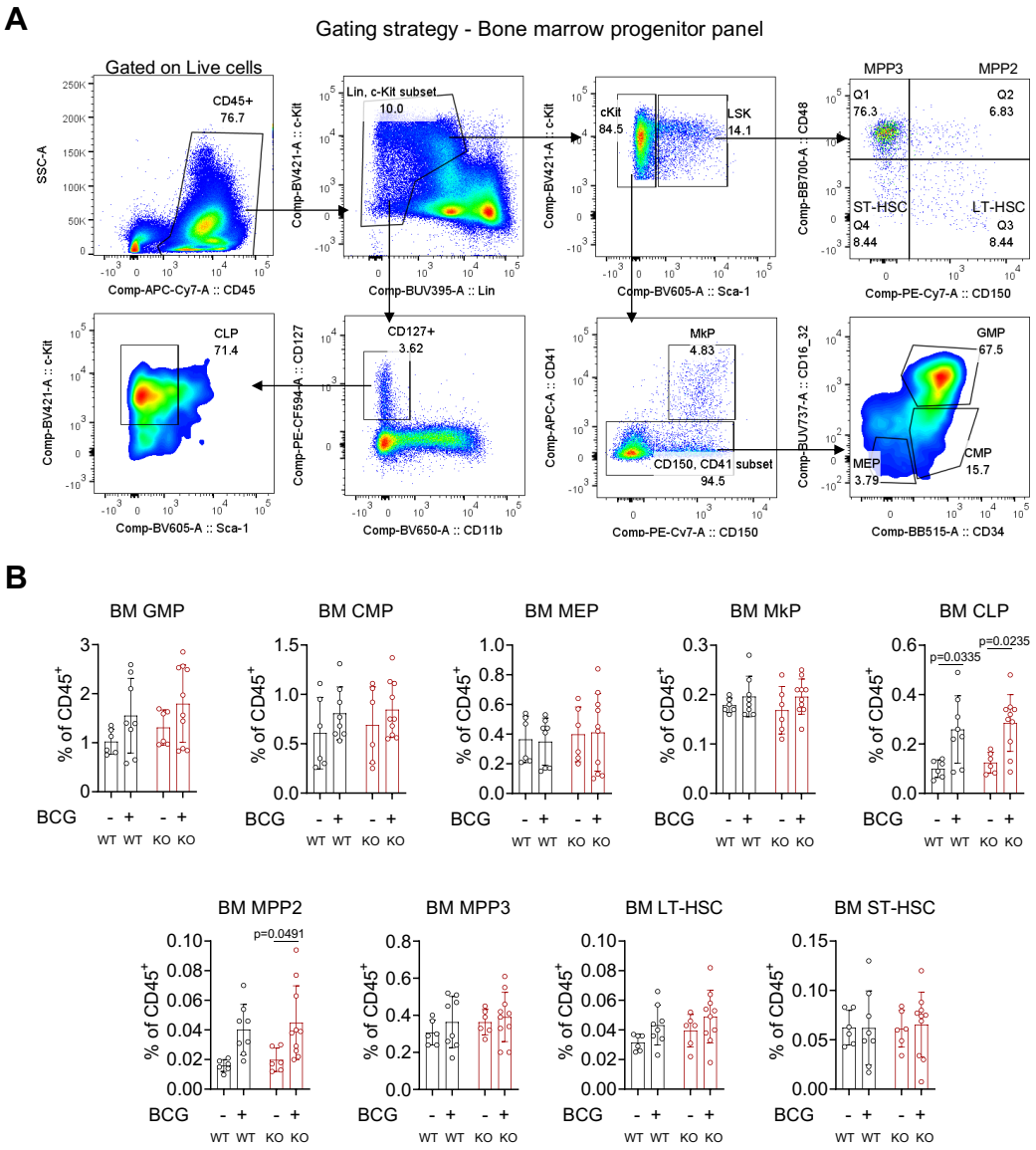

Figure 26. Profiling of bone marrow hematopoietic progenitor populations in uninfected and BCG-infected WT and *Kcnj15*^{KO} mice.

A) Gating strategy for analysis of hematopoietic populations in murine bone marrow. Lin^{-} gating removes lymphoid cells, monocytes and neutrophils by excluding cells expressing CD45R, CD90.2, NK1 and Gr1. **B)** Bone marrow hematopoietic and progenitor populations from WT and *Kcnj15*^{KO} mice at 7 d.p.i. GMP – Granulocyte-monocyte progenitor; CMP – Common myeloid progenitor; MEP – Megakaryocyte-erythrocyte progenitor; MkP – Megakaryocyte progenitor; CLP – Common lymphoid progenitor; MPP – Multipotent progenitors; ST-HSC – Short-term hematopoietic stem cells; LT-HSC – Long-term

hematopoietic stem cells. Each dot represents n=1 mice. Compiled data of n=2 experiments, Mean ± SD. Data are analyzed by Two-way ANOVA.

In our analysis, MCs represent monocyte-derived cells which have been shown to be significantly expanded during *Mtb* infection [428]. Some other groups classify these $CD64^{+}CD11b^{+}CD11c^{+}$ cells together with IMs, and are regarded as a heterogeneous macrophage population [99]. Many studies have tried to delineate the subpopulations within these non-AM macrophages expanded during *Mtb* infection. Using single-cell RNA-seq, Pisu *et al.* identified 3 distinct IM clusters that differed in activation, inflammatory and metabolic signatures [99]. Interestingly, a separate study identified a $CD11c^{hi}$ subset within the lung MC population as a major macrophage compartment infected by *Mtb* [414]. Infection with yellow fluorescent protein-tagged *Mtb* (YFP-*Mtb*) demonstrated that 31% of all YFP-*Mtb*-infected cells were $CD11c^{hi}$ MCs, in comparison to AMs which only comprised 13%, and this high rate of *Mtb* infection persisted up till 6 weeks [414].

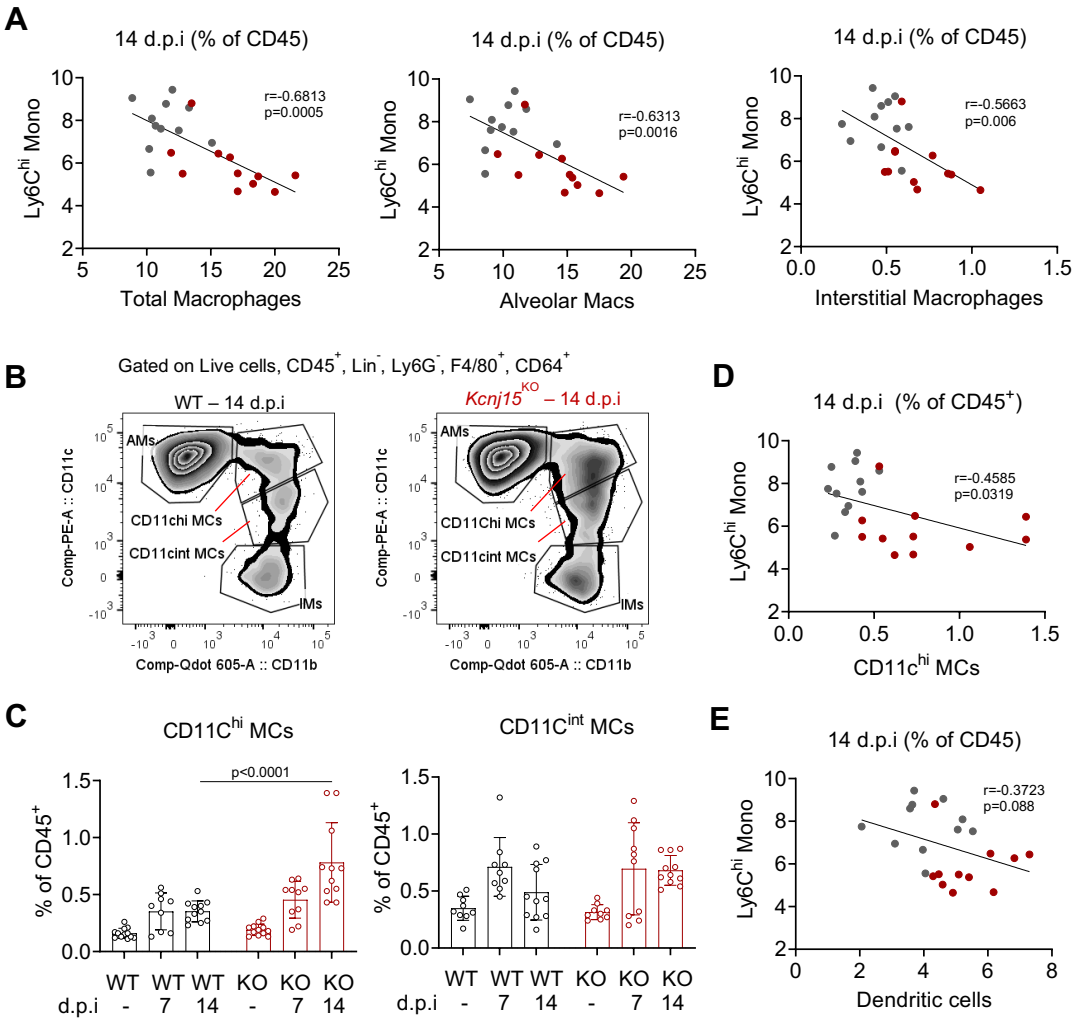

Figure 27. Reduction in *Kcnj15*^{KO} Ly6C^{hi} monocytes correlates with increased macrophages in the lung.
A) Correlation plot of Ly6C^{hi} monocytes vs total macrophages, Alveolar macrophages or Interstitial macrophages (% of CD45^{+}) from WT and *Kcnj15*^{KO} lungs at 14 d.p.i where each dot represents n=1 mice. Red, *Kcnj15*^{KO} mice; Grey, WT mice. **B)** Representative plots showing gating strategy of macrophage subpopulations, specifically of CD11c^{hi} and CD11c^{int} monocyte-derived macrophages (MCs) at 14 d.p.i. **C)** CD11c^{hi} and CD11c^{int} MCs in WT and *Kcnj15*^{KO} lungs represented as a % of CD45^{+} cells. Each dot represents n=1 mice and each bar represents ≥ n=2 experiments, Mean ± SD. **D)** Correlation plot of Ly6C^{hi} monocytes vs CD11c^{hi} MCs or **E)** total DCs where each dot represents n=1 mice. Red, *Kcnj15*^{KO} mice; Grey, WT mice. Data in **A**, **D**, **E** are analyzed by simple linear regression with Pearson's correlation. Data in **C** was analyzed by Two-way ANOVA for differences between WT and *Kcnj15*^{KO} groups (within group analysis not shown). Correlation plots comprise compiled data from n=2 experiments.

We thus segregated our MC population into CD11c^{hi} and CD11c^{int} MCs (Fig 27B) and observed that while proportions of CD11c^{int} MCs were more variable, CD11c^{hi} MCs were increased in *Kcnj15*^{KO} lungs at 14 d.p.i (Fig 27C). This increase in CD11c^{hi} MCs was also significantly correlated with reduction in Ly6C^{hi} monocytes at 14 d.p.i (r=-0.4585, p=0.0319) (Fig 27D). Although CD11c^{hi} MCs were shown to be most infected population in the lungs of mice and thus appeared to be a reservoir for persistent pulmonary *Mtb* infection, these cells express Nos2 [414] and therefore may be able to effectively eliminate BCG bacilli. Of note, Nos2 is important for mycobacterial control [429, 430]. In this way, the expansion of CD11c^{hi} MCs population may be concordant with the improved control of BCG burden in *Kcnj15*^{KO} lungs at 14 d.p.i (Fig 19A).

Infiltrating Ly6C^{hi} monocytes can also differentiate into mo-DCs at sites of infection [431]. Therefore, we additionally analyzed the correlation between Ly6C^{hi} monocytes and total DCs but did not observe a significant negative correlation (r=-0.3723, p=0.088) (Fig 27E). Taken together, we show that reduction of Ly6C^{hi} monocytes in *Kcnj15*^{KO} lungs at 14 d.p.i was well correlated with the expansion of the macrophage compartment but not of DCs. Notably, specifically CD11c^{hi} MCs were increased in BCG-infected *Kcnj15*^{KO} lungs, and these *Nos2*-expressing macrophages may be important for restricting BCG growth.

While we used a correlation analysis to probe whether the expanded macrophage and DCs might have derived from Ly6C^{hi} monocytes, this certainly does not show a causal relationship. There are certainly experimental methods which can be used to properly study this, which were not carried out due to time constraints. Adoptive transfer of WT and *Kcnj15*^{KO} BM monocytes into BCG-infected CD45.1 mice would allow us to examine if *Kcnj15*^{KO} monocytes do have propensity to differentiate into macrophage or DC population (See Chapter 6).

4.9 Transcriptomic analysis of WT and Kcnj15^{KO} alveolar macrophages in uninfected and BCG-infected mice

During pulmonary infection, the primary cells that encounter bacterial assault are AMs and epithelial cells which line the airway, in addition to neutrophils which rapidly arrive at the site of infection. According to the Human Protein Atlas, immunohistochemical staining of *Kcnj15* in lung sections showed significant expression of *Kcnj15* in cells identified as macrophages which were located in the airways [251]. Likewise, it has been shown that intracellular BCG present in the lungs at 14 d.p.i following intranasal BCG administration resided largely in the AM compartment [33]. Hence, we hypothesized that reduced lung bacterial burden in *Kcnj15*^{KO} mice might be attributed to the AMs ability to restrict BCG. Moreover, we had earlier found increased AMs in the lung of BCG-infected *Kcnj15*^{KO} mice (Fig 20B). Therefore, we conducted a genome-wide transcriptomic analysis using RNA-seq on AMs isolated from the bronchoalveolar lavage (BAL) of BCG-infected (14 d.p.i) and uninfected WT and *Kcnj15*^{KO} mice.

Altogether, 208.8 million paired-end reads were obtained by Illumina sequencing of mRNAs extracted from these samples with a median of 13.0 million reads per sample, a median of 80.7% of which were mapped to known mouse transcripts (Fig 28A). Principle component analyses (PCA) of the expression profiles of 15 samples among four groups showed that the transcriptome of AMs was mainly affected by BCG infection, while the distinction between WT and *Kcnj15*^{KO} groups was minimal (Fig 28B). To better understand the differences between WT and *Kcnj15*^{KO} AMs, differential gene expression (DEG) analysis was performed on 12192 genes after genes with log2CPM inter-quartile range (IQR) less than 0.5 across samples were removed (see Methods). The union of 1436 DEGs across all 4 groups were represented by a heirarchical clustering heatmap which separated the genes into four clusters (Fig 28C). Among these cluster 1 (C1) 850 genes were upregulated in AMs from BCG-infected mice regardless of the mice genotype. Expectedly, C1 genes mainly coded for inflammatory proteins and encompassed numerous interferon-inducible genes (*Ifit1*, *Ifit35*, *Ifit 44*, *Cxcl10 , Ciita* [432]), macrophage activation markers (*Nos2*) and inflammatory chemokines (*Cxcl1*, *Cxcl3*).

Cluster 3 (C3, 403 genes) represented genes that were downregulated during BCG-infection and were again independent of genotype. This included *Epor* which promotes immune tolerance and clearance of apoptotic cells by macrophages [433, 434], *Zeb2* which maintains tissue macrophage identity [435] as well as genes linked to anti-inflammatory responses such as *Cavin1* and *Bcl6*. This suggests that BCG-infection activates AM and represses anti-inflammatory mechanisms. Interestingly, Cluster 3 was also enriched for genes involved in intracellular sterol transport (GO:0032366) such as *Abcg1*[436, 437], *Osbp* [438], *Gramd1b*[439], *Gramd1c*[439], *Scp2* [440], *Cd36* and *Syt7*[441], most of which are responsible for the movement of cholesterol between plasma membrane

and various organelles. *Cd36* also plays a role in uptake of oxidized low-density lipoprotein (OxLDL) [442]. Since *Mycobacterium* are known to utilize host cholesterol, this data suggests that BCG-infection elicits changes in intracellular cholesterol and lipid distribution which may have an impact on intracellular mycobacterial survival [443].

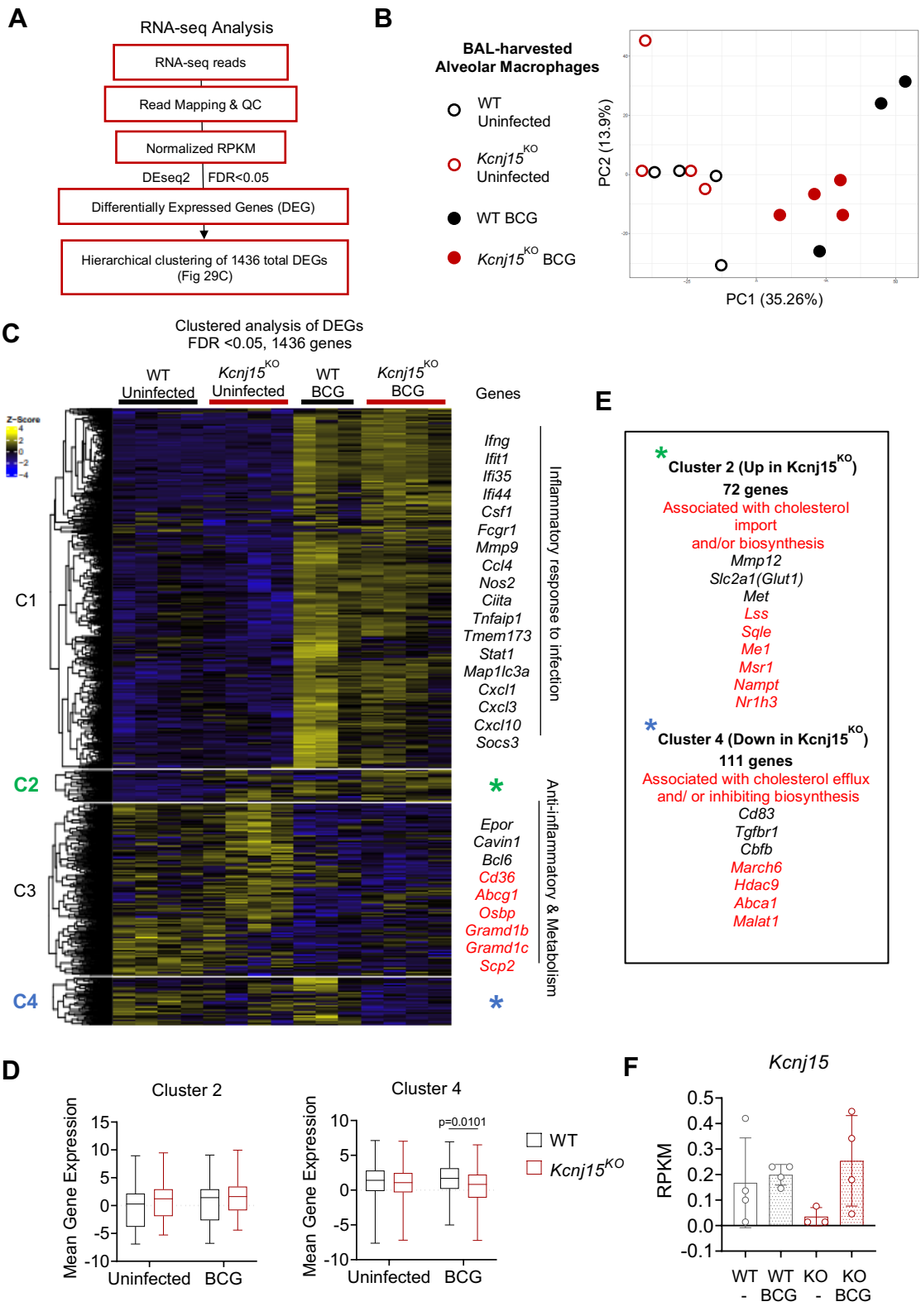

Figure 28. Transcriptomic profile of AMs from WT and *Kcnj15*^{KO} mice in response to BCG infection. **A)** RNA-seq analysis pipeline. **B)** Principle component analysis of RNA-seq data from AMs harvested from uninfected and BCG-infected WT and *Kcnj15*^{KO} mice at 14 d.p.i. **C)** Hierarchical clustering heatmap of Z-scores from total DEGs (1436 genes) between the four groups. Representative genes from each cluster are listed on the right. **D)** Mean normalized Log2RPKM gene expression of genes in Clusters 2 and 4, median with min. and max. values are represented. **E)** Cluster 2 and 4 key genes including those from

cholesterol-related pathways (red). **F)** Normalized expression of *Kcnj15* across four groups (RPKM), Mean ± SD. Each dot represents AMs harvested from n=1 mice. Data in **D** was analyzed by Two-way ANOVA.

Cluster 2 (C2, 72 genes) comprised of genes that were upregulated in uninfected *Kcnj15*^{KO} AMs. Expression of these C2 genes seems to be upregulated in AMs from BCG-infected WT mice as well, although mean gene expression across the groups was not statistically significant (Fig 28D). C2 comprised genes such as *Mmp12* (Elastase), which has been shown to translocate to macrophage phagolysosomes to kill bacteria [444], and *Slc2a1* (Glut1), a glucose uptake transporter (Fig 28E). Indeed, activation of glycolysis, as opposed to FAO, has been shown to be more mycobacterial-restrictive [445]. Contrary to C2 genes, cluster 4 (C4, 111 genes) genes were downregulated specifically in AMs from BCG-infected *Kcnj15*^{KO} mice (Fig 28C, D). Cluster 4 (C4) genes included macrophage-activation marker *Cd83* [446], *Cbfb*, which is important for AM self-renewal [447] and *Tgfbr1* (Fig 28E). TGF-β signaling is important for AM development and homeostasis [448]. Importantly, TGF-β is secreted by AMs during bleomycin-induced lung injury and is an important driver of fibrosis [449, 450]. The increase in bacterial-restrictive gene expression and downregulation of resident AM homeostatic genes may be due to the greater influx of monocyte-differentiated AMs, which are not self-renewable nor require TGF-β signaling for maintenance, but instead are primed towards fighting infection. Furthermore, downregulation of TGF-β signaling in *Kcnj15*^{KO} AMs may dampen *Mtb*-induced lung pathology by ameliorating progression of fibrosis.

Interestingly, we found that both C2 and C4 clusters harbored genes involved in cholesterol metabolism (Fig 28E). C2 genes (upregulated in *Kcnj15*^{KO} AMs) contained cholesterol biosynthesis genes (*Lss*, *Sqle*), genes involved in foam cell formation (*Msr1*), cholesterol sensing (*Nr1h3* which codes for LXRα) [451], and *Nampt* which, when knocked-down, leads to cholesterol efflux [452]. C4 (downregulated in *Kcnj15*^{KO} AMs) comprised genes associated with cholesterol efflux (*Abca1*, *Hdac9*, *Malat1*[453]) and negative regulation of cholesterol synthesis genes (*March6)* [454, 455] (Fig 28E). Taken together, this suggests that *Kcnj15*^{KO} AMs may have dysregulated cholesterol homeostasis and be primed towards cholesterol accumulation, gaining the propensity for foam cell formation which commonly occurs in macrophages in atherosclerotic lesions [456].

Whether or not accumulation of cholesterol aids or hinders AMs in restricting intracellular mycobacteria growth requires further experimentation. Cholesterol-rich regions in the plasma membrane known as membrane rafts were shown to be vital for phagocytosis of *M. bovis*, *P. aeruginosa* and *C. neoformans* [457, 458, 459], and *in vitro* generated human MDM foam cells showed improved ability to control *Mtb* infection [460]. However, foam cells have also been thought to promote *Mtb* persistence by providing a lipid-rich niche [461, 462, 463]. Pertaining to foam cells, its

generation in TB disease is predominantly triglyceride-dependent rather than cholesterol-dependent, which is conversely more common in atherosclerotic foam cells [464]. In summary, it is unclear what downstream effect increasing the cholesterol proportion of foam cells may have in the case of *Mtb* growth.

At steady state, the number of DEGs between WT and *Kcnj15*^{KO} AMs amounted to only 29 genes. We found that the endogenous expression level of *Kcnj15* in mice AMs was very low both in uninfected and BCG-infected conditions (Fig 28F), with RPKM levels falling below 1. This appears to be at odds with *KCNJ15* expression in human AMs which appeared to be strongly expressed as seen by significant immunohistochemical staining by anti-*KCNJ15* antibody in the human airways [251]. A separate transcriptomic study on mice cardiac macrophages likewise found *Kcnj15* expression in these cells to be low, at 0.8 RPKM [465]. While the effect of gene knockout was not readily observable, it is possible that the knockout cassette inserted into the *Kcnj15* exon did not disrupt transcription, thus still producing detectable mRNA which however could not be translated or resulted in truncated or misfolded *Kcnj15* protein. Nonetheless, the low expression of *Kcnj15* accounts heavily for the lack of obvious transcriptomic profile differences. Additionally, we consider that loss of *Kcnj15* may not result in glaring changes at the transcriptomic level since it encodes a K^+ transport channel which additionally lacks a regulatory subunit unlike other Kir family members such as Kir6.x and Kir3.x subtypes. Hence, it is understandable that *Kcnj15* may exert its effects more at the ion homeostasis or protein level.

However, this does not preclude the bystander effects on the AMs deriving from surrounding cell types which may express and actively rely on *Kcnj15* function. These may include infiltrating neutrophils and monocytes, or AEC-II which have been shown (in human) to express *Kcnj15* [466, 467]. AEC-II also produce antimicrobial peptides and pro-inflammatory mediators in response to infection [166, 171].

Overall, this transcriptomic data suggests that the loss of endogenous *Kcnj15* expression in AMs conferred a cholesterol-accumulating gene signature, which may have an effect on intracellular mycobacterial growth.

4.10 Kcnj15^{KO} mice do not show enhanced BCG-specific T cell response in the spleen despite correlation to higher bacterial dissemination and expanded DC population

Increased dissemination of BCG to the spleen (Fig 19B) as well as our observation of expanded DC populations in the *Kcnj15*^{KO} lung (Fig 20B) suggest an effect on antigen presentation and activation of lymphoid cells, which might then result in increased BCG-specific T cell response. A heightened effector T cell response could explain improved control of BCG growth in the lungs

of *Kcnj15*^{KO} mice (Fig 19A). To check if BCG-specific T cells were expanded, spleen cells were harvested and treated with or without purified protein derivative (PPD), which contains a mixture of mycobacterial antigens (Fig 29A). Intracellular cytokine production was assessed by flow cytometry (Fig 29B). We found no significant differences between WT and *Kcnj15*^{KO} CD4^{+} and CD8^{+} T cells in terms of intracellular IFNγ and TNFα accumulation (Fig 29C). While there may have been indications of correlation between lung CFU and spleen dissemination (Fig 19C), the amount of increase in bacterial load and thus antigen presentation in the spleen may not have been sufficient to elicit clear enhancements in T cell response to BCG infection in the lung. Expansion of DC population also does not necessitate additional trafficking of antigens to secondary lymphoid organs, which we know is impaired or delayed in *Mtb* infection [144]. Perhaps evaluation of T cell response in the spleen is insufficient to conclude if the effector T cell response was indeed altered in BCG-infected *Kcnj15*^{KO} mice.

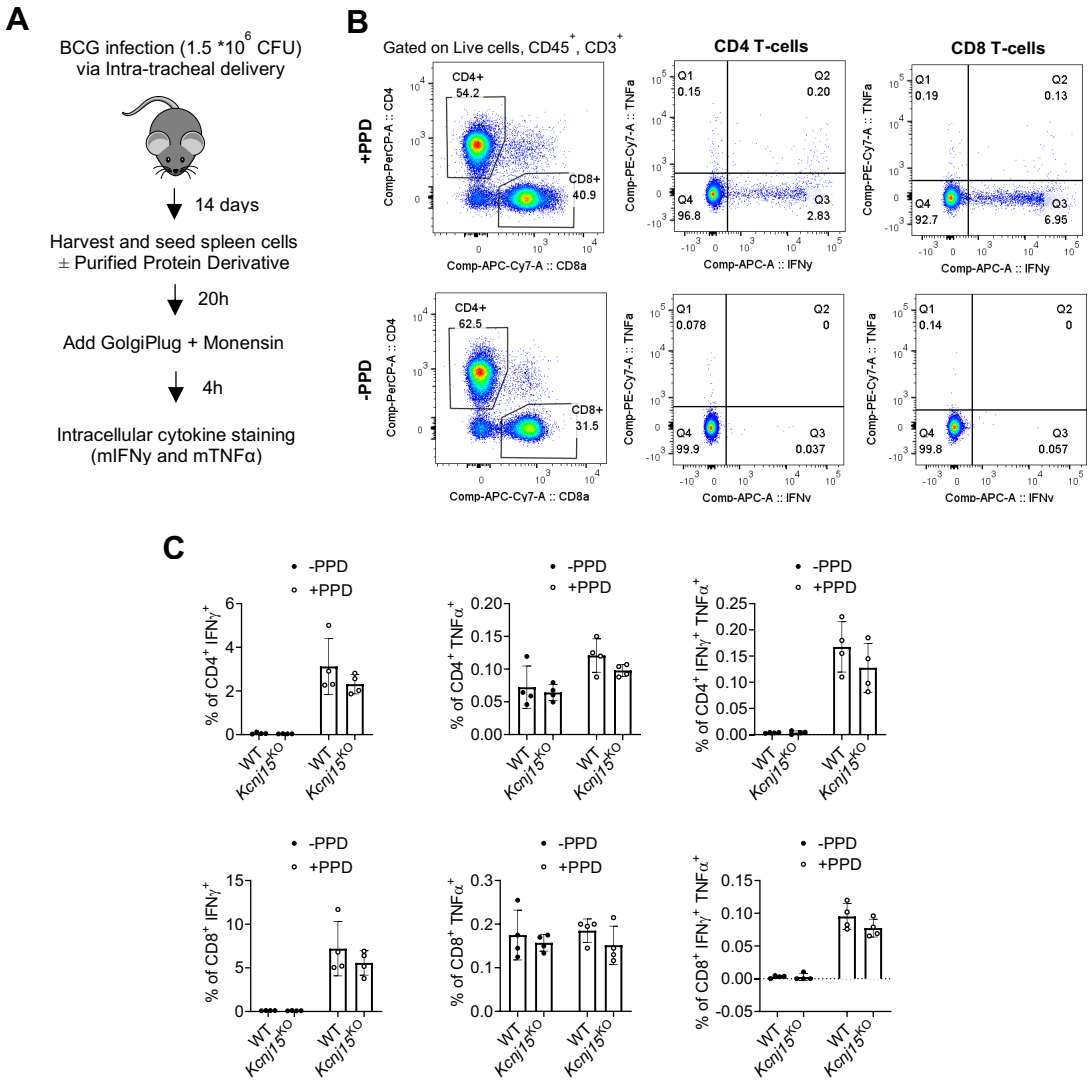

Figure 29. *Kcnj15*^{KO} mice did not show increase in mycobacteria-specific spleen T cell response.
A) Experimental workflow for spleen T cell re-stimulation with PPD to detect mycobacteria-specific response at 14 dp.i. **B)** Gating strategy for analysis of T cell subsets and their expression of intracellular cytokines. **C)** Percentage of $CD4^+$ and $CD8^+$ T cells that responded to PPD stimulation with production of mIFNγ and mTNFα, detected by intracellular cytokine staining and flow cytometry. Each dot represents n=1 mice, Mean ± SD. Data were analyzed by Two-way ANOVA.

4.11 Summary of Chapter 4

In this section of the study, we used *Kcnj15*^{KO} mice to examine the function of *Kcnj15* in the innate immune response to mycobacterial (BCG) infection. Initial examination of immune populations in WT and BCG-infected mice revealed that the Ly6C^{hi} monocyte population was reduced in the lungs of *Kcnj15*^{KO} mice, which was also observed in the blood of uninfected mice (Fig 20B, 23B). Concurrently, an elevated expansion of the macrophage compartment and total DC compartment was observed in *Kcnj15*^{KO} mice through the course of the 14-day infection, the majority of macrophage increase being contributed by AMs and MCs (Fig 20B).

Furthermore, we demonstrated that at 14 d.p.i, *Kcnj15*^{KO} mice were better able to control mycobacterial infection as less BCG CFU were recovered from the lungs (Fig 19). Additionally, we found a negative correlation of lung BCG burden with that of spleen BCG burden at 14 d.p.i, which suggested increased dissemination to peripheral organs in *Kcnj15*^{KO} mice (Fig 19). This, however, did not correlate with increased BCG-specific splenic T cell response (Fig 29).

Multiplexed analysis of cytokines/chemokines in lung homogenates at 14 d.p.i indicated that while infection expectedly increased expression of various cytokines, *Kcnj15*^{KO} mice appeared to express less cytokines/chemokines overall. CCL2 presence in lung and serum at an earlier timepoint of 7 d.p.i was not found to be different in *Kcnj15*^{KO} mice (Fig 22), eliminating the notion that limited CCL2 might have accounted for the lack of Ly6C^{hi} monocyte recruitment to lungs (Fig 20). Nonetheless, reduction of overall inflammatory cytokine production correlated with decreased CFU burden at 14 d.p.i and thus suggests infection resolution (Fig 22).

We also hypothesized that reduced Ly6C^{hi} monocytes in the lung may be attributed to a loss of egress from the BM reserve, which would lead to their accumulation in the BM. To this end, we found no obvious accumulation of monocytes and its progenitors in the bone marrow that could clearly explain the reduced Ly6C^{hi} monocytes (Fig 25, 26), aside from slightly increased BM Ly6C^{lo} monocytes in *Kcnj15*^{KO} mice. While reduced Ly6C^{hi} monocytes was also seen in the blood of naïve *Kcnj15*^{KO} mice, the same was not observed in BCG-infected *Kcnj15*^{KO} mice (Fig 23), suggesting that under inflammatory conditions, reduction of Ly6C^{hi} monocytes may be occurring in the lung niche, strengthening the possibility that Ly6C^{hi} monocytes are contributing to differentiated macrophages and DC pools. To this end, we examined the correlation between Ly6C^{hi} monocyte and macrophage populations and found a significant inverse correlation with

AM, IM and CD11c^{hi} MC populations (Fig 27). CD11c^{hi} MCs are noteworthy as they have been shown to express Nos2 and were previously found to be infected with *Mtb* at a higher rate than other macrophage populations. DCs, however, were not found to significantly correlate with reduction of Ly6C^{hi} monocyte (Fig 27). Hence, this suggests that *Kcnj15*^{KO} mice may harbor fewer lung Ly6C^{hi} monocytes due to an increased differentiation to macrophages during infection. This hypothesis, however, requires much further experimentation.

Lastly, we considered that *Kcnj15*^{KO} AMs, which reside in the airways most proximal to the initial onslaught of infection, might possess some enhanced ability to take on bacterial infections. Transcriptomic analyses of airway AMs revealed that, while AMs may fail to significantly express or upregulate *Kcnj15* during infection, the effect of *Kcnj15* knockout led to transcriptomic changes in genes regulating cholesterol transport and metabolism, which could affect mycobacterial killing or intracellular survival (Fig 28).

In summary, this chapter highlights that the function of *Kcnj15* in different cell types may vary in response to mycobacterial infection. While experiments with monocytes alone in an *in vitro* setting (Chapter 3) may demonstrate that *KCNJ15* expression could benefit the control of intracellular mycobacteria, *in vivo* experiments which involve the coordinated response of various cell types suggest, instead, that the loss of *Kcnj15* restricts mycobacterial growth in lungs. In this respect, differential function of human and mouse *KCNJ15* in our *in vitro* and *in vivo* studies, respectively, can also be a confounding factor. Furthermore, in reality, *Mtb* infections are not limited to monocytes, neither are monocytes the primary infected cells in the lung, therefore it is more meaningful to look at the role of *Kcnj15* from a systemic perspective. Our mice study thus suggests that *Kcnj15* expression may be detrimental in the context of acute pulmonary BCG infection.

Chapter 5: Extracellular K^+ in necrotic granulomas enhance mycobacterial killing via ROS-mediated autophagy

5.1 Mycobacterium-induced necrotic granulomas contain high extracellular K^+

Chronic *Mtb* infection can result in severe lung tissue pathology through the formation of granulomatous lesions, which have both host-protective and host-detrimental properties [468, 469, 470, 471]. To assess extracellular K^+ ($[K^+]_e$) abundance in the necrotic granulomas resulting from virulent mycobacterial infection, we employed a zebrafish model of *Mycobacterium marinum (Mm)* infection. Injection of virulent *Mm* in the neural tube of zebrafish embryos resulted in the formation of typical necrotic granuloma foci along the trunk of the fish at 4 d.p.i [376]. We observed the same in our experiment with *Mm*-tdTomato-infected zebrafish embryos (Fig 30A). When stained with extracellular K^+ indicator, IPG-4, (see Methods, section 2.24) infected zebrafish showed a strong overlap of IPG-4 fluorescence with necrotic granuloma regions in the trunk, suggesting the presence of high $[K^+]_e$ within necrotic lesions (Fig 30A). Conversely, when zebrafish were infected with attenuated strain of *Mm* carrying *ESX-1* deletion (which are impaired in forming necrotic granulomas [472]), IPG-4 staining within bacterial aggregates (a.k.a cellular granulomas) was not detected (Fig 30A). Since injection of *Mm* via the neural tube (trunk) route has been associated with formation of more necrotic and hypoxic granulomas [376, 473], we compared the quantum of IPG-4 fluorescence in the granulomas of zebrafish injected with tdTomato *Mm* either via caudal vein (CV) or trunk. As expected, we observed an increased IPG-4 fluorescence in necrotic granulomas which were more frequent in trunk-injected zebrafish compared to CV-injected zebrafish (Fig 30B).

To study $[K^+]_e$ concentrations within mycobacterial granulomas in mice, we first established a model of hepatic granuloma formation by i.v. injection of BCG, using IFNγ knockout mice. IFNγ knockout mice are more susceptible to mycobacterial infections and have been reported to form hepatic necrotic granulomas upon BCG infection by i.v [153, 474]. We could not investigate $[K^+]_e$ in *Mtb*-infected lung tissues because $[K^+]_e$ staining by IPG-4 cannot be performed on PFA-fixed tissues, and we were unable to remove *Mtb*-infected mice tissues from a BSL3 facility without PFA fixation. Histopathological evaluation (H&E staining) of hepatic tissue from IFNγ knockout mice 6 weeks post-infection by BCG showed early signs of tissue pathology with infiltrating leukocytes forming granulomas with centres showing discolouration and lack of cell structure (Fig. 30C). When stained with IPG-4, these granulomas revealed regions of high $[K^+]_e$ (Fig 30D). As a proof of concept that necrosis or cell death indeed results in the release of intracellular K^+ in the extracellular milieu, we demonstrated that cell lysis leads to elevated $[K^+]_e$ levels that was proportional to cell numbers (Fig 30E). Taken together, the analysis of K^+ IPG-4 staining in *Mycobacterium*-infected zebrafish and IFNγ knockout mice presented a strong indication that

necrotic granulomas indeed contain high $[K^+]_e$ levels.

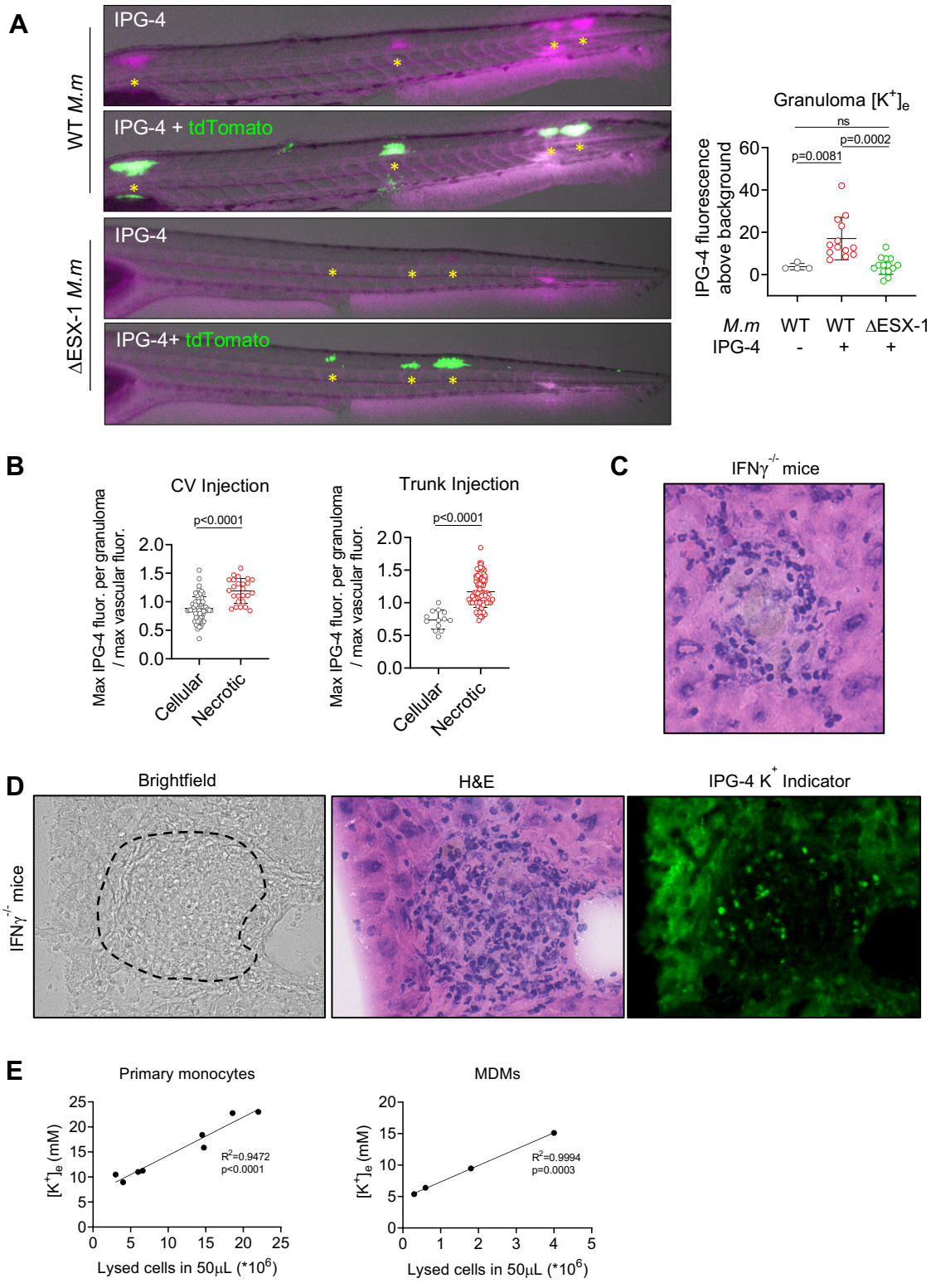

Figure 30. Necrotic mycobacterial granulomas contain high $[K^+]_e$.

A) 48 h post-fertilisation (hpf) zebrafish embryos were infected with approximately 200 CFU *M. marinum*-tdTomato via the neural tube and injected with 5mg/mL IPG-4 via the caudal vein at 4 d.p.i prior to imaging. Yellow (*) marks corresponding fluorescent granuloma regions. Data are from n= 2, 9, 7 fish per group. **B)**

IPG-4 fluorescence from granulomas of zebrafish injected with *M.m* via the caudal vein or neural tube (trunk). Data represents a total of n=25-26 fish. Each dot in **A** and **B** represents n=1 granuloma. **C)** Representative image of a BCG-infection induced hepatic granuloma from IFNγ$^{-/-}$ mice. **D)** Representative image from a liver section of i.v. BCG-infected IFNγ$^{-/-}$ mice visualized by brightfield, hematoxylin & eosin staining and IPG-4 staining. **E)** Scatter plot showing correlation between numbers of primary monocytes (left) and monocyte-derived macrophages (MDMs) (right) lysed in 50µL of media and the resulting extracellular K^+ ($[K^+]_e$). Images in **A** and for **B** were captured at 20X magnification. Images in **C** and **D** were captured at 400X magnification. Data in **A** was analyzed by One-way ANOVA, and data in **B** was analyzed by Unpaired t-test. Data in **E** is analyzed by simple linear regression. Mean ± SD are represented. Zebrafish experiments were conducted in collaboration with Kathryn Wright, Dr Stefan Oehler Lab, Centenary Institute.

5.2 Extracellular K^+ restricts mycobacterial growth in human monocytes/macrophages

To investigate the effects of high $[K^+]_e$ on myeloid immune cells which are present in mycobacterial granulomas [122], we adopted an *in vitro* experimental approach. Eil *et al*. previously reported that K^+ concentrations in the necrotic core of solid tumours reached up to 40mM [475]. Therefore, we first treated monocytes with variable concentrations of $[K^+]_e$ and evaluated intracellular K^+ ($[K^+]_i$) using an intracellular K^+ ion indicator, IPG-4 (AM salt), by flow cytometry (Fig 31A). Adminstration of 20mM and 60mM of $[K^+]_e$ to THP-1 monocytes resulted in mean 150mM to 165mM $[K^+]_I$, which was higher than $[K^+]_I$ of 130mM in control cells which were cultured in complete RPMI medium that contains ~5mM of K^+ (Fig 31B).

We next assessed the effect of $[K^+]_e$ (added as KCl) on intracellular bactericidal activity of monocytes and macrophages. We found that 60mM of $[K^+]_e$ but not 20mM was able to restrict *Mtb* growth in THP-1 cells that was sustained till 48h (Fig 31C). We then used 60mM of $[K^+]_e$ in subsequent experiments. 60mM $[K^+]_e$ was able to restrict the growth of both *Mtb* and BCG after 24h infection in primary monocytes as well (Fig 31D, E). A similar effect of 60mM $[K^+]_e$ was observed in BCG-infected THP-1 monocytes and human monocyte-derived macrophages (MDMs) (Fig 31F,G). To ensure that $[K^+]_e$-mediated restriction of mycobacterial growth was not attributable to host cell death, we evaluated cell viability. No major cytotoxic effect of 60mM $[K^+]_e$ on THP-1 monocytes was observed by trypan blue staining (Fig 32H). Similarly, there was no significant effect of 60mM $[K^+]_e$ on cell death of primary monocytes evaluated using LIVE/DEAD staining and flow cytometry (Fig 31I). Furthermore, to demonstrate that restiction of mycobacterial growth by $[K^+]_e$, was not a result of chloride (Cl^-) ions in the KCl solution added, we treated BCG-infected primary monocytes with 60mM of potassium D-gluconate (KGlu). KGlu also resulted in the decrease in bacterial burden in BCG-infected primary monocytes (Fig 31J). We also ensured that increasing $[K^+]_e$ concentrations were neither directly bactericidal nor bacteriostatic to BCG (Fig 31K), while using anti-*Mtb* antibiotic, isoniazid (INH) as a positive control. In summary, our data suggests that high $[K^+]_e$ can restrict intracellular growth of mycobacteria.

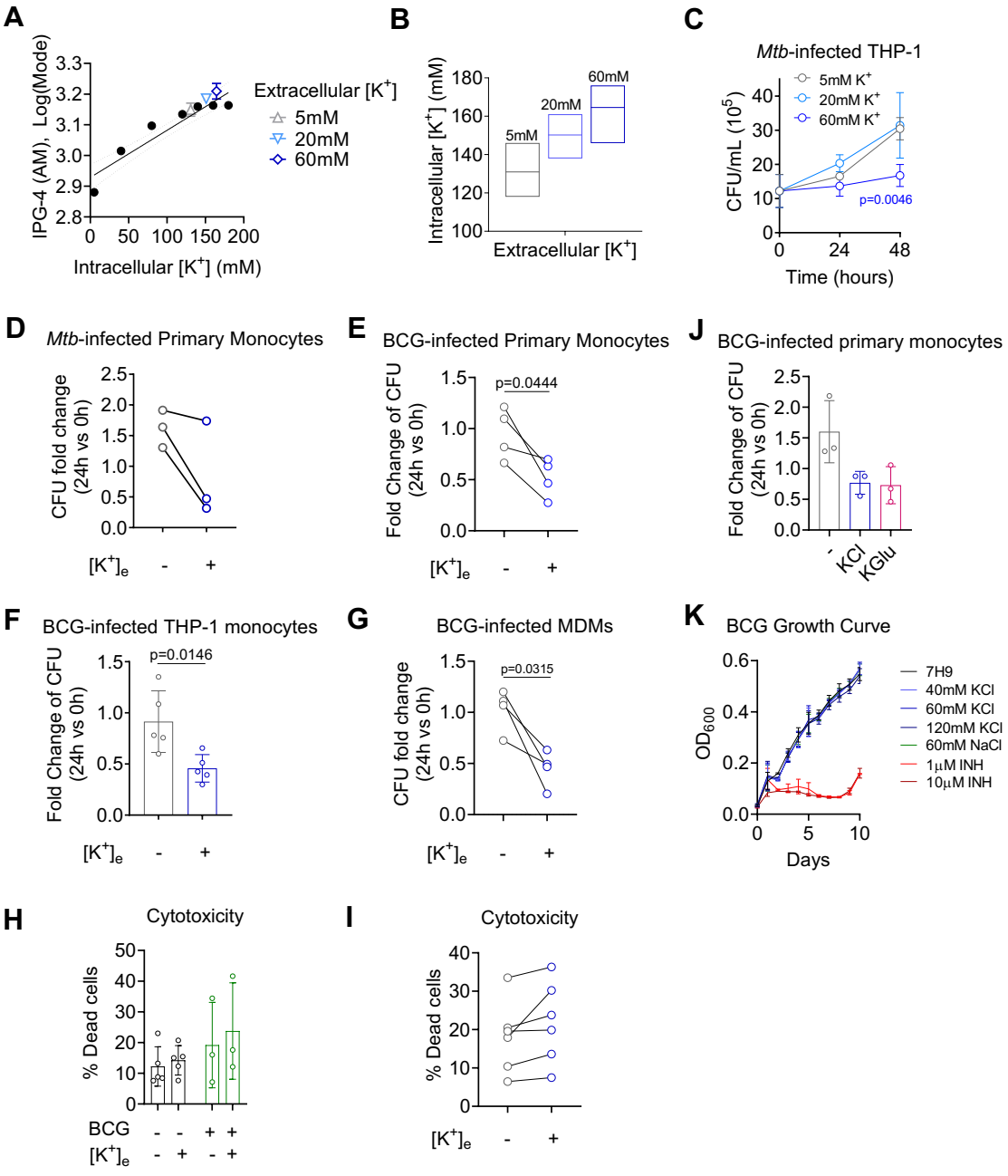

Figure 31. High $[K^+]_e$ promotes monocyte/macrophage restriction of mycobacterial growth.

A) Representative scatter plot depicting the intracellular $[K^+]$ detected by IPG-4 K^+ indicator (AM salt), when THP-1 monocytes are treated with 20mM and 60mM $[K^+]_e$, against a standard curve generated by Amphotericin B treated cells exposed to varying $[K^+]_e$ (left). **B)** Intracellular $[K^+]$ at 5, 20 and 60mM $[K^+]_e$ are depicted in boxplot (n=2 expt). Mean with min. and max. values represented. **C)** *Mtb* growth in infected THP-1 treated with 20mM or 60mM $[K^+]_e$ over 48h. (n=1 expt) **D)** Growth of *Mtb* in $CD14^+$ primary monocytes treated with 60mM $[K^+]_e$. Growth of BCG in **E)** human monocytes **F)** THP-1 monocytes and **G)** monocyte-derived macrophages (MDMs) treated with 60mM $[K^+]_e$. **H)** Percentage of cell death of THP-1 monocytes infected with BCG and exposed to 60mM $[K^+]_e$ after 24h, detected by Trypan blue assay. **I)** Percentage of cell death of human monocytes after 24h of treatment with 60mM $[K^+]_e$ evaluated by LIVE/DEAD viability dye using flow cytometry . **J)** Growth of BCG in human monocytes treated with 60mM potassium chloride (KCl) or potassium D-gluconate (KGlu) (n=2). **K)** Growth curve of BCG over 10 days in 7H9 culture media supplemented with varying $[K^+]_e$ and $[Na^+]_e$. Isoniazid (INH) was used as a positive control. **D-G, K** are reported as fold change of CFU 24 hr vs 0 hr. All experiments were performed

thrice or with n≥3 donors unless otherwise stated. Data in **C** was analyzed by Two-way ANOVA. Data in **D**, **E**, **G**, **I** were analyzed by Paired *t*-test. Bar graphs represent Mean ± SD.

5.3 Extracellular K^+ restricts mycobacterial growth by inducing autophagy via Akt-mTOR pathway

In order to determine the mechanism(s) by which $[K^+]_e$ restricted intracellular replication of mycobacteria, we first evaluated the $[K^+]_e$-treated infected cells for autophagy induction, which is required for an effective control of intracellular pathogens [476]. Of note, the role of autophagy in control of mycobacteria by monocytes and macrophages is well known and perturbations in the autophagy network have previously been associated with *Mtb* virulence [111, 477, 478]. In our experiments, high $[K^+]_e$ induced autophagy, as assessed by upregulation of lipidated form of LC3 (LC3II, an autophagosome marker) in uninfected and BCG-infected monocytes (Fig 32A). We further found a $[K^+]_e$-mediated increase in LC3II puncta in *Mtb*-infected THP-1 monocytes (at 4h), which was further increased with Bafilomycin A treatment, indicating enhanced autophagic flux (Fig 32B). The $[K^+]_e$-mediated induction of autophgy flux was also observed by western immunoblotting of LC3II in uinfected cells (Fig 32C). Blocking autophagy by siRNA-mediated silencing of ATG5 gene, which is crucial for the formation of autophagosomes in both canonical and non-canonical autophagy [479], abolished $[K^+]_e$-mediated restriction of *Mtb* growth (Fig 32D). Indeed, inhibition of autophagy with 3-MA, an inhibitor of class III PI3K (PI3 Kinase), partially limited high $[K^+]_e$ mediated reduction of mycobacterial CFU (Fig 32E). In summary, we show that high $[K^+]_e$-mediated restriction of mycobacterial growth is attributed to $[K^+]_e$-mediated autophagy induction.

The most commonly understood cellular signaling pathway that culminates in autophagy induction is the Akt-mTOR pathway, where inhibition of mTOR relieves suppression of autophagy, leading to the phosphorylation of ULK1 [480, 481] (Fig 32E). This results in the assembly of the autophagosome which comprises the conjugation of ATG12 to ATG5 and the lipidation of LC3I to LC3II, elongating and decorating the autophagosomal membrane respectively [482, 483]. As phosphorylation is a rapid event, we exposed primary monocytes to high $[K^+]_e$ for 1h and observed $[K^+]_e$-dependent inhibition of phosphorylation of Akt, mTOR and its downstream target S6 (Fig 32F). Taken together, these data indicate that high $[K^+]_e$ exposed monocytes/macrophages have enhanced autophagic flux through inhibition of the Akt-mTOR pathway, which could contribute to restriction of mycobacterial growth.

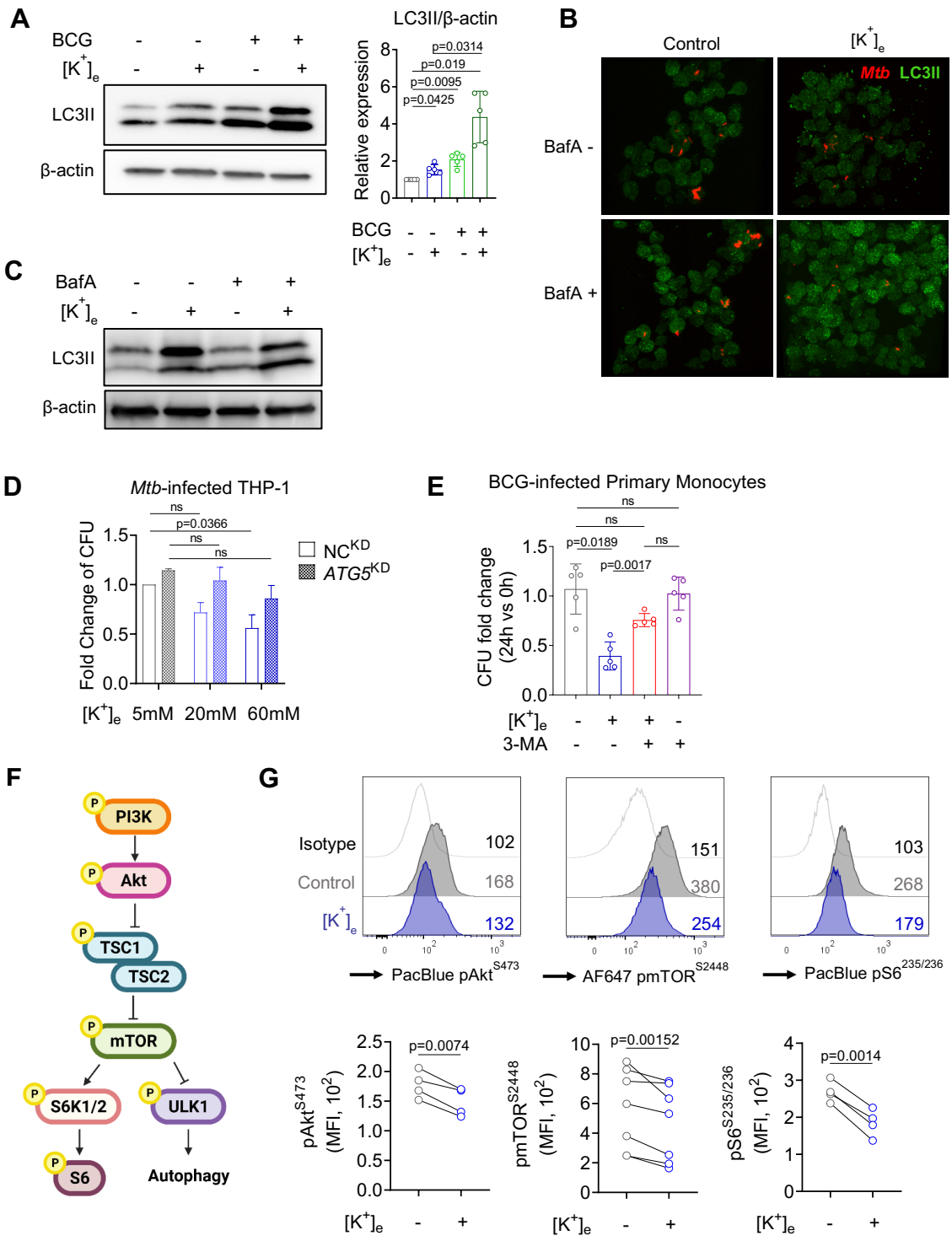

Figure 32. High $[K^+]_e$–mediated mycobacterial restriction in monocytes is dependent on autophagy induction.

A) Western immunoblot of human monocytes infected with BCG and treated with 60mM $[K^+]_e$ and quantification of LC3II band densitometry. **B)** Immunofluorescence staining for LC3II puncta in mCherry-H37Rv-infected THP-1 monocytes treated with 60mM $[K^+]_e$ with or without Bafilomycin A (BafA) for 4h. **C)** Western immunoblot of primary monocytes treated with 60mM $[K^+]_e$ with or without 100nM BafA for 24h. BafA was added 4h prior to cell lysis. **D)** Fold change of *H37Rv Mtb* CFU enumerated from 24h-infected THP-1 monocytes transfected with Control or ATG5 siRNA and treated with 20 and 60mM $[K^+]_e$ (compiled data of n=2 experiments). **E)** Fold change of BCG CFU from 24h-infected human monocytes treated with 60mM $[K^+]_e$ with or without 3-MA inhibitor treatment. 3-MA was added 30 min prior to 60mM

$[K^+]_e$ treatment. **F**) Schematic of canonical PI3K/Akt/mTOR phosphorylation signaling pathway that leads to the formation of autophagosome. **G)** Flow cytometry detection of phospho-Akt/mTOR/S6 in human monocytes after 1h treatment with 60mM $[K^+]_e$. Data is shown as MFI – Mean Fluorescence Intensity. Data in **A, E** were analyzed with One-way ANOVA. Data in **D** was analyzed with Two-way ANOVA. Data in **G** was analyzed with Paired t-test. All experiments were performed thrice or with n≥3 donors unless otherwise stated. Bar graphs represent Mean ± SD. *In vitro Mtb*-infection experiments were conducted in collaboration with Surbhi Verma, Dr Dhiraj Kumar Lab, ICGEB.

5.4 Transcriptomic analysis suggests extracellular K^+ induces oxidative stress response

To gain further mechanistic insights into high $[K^+]_e$-mediated induction of autophagy, we conducted a genome-wide transcriptomic analysis of high extracellular K^+ treated *Mtb*-infected primary monocytes (n=4 donors) (Fig 33A). PCA of the expression profiles of 16 samples among four groups showed that the transcriptome of primary monocytes was affected both by *Mtb* infection and high $[K^+]_e$ treatment at the 24h timepoint (Fig 33C). To better decipher the effect of high $[K^+]_e$, differential gene expression (DEG) analysis was performed (Fig 33B). The union of 8284 DEGs across all 4 groups were represented by a hierarchical clustering heatmap, which separated genes into six clusters (R1-R6; Fig 33D). Among these Clusters R1, R3 and R4 were largely altered by *Mtb* infection and clusters R5 and R6 were modulated by high $[K^+]_e$ (Fig 33D).

Mtb infection-specific clusters demonstrated expected transcriptomic changes, such as the upregulation of an array of pro-inflammatory genes such as *Ifng, Il1b, Il6*, and various chemokines in Clusters R3 and R4. Likewise, *Mtb* infection led to a downregulation of various mitochondrial genes represented in Cluster R1. Notably, *Mtb* infection has been shown to cause mitochondrial dysregulation and metabolic shifts in host cells [484, 485, 486].

Interestingly, Cluster R5 represented genes downregulated by high $[K^+]_e$, consisting of genes involved in antigen presentation such as *Ciita* and numerous HLA genes. Cluster R6 conversely grouped genes upregulated by high $[K^+]_e$ and included genes involved in cellular motility, proliferation and related signaling pathways such as GTPases *Rac2* and *RhoA* [487].

Analysis of the mean expression of genes across the clusters identified Cluster R2 to constitute genes that were upregulated by *Mtb* infection, and their expression was further augmented upon $[K^+]_e$ treatment (Fig 33E). This trend was found to be similar to the induction of LC3II i.e. autophagy induction which was increased by BCG infection and was further enhanced by high $[K^+]_e$ (Fig 32A). Thus, we focused our further analyses on Cluster R2. We hypothesized that cluster R2 genes would reveal a mechanism behind the increase in autophagic flux observed in *Mtb*-infected cells when exposed to high $[K^+]_e$ (Fig 33A,B).

Notably, pathway analysis of genes found in Cluster R2 highlighted the enrichment of genes partaking in oxidative stress response and cholesterol biosynthesis pathways (Fig 33F).

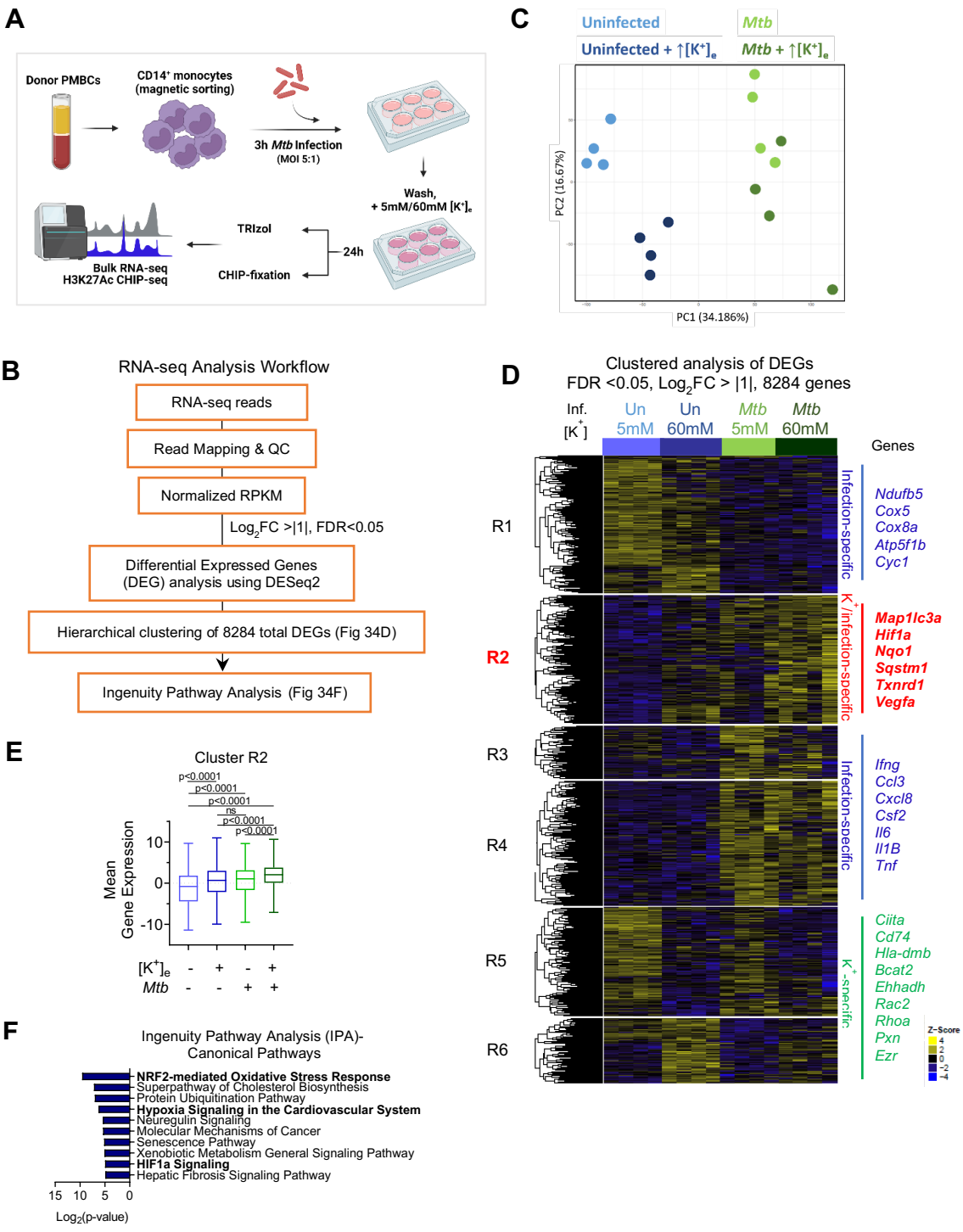

Figure 33. Transcriptomic analyses of *Mtb*-infected human monocytes treated with high $[K^+]_e$.
A) Experimental outline for collection of human monocyte samples for RNA-sequencing and H3K27ac ChIP-sequencing (N=4 donors). **B)** PCA of RNA-seq data of human monocytes uninfected or infected with H37Rv *Mtb*, untreated or exposed to 60mM $[K^+]_e$ for 24h. **C)** RNA-seq analysis pipeline. **D)** Hierarchical clustering analysis of RNA-seq data, FDR<0.05, $Log_2FC>|1|$. Key genes from each cluster are listed on the right. **E)** Box plot showing mean expression of genes derived from Cluster R2. Median with min. and max. values are represented. **E)** Top 10 Canonical Pathway enriched in 1729 Cluster R2 genes using Ingenuity Pathway Analysis (IPA). Data in **E** is analyzed by One-way ANOVA.

A number of studies associate the induction of reactive oxidative species (ROS) and cholesterol production in different contexts, but their precise relationship remains elusive [488]. For example, increase in mitochondrial H_2O_2 efflux led to enhanced cholesterol biosynthesis via SREBP-2 transcription factor activation in hepatocytes [489]. Indeed, another study showed short term treatment of hepatocytes with H_2O_2 also led to HMG-CoA activation, a rate-limiting step in cholesterol biosynthesis, and this was associated with AMPK activation [490]. Treatment with xanthine oxidase, which can produce ROS, also led to enhanced cholesterol biosynthesis in neuroblastoma cell line [491]. While we did not further investigate the effect of high $[K^+]_e$ on cholesterol biosynthesis in our present study, it may prove to be interesting since *Mtb* is known to utilize host cholesterol for intracellular growth and dormancy[492, 493] , although this should, in theory, promote mycobacterial survival instead.

Interestingly, Cluster R2 genes were also enriched for HIF1α and hypoxia signaling pathways. Although HIF1α is traditionally understood to be a hypoxia response element, its functions are not limited to cellular adaptation to changes in oxygen concentrations. While older studies indicate that mitochondrial ROS (mROS) stabilizes HIF1α during hypoxia, newer studies suggested that the role of ROS in HIF1α stabilization is controversial in hypoxia although it is fairly well-established in normoxic conditions [494]. Recently, it was also found that NRF2, which is activated during oxidative stress, binds to an antioxidant response element upstream of HIF1α and induces its transcription [495]. We looked into the normalized gene expression of *HIF1A* in our RNA-seq dataset and indeed we found increased expression of *HIF1A* mRNA in $[K^+]_e$ exposed uninfected and *Mtb*-infected monocytes (Fig 34A). Quantification of intracellular HIF1α protein at 24h post-treatment showed a trend towards accumulation in $[K^+]_e$ exposed uninfected monocytes (Fig 34B).

HIF1α has a short half-life and is continually degraded by prolyl hydroxylases, but its degradation can be inhibited by ROS, thereby permitting its nuclear localization [494]. We found that indeed, at only 1h of $[K^+]_e$ exposure, HIF1α nuclear localization was evident, a phenomenon that was partially inhibited by NAC (ROS quencher) (Fig 34C, D). Inhibition of HIF1α accumulation and transcriptional activity with CAY10585 only trended toward partial inhibition of $[K^+]_e$-mediated LC3II accumulation (Fig 34E). This suggests that $[K^+]_e$ exposure leads to both an increased expression of HIF1α as well as its partial ROS-dependent stabilization and transcriptional activation, which may contribute to some extent to the formation of autophagosomes, as reported earlier [494]. However, inhibiting HIF1α by CAY10585 did not abolish $[K^+]_e$-mediated restriction of mycobacterial growth (Fig 34F). Furthermore, siRNA-mediated silencing of HIF1A in THP-1 monocytes also failed to abolish the $[K^+]_e$-mediated restriction of mycobacterial growth (Fig 34G). This data suggests that though $[K^+]_e$ induces HIF1α activation and translocation into the nucleus, it may not be pivotal for $[K^+]_e$-mediated restriction of mycobacterial growth.

In summary, the transcriptomic analysis of uninfected and *Mtb*-infected monocytes exposed to high $[K^+]_e$ indicated that oxidative stress could be a primary mechanism that activates autophagy most likely directly and not through HIF1α signaling.

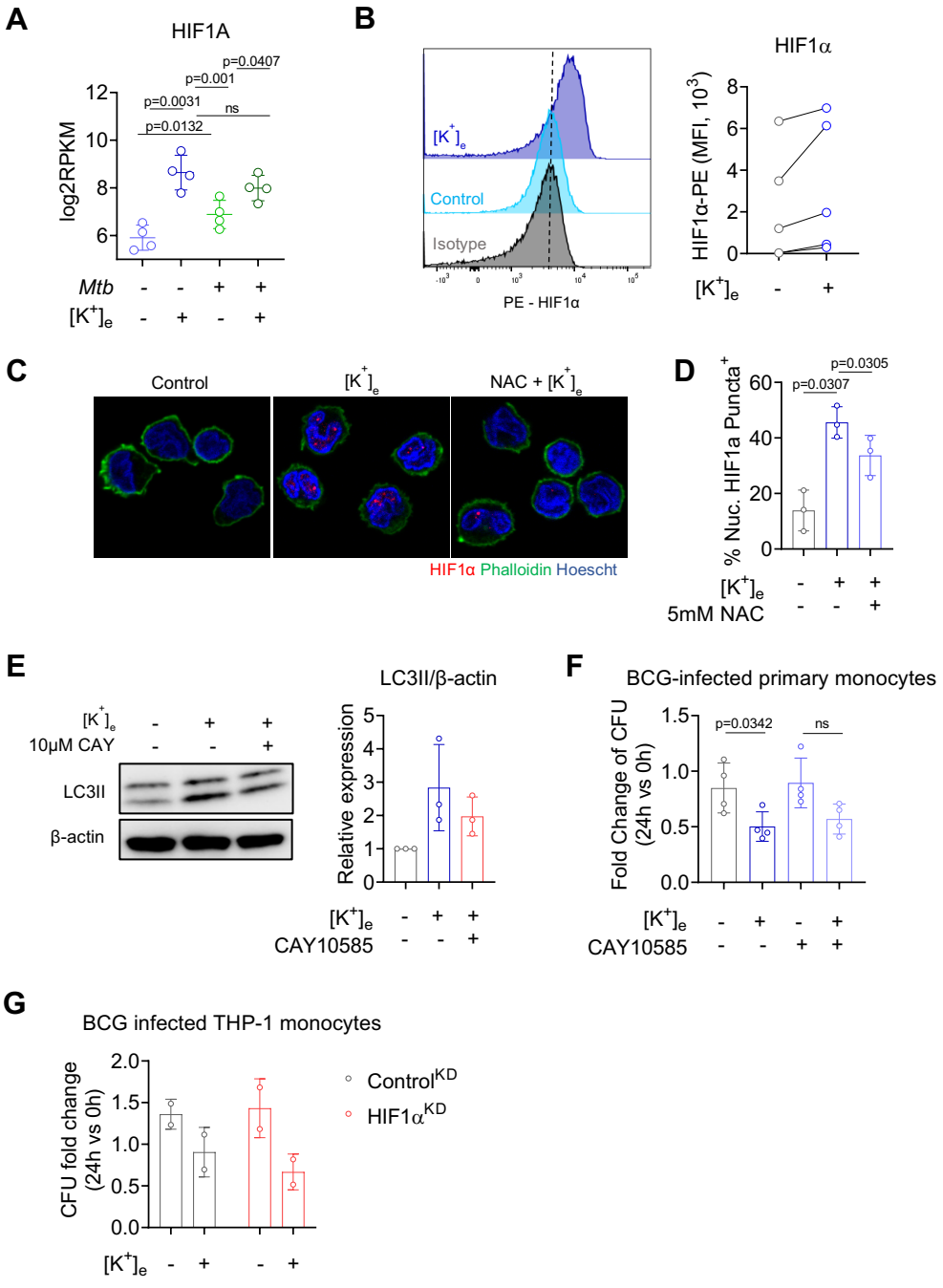

Figure 34. $[K^+]_e$–mediated HIF1α activation is ROS-mediated but does not contribute directly to mycobacterial killing.
A) Log_2(RPKM) values of HIF1A transcripts attained from RNA-seq dataset across four groups. **B)** Flow cytometry of human monocytes untreated or exposed to 60mM $[K^+]_e$ for 24h and stained with anti-HIF1α-PE for intracellular HIF1α detection. **C)** Immunofluorescence images of monocytes treated with 60mM $[K^+]_e$ with or without NAC treatment. 5mM NAC was added 30 min prior to 60mM $[K^+]_e$ treatment. **D)** Percentage of cells containing observable HIF1α-AF488 puncta within nuclei (Hoescht)-stained regions

were calculated per field. Five fields were analyzed with an average of 44 cells in each field. **E)** Western immunoblotting of LC3II in monocytes treated with 60mM $[K^+]_e$ with or without 10μM CAY10585 inhibition. CAY10585 was added 30 min prior to 60mM $[K^+]_e$. Band densitometry is quantified in the graph (right). **F)** Fold change of CFU from monocytes infected for 24h with BCG and treated with 60mM $[K^+]_e$ with or without CAY10585 inhibition. **G)** Fold change of CFU from 24h BCG-infected Negative control ($Control^{KD}$) or siRNA-mediated knockdown of HIF1A ($HIF1\alpha^{KD}$) THP-1 monocytes (n=2). Data in **B** was analyzed by Paired t-test. Data in **A, D, E** and **F** were analyzed by One-way ANOVA. Data in **G** was analyzed by Two-way ANOVA. All experiments were performed thrice or with n≥3 donors unless otherwise stated. Data are represented as Mean ± SD.

5.5 Extracellular K^+ disrupts membrane potential and causes mitochondrial oxidative stress generation

Our transcriptomic investigation indicates $[K^+]_e$-mediated induction of oxidative stress in monocytes, which could be due to production and accumulation of ROS in cells. Of note, ROS production can also result in restriction of intracellular mycobacterial growth [496]. Therefore, we assessed for the production of ROS in $[K^+]_e$-exposed cells. $[K^+]_e$ treatment selectively induced the production of mROS within just 1h of $[K^+]_e$ exposure (Fig 35A, detected by MitoSOX Red), whereas cytoplasmic ROS were not elicited at this early time point (Fig 35B, detected by CM-H2DCFDA).

When cells were exposed to high $[K^+]_e$ till 24 hours, we noticed some induction (not significant) in cellular ROS levels, whereas the increase in mROS became less prominent (Fig 35A, B right). This data suggested that at early exposure to high $[K^+]_e$, the mitochondria begin to generate ROS which may have eventually diffused into the cytoplasmic space, or that NADPH oxidase production of cytoplasmic ROS may have occurred over time. Increase in oxidative stress within the cell that persisted over 24h explains the prominent upregulation of antioxidant response genes (such as *Nqo1*, *Txnrd1*, *Gclc*) in cluster R2 of the transcriptomic data. Generation of mROS in high $[K^+]_e$ exposed cells might be due to the influx of K^+ into the intracellular pool and eventually into the mitochondria, compromising normal mitochondrial function. Indeed, high $[K^+]_e$ led to the depolarization of mitochondrial membrane potential in monocytes as detected by TMRM at 1h (Fig 35C), which correlated with significant depolarization of cell plasma membrane, as detected by $DIBAC_4(3)$ (Fig 35D). Taken together, our data suggests that high $[K^+]_e$ exposure leads to K^+ influx into the cell that might enter the mitochondria, causing mitochondrial depolarization and mROS generation.

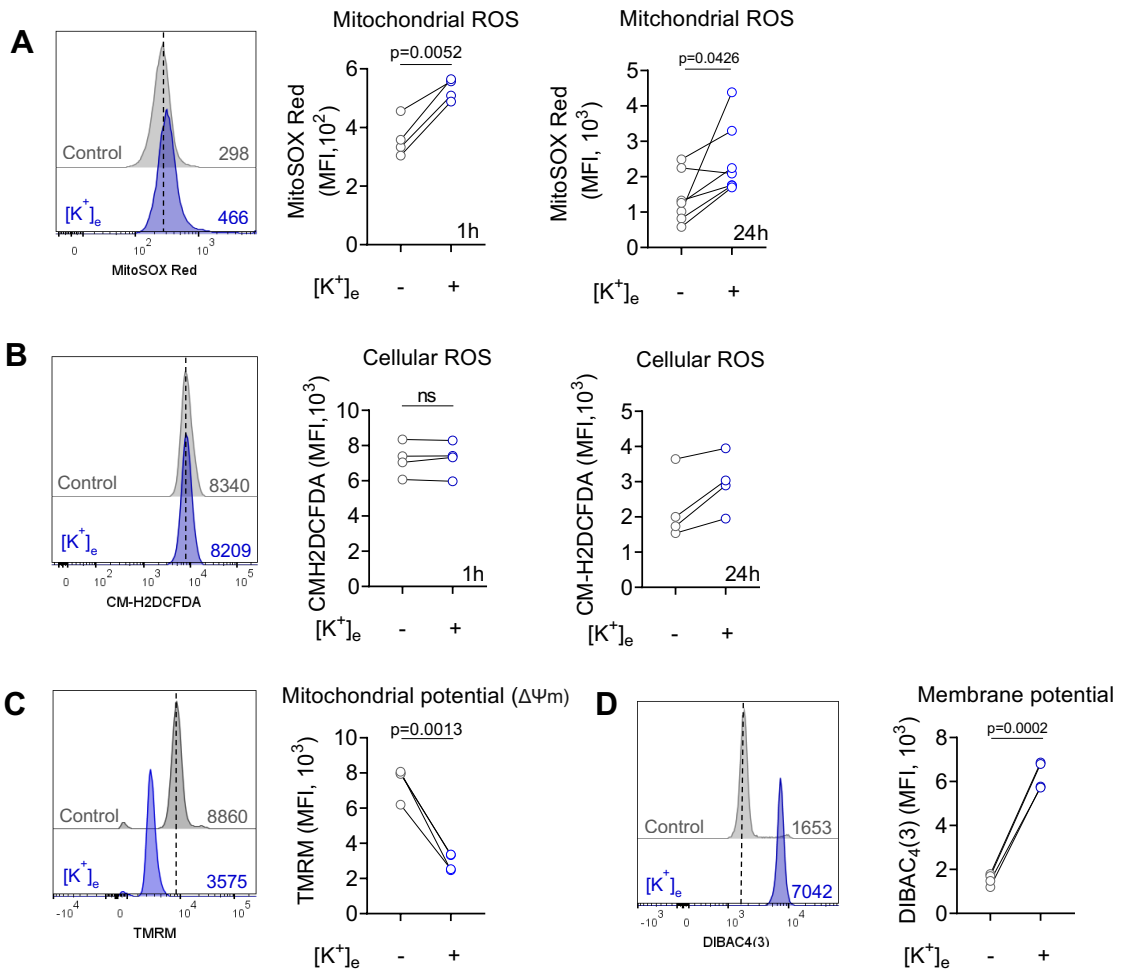

Figure 35. High $[K^+]_e$ depolarizes the mitochondrial membrane and induces mROS.
A) Flow cytometry of human monocytes untreated or exposed to 60mM $[K^+]_e$ for 1h (left) and 24h (right) and stained with **A)** MitoSOX Red and **B)** CM-H2DCFDA. Flow cytometry of monocytes untreated or exposed to 60mM $[K^+]_e$ for 1h and stained with **C)** TMRM and **D)** $DiBAC_4(3)$. Data in **A-D** were analyzed by Paired t-test. All experiments were performed with n≥3 donors.

5.6 Extracellular K^+ leads to mitochondrial dysfunction

Mitochondrial membrane potential perturbation is a strong indicator or instigator of compromised mitochondrial fitness and mitochondrial bioenergetics [497]. Using the Mito Stress Test extracellular flux assay, we examined various parameters of mitochondrial respiration and metabolism in monocytes exposed to high $[K^+]_e$ (Fig 36A). We found that high $[K^+]_e$ exposed primary human monocytes had reduced oxygen consumption rate (OCR) - an indicator of OXPHOS (Fig 36B). Importantly, $[K^+]_e$ exposed human monocytes showed a trend of decreased basal and maximal OCR, which was linked to reduced proton (H^+) leak, as no change in ATP synthesis was observed (Fig 36C). The maximal OCR represents the ability of the cells to respond to increased energy demand when FCCP is administered, allowing maximal electron flow through the electron transport chain, reaching peak oxygen consumption (Fig 36A). $[K^+]_e$-exposed human monocytes also showed reduced SRC (p = 0279, in response to FCCP stress) and a trend of decreased non-

mitochondrial respiration (Fig 36C). SRC symbolizes mitochondrial spare reserve capacity, which may be limited by the number of functional mitochondria present in cells. Overall, this data uggests that high $[K^+]_e$ limits mitochondrial respiration of monocytes.

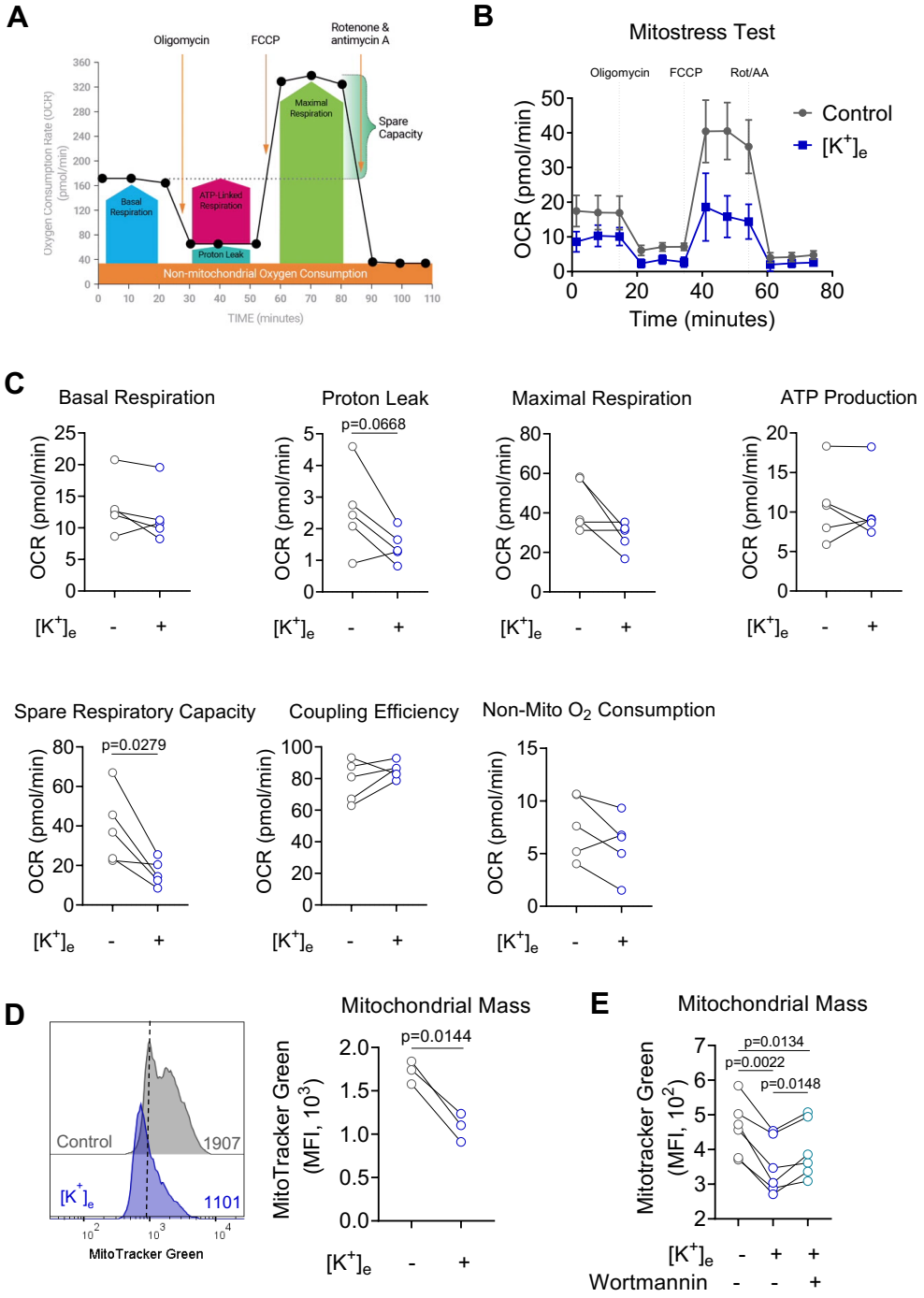

Figure 36. High $[K^+]_e$ causes mitochondrial dysfunction and loss of mitochondrial mass.
A) Exemplar profile of Mito Stress test and quantified parameters of mitochondrial respiration (taken from Agilent). **B)** Representative oxygen consumption rate (OCR) profile from Mito Stress test of human monocytes untreated or treated with 60mM $[K^+]_e$. **C)** OCR values attributed to each parameter of Mito Stress test between untreated and 60mM $[K^+]_e$ conditions. **D)** Quantification of mitochondrial mass by flow cytometry of human monocytes stained with MitoTracker Green after 24h of exposure to 60mM $[K^+]_e$. **E)** Flow cytometry of human monocytes stained with MitoTracker Green after 24h of exposure to 60mM $[K^+]_e$ with or without Wortmannin inhibition. Wortmannin was added 30min prior to 60mM $[K^+]_e$. Data in **C** and

D was analyzed by Paired t-test. Data in **E** was analyzed by One-way ANOVA. All experiments were performed with monocytes from n≥3 donors.

The above mitochondrial respiration data aligns with our finding of reduced mitochondrial potential in $[K^+]_e$ exposed monocytes (Fig 35C), as K^+ ions flooding into the mitochondrial matrix would dissipate the potential, reducing the negative charge that would typically incite H^+ leak. Inhibited H^+ leak would logically boost ATP production which was, however, not observed, possibly since the effect of H^+ leak on overall OCR was small.

We next evaluated the total mitochondrial mass and demonstrated that high $[K^+]_e$ exposure led to a reduction of mitochondrial mass in monocytes at 24h (Fig 36E, MitoTracker Green staining). Importantly, the reduction in high $[K^+]_e$ induced mitochondrial mass was rescued by treatment with autophagy inhibitor Wortmannin (Fig 36F), suggesting that mitophagy (form of mitochondrial-specific autophagy) may be responsible for the loss of mitochondrial mass (Fig 36E) and in turn, spare metabolic capacity (Fig 36C), which is needed to increase oxygen consumption when stressed with FCCP treatment. In summary, high $[K^+]_e$ allowed K^+ ion movement into the mitochondria, causing dysfunction by disrupting ionic gradient-sensitive metabolic mechanisms. Indeed, high $[K^+]_e$-mediated perturbation of mitochondrial potential is also a potent signal which may have triggered mitophagy for the clearance of dysfunctional mitochondria [497, 498].

5.7 Extracellular K^+ mediates H3K27ac epigenetic regulation of oxidative stress response genes

It is known that the transcriptomic changes in host immune cells during perturbations and infections could be chromatin-mediated [499, 500, 501, 502]. Furthermore, oxidative stress, which was enriched among cluster R2 genes (Fig 33D), can affect the expression of genes via epigenetic modulation [503, 504, 505]. Moreover, NRF2, which is induced by oxidative stress helps in the recruitment of histone acetyltransferase CREB binding protein (CBP) to the promoters of antioxidant response genes [506, 507]. Oxidative stress was also shown to activate anti-cancer oxaliplatin-induced autophagy through H3K27ac (Histone H3 acetylation at lysine 27)-mediated expression of NORAD [508]. Hence, we hypothesized that high $[K^+]_e$-mediated mROS generation (Fig 35A) could also result in changes at the chromatin level. We, therefore profiled genome-wide H3K27ac, which is a well-established chromatin signature of active enhancers and promoters [509, 510] and also correlates with gene expression [511]. ChIP-sequencing was used to profile H3K27ac (See Methods and del Rosario *et al.* [211]) in high $[K^+]_e$-exposed primary monocytes (Fig 37A, *same set of donors as for transcriptomic investigation Fig 33A*).

Consensus H3K27ac peaks were evaluated for differential histone acetylation (differential peak height), among infected and high $[K^+]_e$-treated samples, to identify infection- and high $[K^+]_e$-associated changes in regulatory elements i.e differentially acetylated (DA) peaks (Fig 37A). In total, we identified 3729-13618 DA peaks in each combination of differential analysis (between 4 groups, total six differential analyses; Fig 37B). This resulted in 252-12151 unique DA peaks across different comparisons, totaling to 31200 DA peaks (Fig 37B). PCA analysis on this unique 31200 H3K27ac peak set demonstrated an overall chromatin divergence between infected and high $[K^+]_e$-treated monocytes (Fig 37C). These epigenetic perturbations are similar to what we saw in transcriptomic investigation, where the transcriptome of monocytes was affected both by *Mtb* infection and high $[K^+]_e$ treatment (Fig 33C).

We next annotated the unique DA loci to protein coding genes (±100kb from gene TSS) and performed hierarchical clustering. This resulted in identification of 6 unique clusters, C1-C6 (Fig 37D). Cluster C2 comprised genes that had decreased H3K27 acetylation upon *Mtb* infection, comprising genes such as *Icam3* and *Pxn* which were associated with cell adhesion and migration. Cluster C3 genes had reduced acetylation upon both *Mtb* infection and high $[K^+]_e$ exposure and were related to cell signaling for motility and projection formation (*Dmn3*, *Rhou*, *Vcl*). Cluster C5 genes had upregulated H3K27ac peaks that were largely $[K^+]_e$-specific and interestingly included immune activation-related genes such as *Itgam* and *Tlr1*, and apoptosis-related genes like *Casp2* and *Ripk1*. Cluster C6 harbor genes that had reduced H3K27 acetylation by high $[K^+]_e$ only in the context of infection. These C6 genes were involved in T cell activation and regulation such as *Cd28* and *Lck*. Clusters C1 and C4 were closely clustered, both comprising genes that were increased in acetylation with high $[K^+]_e$, with C1 and some C4 genes seeming to be also enhanced during infection (Fig 37D).

In order to investigate the correspondence between histone acetylation changes and differential gene expression, we integrated the genes among the differential clusters of RNA-seq and ChIP-seq datasets. We observed moderate correlation between RNA-seq and ChIP-seq clusters (Fig 37E), which could be due to lower signal-to-noise ratio among two different techniques as observed by us and others before [211, 512]. In particular, we observed that genes in RNAseq cluster R2 intersected most significantly with genes in ChIP-seq Clusters C1 and C4 (Fig 37E, p values: C1 - 1.05E-20, C4 - 1.92E-37). Interestingly, we found a number of antioxidant response-related genes such as *Gclc*, *Gstm5* and *Gsto2* (glutathione transferases) within C1 and C4 clusters, which had increased H3K27ac promoter peaks in high $[K^+]_e$ treated cells (Fig 37F). This was correlated with increased expression (RNAseq reads) of those genes in high $[K^+]_e$ treated cells (Fig 37F). In summary, our data suggests that high $[K^+]_e$ causes the production of ROS that activates the antioxidant response system both at an epigenetic and transcriptomic level.

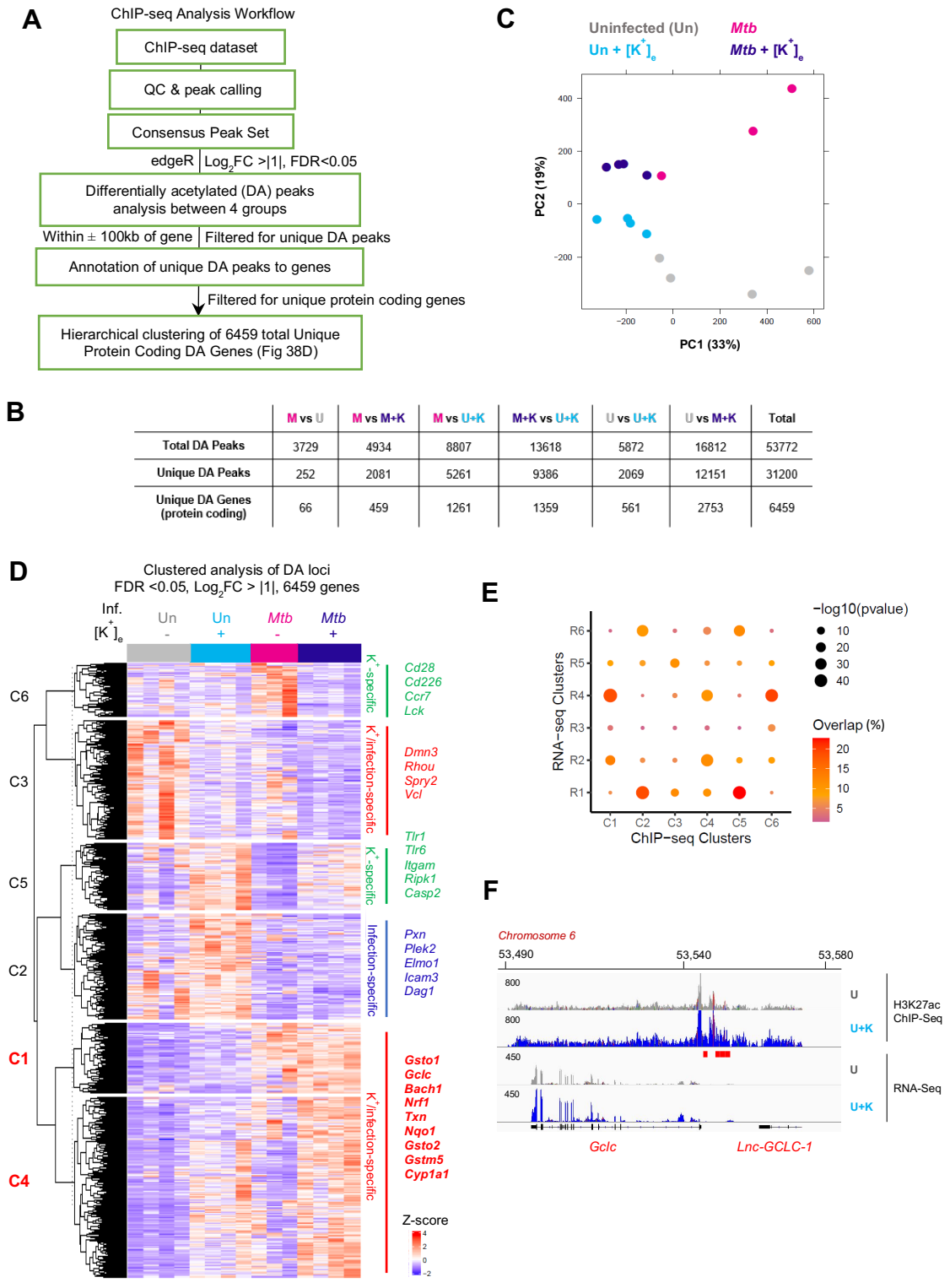

	M vs U	M vs M+K	M vs U+K	M+K vs U+K	U vs U+K	U vs M+K	Total
Total DA Peaks	3729	4934	8807	13618	5872	16812	53772
Unique DA Peaks	252	2081	5261	9386	2069	12151	31200
Unique DA Genes (protein coding)	66	459	1261	1359	561	2753	6459

Figure 37. Epigenetic profile of *Mtb*-infected human monocytes treated with high $[K^+]_e$ via H3K27ac ChIP-sequencing.

A) H3K27ac ChIP-seq analysis pipeline. **B)** Table detailing numbers of differentially acetylated (DA) peaks obtained among all comparisons of the four sample groups as well as annotated unique genes for analysis. U – Uninfected cells; M – Infected cells; U+K - 60mM $[K^+]_e$-treated uninfected cells; M+K - 60mM $[K^+]_e$-treated infected cells. **C)** PCA plot of DA peaks by edgeR across all comparisons. **D)** Hierarchical clustering analysis generated from the binding matrix derived for DA genomic regions associated with the extracted

protein coding genes. FDR<0.05, $Log_2FC>|1|$. Key genes from each cluster are listed on the right. **E)** Dot plot representing the percentage of overlap between DEGs in ChIP-seq and RNA-seq clusters and the derived p-values using hyper-geometric distribution for the same. **F)** Genome tracks aligning RNA-seq transcripts and ChIP-seq H3K27ac peak loci from uninfected primary monocyte samples untreated (Grey) or administered with 60mM $[K^+]_e$ (Blue). Red bar represents DA genomic loci.

5.8 Induction of autophagy by extracellular K^+ is dependent on ROS induction

Our transcriptomic and epigenetic investigation points to the generation of significant oxidative stress following exposure of monocytes to high $[K^+]_e$. However, we did not find any clear upregulation of autophagy pathway-related genes in our H3K27ac profiling in high $[K^+]_e$ treated cells, which was assessed at 24h time point. Therefore, it is likely that autophagy was regulated at an early timepoint at the protein level. We therefore examined the induction of autophagy as a direct consequence of high $[K^+]_e$-induced ROS production. As observed previously (Fig 32A, C), high $[K^+]_e$ induced accumulation of LC3II in primary human monocytes, and this was abolished by treatment with N-acetyl cysteine (NAC, ROS quencher) (Fig 38A). Likewise, NAC also prevented the reduction in phosphorylation of S6 protein (Fig 38B), a downstream mTOR target, dephosphorylation of which was found to be dependent on high $[K^+]_e$ (Fig 32F). Importantly, NAC partially abolished high $[K^+]_e$-mediated reduction of mycobacterial growth (Fig 38C). ROS has been shown to induce autophagy through modulating Akt/mTOR phosphorylation although the exact mechanism is not well understood [513, 514, 515]. Moreover, ROS can also trigger autophagy by indirectly activating AMPK through affecting cellular energy balance [516]. Taken together, this analysis and the above data suggest that ROS are a key driver of high $[K^+]_e$-mediated autophagy induction and restriction of mycobacterial growth in monocytes/macrophages.

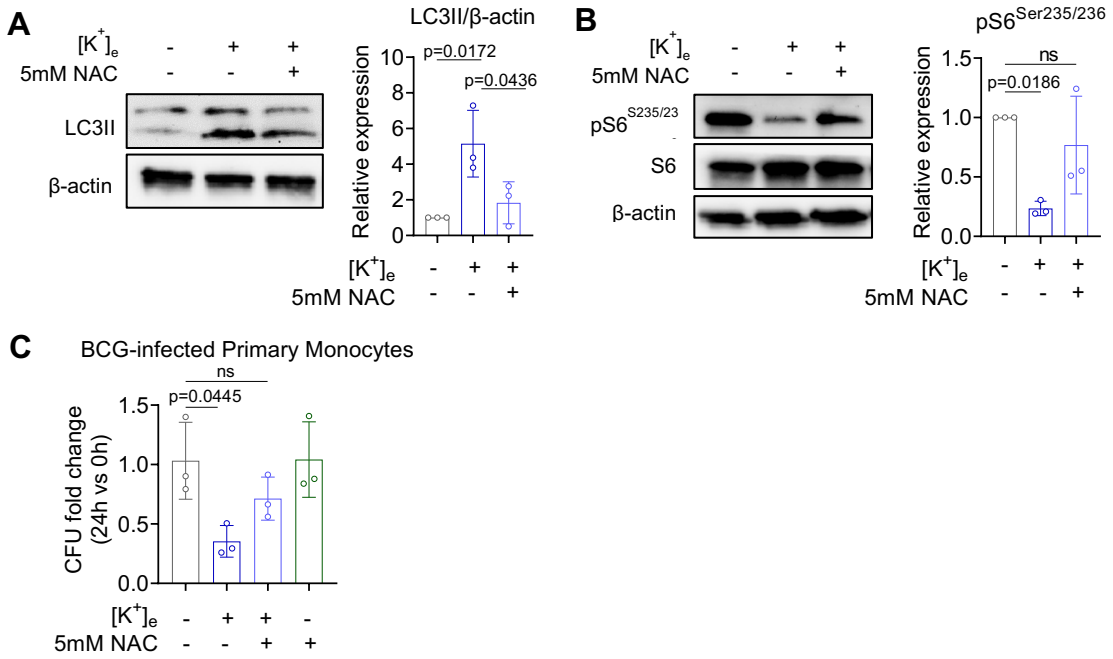

Figure 38. $[K^+]_e$ –mediated autophagic killing is mediated by ROS induction.
A) Western immunoblot for LC3II from primary $CD14^+$ human monocytes exposed to high $[K^+]_e$ with ROS scavenging by 5mM NAC. NAC was added 30 min prior to 60mM $[K^+]_e$. Bar graph demonstrating densitometric analysis of LC3II band relative to β-actin is shown (right). **B)** Western immunoblot for phosphorylated-S6 from human monocytes exposed to high $[K^+]_e$ with ROS scavenging by 5mM NAC. Bar graph demonstrating densitometric analysis of pS6 band relative to β-actin is shown (right). **C)** Fold change of BCG CFU after 24h of infection with and without exposure to 60mM $[K^+]_e$. and 5mM NAC. Data was analyzed with One-way ANOVA. All experiments were performed with n≥3 donors. Data are represented as Mean ± SD.

5.9 Administering high K^+ improves mycobacterial control in vivo in zebrafish.

Our *in vitro* data demonstrated that elevated $[K^+]_e$ can improve control of intracellular *Mtb*/BCG growth. We thus hypothesized that increasing systemic K^+ may provide some benefit to the host in terms of infection or regulation of inflammation. We first used the zebrafish-*Mm* infection model to test the benefits of increasing systemic K^+. Wasabi-*Mm* infected zebrafish embryos were cultivated in medium containing 10mM KCl for 4 days (Fig 39A). We found that KCl exposed zebrafish had enhanced ability to control intracellular *Mm* growth (Fig 39B), which was independent of any direct effect of KCl on *Mm* (Fig 39C). Further experimentation is needed to decipher if there was indeed high extracellular K^+ in the fish as a result of treatment and determine the molecular mechanism that might have resulted in improved bacterial control in high KCl-exposed zebrafish.

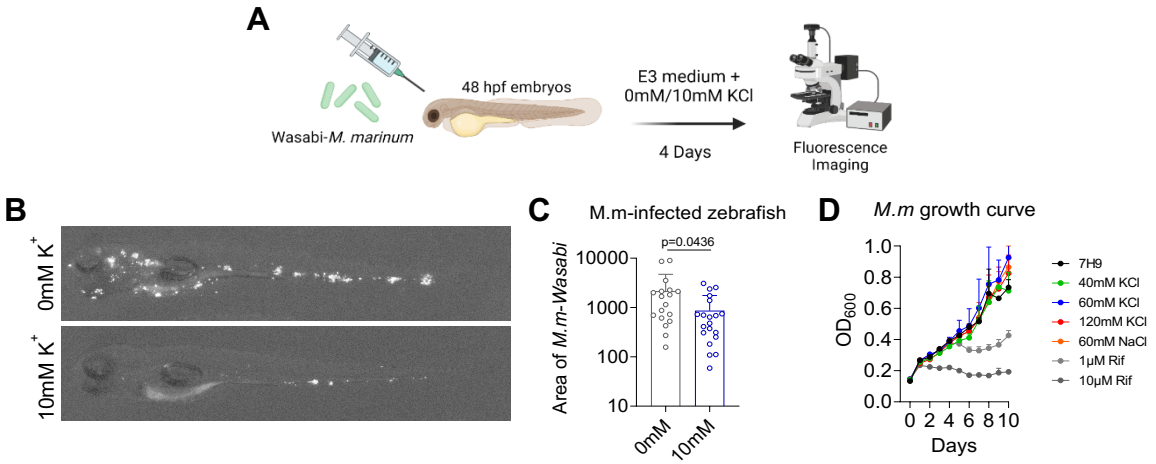

Figure 39. Administering high K^+ enhances mycobacterial control *in vivo* in zebrafish.
A) Schematic of zebrafish infection at 48 hours post-fertilization and injection of *Mm*-Wasabi followed by incubation in E3 medium containing 0 or 10mM additional KCl. Embryos were imaged at 4 d.p.i. and bacterial area was quantified. **B)** Representative images of zebrafish incubated in 0mM or 10mM KCl-containing E3 medium. White areas correspond to bacterial aggregates of *Mm*-Wasabi. Images are taken at 20X. **C)** Area of *Mm*-Wasabi in zebrafish embryos at 4 d.p.i. Each dot represents n=1 zebrafish. **D)** Growth curve of *Mm*-Wasabi over 10 days *in vitro* in 7H9 medium supplemented with 40-120mM KCl or 60mM NaCl or Rifampicin (positive control). Data in **C** was analyzed by Unpaired *t*-test, Mean ± SD are represented. Zebrafish experiments were conducted in collaboration with Ria Sorayah, Dr Stefan Oehler Lab, A*STAR ID Labs.

5.10 Administering high K^+ enhances inflammatory responses and may improve control of mycobacterial infection in mice

Seeing encouraging results in KCl-treated *Mm*-infected zebrafish (Fig 39), we investigated the effect of high K^+ in a mouse model of TB [45]. To this end, we used normal K^+ diet and high K^+ diet regimens (see Methods; Fig 40A). Wild-type C57BL/6 mice were started on the respective diets 3 days before aerosol infection with *Mtb* (Fig 40A). Upon infection mice were maintained on the respective diets. *Mtb*-infected mice maintained on high K^+ diet showed a slight trend of reduced bacillary load in the lung at 15 d.p.i (Fig 40B).

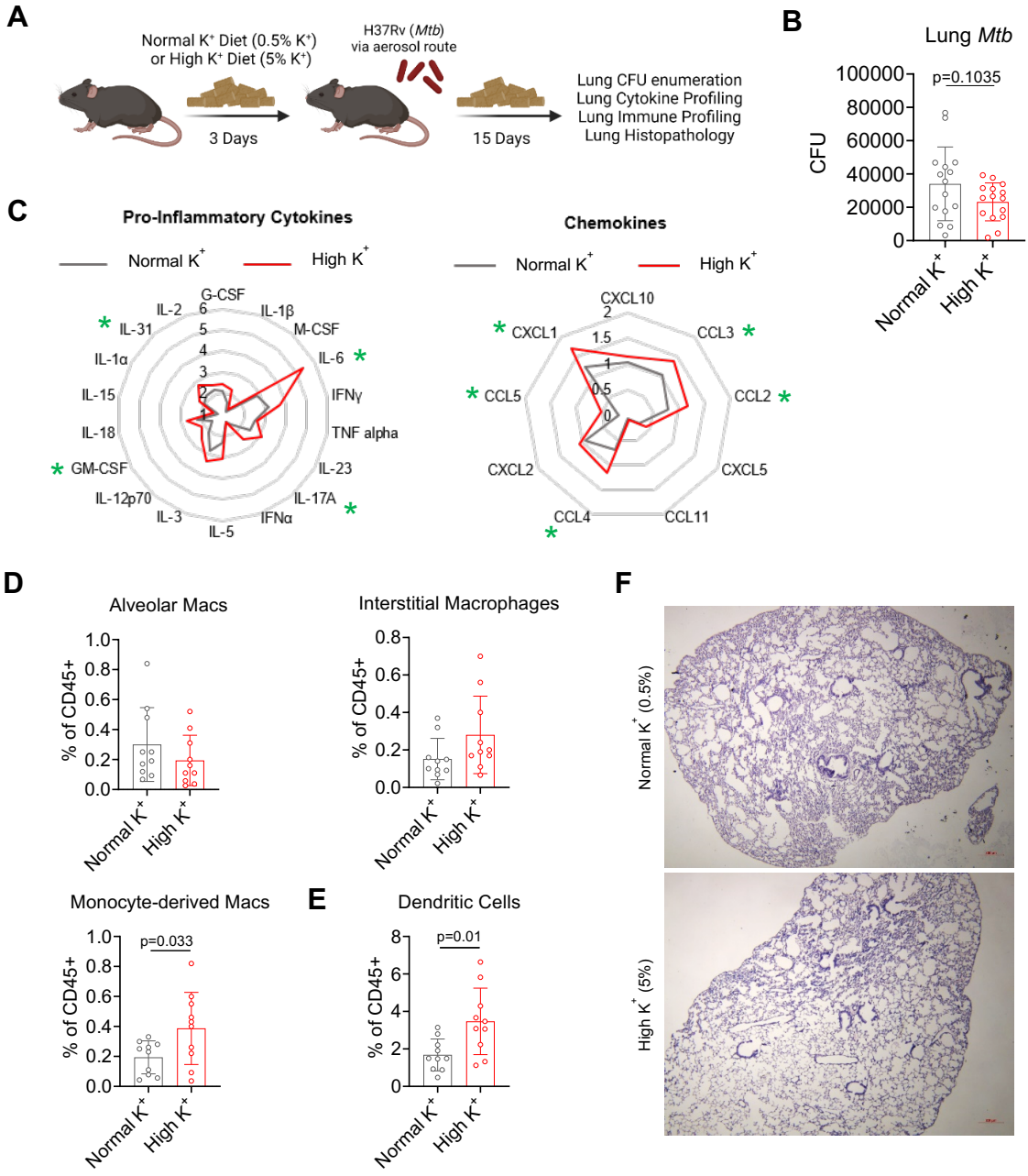

Figure 40. Administering high K^+ diet to *Mtb*-infected mice enhances inflammatory responses and may restrict *Mtb* burden *in vivo*.
A) Schematic of dietary K^+ experiment in mice, where diet was initiated 3 days prior to aerosol H37Rv *Mtb* infection (200 CFU), followed by 15 days of diet maintenance and sacrifice of animals. **B)** *Mtb* CFU enumeration in lungs of mice maintained on normal or high K^+ diet. **C)** Radar plots of inflammatory cytokine and chemokines detected in lung homogenates. Values represent fold-change of the average of analyte concentration in each group compared to that of uninfected, untreated mice (Grey – Normal K^+ diet; Red – High K^+ diet). Green (*) represent analytes that were significantly increased in high K^+ diet-fed mice, Unpaired *t*-test. **D)** Lung macrophage and **E)** dendritic cell populations at 15 d.p.i represented as a percentage of $CD45^+$ cells. In **B** and **D**, each dot represents n=1 mice. **F)** Representative H&E-stained lung tissue sections from *Mtb*-infected mice maintained on normal or high K^+ at 15 d.p.i. Images were acquired at 40X. Data in **B**-**D** were analyzed by Unpaired *t*-test. Data are represented as Mean ± SD. *In vivo Mtb*-infection experiments were conducted in collaboration with Priya Sharma, Dr Dhiraj Kumar Lab, ICGEB, New Delhi.

Multi-analyte quantification in lung homogenates showed that mice maintained on high K^+ diet had elevated pro-inflammatory cytokines and chemokines in the lungs (Fig 40C). Importantly, we found significant increase in IL-6 in mice maintained on high K^+ diet, which has been shown to be required for protective innate immune responses in mice infected with *Mtb* [517]. IL-31, GM-CSF and IL-17A, which have been shown to promote immune control of *Mtb* and other bacterial pathogens [518, 519, 520], were also increased in the lungs of mice maintained on high K^+ diet. We also found significant increase in CCL2, CCL3, CCL4 and CCL5, chemokines that contribute to inflammatory $Ly6C^{hi}$ monocyte recruitment to the tissues [104]. Since infiltration of myeloid cells expressing inflammatory cytokines and chemokines into the tissues can dictate formation of TB granuloma and regulate disease outcome [521, 522], we surveyed the myeloid immune populations in the lungs. Lung cells from high K^+ diet treated *Mtb*-infected mice demonstrated increased IMs and MCs (Fig 40D). Indeed, IMs have been depicted as host-restrictive macrophages in *Mtb*-infected mice [492]. We also noticed an increase in $CD11c^+MHC\text{-}II^+$ DCs in the lung of high K^+ diet-exposed *Mtb*-infected mice (Fig 40E), which may suggest an effect on adaptive immune activation. Histopathological evaluation of the lungs, however, did not demonstrate any effect of high K^+ diet on lung pathology (Fig 40F). This could be because mice were sacrificed at 15 d.p.i, an infection timepoint at which TB lung pathology is generally not developed [471].

Taken together, the *in vivo* experiments suggest that increasing systemic K^+ levels appear to bolster control of mycobacterial growth (observed in zebrafish) and may initiate an early recruitment of restrictive phagocytes by the production of heightened pro-inflammatory mediators (observed in mice).

5.11 Summary of Chapter 5

Necrotic granulomas are characteristic of chronic pulmonary TB disease and allow *Mtb* to exit from its dormancy, likewise the bacteria can become transmissible in the airways [523]. When necrosis begins to happen, infected cells undergo cellular rupture, releasing *Mtb* and intracellular contents in the surrounding. In this chapter, we evaluated if the necrotic lesion microenvironment contained high $[K^+]_e$ resulting from released intracellular K^+, and if a milieu of high $[K^+]_e$ could affect the property of immune cells in their ability to restrict mycobacterial growth.

Applying a zebrafish model of *Mm* infection, we showed that necrotic granulomas contained high $[K^+]_e$, which was not observed in non-necrotic granulomas formed during infection with ΔESX-1 *Mm* (Fig 30A). Similarly, hepatic granulomas formed in BCG-infected IFNγ$^{-/-}$ mice harbored elevated $[K^+]_e$ (Fig 30D). This demonstrated that necrosis in mycobacterial granulomas could result in a high $[K^+]_e$ microenvironment.

We then wanted to understand the mechanistic effect of high $[K^+]_e$ on infected immune (myeloid) cells. We found that high $[K^+]_e$ aided monocytes and macrophages in restricting *Mtb*/BCG growth via autophagy induction that was mediated by Akt-mTOR signaling (Fig 31, 32). Transcriptomic and epigenetic analysis subsequently indicated that high $[K^+]_e$ elicited an antioxidant response in monocytes, suggesting the involvement of ROS generation (Fig 33, 37).

Specifically, we illustrate that high $[K^+]_e$ led to an influx of K^+ ions into the cell which also permeated the mitochondria and impeded metabolic processes that relied on the maintenance of electrochemical gradients (Fig 35, 36). Such mitochondrial perturbation correlated with mROS generation, which was partially necessary for restricting mycobacterial growth via autophagy and possibly mitophagy (Fig 35, 36). Additionally, while it may be practically difficult to accomplish, heightening systemic K^+ may have varying effects on mycobacterial control and the inflammatory response during infection (Fig 39, 40). A summary of the elucidated K^+ induced mechanism is provided in Figure 41.

This study highlights the importance of understanding the necrotic granuloma niche as an environment which exists at the interface of pathology and transmission of infective bacteria. While K^+ is the most abundant intracellular cation, the release of other intracellular contents during necrosis can have other wide-ranging effects, which remain to be investigated. Nonetheless, we demonstrate that a high $[K^+]_e$ milieu can lead to mitochondrial disruption, ROS and autophagy induction which could aid in limiting mycobacterial growth.

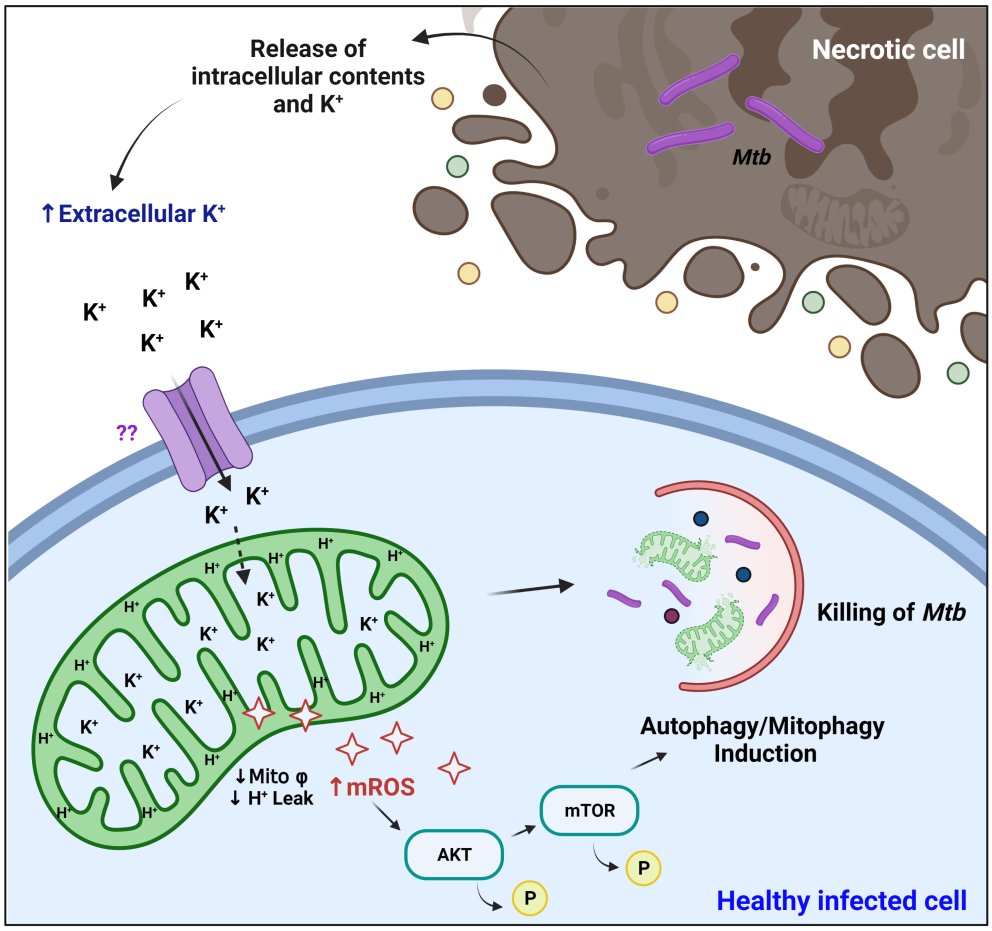

Figure 41. Model of autophagy-mediated mycobacterial restriction resulting from necrotic release of high $[K^+]_e$ into the microenvironment.

Chapter 6: Discussion and Future Directions

Mtb has co-evolved with the host immune system, acquiring a remarkable ability to circumvent immunity and modulate host factors for its own survival [524]. Moreover, the immune response to *Mtb* infection is exceedingly complex, and can be easily modulated by changes in the microenvironment. Ions are an integral component of the host microenvironment, and their transport is controlled by ion channels and transporters. Among these ions, K^+ is the major intracellular ion and plays an important function as a second messenger to regulate intracellular signalling pathways, thus modulating innate and adaptive immunity [525, 526]. In the present study, we examined two potassium-related events, which were hypothesized to impact the way immune cells responded to *in vitro* and *in vivo* mycobacterial infection.

6.1. KCNJ15 in the host response to mycobacterial infection

Our group's histone acetylome-wide association study (HAWAS) discovered that H3K27ac peaks in peripheral blood monocytes from active TB patients (ATB) were enriched near *KCNJ15*, a gene coding for an inwardly rectifying K^+ channel Kir4.2 [211]. This enrichment was correlated with upregulation of *KCNJ15* mRNA in blood monocytes from ATB patients [211]. Since upregulation of a gene upon infection can have either host-protective or host-pathologic effects, in Chapter 3, we aimed to characterize the role of *KCNJ15* in monocytes response to mycobacterial infection.

In *in vitro* experiments, we found that *KCNJ15* induction in monocytes and macrophages was TLR2-mediated (Fig 11F, G) and that *KCNJ15*/Kir4.2 can decorate lysosomal membrane and also can sense pH (Fig 14). We found Kir4.2-mediated cell surface inward currents increased with reduced intracellular pH, which is contrary to the existing literature on Kir4.2 [381]. This unexpected result may be due to different buffering and acidification conditions used during the electrophysiological experiments, as well as the nature of the model systems, such as the usage of Kir4.2-expressing monocytes by us and Kir4.2-expressing *Xenopus* oocytes in said literature [381]. Kir4.2 was also found to be sensitive to extracellular pH, as inward currents also increased with acidification. This finding was unexpected as majority of the literature on K^+ channels have only described intracellular pH sensitivity. Additionally, pH-sensing amino acid residues of Kir4.2 exist on the cytoplasm-facing N and C-termini. Nonetheless, we can conject that the pH-sensitivity of Kir4.2 could act as a feedback mechanism as it provides K^+ counter-ion for the function of H^+ transporting ATPases (Fig 42). Specifically, Kir4.2 might pump K^+ out of the lysosome as H^+ are transported into the lysosome, and as intraluminal H^+ increases, K^+ current also increases to provide sufficient ion counterbalance in the lysosome. Indeed, in the case of parietal cell acid secretion, Kir4.2 was found to co-localize with H^+/K^+ ATPase at the apical membrane, making channel responses to slight local pH changes more likely [262]. Importantly, acidification of the lysosome is crucial to pathogen killing, and can be subverted by pathogens

such as *Mtb* [187]. Overall, our data suggest that Kir4.2 may play a role in lysosome-mediated bacterial killing. However, further work should include investigating endolysosomal acidification itself, and how that might be regulated by Kir4.2 to benefit host.

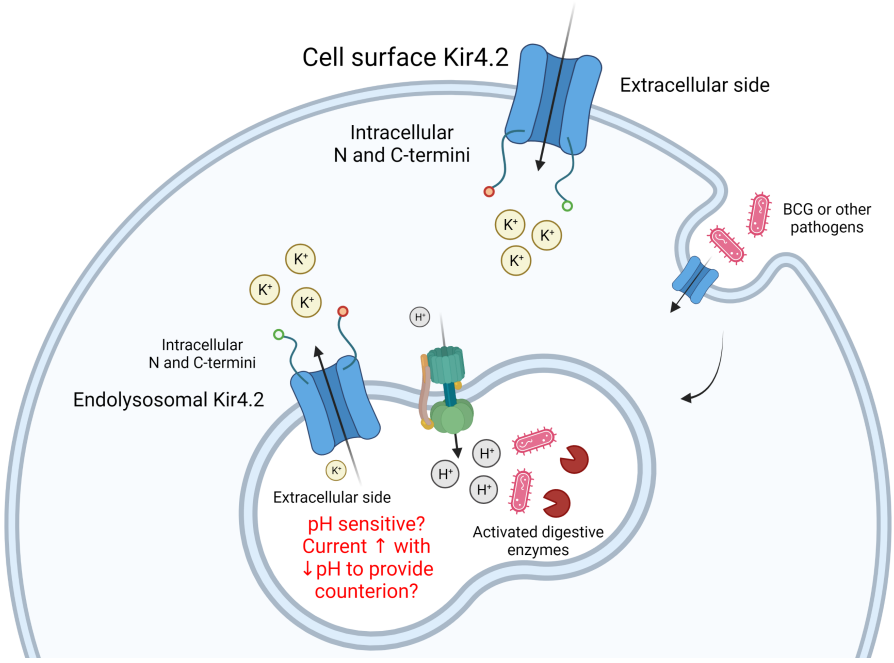

Figure 42. Hypothesized orientation and function of endolysosomal Kir4.2 in pathogen killing by providing counterion for endolysosomal acidification.

We performed gain and loss-of-function experiments to assess the impact of *KCNJ15*/Kir4.2 on mycobacterial growth in human monocytes. For this, we utilized primary monocytes and THP-1 cell line overexpressing Kir4.2 protein or THP-1 carrying heterozygous knockout of *KCNJ15* generated using CRISPR/Cas9 technology. We found that *KCNJ15*^{OE} THP-1 cells had an effect on restricting *Mtb*/BCG growth, although the opposite was not observed in THP-1 *KCNJ15*^{KO} (Fig 15). The low endogenous expression of *KCNJ15* in wild-type THP-1 could explain why we did not see a defect in BCG growth in THP-1 *KCNJ15*^{KO} cells. We also saw that *KCNJ15* expression in THP-1 monocytes was associated with inflammasome activation and secretion of IL-1β in response to BCG infection and TLR agonist stimulation (Fig 16). Likewise, *KCNJ15* expression corresponded with apoptosis-related gene signatures, increased apoptosis induction and APAF-1 protein expression (Table 9, Fig 17). Indeed, enhancing apoptosis have been shown to be an important anti-bacterial mechanism especially in the context of persistent intracellular pathogens such as mycobacteria [333].

The relationship between inflammasome and apoptosis induction and how both processes seem to be modulated by Kir4.2 is certainly interesting. K^+ efflux, or rather, a drop in intracellular K^+

is known to precipitate inflammasome activation and cytokine secretion [527]. APAF-1 is a scaffold protein central to apoptosome formation and downstream effector caspase activation. Curiously, a pre-requisite of a reduction in intracellular K^+ has also been implicated in apoptosome formation [331, 528]. This is particularly interesting as the apoptosome and inflammasome complexes are both caspase-activating scaffold structures which seem to be regulated by intracellular K^+. Unfortunately, while some groups have discovered other K^+ channels which modulate inflammasome activation [237, 300], still little is known about the specific molecular mechanism behind the pre-requisite of K^+ efflux. Nonetheless, as an active K^+ channel, Kir4.2 may indeed play a role in regulating both inflammasome and apoptosis induction at steady state and in the context of mycobacterial infection. To this end, much more study is needed in understanding the electrophysiology of K^+-mediated inflammasome and apoptosis activation during gain and loss of Kir4.2.

What remains unverified is the direction of K^+ flow orchestrated by the Kir4.2 channel during infection or TLR agonist stimulation. While Kir4.2 is a channel that has an electrophysiological current-voltage profile which demonstrates inward current (influx) at more negative membrane voltages (its inwardly-rectifying property) [239], they still carry outward current at higher membrane voltages, which may or may not be the case during the *in vitro/in vivo* infection process or TLR stimulation by agonists. In fact, expression of Kir2.1 (*KCNJ2*) has been associated with maintaining negative membrane potential during LPS treatment of macrophages, meaning it orchestrates K^+ efflux under stimulation [529]. Furthermore, *KCNJ15* expression has so far correlated with enhanced inflammasome and apoptosis induction in this study, both of which are presumably activated by K^+ efflux. Hence, it is possible and maybe even likely that Kir4.2 facilitates efflux under our study conditions. Confirming this would also require extensive electrophysiological study.

In Chapter 4, we developed a whole-body *Kcnj15*^{KO} mouse model to study the role of the channel during airway mycobacterial infection with BCG. Here, we identified that *Kcnj15*^{KO} mice lungs harbored fewer BCG and Ly6C^{hi} monocytes at 14 days post-infection (Fig 19A, 20E). Profiling of cytokines/chemokines in lung homogenate found increased pro-inflammatory cytokine and chemokines in WT BCG-infected mice, that was diminished in *Kcnj15*^{KO} mice (Fig 22), suggesting a pro-inflammatory phenotype of Kir4.2. Reduced lung Ly6C^{hi} monocytes in uninfected and infected *Kcnj15*^{KO} mice (Fig 20E) could be attributed to the possible role of Kir4.2 in cell migration. Of note, Kir4.2 has been implicated in directedness during galvanotaxis of epithelial cells and integrin-VCAM1-mediated transendothelial migration [271, 272, 273]. Moreover, transcriptomic analysis of human blood cells ascribed *KCNJ15* expression to only monocytes and neutrophils [261], which are patrolling innate cells and actively mobilize during infection. Since

monocytes were found to upregulate Kir4.2 during mycobacterial infection, its purpose could be to promote migration from the bone marrow into the site of infection. This might explain the reduction of Ly6C^{hi} monocytes in the blood of uninfected *Kcnj15*^{KO} mice (Fig 23B). Based on this observation, we expected monocytes to accumulate in bone marrow, which was not observed (Fig 25B). It is possible that *Kcnj15*^{KO} monocytes were deficient in transendothelial migration and thus were stuck in the vasculature, which might not have been accurately detected by profiling blood cells.

In conjunction with reduced lung Ly6C^{hi} monocytes, AMs, MCs and DC populations were expanded in BCG-infected *Kcnj15*^{KO} mice (Fig 20B, C). We hypothesize that this expansion was due to the enhanced differentiation of infiltrating lung Ly6C^{hi} monocytes in *Kcnj15*^{KO} mice. Indeed, the reduction of Ly6C^{hi} monocytes are statistically correlated to the expansion of these macrophage populations (Fig 27A), but further experiments are needed to establish a causal relationship. To truly link the expansion of the macrophage and DC populations in *Kcnj15*^{KO} mice with the influx and differentiation of Ly6C^{hi} monocytes, adoptive transfer experiments could be carried out. Transplanting WT or *Kcnj15*^{KO} bone marrow monocytes into CD45.1 WT mice, infecting them with BCG and assaying for CD45.2 macrophage and DCs would inform us if monocyte expression of *Kcnj15* dictates some form of monocyte pro-differentiation property. Furthermore, transplanting CD45.1 WT bone marrow monocytes into BCG-infected CD45.2 WT or *Kcnj15*^{KO} mice would shed light on whether the loss of *Kcnj15* by other cell types influences monocyte differentiation through other means such as modulating cytokine production.

The present study is mostly limited to the investigation of myeloid arm of the lung immune response, hence insight into how *Kcnj15* may regulate adaptive response is lacking. This is important since we observed increased DC populations, which are professional antigen-presenting cells. Furthermore, since we used whole-body the *Kcnj15*^{KO} mouse model, effects of the loss of channel in specific cell types can be masked by that of others, further complicating the analysis. A detailed survey into the expression of *Kcnj15* in each immune cell type during infection is necessary to distinguish the changes in immune responses that are directly mediated by the loss of channel itself, from those which are indirect by-stander effects caused by changes in cytokine or chemokine secretion or other cellular signals. Here, generation of *Kcnj15*^{KO} bone-marrow chimeras would allow us to limit our scope of investigation to hematopoietic immune populations.

Additionally, it is important to consider that Chapter 4 employs BCG-infected mice as a model for TB. This was due to our lack of access to ABSL3 since March 2020 due to the COVID-19 pandemic. Infection with BCG invariably produces a weaker immune response but is more effectively cleared than *Mtb* [530]. One of the key differences between *Mtb* and BCG strains is the

absence of the RD-1 region in BCG, which encodes antigens ESAT6 and CFP-10 that are normally secreted by the ESX-1 secretion system [531]. ESAT6 can potently activate the NLRP3 inflammasome and modulate innate apoptosis in macrophages, and is also key for phagosome escape [179, 532, 533] and both proteins contribute to the immunogenicity of *Mtb* [531]. Since translocation of *Mtb*-carrying AMs into the lung interstitium is ESX-1 dependent [97], we expect majority of BCG-infected AMs to be retained in the airway at early timepoints. Indeed, airway BCG administration found most live bacteria to reside in airway AMs after 14 days, with some dissemination to IMs after 24 days [33]. Furthermore, granuloma formation without necrosis occurs during BCG infection and is associated with bacterial clearance, which is markedly attenuated compared to the necrotic, caseous pathology and uncontrolled bacterial growth in chronic virulent *Mtb* infection [530, 534].

Another point to consider, is that the intra-tracheal BCG infection model we employed is also a suitable mucosal vaccination model [33]. Hence, the immune population changes we found could also be considered in this light, thus demonstrating that absence of *Kcnj15* might have a beneficial role in mucosal vaccination response. Our observation of DC expansion in BCG-infected *Kcnj15*^{KO} mice (Fig 20C) can have implications on the transport of live BCG to lymph nodes and hence T cell stimulation. This efficiency of bacterial and DC trafficking, and antigen presentation needs to be properly studied in the draining lymph nodes over a series of timepoints, as well as investigating differences in activation of the T cell and memory responses.

Furthermore, AMs from BCG-infected *Kcnj15*^{KO} mice showed a gene signature which pointed towards cholesterol accumulation (Fig 28). Interestingly, cholesterol-rich lipid rafts are pivotal for MHC-II antigen presentation [535, 536, 537]. However, AMs are not known to be motile and migrate to lymph nodes. It would be interesting to investigate if migratory cells like monocytes and DCs also show *Kcnj15*^{KO}–mediated cholesterol accumulation and antigen presentation enhancement. Indeed, further experimentation is required to test if *Kcnj15*^{KO} AMs or other cells do accumulate cholesterol and study what effect cholesterol may have on host restriction, antigen presentation, and mycobacterial survival. Importantly, a study on mucosal BCG vaccination demonstrated superior pre-activation of AMs which conferred long-term protection from *Mtb*, compared to subcutaneous vaccination [33].

Expression of *KCNJ15* appeared to be restrictive to mycobacterial infection in our *in vitro* studies in Chapter 3, however experiments with our knockout mouse model in Chapter 4 demonstrate that *KCNJ15* may conversely be permissive to mycobacterial growth in the lungs. As these experimental models are vastly different, this apparent contradiction could be attributed to each model's relevance to a different part of the spectrum of TB disease presentation.

Indeed, the progression of TB from the point of initial infection to chronic disease and transmission is dynamic and involves many changes at the bacterium, immune and tissue pathology levels (Fig 43). Patients are classified along the infection spectrum, some being able to clear initial infection effectively, while others harbour latent infection and may subsequently progress toward active disease, and each stage can be characterized by features such as bacterial burden, inflammatory and pathological states [1].

The *in vivo* intra-tracheal infection model is likely reminiscent of an acute infection where the innate response takes primary control, and leads to eventual clearance of BCG from the lung, and thus would not constitute a chronic "active" infection. On top of that, BCG infection is much less pro-inflammatory and causes insignificant tissue pathology compared to *Mtb* infection. However of course, our infection procedure administers over a million BCG CFU to mice, which is much more than the typical inoculum for a human infection . Conversely, our *in vitro* monocyte infection models are much more acute (24-72 hour timepoints) but they are infected at MOI 5:1 and are quite significantly activated to produce pro-inflammatory mediators. Furthermore, cell death becomes more and more significant as infection duration is prolonged. In this sense, the *in vitro* infection model may emulate a subclinical or active TB infection, where infection is not easily resolved and leads to inflammation and significant cell damage. These attributes, in addition to the consideration that a systemic infection is much more complex than an *in vitro* infection as many different cell types are at play, may account for the contradictory conclusions on *KCNJ15*'s role in controlling intracellular infection. Furthermore, this suggests that altering K^+ homeostasis at different stages of TB disease may have varying effects. Certainly, inflammatory states may differ and a different set of pivotal immune players could be responsible for managing the infection across the TB spectrum.

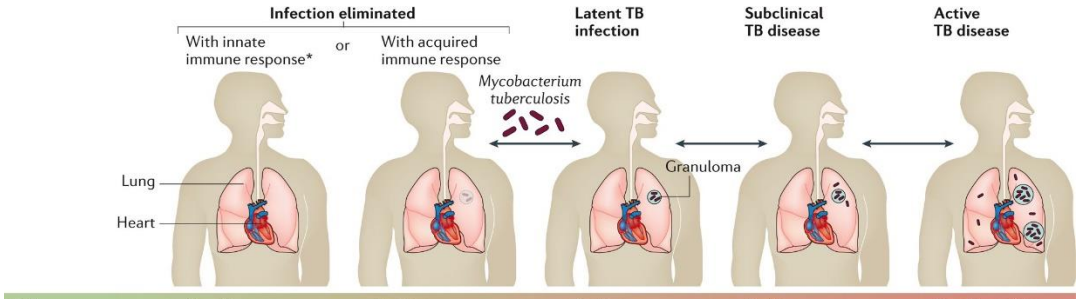

TST	Negative	Positive	Positive	Positive	Usually positive
IGRA	Negative	Positive	Positive	Positive	Usually positive
Culture	Negative	Negative	Negative	Intermittently positive	Positive
Sputum smear	Negative	Negative	Negative	Usually negative	Positive or negative
Infectious	No	No	No	Sporadically	Yes
Symptoms	None	None	None	Mild or none	Mild to severe
Preferred treatment	None	None	Preventive therapy	Multidrug therapy	Multidrug therapy

Nature Reviews | Disease Primers

Figure 43. The spectrum of TB disease, by Pai et al (2016) [1].

Taking the study as a whole, it appears that the loss of *KCNJ15* provides an anti-inflammatory benefit, expands populations capable of controlling infection and engaging the adaptive response, while limiting inflammatory monocyte presence and concurrently reduces lung burden during *in vivo* acute BCG infection. Since there are no specific inhibitors of Kir4.2 currently available, compound screening and *in-silico* design can be conducted for discovery of a Kir4.2 blocker. An anti-inflammatory K^+ channel blocker can have broad applications in inflammation-mediated diseases and pathology. For example, single-cell transcriptomic analyses of lungs of patients with idiopathic fibrosis have shown that AEC-II highly express *KCNJ15* [466]. The AEC-II cells can secrete inflammatory cytokines and chemokines upon infection or injury, which induces immune infiltration that can contribute to lung inflammation and pathology [167, 171]. Blockade of Kir4.2 could thus ameliorate inflammation during fibrosis and chronic infection, limiting lung tissue destruction and improving patient outcomes. Since the administration of Kir4.2 blockers as a treatment would usually be systemic, thus what we gleaned from the whole-body *Kcnj15* knockout mouse model would be very useful in understanding it effects.

6.2. Extracellular K^+ in the necrotic granuloma and its effects on mycobacterial control

Understanding the necrotic granuloma niche may pave the way for further deciphering TB immunopathology and potential host-directed therapeutics (HDT). Here, we show that (i) necrotic granulomas of *M. marinum*-infected zebrafish fluoresced strongly with extracellular K^+ indicator, and (ii) hepatic granulomas in BCG-infected IFN$\gamma^{-/-}$ mice demonstrated regions of higher extracellular K^+ ($[K^+]_e$) (Fig 30). Undeniably, more direct information could be gained from

necrotic granulomas from *Mtb*-infected lungs with the availability of scanning mass spectrometry techniques or better and more stable *in vivo* K^+ indicator dyes. Nonetheless, high $[K^+]_e$ in mycobacterial granulomas can significantly impact surrounding immune cells as it invariably leads to K^+ influx into the cell, which can perturb K^+ homeostasis and cellular function [526].

In our study, we demonstrated that high $[K^+]_e$ leads to uptake of K^+ ions, conferring enhanced control of intracellular mycobacterial burden in monocytes and macrophages (Fig 31). This process is mediated in part by autophagy stemming from inhibition of the Akt-mTOR signalling pathway (Fig 32). Studies on high extracellular NaCl have similarly demonstrated an increase in autophagy flux that culminated in improved control of *E. coli* in bone-marrow derived macrophages [538]. This, and our study, highlight that local ion fluxes can significantly affect immune cell anti-microbial function. However, intracellular Na^+ concentrations exist typically at sub-20mM levels, making its contribution to the extracellular milieu during necrosis not quite as significant as K^+ ions, which is the most abundant intracellular cation (130-150 mM).

Transcriptomic and epigenetic analyses indicated that that oxidative stress was an apparent consequence of exposure to high $[K^+]_e$ in human monocytes (Fig 33, 37). Indeed, necrotic granulomas were observed to be in a state of oxidative stress [359]. Oxidative stress can keenly induce autophagy, through various pathways such as via the AMPK-mTOR, NRF2-p62 and HIF1α-BNIP3-NIX axes [539, 540]. Naturally, ROS production on its own can be bactericidal against intracellular pathogens, thus oxidative pressure on intracellular bacteria in addition to heightened autophagy may be an effective sterilizing combination for innate cells in restricting pathogen growth. However, ROS may also contribute to worsening of granuloma pathology [359]. Whether necrosis and increased $[K^+]_e$ may lead to greater ROS accumulation that perpetuates granuloma pathology is unclear. Additionally, *Mtb* can become dormant in the host niche and establish long-term latency, making them difficult to eradicate by antibiotic regimens [541]. The complex structure of the granuloma alone can prove a formidable diffusion barrier to antibiotic compounds [542]. Increased $[K^+]_e$ may raise ROS levels and activate autophagy in bystander macrophages harboring non-replicative *Mtb*, which may aid in clearance of these intracellular persister bacilli. Admittedly, as production of mROS was found to occur as early as 1h post high $[K^+]_e$ administration (Fig 35A), data from both transcriptomic and epigenetic analyses would have been likely more indicative had samples been collected at an earlier timepoint rather than at 24h. Despite this, we showed that quenching ROS abolishes high $[K^+]_e$ induced autophagy and bacterial growth (Fig 38). In our experiments the role of HIF1α in high $[K^+]_e$-mediated autophagy induction remains unclear. While increased extracellular NaCl was demonstrated to induce autophagy in a HIF1α-dependent manner [538], our experiments did not determine that HIF1α was crucial for $[K^+]_e$-mediated infection control (Fig 34).

Increased $[K^+]_e$ is also expected to limit the inflammasome response and the release of pro-inflammatory IL-1β and IL-18 as K^+ efflux is stifled [527]. In this way extracellular K^+ release may provide an anti-inflammatory balance against the induction of strong inflammasome responses in the granuloma, initiated by the release of intracellular DAMPs by necrosis such as cellular ATP. At the same time, heightening microbicidal function may slow down the progression of granuloma pathology in the long term.

The immune granuloma, while primarily comprised of macrophages, consists also of other cell types such as lymphocytes in the periphery. Eil *et al.* has prior described how high $[K^+]_e$ epigenetically alters tumor-infiltrating $CD8^+$ T cells into a state of improved effector function and tumor control [475]. It is thus conceivable that T cells residing in mycobacterial granulomas may similarly be primed to better control the infection, and that any cell type within the granuloma can be affected by high $[K^+]_e$ resulting in varying outcomes. Certainly, our findings are not limited to the mycobacterial granulomas but may be relevant to other granulomatous diseases or necrotizing conditions such as diabetic ulcers or necrotizing fasciitis.

We also show that increasing systemic K^+ may enhance the control of acute mycobacterial infection and increase pro-inflammatory immune recruitment (Fig 39, 40). The elevation of pro-inflammatory chemokines in the lung of mice maintained on high K^+ diet might have elicited an increased influx of mononuclear cells that allowed increased differentiation into monocyte-derived macrophages (Fig 40). Infiltrating monocytes are efficient anti-bacterial phagocytes, which can differentiate into macrophages at the site of infection, thus benefiting pathogen control [543, 544]. Whether ROS is induced in mycobacterium-infected zebrafish or mice during increased systemic K^+, and whether it is vital for restriction of mycobacterial growth remains to be investigated. Administering high dietary K^+ may not, however, be a feasible therapeutic option as K^+ homeostasis in the blood is tightly regulated by renal function [545]. Furthermore, majority of K^+ intake is expected to be excreted quickly, as hyperkalemia can pose serious risks especially to cardiac function [546]. In our experiments, we have not been able to effectively evaluate if lung interstitial fluid K^+ was increased in mice given high K^+ diet.

In conclusion, we make a case for the presence of high $[K^+]_e$ in necrotic mycobacterial granulomas, similar to what has been observed in necrotic solid tumors [304], and showed that high $[K^+]_e$ environments can strongly impact monocytes/macrophages in their ability to control mycobacterial growth through the induction of ROS-mediated autophagy.

Taken together, this study highlights that potassium homeostasis can play a vital role in regulating immune cell function during mycobacterial infection. K^+ is often overlooked compared to other ions and often thought of as rather inert. This study, therefore, demonstrates that the modulation

of K^+ homeostasis by a Kir channel, Kir4.2, and local cellular necrosis events can impact the immune response to infection at various levels, which may inform future HDT development.

References

1. Pai, M. *et al.* Tuberculosis. *Nature reviews Disease primers* **2**, 1-23 (2016).

2. Global Tuberculosis Report 2021. *World Health Organization* (2021).

3. Bagcchi, S. Dismal global tuberculosis situation due to COVID-19. *The Lancet Infectious Diseases* **21**, 1636 (2021).

4. Houben, R.M. & Dodd, P.J. The Global Burden of Latent Tuberculosis Infection: A Re-estimation Using Mathematical Modelling. *PLoS Med* **13**, e1002152 (2016).

5. Global Tuberculosis Report 2018. (2018).

6. Goenka, A., Casulli, J. & Hussell, T. Mycobacterium tuberculosis joyrides alveolar macrophages into the pulmonary interstitium. *Cell host & microbe* **24**, 331-333 (2018).

7. Orme, I.M. & Basaraba, R.J. The formation of the granuloma in tuberculosis infection. Seminars in immunology; 2014: Elsevier; 2014. p. 601-609.

8. Russell, D.G., Barry, C.E. & Flynn, J.L. Tuberculosis: What We Don't Know Can, and Does, Hurt Us. *Science* **328**, 852-856 (2010).

9. Russell, D.G. Who puts the tubercle in tuberculosis? *Nature Reviews Microbiology* **5**, 39-47 (2007).

10. Flynn, J.L. & Chan, J. What's good for the host is good for the bug. *Trends in microbiology* **13**, 98-102 (2005).

11. Peddireddy, V., Doddam, S.N. & Ahmed, N. Mycobacterial Dormancy Systems and Host Responses in Tuberculosis. *Frontiers in Immunology* **8** (2017).

12. Meghji, J. *et al.* Patient outcomes associated with post-tuberculosis lung damage in Malawi: a prospective cohort study. *Thorax* **75**, 269 (2020).

13. Shuldiner, J., Leventhal, A., Chemtob, D. & Mor, Z. Mortality after anti-tuberculosis treatment completion: results of long-term follow-up. *The International Journal of Tuberculosis and Lung Disease* **20**, 43-48 (2016).

14. Ravimohan, S., Kornfeld, H., Weissman, D. & Bisson, G.P. Tuberculosis and lung damage: from epidemiology to pathophysiology. *European Respiratory Review* **27** (2018).

15. Organization, W.H. *WHO consolidated guidelines on drug-resistant tuberculosis treatment*. World Health Organization, 2019.

16. Cox, E. & Laessig, K. FDA Approval of Bedaquiline — The Benefit–Risk Balance for Drug-Resistant Tuberculosis. *New England Journal of Medicine* **371**, 689-691 (2014).

17. Sarathy, J.P., Gruber, G. & Dick, T. Re-Understanding the Mechanisms of Action of the Anti-Mycobacterial Drug Bedaquiline. *Antibiotics* **8**, 261 (2019).

18. Andries, K. *et al.* A diarylquinoline drug active on the ATP synthase of Mycobacterium tuberculosis. *Science* **307**, 223-227 (2005).

19. Koul, A. *et al.* Delayed bactericidal response of Mycobacterium tuberculosis to bedaquiline involves remodelling of bacterial metabolism. *Nat Commun* **5**, 3369 (2014).

20. Blair, H.A. & Scott, L.J. Delamanid: A Review of Its Use in Patients with Multidrug-Resistant Tuberculosis. *Drugs* **75**, 91-100 (2015).

21. Liu, Y. *et al.* Delamanid: From discovery to its use for pulmonary multidrug-resistant tuberculosis (MDR-TB). *Tuberculosis* **111**, 20-30 (2018).

22. Keam, S.J. Pretomanid: First Approval. *Drugs* **79**, 1797-1803 (2019).

23. Organization, W.H. Rapid communication: key changes to the treatment of drug-resistant tuberculosis: World Health Organization; 2022.

24. Nguyen, T.V.A. *et al.* Bedaquiline Resistance: Its Emergence, Mechanism, and Prevention. *Clinical Infectious Diseases* **66**, 1625-1630 (2017).

25. Veziris, N. *et al.* Rapid emergence of Mycobacterium tuberculosis bedaquiline resistance: lessons to avoid repeating past errors. *European Respiratory Journal* **49**, 1601719 (2017).

26. Ghodousi, A. *et al.* Acquisition of Cross-Resistance to Bedaquiline and Clofazimine following Treatment for Tuberculosis in Pakistan. *Antimicrobial Agents and Chemotherapy* **63**, e00915-00919 (2019).

27. Luca, S. & Mihaescu, T. History of BCG Vaccine. *Maedica (Bucur)* **8**, 53-58 (2013).

28. Mangtani, P. *et al.* Protection by BCG Vaccine Against Tuberculosis: A Systematic Review of Randomized Controlled Trials. *Clinical Infectious Diseases* **58**, 470-480 (2013).

29. Ryan, A.A. *et al.* Antigen Load Governs the Differential Priming of CD8 T Cells in Response to the Bacille Calmette Guérin Vaccine or Mycobacterium tuberculosis Infection. *The Journal of Immunology* **182**, 7172-7177 (2009).

30. Qu, M., Zhou, X. & Li, H. BCG vaccination strategies against tuberculosis: updates and perspectives. *Human Vaccines & Immunotherapeutics* **17**, 5284-5295 (2021).

31. Hoft, D.F. *et al.* PO and ID BCG vaccination in humans induce distinct mucosal and systemic immune responses and CD4+ T cell transcriptomal molecular signatures. *Mucosal Immunology* **11**, 486-495 (2018).

32. Darrah, P.A. *et al.* Prevention of tuberculosis in macaques after intravenous BCG immunization. *Nature* **577**, 95-102 (2020).

33. Mata, E. *et al.* Pulmonary BCG induces lung-resident macrophage activation and confers long-term protection against tuberculosis. *Science Immunology* **6**, eabc2934 (2021).

34. Cirovic, B. *et al.* BCG Vaccination in Humans Elicits Trained Immunity via the Hematopoietic Progenitor Compartment. *Cell Host Microbe* **28**, 322-334.e325 (2020).

35. Bull, N.C. *et al.* Enhanced protection conferred by mucosal BCG vaccination associates with presence of antigen-specific lung tissue-resident PD-1(+) KLRG1(-) CD4(+) T cells. *Mucosal Immunol* **12**, 555-564 (2019).

36. Kaufmann, S.H.E. Vaccination Against Tuberculosis: Revamping BCG by Molecular Genetics Guided by Immunology. *Frontiers in Immunology* **11** (2020).

37. Kaushal, D. *et al.* Mucosal vaccination with attenuated Mycobacterium tuberculosis induces strong central memory responses and protects against tuberculosis. *Nature Communications* **6**, 8533 (2015).

38. Tameris, M. *et al.* The candidate TB vaccine, MVA85A, induces highly durable Th1 responses. *PLoS One* **9**, e87340 (2014).

39. Leroux-Roels, I. *et al.* Improved CD4+ T cell responses to Mycobacterium tuberculosis in PPD-negative adults by M72/AS01 as compared to the M72/AS02 and Mtb72F/AS02 tuberculosis candidate vaccine formulations: A randomized trial. *Vaccine* **31**, 2196-2206 (2013).

40. Wallis, R.S. & Hafner, R. Advancing host-directed therapy for tuberculosis. *Nature Reviews Immunology* **15**, 255-263 (2015).

41. Sachan, M. *et al.* Opportunities and Challenges for Host-Directed Therapies in Tuberculosis. *Current Pharmaceutical Design* **22**, 2599-2604 (2016).

42. van der Wel, N. *et al.* M. tuberculosis and M. leprae Translocate from the Phagolysosome to the Cytosol in Myeloid Cells. *Cell* **129**, 1287-1298 (2007).

43. Queval, C.J., Brosch, R. & Simeone, R. The Macrophage: A Disputed Fortress in the Battle against Mycobacterium tuberculosis. *Frontiers in Microbiology* **8** (2017).

44. Young, C., Walzl, G. & Du Plessis, N. Therapeutic host-directed strategies to improve outcome in tuberculosis. *Mucosal immunology* **13**, 190-204 (2020).

45. Cheng, C.Y. *et al.* Host sirtuin 1 regulates mycobacterial immunopathogenesis and represents a therapeutic target against tuberculosis. *Science Immunology* **2**, eaaj1789 (2017).

46. Singhal, A. *et al.* Metformin as adjunct antituberculosis therapy. *Science Translational Medicine* **6**, 263ra159-263ra159 (2014).

47. Paik, S., Kim, J.K., Chung, C. & Jo, E.K. Autophagy: A new strategy for host-directed therapy of tuberculosis. *Virulence* **10**, 448-459 (2019).

48. Zhang, Q. *et al.* Antimycobacterial and Anti-inflammatory Mechanisms of Baicalin via Induced Autophagy in Macrophages Infected with Mycobacterium tuberculosis. *Frontiers in Microbiology* **8** (2017).

49. Sogi, K.M., Lien, K.A., Johnson, J.R., Krogan, N.J. & Stanley, S.A. The Tyrosine Kinase Inhibitor Gefitinib Restricts Mycobacterium tuberculosis Growth through Increased Lysosomal Biogenesis and Modulation of Cytokine Signaling. *ACS Infectious Diseases* **3**, 564-574 (2017).

50. Skerry, C. *et al.* Simvastatin increases the in vivo activity of the first-line tuberculosis regimen. *Journal of Antimicrobial Chemotherapy* **69**, 2453-2457 (2014).

51. Parihar, S.P. *et al.* Statin therapy reduces the mycobacterium tuberculosis burden in human macrophages and in mice by enhancing autophagy and phagosome maturation. *J Infect Dis* **209**, 754-763 (2014).

52. Etna, M.P., Giacomini, E., Severa, M. & Coccia, E.M. Pro- and anti-inflammatory cytokines in tuberculosis: A two-edged sword in TB pathogenesis. *Seminars in Immunology* **26**, 543-551 (2014).

53. Torrado, E. & Cooper, A.M. IL-17 and Th17 cells in tuberculosis. *Cytokine Growth Factor Rev* **21**, 455-462 (2010).

54. Elkington, P.T., Ugarte-Gil, C.A. & Friedland, J.S. Matrix metalloproteinases in tuberculosis. *European Respiratory Journal* **38**, 456-464 (2011).

55. Sheen, P. *et al.* High MMP-9 activity characterises pleural tuberculosis correlating with granuloma formation. *European Respiratory Journal* **33**, 134-141 (2009).

56. Sacks, L.V. & Pendle, S. Factors Related to In-hospital Deaths in Patients With Tuberculosis. *Archives of Internal Medicine* **158**, 1916-1922 (1998).

57. Guler, R. *et al.* Targeting Molecular Inflammatory Pathways in Granuloma as Host-Directed Therapies for Tuberculosis. *Front Immunol* **12**, 733853 (2021).

58. Krug, S., Parveen, S. & Bishai, W.R. Host-Directed Therapies: Modulating Inflammation to Treat Tuberculosis. *Frontiers in Immunology* **12** (2021).

59. Kroesen, V.M. *et al.* Non-Steroidal Anti-inflammatory Drugs As Host-Directed Therapy for Tuberculosis: A Systematic Review. *Frontiers in Immunology* **8** (2017).

60. Wallis, R.S. Corticosteroid Effects on Sputum Culture in Pulmonary Tuberculosis: A Meta-Regression Analysis. *Open Forum Infectious Diseases* **1** (2014).

61. Maiga Mariama, C., Ahidjo Bintou, A., Maiga, M. & Bishai William, R. Roflumilast, a Type 4 Phosphodiesterase Inhibitor, Shows Promising Adjunctive, Host-Directed Therapeutic Activity in a Mouse Model of Tuberculosis. *Antimicrobial Agents and Chemotherapy* **59**, 7888-7890.

62. Dutta, N.K. *et al.* Adjunctive Host-Directed Therapy With Statins Improves Tuberculosis-Related Outcomes in Mice. *The Journal of Infectious Diseases* **221**, 1079-1087 (2019).

63. Kaufmann, S.H.E. *et al.* Neutrophils Play a Protective Nonphagocytic Role in Systemic Mycobacterium tuberculosis Infection of Mice. *Infection and Immunity* **68**, 577-583 (2000).

64. Seiler, P. *et al.* Early granuloma formation after aerosol Mycobacterium tuberculosis infection is regulated by neutrophils via CXCR3-signaling chemokines. *European Journal of Immunology* **33**, 2676-2686 (2003).

65. Yang, C.-T. *et al.* Neutrophils Exert Protection in the Early Tuberculous Granuloma by Oxidative Killing of Mycobacteria Phagocytosed from Infected Macrophages. *Cell Host & Microbe* **12**, 301-312 (2012).

66. Lowe, D.M. *et al.* Neutrophilia independently predicts death in tuberculosis. *European Respiratory Journal* **42**, 1752-1757 (2013).

67. Ndlovu, L.N. *et al.* Increased Neutrophil Count and Decreased Neutrophil CD15 Expression Correlate With TB Disease Severity and Treatment Response Irrespective of HIV Co-infection. *Frontiers in Immunology* **11** (2020).

68. Eum, S.-Y. *et al.* Neutrophils Are the Predominant Infected Phagocytic Cells in the Airways of Patients With Active Pulmonary TB. *Chest* **137**, 122-128 (2010).

69. Ramos-Kichik, V. *et al.* Neutrophil extracellular traps are induced by Mycobacterium tuberculosis. *Tuberculosis* **89**, 29-37 (2009).

70. Papayannopoulos, V. & Zychlinsky, A. NETs: a new strategy for using old weapons. *Trends in Immunology* **30**, 513-521 (2009).

71. Braian, C., Hogea, V. & Stendahl, O. Mycobacterium tuberculosis-Induced Neutrophil Extracellular Traps Activate Human Macrophages. *Journal of Innate Immunity* **5**, 591-602 (2013).

72. Hilda, J.N., Das, S., Tripathy, S.P. & Hanna, L.E. Role of neutrophils in tuberculosis: A bird's eye view. *Innate Immunity* **26**, 240-247 (2019).

73. Steinwede, K. *et al.* Cathepsin G and Neutrophil Elastase Contribute to Lung-Protective Immunity against Mycobacterial Infections in Mice. *The Journal of Immunology* **188**, 4476-4487 (2012).

74. Alvarez-Jiménez, V.D. *et al.* Extracellular Vesicles Released from Mycobacterium tuberculosis-Infected Neutrophils Promote Macrophage Autophagy and Decrease Intracellular Mycobacterial Survival. *Frontiers in Immunology* **9** (2018).

75. La Manna, M.P. *et al.* Mycobacterium tuberculosis Drives Expansion of Low-Density Neutrophils Equipped With Regulatory Activities. *Frontiers in Immunology* **10** (2019).

76. Deng, Y. *et al.* Low-Density Granulocytes Are Elevated in Mycobacterial Infection and Associated with the Severity of Tuberculosis. *PLOS ONE* **11**, e0153567 (2016).

77. Morrissey, S.M. *et al.* A specific low-density neutrophil population correlates with hypercoagulation and disease severity in hospitalized COVID-19 patients. *JCI Insight* **6**, e148435 (2021).

78. Tay, S.H., Celhar, T. & Fairhurst, A.-M. Low-Density Neutrophils in Systemic Lupus Erythematosus. *Arthritis & Rheumatology* **72**, 1587-1595 (2020).

79. Ng, L.G., Ostuni, R. & Hidalgo, A. Heterogeneity of neutrophils. *Nature Reviews Immunology* **19**, 255-265 (2019).

80. van Gisbergen , K.P.J.M., Sanchez-Hernandez , M., Geijtenbeek , T.B.H. & van Kooyk , Y. Neutrophils mediate immune modulation of dendritic cells through glycosylation-dependent interactions between Mac-1 and DC-SIGN. *Journal of Experimental Medicine* **201**, 1281-1292 (2005).

81. Blomgran, R., Desvignes, L., Briken, V. & Ernst, Joel D. Mycobacterium tuberculosis Inhibits Neutrophil Apoptosis, Leading to Delayed Activation of Naive CD4 T cells. *Cell Host & Microbe* **11**, 81-90 (2012).

82. Hedlund, S. *et al.* Dendritic cell activation by sensing Mycobacterium tuberculosis–induced apoptotic neutrophils via DC-SIGN. *Human Immunology* **71**, 535-540 (2010).

83. Blomgran, R. & Ernst, J.D. Lung Neutrophils Facilitate Activation of Naive Antigen-Specific CD4+ T Cells during Mycobacterium tuberculosis Infection. *The Journal of Immunology* **186**, 7110-7119 (2011).

84. Almeida, F.M. *et al.* Hypervirulent Mycobacterium tuberculosis strain triggers necrotic lung pathology associated with enhanced recruitment of neutrophils in resistant C57BL/6 mice. *PLOS ONE* **12**, e0173715 (2017).

85. Gopal, R. *et al.* S100A8/A9 Proteins Mediate Neutrophilic Inflammation and Lung Pathology during Tuberculosis. *American Journal of Respiratory and Critical Care Medicine* **188**, 1137-1146 (2013).

86. Keller, C. *et al.* Genetically Determined Susceptibility to Tuberculosis in Mice Causally Involves Accelerated and Enhanced Recruitment of Granulocytes. *Infection and Immunity* **74**, 4295-4309 (2006).

87. Mishra, B.B. *et al.* Nitric oxide prevents a pathogen-permissive granulocytic inflammation during tuberculosis. *Nature Microbiology* **2**, 17072 (2017).

88. Dallenga, T. & Schaible, U.E. Neutrophils in tuberculosis : first line of defence or booster of disease and targets for host-directed therapy? *Pathogens and Disease* **74** (2016).

89. Muefong, C.N. & Sutherland, J.S. Neutrophils in Tuberculosis-Associated Inflammation and Lung Pathology. *Frontiers in Immunology* **11** (2020).

90. Miow, Q.H. *et al.* Doxycycline host-directed therapy in human pulmonary tuberculosis. *The Journal of Clinical Investigation* **131** (2021).

91. Ong, C.W.M. *et al.* Neutrophil-Derived MMP-8 Drives AMPK-Dependent Matrix Destruction in Human Pulmonary Tuberculosis. *PLOS Pathogens* **11**, e1004917 (2015).

92. Hu, G. & Christman, J.W. Editorial: Alveolar Macrophages in Lung Inflammation and Resolution. *Frontiers in Immunology* **10** (2019).

93. Byrne, A.J., Mathie, S.A., Gregory, L.G. & Lloyd, C.M. Pulmonary macrophages: key players in the innate defence of the airways. *Thorax* **70**, 1189 (2015).

94. Chatterjee, S. The Lung Immune Niche in Tuberculosis: Insights from Studies on Human Alveolar Macrophages. *Current Tropical Medicine Reports* **2**, 49-53 (2015).

95. Lavalett, L. *et al.* Alveolar macrophages from tuberculosis patients display an altered inflammatory gene expression profile. *Tuberculosis* **107**, 156-167 (2017).

96. Huang, L., Nazarova, E.V., Tan, S., Liu, Y. & Russell, D.G. Growth of Mycobacterium tuberculosis in vivo segregates with host macrophage metabolism and ontogeny. *Journal of Experimental Medicine* **215**, 1135-1152 (2018).

97. Cohen, S.B. *et al.* Alveolar Macrophages Provide an Early Mycobacterium tuberculosis Niche and Initiate Dissemination. *Cell Host & Microbe* **24**, 439-446.e434 (2018).

98. Neupane, A.S. *et al.* Patrolling Alveolar Macrophages Conceal Bacteria from the Immune System to Maintain Homeostasis. *Cell* **183**, 110-125.e111 (2020).

99. Pisu, D. *et al.* Single cell analysis of M. tuberculosis phenotype and macrophage lineages in the infected lung. *Journal of Experimental Medicine* **218** (2021).

100. Xu-Vanpala, S. *et al.* Functional heterogeneity of alveolar macrophage population based on expression of CXCL2. *Science Immunology* **5**, eaba7350 (2020).

101. Guilliams, M. *et al.* Alveolar macrophages develop from fetal monocytes that differentiate into long-lived cells in the first week of life via GM-CSF. *Journal of Experimental Medicine* **210**, 1977-1992 (2013).

102. Aegerter, H. *et al.* Influenza-induced monocyte-derived alveolar macrophages confer prolonged antibacterial protection. *Nature Immunology* **21**, 145-157 (2020).

103. McQuattie-Pimentel, A.C., Budinger, G.R.S. & Ballinger, M.N. Monocyte-derived Alveolar Macrophages: The Dark Side of Lung Repair? *American Journal of Respiratory Cell and Molecular Biology* **58**, 5-6 (2018).

104. Shi, C. & Pamer, E.G. Monocyte recruitment during infection and inflammation. *Nature Reviews Immunology* **11**, 762-774 (2011).

105. Kurihara, T., Warr, G., Loy, J. & Bravo, R. Defects in Macrophage Recruitment and Host Defense in Mice Lacking the CCR2 Chemokine Receptor. *Journal of Experimental Medicine* **186**, 1757-1762 (1997).

106. Mildner, A. *et al.* Genomic Characterization of Murine Monocytes Reveals C/EBPβ Transcription Factor Dependence of Ly6C(-) Cells. *Immunity* **46**, 849-862.e847 (2017).

107. Patel, A.A. *et al.* The fate and lifespan of human monocyte subsets in steady state and systemic inflammation. *The Journal of experimental medicine* **214**, 1913-1923 (2017).

108. Yuk, J.-M. *et al.* Vitamin D3 Induces Autophagy in Human Monocytes/Macrophages via Cathelicidin. *Cell Host & Microbe* **6**, 231-243 (2009).

109. Biswas, D. *et al.* ATP-induced autophagy is associated with rapid killing of intracellular mycobacteria within human monocytes/macrophages. *BMC Immunology* **9**, 35 (2008).

110. Ciaramella, A. *et al.* Proinflammatory Cytokines in the Course of Mycobacteriumtuberculosis–Induced Apoptosis in Monocytes/Macrophages. *The Journal of Infectious Diseases* **186**, 1277-1282 (2002).

111. Lam, A. *et al.* Role of apoptosis and autophagy in tuberculosis. *American Journal of Physiology-Lung Cellular and Molecular Physiology* **313**, L218-L229 (2017).

112. Cheng, S.-C. *et al.* mTOR- and HIF-1alpha-mediated aerobic glycolysis as metabolic basis for trained immunity. *Science* **345**, 1250684 (2014).

113. Moorlag, S.J.C.F.M. *et al.* β-Glucan Induces Protective Trained Immunity against Mycobacterium tuberculosis Infection: A Key Role for IL-1. *Cell Reports* **31**, 107634 (2020).

114. Samstein, M. *et al.* Essential yet limited role for $CCR2^{+}$ inflammatory monocytes during Mycobacterium tuberculosis-specific T cell priming. *Elife* **2**, e01086 (2013).

115. Cambier, C.J., O'Leary, S.M., O'Sullivan, M.P., Keane, J. & Ramakrishnan, L. Phenolic Glycolipid Facilitates Mycobacterial Escape from Microbicidal Tissue-Resident Macrophages. *Immunity* **47**, 552-565.e554 (2017).

116. Herbath, M., Harding, J.S., Fabry, Z. & Sandor, M. Expression of CCR2 and VEGFR1 is required for monocyte migration into Mycobacterium tuberculosis-induced lung granulomas. *The Journal of Immunology* **206**, 99.27-99.27 (2021).

117. Scott, H.M. & Flynn, J.L. Mycobacterium tuberculosis in Chemokine Receptor 2-Deficient Mice: Influence of Dose on Disease Progression. *Infection and Immunity* **70**, 5946-5954 (2002).

118. Sköld, M. & Behar, S.M. Tuberculosis Triggers a Tissue-Dependent Program of Differentiation and Acquisition of Effector Functions by Circulating Monocytes. *The Journal of Immunology* **181**, 6349-6360 (2008).

119. Pisu, D., Huang, L., Grenier, J.K. & Russell, D.G. Dual RNA-Seq of Mtb-Infected Macrophages In Vivo Reveals Ontologically Distinct Host-Pathogen Interactions. *Cell Reports* **30**, 335-350.e334 (2020).

120. Shim, D., Kim, H. & Shin, S.J. Mycobacterium tuberculosis Infection-Driven Foamy Macrophages and Their Implications in Tuberculosis Control as Targets for Host-Directed Therapy. *Frontiers in Immunology* **11** (2020).

121. Singh, V. *et al.* Mycobacterium tuberculosis-Driven Targeted Recalibration of Macrophage Lipid Homeostasis Promotes the Foamy Phenotype. *Cell Host & Microbe* **12**, 669-681 (2012).

122. Russell, D.G., Cardona, P.-J., Kim, M.-J., Allain, S. & Altare, F. Foamy macrophages and the progression of the human tuberculosis granuloma. *Nature immunology* **10**, 943-948 (2009).

123. Hwang, S.-A., Ali, Y., Fedotova, E., Hunter, R.L. & Brown, R.E. Morphoproteomics identifies the foamy alveolar macrophage as an M2 phenotype with PD-L1 expression in the early lesion of post-primary tuberculosis: implications for host immune surveillance and therapy. *Annals of Clinical & Laboratory Science* **50**, 429-438 (2020).

124. Refai, A., Gritli, S., Barbouche, M.-R. & Essafi, M. Mycobacterium tuberculosis Virulent Factor ESAT-6 Drives Macrophage Differentiation Toward the Pro-inflammatory M1 Phenotype and Subsequently Switches It to the Anti-inflammatory M2 Phenotype. *Frontiers in Cellular and Infection Microbiology* **8** (2018).

125. Huang, Z. *et al.* Mycobacterium tuberculosis-Induced Polarization of Human Macrophage Orchestrates the Formation and Development of Tuberculous Granulomas In Vitro. *PLOS ONE* **10**, e0129744 (2015).

126. Veglia, F., Sanseviero, E. & Gabrilovich, D.I. Myeloid-derived suppressor cells in the era of increasing myeloid cell diversity. *Nature Reviews Immunology* **21**, 485-498 (2021).

127. Cassetta, L. *et al.* Deciphering myeloid-derived suppressor cells: isolation and markers in humans, mice and non-human primates. *Cancer Immunology, Immunotherapy* **68**, 687-697 (2019).

128. Munansangu, B.S.M. *et al.* Immunometabolism of Myeloid-Derived Suppressor Cells: Implications for Mycobacterium tuberculosis Infection and Insights from Tumor Biology. *International Journal of Molecular Sciences* **23** (2022).

129. Knaul, J.K. *et al.* Lung-Residing Myeloid-derived Suppressors Display Dual Functionality in Murine Pulmonary Tuberculosis. *American Journal of Respiratory and Critical Care Medicine* **190**, 1053-1066 (2014).

130. Grassi, G. *et al.* PMN-MDSC Frequency Discriminates Active Versus Latent Tuberculosis and Could Play a Role in Counteracting the Immune-Mediated Lung Damage in Active Disease. *Frontiers in immunology* **12**, 594376-594376 (2021).

131. Davids, M., Pooran, A., Smith, L., Tomasicchio, M. & Dheda, K. The Frequency and Effect of Granulocytic Myeloid-Derived Suppressor Cells on Mycobacterial Survival in Patients With Tuberculosis: A Preliminary Report. *Frontiers in Immunology* **12** (2021).

132. Plessis, N.d. *et al.* Increased Frequency of Myeloid-derived Suppressor Cells during Active Tuberculosis and after Recent Mycobacterium tuberculosis Infection Suppresses T-Cell Function. *American Journal of Respiratory and Critical Care Medicine* **188**, 724-732 (2013).

133. Kumar, R. & Subbian, S. Immune Correlates of Non-Necrotic and Necrotic Granulomas in Pulmonary Tuberculosis: A Pilot Study. *Journal of Respiration* **1**, 248-259 (2021).

134. Tsiganov, E.N. *et al.* Gr-1 dim CD11b Immature Myeloid-Derived Suppressor Cells but Not Neutrophils Are Markers of Lethal Tuberculosis Infection in Mice. *The Journal of Immunology* **192**, 4718-4727 (2014).

135. Hossain, F. *et al.* Inhibition of Fatty Acid Oxidation Modulates Immunosuppressive Functions of Myeloid-Derived Suppressor Cells and Enhances Cancer Therapies. *Cancer Immunol Res* **3**, 1236-1247 (2015).

136. Munansangu, B.S.M. *et al.* Immunometabolism of Myeloid-Derived Suppressor Cells: Implications for Mycobacterium tuberculosis Infection and Insights from Tumor Biology. *International Journal of Molecular Sciences* **23**, 3512 (2022).

137. Roth, F. *et al.* Aptamer-mediated blockade of IL4Rα triggers apoptosis of MDSCs and limits tumor progression. *Cancer Res* **72**, 1373-1383 (2012).

138. Parveen, S. *et al.* Effective Host-Directed Therapy for Tuberculosis by Depletion of Myeloid-Derived Suppressor Cells and Related Cells Using a Diphtheria Toxin Fusion Protein. *The Journal of Infectious Diseases* **224**, 1962-1972 (2021).

139. Pecora, N.D., Gehring, A.J., Canaday, D.H., Boom, W.H. & Harding, C.V. Mycobacterium tuberculosis LprA Is a Lipoprotein Agonist of TLR2 That Regulates Innate Immunity and APC Function. *The Journal of Immunology* **177**, 422 (2006).

140. Geijtenbeek, T.B.H. *et al.* Mycobacteria Target DC-SIGN to Suppress Dendritic Cell Function. *Journal of Experimental Medicine* **197**, 7-17 (2002).

141. Geijtenbeek, T.B.H. *et al.* DC-SIGN–ICAM-2 interaction mediates dendritic cell trafficking. *Nature Immunology* **1**, 353-357 (2000).

142. Reiley, W.W. *et al.* ESAT-6-specific CD4 T cell responses to aerosol Mycobacterium tuberculosis infection are initiated in the mediastinal lymph nodes. *Proceedings of the National Academy of Sciences* **105**, 10961-10966 (2008).

143. Khan, N., Vidyarthi, A., Javed, S. & Agrewala, J.N. Innate Immunity Holding the Flanks until Reinforced by Adaptive Immunity against Mycobacterium tuberculosis Infection. *Frontiers in Microbiology* **7** (2016).

144. Wolf , A.J. *et al.* Initiation of the adaptive immune response to Mycobacterium tuberculosis depends on antigen production in the local lymph node, not the lungs. *Journal of Experimental Medicine* **205**, 105-115 (2007).

145. Urdahl, K.B. Understanding and overcoming the barriers to T cell-mediated immunity against tuberculosis. *Seminars in Immunology* **26**, 578-587 (2014).

146. Srivastava, S., Grace, Patricia S. & Ernst, Joel D. Antigen Export Reduces Antigen Presentation and Limits T Cell Control of M. tuberculosis. *Cell Host & Microbe* **19**, 44-54 (2016).

147. Harding, J.S., Rayasam, A., Schreiber, H.A., Fabry, Z. & Sandor, M. Mycobacterium-Infected Dendritic Cells Disseminate Granulomatous Inflammation. *Scientific Reports* **5**, 15248 (2015).

148. Lande, R. *et al.* IFN-αβ Released by Mycobacterium tuberculosis-Infected Human Dendritic Cells Induces the Expression of CXCL10: Selective Recruitment of NK and Activated T Cells. *The Journal of Immunology* **170**, 1174-1182 (2003).

149. Khader, S.A. *et al.* Interleukin 12p40 is required for dendritic cell migration and T cell priming after Mycobacterium tuberculosis infection. *Journal of Experimental Medicine* **203**, 1805-1815 (2006).

150. Tzelepis, F. *et al.* Annexin1 regulates DC efferocytosis and cross-presentation during Mycobacterium tuberculosis infection. *The Journal of Clinical Investigation* **125**, 752-768 (2015).

151. Green, A.M., DiFazio, R. & Flynn, J.L. IFN-γ from CD4 T Cells Is Essential for Host Survival and Enhances CD8 T Cell Function during Mycobacterium tuberculosis Infection. *The Journal of Immunology* **190**, 270-277 (2013).

152. Serbina, N.V., Lazarevic, V. & Flynn, J.L. CD4(+) T cells are required for the development of cytotoxic CD8(+) T cells during Mycobacterium tuberculosis infection. *J Immunol* **167**, 6991-7000 (2001).

153. Flynn, J.L. *et al.* An essential role for interferon gamma in resistance to Mycobacterium tuberculosis infection. *The Journal of experimental medicine* **178**, 2249-2254 (1993).

154. Braverman, J., Sogi, K.M., Benjamin, D., Nomura, D.K. & Stanley, S.A. HIF-1α Is an Essential Mediator of IFN-γ-Dependent Immunity to Mycobacterium tuberculosis. *J Immunol* **197**, 1287-1297 (2016).

155. Ghanavi, J., Farnia, P., Farnia, P. & Velayati, A. The role of interferon-gamma and interferon-gamma receptor in tuberculosis and nontuberculous mycobacterial infections. *International Journal of Mycobacteriology* **10**, 349-357 (2021).

156. Woodworth, J.S., Wu, Y. & Behar, S.M. Mycobacterium tuberculosis-Specific CD8+ T Cells Require Perforin to Kill Target Cells and Provide Protection In Vivo. *The Journal of Immunology* **181**, 8595 (2008).

157. Canaday, D.H. *et al.* CD4+ and CD8+ T Cells Kill Intracellular Mycobacterium tuberculosis by a Perforin and Fas/Fas Ligand-Independent Mechanism. *The Journal of Immunology* **167**, 2734 (2001).

158. Fehrenbach, H. Alveolar epithelial type II cell: defender of the alveolus revisited. *Respiratory Research* **2**, 33 (2001).

159. Bermudez, L.E. & Goodman, J. Mycobacterium tuberculosis invades and replicates within type II alveolar cells. *Infection and Immunity* **64**, 1400-1406 (1996).

160. Ryndak, M.B., Singh, K.K., Peng, Z. & Laal, S. Transcriptional Profile of Mycobacterium tuberculosis Replicating in Type II Alveolar Epithelial Cells. *PLOS ONE* **10**, e0123745 (2015).

161. Rivas-Santiago, B. *et al.* Expression of Cathelicidin LL-37 during Mycobacterium tuberculosis Infection in Human Alveolar Macrophages, Monocytes, Neutrophils, and Epithelial Cells. *Infection and Immunity* **76**, 935-941 (2008).

162. Sow, F.B. *et al.* Mycobacterium tuberculosis components stimulate production of the antimicrobial peptide hepcidin. *Tuberculosis* **91**, 314-321 (2011).

163. Rivas-Santiago, B. *et al.* Human Defensin 2 Is Expressed and Associated with Mycobacterium tuberculosis during Infection of Human Alveolar Epithelial Cells. *Infection and Immunity* **73**, 4505-4511 (2005).

164. Droemann, D. *et al.* Toll-like receptor 2 is expressed by alveolar epithelial cells type II and macrophages in the human lung. *Histochemistry and Cell Biology* **119**, 103-108 (2003).

165. Zhou, M., Wan, H.-Y., Huang, S.-G., Li, B. & Li, M. [Expression of toll-like receptor 4 in human alveolar epithelial cells and its role in cellular inflammation]. *Zhonghua Yi Xue Za Zhi* **88**, 2112-2116 (2008).

166. Whitsett, J.A. & Alenghat, T. Respiratory epithelial cells orchestrate pulmonary innate immunity. *Nature Immunology* **16**, 27-35 (2015).

167. Sharma, M., Sharma, S., Roy, S., Varma, S. & Bose, M. Pulmonary epithelial cells are a source of interferon-γ in response to Mycobacterium tuberculosis infection. *Immunology and cell biology* **85**, 229-237 (2007).

168. Méndez-Samperio, P., Alba, L. & Pérez, A. Mycobacterium bovis bacillus Calmette–Guérin (BCG)-induced CXCL8 production is mediated through PKCα-dependent activation of the IKKαβ signaling pathway in epithelial cells. *Cellular immunology* **245**, 111-118 (2007).

169. Méndez-Samperio, P., Trejo, A. & Pérez, A. Mycobacterium bovis bacillus calmette–Guérin (BCG) stimulates IL-10 production via the PI3K/Akt and p38 MAPK pathways in human lung epithelial cells. *Cellular immunology* **251**, 37-42 (2008).

170. Méndez-Samperio, P., Pérez, A. & Rivera, L. Mycobacterium bovis Bacillus Calmette-Guerin (BCG)-induced activation of PI3K/Akt and NF-kB signaling pathways regulates expression of CXCL10 in epithelial cells. *Cellular immunology* **256**, 12-18 (2009).

171. Pechkovsky, D.V., Goldmann, T., Vollmer, E., Müller-Quernheim, J. & Zissel, G. Interleukin-18 expression by alveolar epithelial cells type II in tuberculosis and sarcoidosis. *FEMS Immunology & Medical Microbiology* **46**, 30-38 (2006).

172. Debbabi, H. *et al.* Primary type II alveolar epithelial cells present microbial antigens to antigen-specific CD4+ T cells. *American Journal of Physiology-Lung Cellular and Molecular Physiology* **289**, L274-L279 (2005).

173. Corbière, V. *et al.* Phenotypic characteristics of human type II alveolar epithelial cells suitable for antigen presentation to T lymphocytes. *Respiratory Research* **12**, 15 (2011).

174. Wirth, T. *et al.* Origin, Spread and Demography of the Mycobacterium tuberculosis Complex. *PLOS Pathogens* **4**, e1000160 (2008).

175. Hershkovitz, I. *et al.* Tuberculosis origin: The Neolithic scenario. *Tuberculosis* **95**, S122-S126 (2015).

176. Plumlee, C.R. *et al.* Ultra-low Dose Aerosol Infection of Mice with Mycobacterium tuberculosis More Closely Models Human Tuberculosis. *Cell Host Microbe* **29**, 68-82.e65 (2021).

177. Donald, P.R. *et al.* Droplets, dust and guinea pigs: an historical review of tuberculosis transmission research. *The International Journal of Tuberculosis and Lung Disease* **22**, 972-982 (2018).

178. Kramnik, I. & Beamer, G. Mouse models of human TB pathology: roles in the analysis of necrosis and the development of host-directed therapies. *Seminars in Immunopathology* **38**, 221-237 (2016).

179. Houben, D. *et al.* ESX-1-mediated translocation to the cytosol controls virulence of mycobacteria. *Cellular Microbiology* **14**, 1287-1298 (2012).

180. Ferrari, G., Langen, H., Naito, M. & Pieters, J. A Coat Protein on Phagosomes Involved in the Intracellular Survival of Mycobacteria. *Cell* **97**, 435-447 (1999).

181. Deghmane, A.-E. *et al.* Lipoamide dehydrogenase mediates retention of coronin-1 on BCG vacuoles, leading to arrest in phagosome maturation. *Journal of Cell Science* **120**, 2796-2806 (2007).

182. Esposito, C., Marasco, D., Delogu, G., Pedone, E. & Berisio, R. Heparin-binding hemagglutinin HBHA from Mycobacterium tuberculosis affects actin polymerisation. *Biochemical and Biophysical Research Communications* **410**, 339-344 (2011).

183. Carranza, C. & Chavez-Galan, L. Several Routes to the Same Destination: Inhibition of Phagosome-Lysosome Fusion by Mycobacterium tuberculosis. *The American Journal of the Medical Sciences* **357**, 184-194 (2019).

184. Harrison, R.E., Bucci, C., Vieira, O.V., Schroer, T.A. & Grinstein, S. Phagosomes fuse with late endosomes and/or lysosomes by extension of membrane protrusions along microtubules: role of Rab7 and RILP. *Mol Cell Biol* **23**, 6494-6506 (2003).

185. Sun, J. *et al.* Mycobacterium bovis BCG disrupts the interaction of Rab7 with RILP contributing to inhibition of phagosome maturation. *J Leukoc Biol* **82**, 1437-1445 (2007).

186. Kyei, G.B. *et al.* Rab14 is critical for maintenance of Mycobacterium tuberculosis phagosome maturation arrest. *The EMBO Journal* **25**, 5250-5259 (2006).

187. Buter, J. *et al.* Mycobacterium tuberculosis releases an antacid that remodels phagosomes. *Nature Chemical Biology* **15**, 889-899 (2019).

188. Khare, G., Reddy, P.V., Sidhwani, P. & Tyagi, A.K. KefB inhibits phagosomal acidification but its role is unrelated to M. tuberculosis survival in host. *Scientific Reports* **3**, 3527 (2013).

189. Queval, C.J. *et al.* Mycobacterium tuberculosis Controls Phagosomal Acidification by Targeting CISH-Mediated Signaling. *Cell Reports* **20**, 3188-3198 (2017).

190. van Deurs, B., Holm, P.K. & Sandvig, K. Inhibition of the vacuolar H(+)-ATPase with bafilomycin reduces delivery of internalized molecules from mature multivesicular endosomes to lysosomes in HEp-2 cells. *Eur J Cell Biol* **69**, 343-350 (1996).

191. Huynh, K.K. & Grinstein, S. Regulation of Vacuolar pH and Its Modulation by Some Microbial Species. *Microbiology and Molecular Biology Reviews* **71**, 452-462 (2007).

192. Singh, C.R. *et al.* Processing and presentation of a mycobacterial antigen 85B epitope by murine macrophages is dependent on the phagosomal acquisition of vacuolar proton ATPase and in situ activation of cathepsin D. *J Immunol* **177**, 3250-3259 (2006).

193. Shah, S. *et al.* Cutting Edge: Mycobacterium tuberculosis but Not Nonvirulent Mycobacteria Inhibits IFN-β and AIM2 Inflammasome–Dependent IL-1β Production via Its ESX-1 Secretion System. *The Journal of Immunology* **191**, 3514-3518 (2013).

194. Rastogi, S., Ellinwood, S., Augenstreich, J., Mayer-Barber, K.D. & Briken, V. Mycobacterium tuberculosis inhibits the NLRP3 inflammasome activation via its phosphokinase PknF. *PLOS Pathogens* **17**, e1009712 (2021).

195. Danelishvili, L. *et al.* Mycobacterium tuberculosis Alters the Metalloprotease Activity of the COP9 Signalosome. *mBio* **5**, e01278-01214 (2014).

196. Wang, J. *et al.* The ubiquitin ligase TRIM27 functions as a host restriction factor antagonized by Mycobacterium tuberculosis PtpA during mycobacterial infection. *Scientific Reports* **6**, 34827 (2016).

197. Wang, L. *et al.* Host-mediated ubiquitination of a mycobacterial protein suppresses immunity. *Nature* **577**, 682-688 (2020).

198. Yaseen, I., Kaur, P., Nandicoori, V.K. & Khosla, S. Mycobacteria modulate host epigenetic machinery by Rv1988 methylation of a non-tail arginine of histone H3. *Nature Communications* **6**, 8922 (2015).

199. Behrouzi, A. *et al.* Aberrant methylation of host macrophages induced by tuberculosis infection. *World Journal of Microbiology and Biotechnology* **35**, 168 (2019).

200. Sharma, G., Upadhyay, S., Srilalitha, M., Nandicoori, V.K. & Khosla, S. The interaction of mycobacterial protein Rv2966c with host chromatin is mediated through non-CpG methylation and histone H3/H4 binding. *Nucleic Acids Research* **43**, 3922-3937 (2015).

201. Singh, V. *et al.* Histone Methyltransferase SET8 Epigenetically Reprograms Host Immune Responses to Assist Mycobacterial Survival. *The Journal of Infectious Diseases* **216**, 477-488 (2017).

202. Moores, R.C., Brilha, S., Schutgens, F., Elkington, P.T. & Friedland, J.S. Epigenetic Regulation of Matrix Metalloproteinase-1 and -3 Expression in Mycobacterium tuberculosis Infection. *Frontiers in Immunology* **8** (2017).

203. Pennini, M.E., Pai, R.K., Schultz, D.C., Boom, W.H. & Harding, C.V. Mycobacterium tuberculosis 19-kDa Lipoprotein Inhibits IFN-γ-Induced Chromatin Remodeling of MHC2TA by TLR2 and MAPK Signaling. *The Journal of Immunology* **176**, 4323-4330 (2006).

204. Chen, Y.C. *et al.* Histone H3K14 hypoacetylation and H3K27 hypermethylation along with HDAC1 up-regulation and KDM6B down-regulation are associated with active pulmonary tuberculosis disease. *Am J Transl Res* **9**, 1943-1955 (2017).

205. Chandran, A. *et al.* Mycobacterium tuberculosis Infection Induces HDAC1-Mediated Suppression of IL-12B Gene Expression in Macrophages. *Frontiers in Cellular and Infection Microbiology* **5** (2015).

206. Duan, L., Yi, M., Chen, J., Li, S. & Chen, W. Mycobacterium tuberculosis EIS gene inhibits macrophage autophagy through up-regulation of IL-10 by increasing the acetylation of histone H3. *Biochemical and Biophysical Research Communications* **473**, 1229-1234 (2016).

207. Chen, Y.-C. *et al.* Whole Genome DNA Methylation Analysis of Active Pulmonary Tuberculosis Disease Identifies Novel Epigenotypes: PARP9/miR-505/RASGRP4/GNG12 Gene Methylation and Clinical Phenotypes. *International Journal of Molecular Sciences* **21**, 3180 (2020).

208. Zheng, L. *et al.* Unraveling methylation changes of host macrophages in Mycobacterium tuberculosis infection. *Tuberculosis* **98**, 139-148 (2016).

209. Chen, Y.-C. *et al.* Aberrant Toll-like receptor 2 promoter methylation in blood cells from patients with pulmonary tuberculosis. *Journal of Infection* **69**, 546-557 (2014).

210. Wei, M. *et al.* NLRP3 Activation Was Regulated by DNA Methylation Modification during Mycobacterium tuberculosis Infection. *BioMed Research International* **2016**, 4323281 (2016).

211. del Rosario, R.C.H. *et al.* Histone acetylome-wide associations in immune cells from individuals with active Mycobacterium tuberculosis infection. *Nature Microbiology* **7**, 312-326 (2022).

212. Stone, M.S., Martyn, L. & Weaver, C.M. Potassium Intake, Bioavailability, Hypertension, and Glucose Control. *Nutrients* **8**, 444 (2016).

213. McDonough, A.A. & Youn, J.H. Potassium Homeostasis: The Knowns, the Unknowns, and the Health Benefits. *Physiology* **32**, 100-111 (2017).

214. Aburto, N.J. *et al.* Effect of increased potassium intake on cardiovascular risk factors and disease: systematic review and meta-analyses. *BMJ : British Medical Journal* **346**, f1378 (2013).

215. Ekmekcioglu, C., Elmadfa, I., Meyer, A.L. & Moeslinger, T. The role of dietary potassium in hypertension and diabetes. *J Physiol Biochem* **72**, 93-106 (2016).

216. Weaver, C.M. Potassium and Health. *Advances in Nutrition* **4**, 368S-377S (2013).

217. Khaw, K.T. & Barrett-Connor, E. Dietary potassium and stroke-associated mortality. A 12-year prospective population study. *N Engl J Med* **316**, 235-240 (1987).

218. Sidhu, K., Sanjanwala, R. & Zieroth, S. Hyperkalemia in heart failure. *Curr Opin Cardiol* **35**, 150-155 (2020).

219. Hunter, R.W. & Bailey, M.A. Hyperkalemia: pathophysiology, risk factors and consequences. *Nephrology Dialysis Transplantation* **34**, iii2-iii11 (2019).

220. Kardalas, E. *et al.* Hypokalemia: a clinical update. *Endocrine Connections* **7**, R135-R146 (2018).

221. Lindestam Arlehamn, C.S., Petrilli, V., Gross, O., Tschopp, J. & Evans, T.J. The role of potassium in inflammasome activation by bacteria. *Journal of Biological Chemistry* (2010).

222. C., H. *et al.* The calcium-activated potassium channel KCa3.1 plays a central role in the chemotactic response of mammalian neutrophils. *Acta Physiologica* **216**, 132-145 (2016).

223. Ma, X.-Z. *et al.* The role and mechanism of KCa3.1 channels in human monocyte migration induced by palmitic acid. *Experimental Cell Research* **369**, 208-217 (2018).

224. Miller, C. An overview of the potassium channel family. *Genome Biology* **1**, reviews0004.0001 (2000).

225. Zhong, Y.S., Wang, J., Liu, W.M. & Zhu, Y.H. Potassium ion channels in retinal ganglion cells (Review). *Mol Med Rep* **8**, 311-319 (2013).

226. Nerbonne, J.M. Molecular basis of functional voltage-gated K+ channel diversity in the mammalian myocardium. *The Journal of Physiology* **525**, 285-298 (2000).

227. Jan, L.Y. & Jan, Y.N. Voltage-gated potassium channels and the diversity of electrical signalling. *The Journal of Physiology* **590**, 2591-2599 (2012).

228. Gu, C. & Barry, J. Function and mechanism of axonal targeting of voltage-sensitive potassium channels. *Progress in Neurobiology* **94**, 115-132 (2011).

229. Ko, E.A. *et al.* Pathophysiology of voltage-gated K+ channels in vascular smooth muscle cells: Modulation by protein kinases. *Progress in Biophysics and Molecular Biology* **103**, 95-101 (2010).

230. Koo, G.C. *et al.* Blockade of the voltage-gated potassium channel Kv1.3 inhibits immune responses in vivo. *The Journal of Immunology* **158**, 5120-5128 (1997).

231. Vicente, R. *et al.* Differential Voltage-dependent K+ Channel Responses during Proliferation and Activation in Macrophages. *Journal of Biological Chemistry* **278**, 46307-46320 (2003).

232. Yazejian, B., Sun, X.-P. & Grinnell, A.D. Tracking presynaptic Ca2+ dynamics during neurotransmitter release with Ca2+-activated K+ channels. *Nature Neuroscience* **3**, 566-571 (2000).

233. Brayden, J.E. & Nelson, M.T. Regulation of Arterial Tone by Activation of Calcium-Dependent Potassium Channels. *Science* **256**, 532-535 (1992).

234. Kshatri, A.S., Gonzalez-Hernandez, A. & Giraldez, T. Physiological Roles and Therapeutic Potential of Ca2+ Activated Potassium Channels in the Nervous System. *Frontiers in Molecular Neuroscience* **11** (2018).

235. Kaushal, V., Koeberle, P.D., Wang, Y. & Schlichter, L.C. The Ca2+-Activated K+ Channel KCNN4/KCa3.1 Contributes to Microglia Activation and Nitric Oxide-Dependent Neurodegeneration. *The Journal of Neuroscience* **27**, 234 (2007).

236. Feliciangeli, S., Chatelain, F.C., Bichet, D. & Lesage, F. The family of K2P channels: salient structural and functional properties. *The Journal of Physiology* **593**, 2587-2603 (2015).

237. Di, A. *et al.* The TWIK2 Potassium Efflux Channel in Macrophages Mediates NLRP3 Inflammasome-Induced Inflammation. *Immunity* **49**, 56-65.e54 (2018).

238. Nie, X. *et al.* Expression and insights on function of potassium channel TWIK-1 in mouse kidney. *Pflügers Archiv* **451**, 479-488 (2005).

239. Hibino, H. *et al.* Inwardly rectifying potassium channels: their structure, function, and physiological roles. *Physiological reviews* **90**, 291-366 (2010).

240. Al Shibli, A. & Narchi, H. Bartter and Gitelman syndromes: Spectrum of clinical manifestations caused by different mutations. *World J Methodol* **5**, 55-61 (2015).

241. Scholl, U.I. *et al.* Seizures, sensorineural deafness, ataxia, mental retardation, and electrolyte imbalance (SeSAME syndrome) caused by mutations in KCNJ10. *Proceedings of the National Academy of Sciences* **106**, 5842-5847 (2009).

242. Buono, R.J. *et al.* Association between variation in the human KCNJ10 potassium ion channel gene and seizure susceptibility. *Epilepsy Research* **58**, 175-183 (2004).

243. Bandulik, S. *et al.* The salt-wasting phenotype of EAST syndrome, a disease with multifaceted symptoms linked to the KCNJ10 K+ channel. *Pflügers Archiv - European Journal of Physiology* **461**, 423-435 (2011).

244. Schlingmann, K.P. *et al.* Defects in KCNJ16 Cause a Novel Tubulopathy with Hypokalemia, Salt Wasting, Disturbed Acid-Base Homeostasis, and Sensorineural Deafness. *Journal of the American Society of Nephrology* **32**, 1498-1512 (2021).

245. Roman, D., Zhong, H., Yaklichkin, S., Chen, R. & Mardon, G. Conditional loss of Kcnj13 in the retinal pigment epithelium causes photoreceptor degeneration. *Experimental Eye Research* **176**, 219-226 (2018).

246. Xia, M. *et al.* A Kir2. 1 gain-of-function mutation underlies familial atrial fibrillation. *Biochemical and biophysical research communications* **332**, 1012-1019 (2005).

247. Bendahhou, S. *et al.* Defective potassium channel Kir2. 1 trafficking underlies Andersen-Tawil syndrome. *Journal of Biological Chemistry* **278**, 51779-51785 (2003).

248. Donaldson, M. *et al.* PIP2 binding residues of Kir2. 1 are common targets of mutations causing Andersen syndrome. *Neurology* **60**, 1811-1816 (2003).

249. Masia, R., Krause, D.S. & Yellen, G. The inward rectifier potassium channel Kir2.1 is expressed in mouse neutrophils from bone marrow and liver. *American Journal of Physiology-Cell Physiology* **308**, C264-C276 (2015).

250. Lam, D. & Schlichter, L.C. Expression and contributions of the Kir2.1 inward-rectifier K+ channel to proliferation, migration and chemotaxis of microglia in unstimulated and anti-inflammatory states. *Frontiers in Cellular Neuroscience* **9** (2015).

251. Uhlén, M. *et al.* Tissue-based map of the human proteome. *Science* **347**, 1260419 (2015).

252. Mulatero, P., Monticone, S., Rainey, W.E., Veglio, F. & Williams, T.A. Role of KCNJ5 in familial and sporadic primary aldosteronism. *Nature Reviews Endocrinology* **9**, 104-112 (2013).

253. Clarke, T.-K. *et al.* KCNJ6 is Associated with Adult Alcohol Dependence and Involved in Gene × Early Life Stress Interactions in Adolescent Alcohol Drinking. *Neuropsychopharmacology* **36**, 1142-1148 (2011).

254. Bruehl, S. *et al.* Associations between KCNJ6 (GIRK2) gene polymorphisms and pain-related phenotypes. *PAIN*® **154**, 2853-2859 (2013).

255. Herman, M.A. *et al.* GIRK3 gates activation of the mesolimbic dopaminergic pathway by ethanol. *Proceedings of the National Academy of Sciences* **112**, 7091-7096 (2015).

256. Smith, S.B. *et al.* Quantitative trait locus and computational mapping identifies Kcnj9 (GIRK3) as a candidate gene affecting analgesia from multiple drug classes. *Pharmacogenetics and Genomics* **18** (2008).

257. Gloyn, A.L. *et al.* Activating Mutations in the Gene Encoding the ATP-Sensitive Potassium-Channel Subunit Kir6.2 and Permanent Neonatal Diabetes. *New England Journal of Medicine* **350**, 1838-1849 (2004).

258. Sagen, J.V. *et al.* Permanent Neonatal Diabetes due to Mutations in KCNJ11 Encoding Kir6.2. *Patient Characteristics and Initial Response to Sulfonylurea Therapy* **53**, 2713-2718 (2004).

259. Gloyn, A.L. *et al.* Large-scale association studies of variants in genes encoding the pancreatic β-cell KATP channel subunits Kir6. 2 (KCNJ11) and SUR1 (ABCC8) confirm that the KCNJ11 E23K variant is associated with type 2 diabetes. *Diabetes* **52**, 568-572 (2003).

260. Wang, Q. *et al.* Genetic screening of KCNJ8 in Japanese patients with J-wave syndromes or idiopathic ventricular fibrillation. *Journal of Arrhythmia* **29**, 261-264 (2013).

261. Uhlen, M. *et al.* A genome-wide transcriptomic analysis of protein-coding genes in human blood cells. *Science* **366**, eaax9198 (2019).

262. He, W. *et al.* Acid secretion-associated translocation of KCNJ15 in gastric parietal cells. *Am J Physiol Gastrointest Liver Physiol* **301**, G591-600 (2011).

263. Yuan, J. *et al.* Potassium channel KCNJ15 is required for histamine-stimulated gastric acid secretion. *American Journal of Physiology-Cell Physiology* **309**, C264-C270 (2015).

264. Wu, J.V., Krouse, M.E., Rustagi, A., Joo, N.S. & Wine, J.J. An Inwardly Rectifying Potassium Channel in Apical Membrane of Calu-3 Cells. *Journal of Biological Chemistry* **279**, 46558-46565 (2004).

265. Okamoto, K. *et al.* Inhibition of glucose-stimulated insulin secretion by KCNJ15, a newly identified susceptibility gene for type 2 diabetes. *Diabetes* **61**, 1734-1741 (2012).

266. Okamoto, K. *et al.* Identification of KCNJ15 as a susceptibility gene in Asian patients with type 2 diabetes mellitus. *Am J Hum Genet* **86**, 54-64 (2010).

267. Fukuda, H. *et al.* Replication study for the association of a single-nucleotide polymorphism, rs3746876, within KCNJ15, with susceptibility to type 2 diabetes in a Japanese population. *J Hum Genet* **58**, 490-493 (2013).

268. Zhou, X. *et al.* Identification of genetic risk factors in the Chinese population implicates a role of immune system in Alzheimer's disease pathogenesis. *Proceedings of the National Academy of Sciences* **115**, 1697 (2018).

269. Gosset, P. *et al.* A New Inward Rectifier Potassium Channel Gene (KCNJ15) Localized on Chromosome 21 in the Down Syndrome Chromosome Region 1 (DCR1). *Genomics* **44**, 237-241 (1997).

270. Masotti, A. *et al.* Keppen-Lubinsky Syndrome Is Caused by Mutations in the Inwardly Rectifying K+ Channel Encoded by KCNJ6. *The American Journal of Human Genetics* **96**, 295-300 (2015).

271. Nakajima, K.-i. *et al.* KCNJ15/Kir4.2 couples with polyamines to sense weak extracellular electric fields in galvanotaxis. *Nature Communications* **6**, 8532 (2015).

272. DeHart, G.W., Jin, T., McCloskey, D.E., Pegg, A.E. & Sheppard, D. The α9β1 integrin enhances cell migration by polyamine-mediated modulation of an inward-rectifier potassium channel. *Proceedings of the National Academy of Sciences* **105**, 7188-7193 (2008).

273. Veeravalli, K.K. *et al.* Integrin α9β1-mediated cell migration in glioblastoma via SSAT and Kir4.2 potassium channel pathway. *Cellular Signalling* **24**, 272-281 (2012).

274. Cassat, James E. & Skaar, Eric P. Iron in Infection and Immunity. *Cell Host & Microbe* **13**, 509-519 (2013).

275. Ammendola, S. *et al.* High-Affinity Zn2+ Uptake System ZnuABC Is Required for Bacterial Zinc Homeostasis in Intracellular Environments and Contributes to the Virulence of Salmonella enterica. *Infection and Immunity* **75**, 5867 (2007).

276. Mortensen, B.L., Rathi, S., Chazin, W.J. & Skaar, E.P. Acinetobacter baumannii Response to Host-Mediated Zinc Limitation Requires the Transcriptional Regulator Zur. *Journal of Bacteriology* **196**, 2616 (2014).

277. Gabbianelli, R. *et al.* Role of ZnuABC and ZinT in Escherichia coli O157:H7 zinc acquisition and interaction with epithelial cells. *BMC Microbiology* **11**, 36 (2011).

278. Kapetanovic, R. *et al.* Salmonella employs multiple mechanisms to subvert the TLR-inducible zinc-mediated antimicrobial response of human macrophages. *The FASEB Journal* **30**, 1901-1912 (2016).

279. Achard, Maud E.S. *et al.* Copper redistribution in murine macrophages in response to Salmonella infection. *Biochemical Journal* **444**, 51-57 (2012).

280. White, C., Lee, J., Kambe, T., Fritsche, K. & Petris, M.J. A Role for the ATP7A Copper-transporting ATPase in Macrophage Bactericidal Activity. *Journal of Biological Chemistry* **284**, 33949-33956 (2009).

281. Zhang, W.C. *et al.* High salt primes a specific activation state of macrophages, M(Na). *Cell Res* **25**, 893-910 (2015).

282. Hucke, S. *et al.* Sodium chloride promotes pro-inflammatory macrophage polarization thereby aggravating CNS autoimmunity. *Journal of Autoimmunity* **67**, 90-101 (2016).

283. Corratge-Faillie, C. *et al.* Potassium and sodium transport in non-animal cells: the Trk/Ktr/HKT transporter family. *Cellular and molecular life sciences : CMLS* **67**, 2511-2532 (2010).

284. Su, J., Gong, H., Lai, J., Main, A. & Lu, S. The Potassium Transporter Trk and External Potassium Modulate Salmonella enterica Protein Secretion and Virulence. *Infection and Immunity* **77**, 667-675 (2009).

285. Dubnau, E., Fontan, P., Manganelli, R., Soares-Appel, S. & Smith, I. Mycobacterium tuberculosis genes induced during infection of human macrophages. *Infect Immun* **70**, 2787-2795 (2002).

286. Alkhuder, K., Meibom, K.L., Dubail, I., Dupuis, M. & Charbit, A. Identification of trkH, encoding a potassium uptake protein required for Francisella tularensis systemic dissemination in mice. *PLoS One* **5**, e8966 (2010).

287. Epstein, W. Chapter 9 The Kdp System: A Bacterial K+ Transport ATPase. In: Bronner, F. & Kleinzeller, A. (eds). *Current Topics in Membranes and Transport*, vol. 23. Academic Press, 1985, pp 153-175.

288. Betts, J.C., Lukey, P.T., Robb, L.C., McAdam, R.A. & Duncan, K. Evaluation of a nutrient starvation model of Mycobacterium tuberculosis persistence by gene and protein expression profiling. *Molecular microbiology* **43**, 717-731 (2002).

289. Parish, T. *et al.* Deletion of two-component regulatory systems increases the virulence of Mycobacterium tuberculosis. *Infect Immun* **71**, 1134-1140 (2003).

290. Pétrilli, V. *et al.* Activation of the NALP3 inflammasome is triggered by low intracellular potassium concentration. *Cell Death And Differentiation* **14**, 1583 (2007).

291. Gong, T., Yang, Y., Jin, T., Jiang, W. & Zhou, R. Orchestration of NLRP3 inflammasome activation by ion fluxes. *Trends in immunology* **39**, 393-406 (2018).

292. Rivers-Auty, J. & Brough, D. Potassium efflux fires the canon: Potassium efflux as a common trigger for canonical and noncanonical NLRP3 pathways. *European Journal of Immunology* **45**, 2758-2761 (2015).

293. Yaron, J.R. *et al.* K+ regulates Ca2+ to drive inflammasome signaling: dynamic visualization of ion flux in live cells. *Cell Death &Amp; Disease* **6**, e1954 (2015).

294. Groß, Christina J. *et al.* K+ Efflux-Independent NLRP3 Inflammasome Activation by Small Molecules Targeting Mitochondria. *Immunity* **45**, 761-773 (2016).

295. He, Y., Zeng, M.Y., Yang, D., Motro, B. & Núñez, G. NEK7 is an essential mediator of NLRP3 activation downstream of potassium efflux. *Nature* **530**, 354 (2016).

296. Shi, H. *et al.* NLRP3 activation and mitosis are mutually exclusive events coordinated by NEK7, a new inflammasome component. *Nature Immunology* **17**, 250 (2015).

297. Madry, C. *et al.* Microglial Ramification, Surveillance, and Interleukin-1β Release Are Regulated by the Two-Pore Domain K+ Channel THIK-1. *Neuron* **97**, 299-312.e296 (2018).

298. Papavlassopoulos, M. *et al.* MaxiK Blockade Selectively Inhibits the Lipopolysaccharide-Induced IκB-α/NF-κB Signaling Pathway in Macrophages. *The Journal of Immunology* **177**, 4086-4093 (2006).

299. Li, P. *et al.* Kv1.5 channel mediates monosodium urate-induced activation of NLRP3 inflammasome in macrophages and arrhythmogenic effects of urate on cardiomyocytes. *Molecular Biology Reports* (2022).

300. Du, R.H. *et al.* Kir6.2 knockout aggravates lipopolysaccharide-induced mouse liver injury via enhancing NLRP3 inflammasome activation. *J Gastroenterol* **49**, 727-736 (2014).

301. Kennedy, J.A. *et al.* The Two-Pore Potassium Channel TREK-1 Alters Inflammasome Activation in Alveolar Macrophages. *C29. PROTECTORS OF THE LUNG: INNATE IMMUNE RESPONSES IN ACUTE LUNG INJURY*, pp A4791-A4791.

302. Chen, L. *et al.* Alpha1-adrenoceptors activate NLRP3 inflammasome through downregulation of Kir2.1 in cardiac inflammation. *Experimental Physiology* **n/a**.

303. Wu, X.-y. *et al.* ML365 inhibits TWIK2 channel to block ATP-induced NLRP3 inflammasome. *Acta Pharmacologica Sinica* **43**, 992-1000 (2022).

304. Eil, R. *et al.* Ionic immune suppression within the tumour microenvironment limits T cell effector function. *Nature* **537**, 539 (2016).

305. Vodnala, S.K. *et al.* T cell stemness and dysfunction in tumors are triggered by a common mechanism. *Science* **363** (2019).

306. Extracellular K+ Dampens T Cell Functions: Implications for Immune Suppression in the Tumor Microenvironment. *Bioelectricity* **1**, 169-179 (2019).

307. Ashida, H. *et al.* Cell death and infection: a double-edged sword for host and pathogen survival. *The Journal of cell biology* **195**, 931-942 (2011).

308. Beeton, C. *et al.* Kv1.3 channels are a therapeutic target for T cell-mediated autoimmune diseases. *Proc Natl Acad Sci U S A* **103**, 17414-17419 (2006).

309. Singh, D.K. *et al.* Blockade of the Kv1.3 K+ Channel Enhances BCG Vaccine Efficacy by Expanding Central Memory T Lymphocytes. *The Journal of Infectious Diseases* **214**, 1456-1464 (2016).

310. Ren, Y.R. *et al.* Clofazimine Inhibits Human Kv1.3 Potassium Channel by Perturbing Calcium Oscillation in T Lymphocytes. *PLOS ONE* **3**, e4009 (2008).

311. Zhao, Y. *et al.* Blockade of Kv1.3 potassium channel inhibits CD8+ T cell-mediated neuroinflammation via PD-1/Blimp-1 signaling. *The FASEB Journal* **34**, 15492-15503 (2020).

312. Gocke, A.R. *et al.* Kv1.3 Deletion Biases T Cells toward an Immunoregulatory Phenotype and Renders Mice Resistant to Autoimmune Encephalomyelitis. *The Journal of Immunology* **188**, 5877 (2012).

313. Koch Hansen, L. *et al.* Expression of T-cell KV1.3 potassium channel correlates with pro-inflammatory cytokines and disease activity in ulcerative colitis. *J Crohns Colitis* **8**, 1378-1391 (2014).

314. Rangaraju, S., Gearing, M., Jin, L.W. & Levey, A. Potassium channel Kv1.3 is highly expressed by microglia in human Alzheimer's disease. *Journal of Alzheimer's disease : JAD* **44**, 797-808 (2015).

315. Ortega, F.J. *et al.* ATP-dependent potassium channel blockade strengthens microglial neuroprotection after hypoxia–ischemia in rats. *Experimental Neurology* **235**, 282-296 (2012).

316. Villalonga, N. *et al.* Immunomodulatory effects of diclofenac in leukocytes through the targeting of Kv1.3 voltage-dependent potassium channels. *Biochemical Pharmacology* **80**, 858-866 (2010).

317. Kan, X.-H. *et al.* Kv1.3 potassium channel mediates macrophage migration in atherosclerosis by regulating ERK activity. *Archives of Biochemistry and Biophysics* **591**, 150-156 (2016).

318. Wu, B. *et al.* Blockage of Kv1.3 regulates macrophage migration in acute liver injury by targeting δ-catenin through RhoA signaling. *Int J Biol Sci* **16**, 671-681 (2020).

319. Rus, H. *et al.* The voltage-gated potassium channel Kv1.3 is highly expressed on inflammatory infiltrates in multiple sclerosis brain. *Proceedings of the National Academy of Sciences* **102**, 11094-11099 (2005).

320. Chimote, A.A. *et al.* A defect in KCa3.1 channel activity limits the ability of CD8+ T cells from cancer patients to infiltrate an adenosine-rich microenvironment. *Science Signaling* **11**, eaaq1616 (2018).

321. Cruse, G., Duffy, S.M., Brightling, C.E. & Bradding, P. Functional KCa3.1 K+ channels are required for human lung mast cell migration. *Thorax* **61**, 880-885 (2006).

322. Shumilina, E. *et al.* Blunted IgE-Mediated Activation of Mast Cells in Mice Lacking the Ca2+-Activated K+ Channel KCa3.1. *The Journal of Immunology* **180**, 8040-8047 (2008).

323. Henríquez, C. *et al.* The calcium-activated potassium channel KCa3.1 plays a central role in the chemotactic response of mammalian neutrophils. *Acta Physiologica* **216**, 132-145 (2016).

324. Schwab, A. Function and spatial distribution of ion channels and transporters in cell migration. *Am J Physiol Renal Physiol* **280**, F739-747 (2001).

325. Gulbins, E., Sassi, N., Grassmè, H., Zoratti, M. & Szabò, I. Role of Kv1.3 mitochondrial potassium channel in apoptotic signalling in lymphocytes. *Biochimica et Biophysica Acta (BBA) - Bioenergetics* **1797**, 1251-1259 (2010).

326. Szabò, I., Zoratti, M. & Gulbins, E. Contribution of voltage-gated potassium channels to the regulation of apoptosis. *FEBS Letters* **584**, 2049-2056 (2010).

327. Leanza, L., Zoratti, M., Gulbins, E. & Szabo, I. Induction of Apoptosis in Macrophages via Kv1.3 and Kv1.5 Potassium Channels. *Current Medicinal Chemistry* **19**, 5394-5404 (2012).

328. Fay, A.J., Qian, X., Jan, Y.N. & Jan, L.Y. SK channels mediate NADPH oxidase-independent reactive oxygen species production and apoptosis in granulocytes. *Proceedings of the National Academy of Sciences* **103**, 17548-17553 (2006).

329. Gerhardt, E. *et al.* Cascade of Caspase Activation in Potassium-Deprived Cerebellar Granule Neurons: Targets for Treatment with Peptide and Protein Inhibitors of Apoptosis. *Molecular and Cellular Neuroscience* **17**, 717-731 (2001).

330. Trotter, L. *et al.* Mitogen-activated protein kinase kinase 7 is activated during low potassium-induced apoptosis in rat cerebellar granule neurons. *Neuroscience Letters* **320**, 29-32 (2002).

331. Karki, P. *et al.* Intracellular K+ inhibits apoptosis by suppressing the Apaf-1 apoptosome formation and subsequent downstream pathways but not cytochrome c release. *Cell Death & Differentiation* **14**, 2068-2075 (2007).

332. Hughes, F.M. & Cidlowski, J.A. Potassium is a critical regulator of apoptotic enzymes in vitro and in vivo. *Adv Enzyme Regul* **39**, 157-171 (1999).

333. Behar, S.M. *et al.* Apoptosis is an innate defense function of macrophages against Mycobacterium tuberculosis. *Mucosal Immunology* **4**, 279-287 (2011).

334. Anwar, S. & Whyte, M.K.B. Neutrophil Apoptosis In Infectious Disease. *Experimental Lung Research* **33**, 519-528 (2007).

335. Bocchino, M. *et al.* Role of mycobacteria-induced monocyte/macrophage apoptosis in the pathogenesis of human tuberculosis. *The International Journal of Tuberculosis and Lung Disease* **9**, 375-383 (2005).

336. Zhou, Y. *et al.* Inflammasomes-dependent regulation of IL-1beta secretion induced by the virulent Mycobacterium bovis Beijing strain in THP-1 macrophages. *Antonie van Leeuwenhoek* **108**, 163-171 (2015).

337. Reeves, E.P. *et al.* Killing activity of neutrophils is mediated through activation of proteases by K+ flux. *Nature* **416**, 291-297 (2002).

338. Cang, C., Aranda, K., Seo, Y.-j., Gasnier, B. & Ren, D. TMEM175 is an organelle K+ channel regulating lysosomal function. *Cell* **162**, 1101-1112 (2015).

339. Martins, M., Viveiros, M. & Amaral, L. Inhibitors of Ca2+ and K+ transport enhance intracellular killing of M. tuberculosis by non-killing macrophages. *In vivo (Athens, Greece)* **22**, 69-75 (2008).

340. Amaral, L., Martins, M. & Viveiros, M. Enhanced killing of intracellular multidrug-resistant Mycobacterium tuberculosis by compounds that affect the activity of efflux pumps. *Journal of Antimicrobial Chemotherapy* **59**, 1237-1246 (2007).

341. Hover, S. *et al.* Modulation of Potassium Channels Inhibits Bunyavirus Infection. *The Journal of Biological Chemistry* **291**, 3411-3422 (2016).

342. Kondratskyi, A., Kondratska, K., Skryma, R., Klionsky, D.J. & Prevarskaya, N. Ion channels in the regulation of autophagy. *Autophagy* **14**, 3-21 (2018).

343. Perez-Neut, M. *et al.* Activation of hERG3 channel stimulates autophagy and promotes cellular senescence in melanoma. *Oncotarget* **7**, 21991-22004 (2016).

344. Yu, K.-Y. *et al.* Mitochondrial KATP channel involvement in angiotensin II-induced autophagy in vascular smooth muscle cells. *Basic Research in Cardiology* **109**, 416 (2014).

345. Co, D.O., Hogan, L.H., Kim, S.-I. & Sandor, M. Mycobacterial granulomas: keys to a long-lasting host–pathogen relationship. *Clinical Immunology* **113**, 130-136 (2004).

346. Hogan, L.H. *et al.* Mycobacterium bovis BCG-induced granuloma formation depends on gamma interferon and CD40 ligand but does not require CD28. *Infection and Immunity* **69**, 2596-2603 (2001).

347. Wallis, R.S. & Ehlers, S. Tumor necrosis factor and granuloma biology: explaining the differential infection risk of etanercept and infliximab. Seminars in arthritis and rheumatism; 2005: Elsevier; 2005. p. 34-38.

348. Lin, P.L. *et al.* Sterilization of granulomas is common in active and latent tuberculosis despite within-host variability in bacterial killing. *Nature medicine* **20**, 75-79 (2014).

349. Cadena, A.M., Fortune, S.M. & Flynn, J.L. Heterogeneity in tuberculosis. *Nature Reviews Immunology* **17**, 691-702 (2017).

350. Gideon, H.P. *et al.* Multimodal profiling of lung granulomas in macaques reveals cellular correlates of tuberculosis control. *Immunity* (2022).

351. Bhattacharya, B. *et al.* The integrated stress response mediates necrosis in murine Mycobacterium tuberculosis granulomas. *The Journal of clinical investigation* **131** (2021).

352. Amaral, E.P. *et al.* A major role for ferroptosis in Mycobacterium tuberculosis–induced cell death and tissue necrosis. *Journal of Experimental Medicine* **216**, 556-570 (2019).

353. Divangahi, M. *et al.* Mycobacterium tuberculosis evades macrophage defenses by inhibiting plasma membrane repair. *Nature Immunology* **10**, 899-906 (2009).

354. Chen , M. *et al.* Lipid mediators in innate immunity against tuberculosis: opposing roles of PGE2 and LXA4 in the induction of macrophage death. *Journal of Experimental Medicine* **205**, 2791-2801 (2008).

355. Pajuelo, D. *et al.* NAD+ Depletion Triggers Macrophage Necroptosis, a Cell Death Pathway Exploited by Mycobacterium tuberculosis. *Cell Reports* **24**, 429-440 (2018).

356. D'Arcy, M.S. Cell death: a review of the major forms of apoptosis, necrosis and autophagy. *Cell biology international* **43**, 582-592 (2019).

357. Via, L.E. *et al.* Tuberculous granulomas are hypoxic in guinea pigs, rabbits, and nonhuman primates. *Infection and immunity* **76**, 2333-2340 (2008).

358. Harper, J. *et al.* Mouse Model of Necrotic Tuberculosis Granulomas Develops Hypoxic Lesions. *The Journal of Infectious Diseases* **205**, 595-602 (2011).

359. Palanisamy, G.S. *et al.* Evidence for Oxidative Stress and Defective Antioxidant Response in Guinea Pigs with Tuberculosis. *PLOS ONE* **6**, e26254 (2011).

360. Martin, C.J., Carey, A.F. & Fortune, S.M. A bug's life in the granuloma. *Semin Immunopathol* **38**, 213-220 (2016).

361. Vodnala, S.K. *et al.* T cell stemness and dysfunction in tumors are triggered by a common mechanism. *Science* **363** (2019).

362. Kent, W.J. *et al.* The Human Genome Browser at UCSC. *Genome Research* **12**, 996-1006 (2002).

363. Singhal, A. *et al.* BCG Induces Protection against Mycobacterium tuberculosis Infection in the Wistar Rat Model. *PLOS ONE* **6**, e28082 (2011).

364. Picelli, S. *et al.* Full-length RNA-seq from single cells using Smart-seq2. *Nat Protoc* **9**, 171-181 (2014).

365. Dobin, A. *et al.* STAR: ultrafast universal RNA-seq aligner. *Bioinformatics* **29**, 15-21 (2013).

366. Liao, Y., Smyth, G.K. & Shi, W. featureCounts: an efficient general purpose program for assigning sequence reads to genomic features. *Bioinformatics* **30**, 923-930 (2014).

367. Harrow, J. *et al.* GENCODE: producing a reference annotation for ENCODE. *Genome Biology* **7**, S4 (2006).

368. Robinson, M.D., McCarthy, D.J. & Smyth, G.K. edgeR: a Bioconductor package for differential expression analysis of digital gene expression data. *Bioinformatics* **26**, 139-140 (2010).

369. Love, M.I., Huber, W. & Anders, S. Moderated estimation of fold change and dispersion for RNA-seq data with DESeq2. *Genome Biology* **15**, 550 (2014).

370. Benjamini, Y. & Hochberg, Y. Controlling the False Discovery Rate: A Practical and Powerful Approach to Multiple Testing. *Journal of the Royal Statistical Society. Series B (Methodological)* **57**, 289-300 (1995).

371. Langmead, B. & Salzberg, S.L. Fast gapped-read alignment with Bowtie 2. *Nature Methods* **9**, 357-359 (2012).

372. Amemiya, H.M., Kundaje, A. & Boyle, A.P. The ENCODE Blacklist: Identification of Problematic Regions of the Genome. *Scientific Reports* **9**, 9354 (2019).

373. Zhang, Y. *et al.* Model-based Analysis of ChIP-Seq (MACS). *Genome Biology* **9**, R137 (2008).

374. Stark, R. & Brown, G. DiffBind: differential binding analysis of ChIP-Seq peak data. *R package version* **100** (2011).

375. Akalin, A., Franke, V., Vlahoviček, K., Mason, C.E. & Schübeler, D. Genomation: a toolkit to summarize, annotate and visualize genomic intervals. *Bioinformatics* **31**, 1127-1129 (2015).

376. Oehlers, S.H. *et al.* Interception of host angiogenic signalling limits mycobacterial growth. *Nature* **517**, 612-615 (2015).

377. Cunningham, F. *et al.* Ensembl 2022. *Nucleic Acids Research* **50**, D988-D995 (2021).

378. Ravesloot-Chávez, M.M., Dis, E.V. & Stanley, S.A. The Innate Immune Response to Mycobacterium tuberculosis Infection. *Annual Review of Immunology* **39**, 611-637 (2021).

379. Abel, B. *et al.* Toll-Like Receptor 4 Expression Is Required to Control Chronic Mycobacterium tuberculosis Infection in Mice. *The Journal of Immunology* **169**, 3155-3162 (2002).

380. Sánchez, D. *et al.* Role of TLR2- and TLR4-mediated signaling in Mycobacterium tuberculosis-induced macrophage death. *Cellular Immunology* **260**, 128-136 (2010).

381. Pessia, M., Imbrici, P., D'Adamo, M.C., Salvatore, L. & Tucker, S.J. Differential pH sensitivity of Kir4.1 and Kir4.2 potassium channels and their modulation by heteropolymerisation with Kir5.1. *The Journal of Physiology* **532**, 359-367 (2001).

382. Choe, H., Zhou, H., Palmer, L.G. & Sackin, H. A conserved cytoplasmic region of ROMK modulates pH sensitivity, conductance, and gating. *Am J Physiol* **273**, F516-529 (1997).

383. Sia, J.K. *et al.* Immunology of Mycobacterium tuberculosis Infections. *Microbiology Spectrum* **7**, 7.4.6 (2019).

384. Jo, E.-K., Kim, J.K., Shin, D.-M. & Sasakawa, C. Molecular mechanisms regulating NLRP3 inflammasome activation. *Cellular & Molecular Immunology* **13**, 148-159 (2016).

385. Thornberry, N.A. *et al.* A novel heterodimeric cysteine protease is required for interleukin-1 beta processing in monocytes. *Nature* **356**, 768-774 (1992).

386. Gaidt, Moritz M. *et al.* Human Monocytes Engage an Alternative Inflammasome Pathway. *Immunity* **44**, 833-846 (2016).

387. Xiao, C. & Ghosh, S. NF-κB, an evolutionarily conserved mediator of immune and inflammatory responses. *Mechanisms of lymphocyte activation and immune regulation X*, 41-45 (2005).

388. Yamamoto, Y. & Gaynor, R.B. Role of the NF-kB pathway in the pathogenesis of human disease states. *Current molecular medicine* **1**, 287-296 (2001).

389. Keane, J., Remold, H.G. & Kornfeld, H. Virulent Mycobacterium tuberculosis strains evade apoptosis of infected alveolar macrophages. *The Journal of Immunology* **164**, 2016-2020 (2000).

390. Molloy, A., Laochumroonvorapong, P. & Kaplan, G. Apoptosis, but not necrosis, of infected monocytes is coupled with killing of intracellular bacillus Calmette-Guérin. *Journal of Experimental Medicine* **180**, 1499-1509 (1994).

391. Behar, S.M. & Briken, V. Apoptosis inhibition by intracellular bacteria and its consequence on host immunity. *Current Opinion in Immunology* **60**, 103-110 (2019).

392. Shakeri, R., Kheirollahi, A. & Davoodi, J. Apaf-1: Regulation and function in cell death. *Biochimie* **135**, 111-125 (2017).

393. Shinoura, N., Sakurai, S., Asai, A., Kirino, T. & Hamada, H. Over-expression of APAF-1 and caspase-9 augments radiation-induced apoptosis in U-373MG glioma cells. *International Journal of Cancer* **93**, 252-261 (2001).

394. Kamarajan, P., Sun, N.-K., Sun, C.-L. & Chao, C.C.K. Apaf-1 overexpression partially overcomes apoptotic resistance in a cisplatin-selected HeLa cell line. *FEBS Letters* **505**, 206-212 (2001).

395. Bosshart, H. & Heinzelmann, M. THP-1 cells as a model for human monocytes. *Ann Transl Med* **4**, 438 (2016).

396. Zhang, X., Lu, X., Akhter, S., Georgescu, M.-M. & Legerski, R.J. FANCI is a negative regulator of Akt activation. *Cell Cycle* **15**, 1134-1143 (2016).

397. Wu, H. *et al.* PRDM5 promotes the apoptosis of epithelial cells induced by IFN-γ during Crohn's disease. *Pathol Res Pract* **213**, 666-673 (2017).

398. Wang, J. *et al.* Knockdown of cyclin D1 inhibits proliferation, induces apoptosis, and attenuates the invasive capacity of human glioblastoma cells. *J Neurooncol* **106**, 473-484 (2012).

399. Han, B. *et al.* PRSS23 knockdown inhibits gastric tumorigenesis through EIF2 signaling. *Pharmacol Res* **142**, 50-57 (2019).

400. Liang, X. *et al.* Follistatin-like 1 attenuates apoptosis via disco-interacting protein 2 homolog A/Akt pathway after middle cerebral artery occlusion in rats. *Stroke* **45**, 3048-3054 (2014).

401. Ogura, Y. *et al.* Therapeutic impact of follistatin-like 1 on myocardial ischemic injury in preclinical models. *Circulation* **126**, 1728-1738 (2012).

402. Rebucci, M. *et al.* miRNA-196b inhibits cell proliferation and induces apoptosis in HepG2 cells by targeting IGF2BP1. *Mol Cancer* **14**, 79 (2015).

403. Ding, W., Wu, Q., Sun, L., Pan, N.C. & Wang, X. Cenpj Regulates Cilia Disassembly and Neurogenesis in the Developing Mouse Cortex. *J Neurosci* **39**, 1994-2010 (2019).

404. Noguchi, S. *et al.* socs7, a target gene of microRNA-145, regulates interferon-β induction through STAT3 nuclear translocation in bladder cancer cells. *Cell Death Dis* **4**, e482 (2013).

405. Brophy, M.L. *et al.* Myeloid-Specific Deletion of Epsins 1 and 2 Reduces Atherosclerosis by Preventing LRP-1 Downregulation. *Circ Res* **124**, e6-e19 (2019).

406. Aoyama, T. *et al.* Identification of Coiled-Coil Domain-Containing Protein 180 and Leucine-Rich Repeat-Containing Protein 4 as Potential Immunohistochemical Markers for Liposarcoma Based on Proteomic Analysis Using Formalin-Fixed, Paraffin-Embedded Tissue. *Am J Pathol* **189**, 1015-1028 (2019).

407. Bullock, S.A. *Neurabin, a neuronal F-actin binding protein and regulator of protein phosphatase-1*. Weill Medical College of Cornell University, 2005.

408. Gao, Y. *et al.* Down-regulation of MRPS23 inhibits rat breast cancer proliferation and metastasis. *Oncotarget* **8**, 71772-71781 (2017).

409. Qin, T. *et al.* Abnormally elevated USP37 expression in breast cancer stem cells regulates stemness, epithelial-mesenchymal transition and cisplatin sensitivity. *J Exp Clin Cancer Res* **37**, 287 (2018).

410. Xue, J., Scotti, E. & Stoffel, M. CDK8 Regulates Insulin Secretion and Mediates Postnatal and Stress-Induced Expression of Neuropeptides in Pancreatic β Cells. *Cell Rep* **28**, 2892-2904.e2897 (2019).

411. Thul, P.J. *et al.* A subcellular map of the human proteome. *Science* **356**, eaal3321 (2017).

412. Bignon, Y. *et al.* Defective bicarbonate reabsorption in Kir4.2 potassium channel deficient mice impairs acid-base balance and ammonia excretion. *Kidney International* **97**, 304-315 (2020).

413. Urdahl, K.B., Shafiani, S. & Ernst, J.D. Initiation and regulation of T-cell responses in tuberculosis. *Mucosal Immunology* **4**, 288-293 (2011).

414. Lee, J. *et al.* CD11cHi monocyte-derived macrophages are a major cellular compartment infected by Mycobacterium tuberculosis. *PLOS Pathogens* **16**, e1008621 (2020).

415. Corleis, B. & Dorhoi, A. Early dynamics of innate immunity during pulmonary tuberculosis. *Immunology Letters* **221**, 56-60 (2020).

416. Segura, E. Human dendritic cell subsets: An updated view of their ontogeny and functional specialization. *European Journal of Immunology* **n/a**.

417. Di Sabatino, A., Calarota, S.A., Vidali, F., MacDonald, T.T. & Corazza, G.R. Role of IL-15 in immune-mediated and infectious diseases. *Cytokine & Growth Factor Reviews* **22**, 19-33 (2011).

418. Rausch, A. *et al.* Interleukin-15 mediates protection against experimental tuberculosis: A role for NKG2D-dependent effector mechanisms of CD8+ T cells. *European Journal of Immunology* **36**, 1156-1167 (2006).

419. Hu, S. *et al.* IL-17 Production of Neutrophils Enhances Antibacteria Ability but Promotes Arthritis Development During Mycobacterium tuberculosis Infection. *EBioMedicine* **23**, 88-99 (2017).

420. Freches, D. *et al.* Mice genetically inactivated in interleukin-17A receptor are defective in long-term control of Mycobacterium tuberculosis infection. *Immunology* **140**, 220-231 (2013).

421. Bryson, B.D. *et al.* Heterogeneous GM-CSF signaling in macrophages is associated with control of Mycobacterium tuberculosis. *Nature Communications* **10**, 2329 (2019).

422. Benmerzoug, S. *et al.* GM-CSF targeted immunomodulation affects host response to M. tuberculosis infection. *Scientific Reports* **8**, 8652 (2018).

423. Serbina, N.V. & Pamer, E.G. Monocyte emigration from bone marrow during bacterial infection requires signals mediated by chemokine receptor CCR2. *Nature Immunology* **7**, 311-317 (2006).

424. Chong, S.Z. *et al.* CXCR4 identifies transitional bone marrow premonocytes that replenish the mature monocyte pool for peripheral responses. *Journal of Experimental Medicine* **213**, 2293-2314 (2016).

425. Noetzli, L.J., French, S.L. & Machlus, K.R. New Insights Into the Differentiation of Megakaryocytes From Hematopoietic Progenitors. *Arteriosclerosis, Thrombosis, and Vascular Biology* **39**, 1288-1300 (2019).

426. Jung, H., Mithal, D.S., Park, J.E. & Miller, R.J. Localized CCR2 Activation in the Bone Marrow Niche Mobilizes Monocytes by Desensitizing CXCR4. *PLOS ONE* **10**, e0128387 (2015).

427. Lastrucci, C. *et al.* Tuberculosis is associated with expansion of a motile, permissive and immunomodulatory CD16+ monocyte population via the IL-10/STAT3 axis. *Cell Research* **25**, 1333-1351 (2015).

428. Sköld, M. & Behar, S.M. Tuberculosis Triggers a Tissue-Dependent Program of Differentiation and Acquisition of Effector Functions by Circulating Monocytes. *The Journal of Immunology* **181**, 6349 (2008).

429. MacMicking, J.D. *et al.* Identification of nitric oxide synthase as a protective locus against tuberculosis. *Proceedings of the National Academy of Sciences of the United States of America* **94**, 5243-5248 (1997).

430. Costa, D.L. *et al.* Heme oxygenase-1 inhibition promotes IFNγ- and NOS2-mediated control of Mycobacterium tuberculosis infection. *Mucosal Immunol* **14**, 253-266 (2021).

431. Solano-Gálvez, S.G. *et al.* Human Dendritic Cells: Ontogeny and Their Subsets in Health and Disease. *Medical Sciences* **6**, 88 (2018).

432. Tur, J. *et al.* Induction of CIITA by IFN-γ in macrophages involves STAT1 activation by JAK and JNK. *Immunobiology* **226**, 152114 (2021).

433. Luo, B. *et al.* Erythropoeitin Signaling in Macrophages Promotes Dying Cell Clearance and Immune Tolerance. *Immunity* **44**, 287-302 (2016).

434. Luo, B. *et al.* Phagocyte respiratory burst activates macrophage erythropoietin signalling to promote acute inflammation resolution. *Nature Communications* **7**, 12177 (2016).

435. Scott, C.L. *et al.* The Transcription Factor ZEB2 Is Required to Maintain the Tissue-Specific Identities of Macrophages. *Immunity* **49**, 312-325.e315 (2018).

436. Sturek, J.M. *et al.* An intracellular role for ABCG1-mediated cholesterol transport in the regulated secretory pathway of mouse pancreatic β cells. *The Journal of Clinical Investigation* **120**, 2575-2589 (2010).

437. Kennedy, M.A. *et al.* ABCG1 has a critical role in mediating cholesterol efflux to HDL and preventing cellular lipid accumulation. *Cell Metabolism* **1**, 121-131 (2005).

438. Wang, P.-y., Weng, J. & Anderson, R.G.W. OSBP Is a Cholesterol-Regulated Scaffolding Protein in Control of ERK1/2 Activation. *Science* **307**, 1472-1476 (2005).

439. Naito, T. *et al.* Movement of accessible plasma membrane cholesterol by the GRAMD1 lipid transfer protein complex. *eLife* **8**, e51401 (2019).

440. Li, N.C., Fan, J. & Papadopoulos, V. Sterol Carrier Protein-2, a Nonspecific Lipid-Transfer Protein, in Intracellular Cholesterol Trafficking in Testicular Leydig Cells. *PloS one* **11**, e0149728-e0149728 (2016).

441. Chu, B.-B. *et al.* Cholesterol Transport through Lysosome-Peroxisome Membrane Contacts. *Cell* **161**, 291-306 (2015).

442. Collot-Teixeira, S., Martin, J., McDermott-Roe, C., Poston, R. & McGregor, J.L. CD36 and macrophages in atherosclerosis. *Cardiovascular Research* **75**, 468-477 (2007).

443. Pawełczyk, J. *et al.* Cholesterol-dependent transcriptome remodeling reveals new insight into the contribution of cholesterol to Mycobacterium tuberculosis pathogenesis. *Scientific Reports* **11**, 12396 (2021).

444. Houghton, A.M., Hartzell, W.O., Robbins, C.S., Gomis-Rüth, F.X. & Shapiro, S.D. Macrophage elastase kills bacteria within murine macrophages. *Nature* **460**, 637-641 (2009).

445. Huang, L., Nazarova, E.V., Tan, S., Liu, Y. & Russell, D.G. Growth of Mycobacterium tuberculosis in vivo segregates with host macrophage metabolism and ontogeny. *The Journal of Experimental Medicine* (2018).

446. Cao, W., Lee, S.H. & Lu, J. CD83 is preformed inside monocytes, macrophages and dendritic cells, but it is only stably expressed on activated dendritic cells. *Biochem J* **385**, 85-93 (2005).

447. Wu, Y. *et al.* Zom-biecoming: Single-Cell RNA-seq reveals senescence-like features of alveolar macrophages during aging. *The Journal of Immunology* **206**, 55.06-55.06 (2021).

448. Yu, X. *et al.* The Cytokine TGF-β Promotes the Development and Homeostasis of Alveolar Macrophages. *Immunity* **47**, 903-912.e904 (2017).

449. Caja, L. *et al.* TGF-β and the Tissue Microenvironment: Relevance in Fibrosis and Cancer. *International Journal of Molecular Sciences* **19** (2018).

450. Khalil, N., Whitman, C., Zuo, L., Danielpour, D. & Greenberg, A. Regulation of alveolar macrophage transforming growth factor-beta secretion by corticosteroids in bleomycin-induced pulmonary inflammation in the rat. *The Journal of Clinical Investigation* **92**, 1812-1818 (1993).

451. Bilotta, M.T., Petillo, S., Santoni, A. & Cippitelli, M. Liver X Receptors: Regulators of Cholesterol Metabolism, Inflammation, Autoimmunity, and Cancer. *Frontiers in Immunology* **11** (2020).

452. Li, S. *et al.* NAMPT knockdown attenuates atherosclerosis and promotes reverse cholesterol transport in ApoE KO mice with high-fat-induced insulin resistance. *Scientific Reports* **6**, 26746 (2016).

453. Liu, L., Tan, L., Yao, J. & Yang, L. Long non-coding RNA MALAT1 regulates cholesterol accumulation in ox-LDL-induced macrophages via the microRNA-17-5p/ABCA1 axis. *Molecular medicine reports* **21**, 1761-1770 (2020).

454. Sharpe, L.J. *et al.* Cholesterol increases protein levels of the E3 ligase MARCH6 and thereby stimulates protein degradation. *The Journal of Biological Chemistry* **294**, 2436-2448 (2019).

455. Tan, J.M.E. *et al.* The MARCH6-SQLE Axis Controls Endothelial Cholesterol Homeostasis and Angiogenic Sprouting. *Cell Rep* **32**, 107944 (2020).

456. Pennings, M. *et al.* Regulation of cholesterol homeostasis in macrophages and consequences for atherosclerotic lesion development. *FEBS Letters* **580**, 5588-5596 (2006).

457. Kannan, S., Audet, A., Huang, H., Chen, L.-j. & Wu, M. Cholesterol-Rich Membrane Rafts and Lyn Are Involved in Phagocytosis during Pseudomonas aeruginosa Infection. *The Journal of Immunology* **180**, 2396-2408 (2008).

458. Au - Bryan, A.M., Au - Farnoud, A.M., Au - Mor, V. & Au - Del Poeta, M. Macrophage Cholesterol Depletion and Its Effect on the Phagocytosis of Cryptococcus neoformans. *JoVE*, e52432 (2014).

459. Gatfield, J. & Pieters, J. Essential Role for Cholesterol in Entry of Mycobacteria into Macrophages. *Science* **288**, 1647-1651 (2000).

460. Agarwal, P. *et al.* Foam Cells Control Mycobacterium tuberculosis Infection. *Frontiers in Microbiology* **11** (2020).

461. Daniel, J., Maamar, H., Deb, C., Sirakova, T.D. & Kolattukudy, P.E. Mycobacterium tuberculosis Uses Host Triacylglycerol to Accumulate Lipid Droplets and Acquires a Dormancy-Like Phenotype in Lipid-Loaded Macrophages. *PLOS Pathogens* **7**, e1002093 (2011).

462. de Chastellier, C. The many niches and strategies used by pathogenic mycobacteria for survival within host macrophages. *Immunobiology* **214**, 526-542 (2009).

463. Vrieling, F. *et al.* Oxidized low-density lipoprotein (oxLDL) supports Mycobacterium tuberculosis survival in macrophages by inducing lysosomal dysfunction. *PLOS Pathogens* **15**, e1007724 (2019).

464. Guerrini, V. *et al.* Storage lipid studies in tuberculosis reveal that foam cell biogenesis is disease-specific. *PLoS Pathog* **14**, e1007223 (2018).

465. Simon-Chica, A. *et al.* Novel insights into the electrophysiology of murine cardiac macrophages: relevance of voltage-gated potassium channels. *Cardiovascular Research* **118**, 798-813 (2022).

466. Adams, T.S. *et al.* Single-cell RNA-seq reveals ectopic and aberrant lung-resident cell populations in idiopathic pulmonary fibrosis. *Science Advances* **6**, eaba1983 (2020).

467. Habermann, A.C. *et al.* Single-cell RNA sequencing reveals profibrotic roles of distinct epithelial and mesenchymal lineages in pulmonary fibrosis. *Science Advances* **6**, eaba1972 (2020).

468. Orme, I.M. & Basaraba, R.J. The formation of the granuloma in tuberculosis infection. *Seminars in Immunology* **26**, 601-609 (2014).

469. Leong, F.J.W.-M. *et al.* Pathology of tuberculosis in the human lung. *A color atlas of comparative pathology of pulmonary tuberculosis*, 53-81 (2011).

470. Ndlovu, H. & Marakalala, M.J. Granulomas and Inflammation: Host-Directed Therapies for Tuberculosis. *Frontiers in immunology* **7**, 434-434 (2016).

471. Tsenova, L. & Singhal, A. Effects of host-directed therapies on the pathology of tuberculosis. *The Journal of Pathology* **250**, 636-646 (2020).

472. Chen, Z. *et al.* Mycobacterial WhiB6 Differentially Regulates ESX-1 and the Dos Regulon to Modulate Granuloma Formation and Virulence in Zebrafish. *Cell Reports* **16**, 2512-2524 (2016).

473. Fenaroli, F. *et al.* Polymersomes Eradicating Intracellular Bacteria. *ACS Nano* **14**, 8287-8298 (2020).

474. Kamijo, R. *et al.* Mice that lack the interferon-gamma receptor have profoundly altered responses to infection with Bacillus Calmette-Guérin and subsequent challenge with lipopolysaccharide. *The Journal of experimental medicine* **178**, 1435-1440 (1993).

475. Eil, R. *et al.* Ionic immune suppression within the tumour microenvironment limits T cell effector function. *Nature* **537**, 539-543 (2016).

476. Siqueira, M.d.S., Ribeiro, R.d.M. & Travassos, L.H. Autophagy and Its Interaction With Intracellular Bacterial Pathogens. *Frontiers in Immunology* **9** (2018).

477. Saini, N.K. *et al.* Suppression of autophagy and antigen presentation by Mycobacterium tuberculosis PE_PGRS47. *Nature microbiology* **1**, 1-12 (2016).

478. Songane, M., Kleinnijenhuis, J., Netea, M.G. & van Crevel, R. The role of autophagy in host defence against Mycobacterium tuberculosis infection. *Tuberculosis* **92**, 388-396 (2012).

479. Ye, X., Zhou, X.-J. & Zhang, H. Exploring the Role of Autophagy-Related Gene 5 (ATG5) Yields Important Insights Into Autophagy in Autoimmune/Autoinflammatory Diseases. *Frontiers in Immunology* **9** (2018).

480. Egan, D., Kim, J., Shaw, R.J. & Guan, K.-L. The autophagy initiating kinase ULK1 is regulated via opposing phosphorylation by AMPK and mTOR. *Autophagy* **7**, 643-644 (2011).

481. Xu, Z. *et al.* Targeting PI3K/AKT/mTOR-mediated autophagy for tumor therapy. *Applied Microbiology and Biotechnology* **104**, 575-587 (2020).

482. Kraft, C. & Martens, S. Mechanisms and regulation of autophagosome formation. *Current opinion in cell biology* **24**, 496-501 (2012).

483. Xie, Z. & Klionsky, D.J. Autophagosome formation: core machinery and adaptations. *Nature cell biology* **9**, 1102-1109 (2007).

484. Russell, S.L. *et al.* Compromised Metabolic Reprogramming Is an Early Indicator of CD8+ T Cell Dysfunction during Chronic Mycobacterium tuberculosis Infection. *Cell Reports* **29**, 3564-3579.e3565 (2019).

485. Chen, M., Gan, H. & Remold, H.G. A Mechanism of Virulence: Virulent Mycobacterium tuberculosis Strain H37Rv, but Not Attenuated H37Ra, Causes Significant Mitochondrial Inner Membrane Disruption in Macrophages Leading to Necrosis. *The Journal of Immunology* **176**, 3707 (2006).

486. Smulan, L.J. *et al.* Sirtuin 3 Downregulation in Mycobacterium tuberculosis-Infected Macrophages Reprograms Mitochondrial Metabolism and Promotes Cell Death. *mBio* **12**, e03140-03120 (2021).

487. Zhang, J.-Y. *et al.* Long noncoding RNA AFAP1-AS1 indicates a poor prognosis of hepatocellular carcinoma and promotes cell proliferation and invasion via upregulation of the RhoA/Rac2 signaling. *Int J Oncol* **48**, 1590-1598 (2016).

488. Wang, H. *et al.* Deletion of OSBPL2 in auditory cells increases cholesterol biosynthesis and drives reactive oxygen species production by inhibiting AMPK activity. *Cell Death & Disease* **10**, 627 (2019).

489. Danielli, M., Marrone, J., Capiglioni, A.M. & Marinelli, R.A. Mitochondrial aquaporin-8 is involved in SREBP-controlled hepatocyte cholesterol biosynthesis. *Free Radical Biology and Medicine* **131**, 370-375 (2019).

490. Pallottini, V. *et al.* Age-related HMG-CoA reductase deregulation depends on ROS-induced p38 activation. *Mechanisms of Ageing and Development* **128**, 688-695 (2007).

491. Recuero, M. *et al.* A free radical-generating system induces the cholesterol biosynthesis pathway: a role in Alzheimer's disease. *Aging Cell* **8**, 128-139 (2009).

492. Huang, L., Nazarova, E.V. & Russell, D.G. Mycobacterium tuberculosis: Bacterial Fitness within the Host Macrophage. *Microbiol Spectr* **7** (2019).

493. Lee, W., VanderVen, B.C., Fahey, R.J. & Russell, D.G. Intracellular Mycobacterium tuberculosis exploits host-derived fatty acids to limit metabolic stress. *The Journal of Biological Chemistry* **288**, 6788-6800 (2013).

494. Movafagh, S., Crook, S. & Vo, K. Regulation of Hypoxia-Inducible Factor-1a by Reactive Oxygen Species : New Developments in an Old Debate. *Journal of Cellular Biochemistry* **116**, 696-703 (2015).

495. Lacher, S.E., Levings, D.C., Freeman, S. & Slattery, M. Identification of a functional antioxidant response element at the HIF1A locus. *Redox Biology* **19**, 401-411 (2018).

496. Singhal, A. *et al.* Metformin as adjunct antituberculosis therapy. *Sci Transl Med* **6**, 263ra159 (2014).

497. Zorova, L.D. *et al.* Mitochondrial membrane potential. *Analytical Biochemistry* **552**, 50-59 (2018).

498. Jin, S.M. *et al.* Mitochondrial membrane potential regulates PINK1 import and proteolytic destabilization by PARL. *Journal of Cell Biology* **191**, 933-942 (2010).

499. Novakovic, B. *et al.* β-Glucan reverses the epigenetic state of LPS-induced immunological tolerance. *Cell* **167**, 1354-1368. e1314 (2016).

500. Russ, B.E. *et al.* Distinct epigenetic signatures delineate transcriptional programs during virus-specific CD8+ T cell differentiation. *Immunity* **41**, 853-865 (2014).

501. Saeed, S. *et al.* Epigenetic programming of monocyte-to-macrophage differentiation and trained innate immunity. *science* **345**, 1251086 (2014).

502. Esterhuyse, M.M. *et al.* Epigenetics and proteomics join transcriptomics in the quest for tuberculosis biomarkers. *MBio* **6**, e01187-01115 (2015).

503. García-Giménez, J.-L., Garcés, C., Romá-Mateo, C. & Pallardó, F.V. Oxidative stress-mediated alterations in histone post-translational modifications. *Free Radical Biology and Medicine* **170**, 6-18 (2021).

504. Niu, Y., DesMarais, T.L., Tong, Z., Yao, Y. & Costa, M. Oxidative stress alters global histone modification and DNA methylation. *Free Radical Biology and Medicine* **82**, 22-28 (2015).

505. Gu, X., Sun, J., Li, S., Wu, X. & Li, L. Oxidative stress induces DNA demethylation and histone acetylation in SH-SY5Y cells: potential epigenetic mechanisms in gene transcription in Aβ production. *Neurobiology of Aging* **34**, 1069-1079 (2013).

506. Katoh, Y. *et al.* Two domains of Nrf2 cooperatively bind CBP, a CREB binding protein, and synergistically activate transcription. *Genes to Cells* **6**, 857-868 (2001).

507. Alam, M.M. *et al.* Glucocorticoid receptor signaling represses the antioxidant response by inhibiting histone acetylation mediated by the transcriptional activator NRF2. *Journal of Biological Chemistry* **292**, 7519-7530 (2017).

508. Wang, J. *et al.* Oxidative stress activates NORAD expression by H3K27ac and promotes oxaliplatin resistance in gastric cancer by enhancing autophagy flux via targeting the miR-433-3p. *Cell Death & Disease* **12**, 90 (2021).

509. Kundaje, A. *et al.* Integrative analysis of 111 reference human epigenomes. *Nature* **518**, 317-330 (2015).

510. Consortium, E.P. An integrated encyclopedia of DNA elements in the human genome. *Nature* **489**, 57 (2012).

511. Kumar, V. *et al.* Uniform, optimal signal processing of mapped deep-sequencing data. *Nature biotechnology* **31**, 615-622 (2013).

512. Sun, W. *et al.* Histone acetylome-wide association study of autism spectrum disorder. *Cell* **167**, 1385-1397. e1311 (2016).

513. Li, P. *et al.* Streptococcus pneumoniae Induces Autophagy through the Inhibition of the PI3K-I/Akt/mTOR Pathway and ROS Hypergeneration in A549 Cells. *PLOS ONE* **10**, e0122753 (2015).

514. Zhang, L., Wang, H., Xu, J., Zhu, J. & Ding, K. Inhibition of cathepsin S induces autophagy and apoptosis in human glioblastoma cell lines through ROS-mediated PI3K/AKT/mTOR/p70S6K and JNK signaling pathways. *Toxicology Letters* **228**, 248-259 (2014).

515. Guo, C. *et al.* Amorphous silica nanoparticles trigger vascular endothelial cell injury through apoptosis and autophagy via reactive oxygen species-mediated MAPK/Bcl-2 and PI3K/Akt/mTOR signaling. *Int J Nanomedicine* **11**, 5257-5276 (2016).

516. Hinchy, E.C. *et al.* Mitochondria-derived ROS activate AMP-activated protein kinase (AMPK) indirectly. *Journal of Biological Chemistry* **293**, 17208-17217 (2018).

517. Martinez, A.N., Mehra, S. & Kaushal, D. Role of interleukin 6 in innate immunity to Mycobacterium tuberculosis infection. *J Infect Dis* **207**, 1253-1261 (2013).

518. Perrigoue, J.G. *et al.* IL-31-IL-31R interactions negatively regulate type 2 inflammation in the lung. *J Exp Med* **204**, 481-487 (2007).

519. Ogongo, P. *et al.* Tissue-resident-like CD4+ T cells secreting IL-17 control Mycobacterium tuberculosis in the human lung. *J Clin Invest* **131** (2021).

520. Arbués, A., Schmidiger, S., Kammüller, M. & Portevin, D. Extracellular Matrix-Induced GM-CSF and Hypoxia Promote Immune Control of Mycobacterium tuberculosis in Human In Vitro Granulomas. *Front Immunol* **12**, 727508 (2021).

521. Cohen, S.B., Gern, B.H. & Urdahl, K.B. The Tuberculous Granuloma and Preexisting Immunity. *Annual Review of Immunology* **40**, 589-614 (2022).

522. Chai, Q., Wang, L., Liu, C.H. & Ge, B. New insights into the evasion of host innate immunity by Mycobacterium tuberculosis. *Cellular & Molecular Immunology* **17**, 901-913 (2020).

523. Silva Miranda, M., Breiman, A., Allain, S., Deknuydt, F. & Altare, F. The tuberculous granuloma: an unsuccessful host defence mechanism providing a safety shelter for the bacteria? *Clin Dev Immunol* **2012**, 139127 (2012).

524. Cambier, C.J., Falkow, S. & Ramakrishnan, L. Host evasion and exploitation schemes of Mycobacterium tuberculosis. *Cell* **159**, 1497-1509 (2014).

525. Feske, S., Wulff, H. & Skolnik, E.Y. Ion Channels in Innate and Adaptive Immunity. *Annual Review of Immunology* **33**, 291-353 (2015).

526. Baixauli, F., Villa, M. & Pearce, E.L. Potassium shapes antitumor immunity. *Science* **363**, 1395-1396 (2019).

527. Muñoz-Planillo, R. *et al.* K+ efflux is the common trigger of NLRP3 inflammasome activation by bacterial toxins and particulate matter. *Immunity* **38**, 1142-1153 (2013).

528. Cain, K., Langlais, C., Sun, X.-M., Brown, D.G. & Cohen, G.M. Physiological Concentrations of K+ Inhibit Cytochrome c-dependent Formation of the Apoptosome. *Journal of Biological Chemistry* **276**, 41985-41990 (2001).

529. Yu, W. *et al.* Kir2.1-mediated membrane potential promotes nutrient acquisition and inflammation through regulation of nutrient transporters. *Nature Communications* **13**, 3544 (2022).

530. Fulton, S.A., Martin, T.D., Redline, R.W. & Boom, W.H. Pulmonary Immune Responses during Primary Mycobacterium bovis– Calmette-Guerin Bacillus Infection in C57Bl/6 Mice. *American Journal of Respiratory Cell and Molecular Biology* **22**, 333-343 (2000).

531. Lewis, K.N. *et al.* Deletion of RD1 from Mycobacterium tuberculosis mimics bacille Calmette-Guérin attenuation. *The Journal of infectious diseases* **187**, 117-123 (2003).

532. Lin, J. *et al.* Early secreted antigenic target of 6-kDa of Mycobacterium tuberculosis promotes caspase-9/caspase-3-mediated apoptosis in macrophages. *Molecular and Cellular Biochemistry* **457**, 179-189 (2019).

533. Mishra, B.B. *et al.* Mycobacterium tuberculosis protein ESAT-6 is a potent activator of the NLRP3/ASC inflammasome. *Cellular Microbiology* **12**, 1046-1063 (2010).

534. Rhoades, E.R., Frank, A.A. & Orme, I.M. Progression of chronic pulmonary tuberculosis in mice aerogenically infected with virulent Mycobacterium tuberculosis. *Tubercle and Lung Disease* **78**, 57-66 (1997).

535. Chakraborty, D. *et al.* Leishmania donovani Affects Antigen Presentation of Macrophage by Disrupting Lipid Rafts. *The Journal of Immunology* **175**, 3214-3224 (2005).

536. Roy, K., Ghosh, M., Pal, T.K., Chakrabarti, S. & Roy, S. Cholesterol lowering drug may influence cellular immune response by altering MHC II function. *Journal of Lipid Research* **54**, 3106-3115 (2013).

537. Hughes, D.A., Townsend, P.J. & Haslam, P.L. Enhancement of the antigen-presenting function of monocytes by cholesterol: possible relevance to inflammatory mechanisms in extrinsic allergic alveolitis and atherosclerosis. *Clinical and Experimental Immunology* **87**, 279-286 (2008).

538. Neubert, P. *et al.* HIF1A and NFAT5 coordinate Na+-boosted antibacterial defense via enhanced autophagy and autolysosomal targeting. *Autophagy* **15**, 1899-1916 (2019).

539. Li, L., Tan, J., Miao, Y., Lei, P. & Zhang, Q. ROS and Autophagy: Interactions and Molecular Regulatory Mechanisms. *Cellular and Molecular Neurobiology* **35**, 615-621 (2015).

540. Scherz-Shouval, R. & Elazar, Z. Regulation of autophagy by ROS: physiology and pathology. *Trends in Biochemical Sciences* **36**, 30-38 (2011).

541. Sarathy, J.P. *et al.* Extreme Drug Tolerance of Mycobacterium tuberculosis in Caseum. *Antimicrobial Agents and Chemotherapy* **62**, e02266-02217 (2018).

542. Prideaux, B. *et al.* The association between sterilizing activity and drug distribution into tuberculosis lesions. *Nature Medicine* **21**, 1223-1227 (2015).

543. Lauvau, G. & Hohl, T.M. Monocyte-mediated defense against bacteria, fungi, and parasites. Seminars in immunology; 2015: Elsevier; 2015. p. 397-409.

544. Sampath, P., Moideen, K., Ranganathan, U.D. & Bethunaickan, R. Monocyte Subsets: Phenotypes and Function in Tuberculosis Infection. *Frontiers in Immunology* **9** (2018).

545. Palmer, B.F. Regulation of potassium homeostasis. *Clinical Journal of the American Society of Nephrology* **10**, 1050-1060 (2015).

546. Parham, W.A., Mehdirad, A.A., Biermann, K.M. & Fredman, C.S. Hyperkalemia revisited. *Texas Heart Institute Journal* **33**, 40 (2006).